UNIVERSITÀ DEGLI STUDI DI TRIESTE

DIPARTIMENTO DI SCIENZE CHIMICHE E FARMACEUTICHE, UNIVERSITÀ DEGLI STUDI DI TRIESTE, TRIESTE (ITALY)

Time-dependent first-principle methods for photoinduced electronic processes in molecules and composite systems

---

Leonardo Biancorosso

Composition of the Committee

Prof.	**Ana Carmen ALBENIZ**	Universidad de Valladolid	
Dr.	**Valeria LANZILLOTTO**	Università di Trieste	
Dr.	**Silvia ONESTI**	ELETTRA Sincrotrone di Trieste	
Prof.	**Mariachiara PASTORE**	Université de Lorraine & CNRS	
Prof.	**Emanuele COCCIA**	Università di Trieste	Supervisor

UNIVERSITÀ DEGLI STUDI DI TRIESTE

Università Ca'Foscari Venezia

UNIVERSITÀ DEGLI STUDI DI TRIESTE
E
UNIVERSITÀ CA' FOSCARI DI VENEZIA

XXXVIII CICLO DEL DOTTORATO DI RICERCA IN

CHIMICA

Time-dependent first-principle methods for photoinduced electronic processes in molecules and composite systems

Settore scientifico-disciplinare:**CHIM/02**

DOTTORANDO / A
LEONARDO BIANCOROSSO

COORDINATORE
PROF. ENZO ALESSIO

SUPERVISORE DI TESI

PROF. EMANUELE COCCIA

ANNO ACCADEMICO 2024/2025

Abstract

Time-dependent first-principle methods for photoinduced electronic processes in molecules and composite systems

by Leonardo Biancorosso

Simulating light-molecule interactions is crucial for understanding fundamental processes in physics and chemistry. In this thesis, I employed electron-dynamics simulations to investigate molecular responses to electromagnetic fields, also including the influence of plasmonic nanoparticles. One of the explored topics is chirality. In particular, I examined how a gold nanoparticle alters the circular dichroism (CD) spectra of chiral molecules, observing a remarkable 20-fold signal enhancement in peridinin. I also explored the interaction of chiral light with an achiral system, endofullerene, where the encapsulated atom mediates angular momentum transfer and induces circular electronic motion. Time-resolved CD simulations are further applied to a molecular motor, linking spectral evolution with the structural pathway of its photoisomerization. Another important theme of this thesis is plasmon-mediated photocatalysis, i.e. how plasmonic excitations affects the fate of a photocatlytic reaction. In this context, I investigated the dehydrogenation of formic acid on the antenna reactor complex Au–Pd to generate molecular hydrogen. By studying the photoinduced electron dynamics of the adsorbed (on Pd) intermediate (HCOO*) also in presence of an Au nanorod, I provided a microscopic explanation, in terms of increased charge asymmetry on HCOO*, of the experimentally observed enhanced hydrogen production. Finally, I developed an original computational procedure for the calculation of excited–state NEXAFS spectra going beyond core–valence separation and applied it to probe the internal conversion of gas–phase thymine.

Abstract

Time-dependent first-principle methods for photoinduced electronic processes in molecules and composite systems

by Leonardo Biancorosso

La simulazione delle interazioni luce-molecola riveste un ruolo fondamentale nello studio dei processi fondamentali della fisica e della chimica. In questa tesi vengono impiegate simulazioni di dinamica elettronica per investigare la risposta molecolare ai campi elettromagnetici, anche includendo linfluenza esercitata da nanoparticelle plasmoniche. Una parte del lavoro è dedicata allo studio della chiralità. In particolare, è stato analizzato come una nanoparticella doro possa modificare gli spettri di dicroismo circolare (CD) di molecole chirali, mostrando un notevole incremento del segnale fino a venti volte nel caso della peridinina. È stata inoltre esaminata linterazione tra luce chirale e sistemi achirali, gli endofullereni, nel quale latomo incapsulato nel fullerene media il trasferimento di momento angolare e induce un moto circolare degli elettroni del sistema. Simulazioni CD risolte nel tempo sono state poi applicate a un motore molecolare, permettendo di correlare levoluzione spettrale al percorso strutturale di fotoisomerizzazione. Un ulteriore filone di ricerca riguarda la fotocatalisi mediata da plasmoni, ossia il modo in cui le eccitazioni plasmoniche influenzano lesito di una reazione fotocatalitica. In questo contesto è stata studiata la deidrogenazione dellacido formico sul complesso antenna-reattore Au-Pd finalizzata alla produzione di idrogeno molecolare. Lo studio della dinamica elettronica fotoindotta dellintermedio adsorbito (HCOO*) sul palladio, anche in presenza di un nanorod doro, ha permesso di fornire una spiegazione microscopica in termini di maggiore asimmetria di carica su HCOO* dell'aumentata produzione di idrogeno osservata nel sistema sperimentale. Infine, è stata sviluppata una procedura computazionale originale per il calcolo di spettri NEXAFS di stati eccitati, che supera lapprossimazione della separazione core-valenza. Tale metodologia è stata applicata allo studio del processo di conversione interna della timina in fase gassosa, consentendo di sondare la dinamica ultrarapida dei processi di rilassamento elettronico.

Contents

Chapter 1

Introduction

This work focuses on the theoretical and computational investigation of photoinduced electron dynamics in molecules and composite systems. In this introductory chapter, I present a concise overview of the main research topics explored throughout the three years of my PhD project. Section 1.1 provides a brief introduction to light-matter interactions in general terms. Section 1.2 discusses the key phenomena that emerge at the molecular scale, with particular emphasis on the concept of chirality and on core spectroscopy. Section 1.3 addresses light-matter interactions at the nanoscale, with a specific focus on plasmon-enhanced electronic circular dichroism (ECD) and plasmon-assisted photocatalysis.

1.1 Light–Matter Interaction

The interaction of light with matter lies at the heart of modern science, shaping fundamental discoveries in physics, chemistry, and biology. Understanding and controlling this interaction is crucial not only for studying and characterizing materials, but also for designing systems with custom optical and electronic properties [1]. At its foundation, light-matter coupling arises from the dynamics between photons, electrons, and vibrations/phonons, producing a wide range of excitations and phenomena [2, 3]. These mechanisms highlight the complexity of microscopic processes and also serve as the basis for technological developments.

1.2 Molecular systems

At the molecular level, the light-matter interaction fundamentally arises from the interplay of the degree of freedom of the system–such as electrons and nuclei–with the external electromagnetic environment [4] (Figure 1.1). A first–principles theoretical description of these phenomena requires a unified framework which combines electronic structure theory with electrodynamics [5]. In principle, a complete description of light-matter interactions requires the framework of quantum electrodynamics (QED)[6], in which both the matter and the electromagnetic field are quantized.

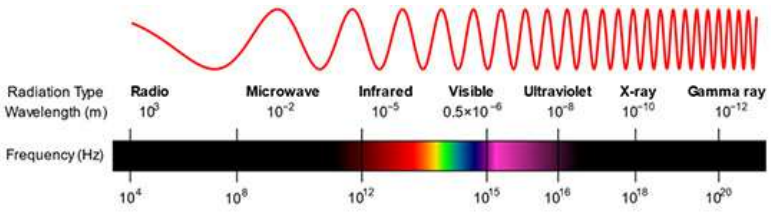

Spectral Region	Technique	Transition	Units
Gamma Ray	Mixed Gamma	Nuclear	MeV/keV
X-ray	Absorption/Fluorescence	Core Electrons	keV/eV
UV-VIS	Absorption/Fluorescence	Valence Electrons	nm/
Infrared	Absorption	Vibrations	cm^{-1}
Microwave	Absorption	Rotations	MHz/GHz/THz/cm^{-1}

FIGURE 1.1: Overview of spectroscopic techniques. Source: https://andor.oxinst.com/learning/view/article/fundamentals-of-spectroscopy-history-explanations-and-applications.

However, a semiclassical approach is typically adopted, where the electronic degrees of freedom are treated quantum mechanically, while the electromagnetic field is represented as a deterministic classical wave [7]. This framework, which underlies both linear response theory and real–time electronic dynamics, is sufficient to accurately describe most standard spectroscopic processes, while neglecting purely quantum features of the field, which need to be considered in strong coupling regime. In this semiclassical picture, the Hamiltonian of a molecular system written in length gauge in presence of an external electric field $\vec{F}(t)$, which is coupled to the molecule dipole operator $\vec{\hat{\mu}}$, is written as:

$$\hat{H}(t) = \hat{H}_0 - \vec{\hat{\mu}} \cdot \vec{F}(t). \tag{1.1}$$

An immediate consequence of introducing the interaction term is that the Hamiltonian becomes explicitly time–dependent [7]. In this condition, the stationary eigenstates of $\hat{H}_0$ are no longer sufficient to describe the dynamics. Instead, the system evolves as a superposition of states whose populations change in time, e.g. requiring the full solution of the time–dependent Schrödinger equation (TDSE, see Section 2.1.1 in Chapter 2). To better understand how the external field couples to the system, it is useful to introduce the concept of transition dipole moments [2]. By expanding the dipole operator $\hat{\mu}$ in the basis of the eigenstates of $\hat{H}_0$, one obtains the matrix elements

$$\mu_{\lambda\lambda'} = \langle \lambda | \hat{\mu} | \lambda' \rangle, \tag{1.2}$$

which quantify the strength of the interaction between two (electronic, vibronic or vibrational) states. Only transitions with non-vanishing $\mu_{\lambda\lambda'}$ can be induced by the field. The selection rules governing the dipole operator, together with the relative orientation between the molecular dipole and the field polarization, determine

which processes are allowed and how efficiently they occur[2].

At this point it is necessary to categorize the landscape of this interaction into two different regimes: linear and nonlinear. This distinction is based on the proportionality of the material response to the strength of the perturbation electric field. Linear optics operates at low intensities where the material response is directly proportional to the field strength, and the principles of superposition and additivity hold. In contrast, nonlinear optics emerges at high pulse intensities, where this proportionality breaks down, leading to more complex and non–additive interactions [8, 9, 10, 3]. In this thesis the investigated phenomena regarding spectroscopy and photocatalysis refer only to linear response so we will focus on the description of the fundamental processes occurring in this regime.

1.2.1 Chirality

Chirality is the geometrical property of an object which cannot be superimposed with its mirror image by any translation or rotation. This peculiar characteristic is omnipresent in nature, from elementary particles to astronomical objects. In chemistry, we name two chiral molecules which are non–superimposable images as enantiomers. They show the exact same chemical and physical properties but act different in a chiral environment and have opposite optical rotation. When enantiomers interact with circularly polarized light, one enantiomer rotates the plane clockwise, while the other one rotates the plane anticlockwise.

The concept of chirality is extremely important for a great number of fields such as drug design, catalysis, as well as for enantioselective synthesis and chiral sensing [11, 12, 13]. This concept not only encompasses molecules and materials but also light [14, 15, 16, 17].

Focusing on the spectroscopical response of chiral molecules we can define circular dichroism (CD) as the differential absorption of left–, and right–handed circularly polarized light, A_L and A_R respectively, by a chiral molecule:

$$\mathrm{CD} = A_L - A_R. \tag{1.3}$$

In this context many different types of chiral light–matter interactions can be studied and investigated, such as electronic absorption, vibrational absorption or luminescence. This led to the rising of many different spectroscopic techniques based on these different interactions, such as ECD and optical rotatory dispersion (ORD), [18] vibrational CD [19] or circularly polarized luminescence [20]. The investigation reported in this thesis only refers to ECD.
To follow the evolution of ECD features over time, it is necessary to move from static to time-resolved ECD (TR–ECD) spectroscopy. The accessible timescales depend on the process under investigation. In the femtosecond regime, molecular vibrations

and bond–breaking events can be resolved, often acting as the trigger for conformational changes. Processes such as fluorescence and excited–state dynamics are typically probed on the picosecond scale, while structural rearrangements in proteins and other complex systems generally require nanosecond resolution [21]. Although large–scale modifications occur on much longer timescales [22], local structural changes in proteins and macromolecules can be captured already in the femtosecond and picosecond regimes. Achieving such resolutions requires pump–probe experiments. In pump-probe spectroscopy, the sample is first excited by an initial laser pulse (the pump), and its subsequent evolution is monitored by a delayed second pulse (the probe). Capturing processes on the femtosecond and picosecond timescale requires theoretical approaches capable of resolving the ultrafast electronic changes that take place in the system.
Circularly polarized light interacting with an achiral target has been studied in Section 3.1 of Chapter 3, while a preliminary study of TR-ECD is reported in Section 3.2 of Chapter 3.

1.2.2 NEXAFS

In the X-ray regime, electrons from core orbitals localized on specific atoms are excited up to unoccupied molecular orbitals or ejected by ionizing the system. In Near Edge X-ray Absorption Fine Structure (NEXAFS) spectroscopy we sample a region of absorption which goes from below the edge of ionization up to 50 eV above the edge. NEXAFS has emerged as a powerful technique for investigating the molecular and electronic structure of materials at surfaces and interfaces. This technique is particularly valuable in organic materials and thin film studies, where it enables detailed understanding of molecular orientation, chemical composition, and electronic state distribution [23, 24, 25, 26]. This technique offers several advantages: (1) since X-ray absorption involves the excitation of core electrons, the method is element-specific; (2) the spectral features are highly sensitive to the local electronic environment, revealing the extent of adsorbate-surface interactions; (3) transitions obey dipole selection rules, making it possible to determine molecular orientation by tuning the incidence angle of polarized synchrotron radiation; and (4) the high brightness of synchrotron sources enables measurements even at submonolayer coverages. [26].
This technique can be used in combination with transient absorption spectroscopy and it is therefore named time–resolved NEXAFS (TR–NEXAFS) [27]. In this configuration, it is possible to probe not only the ground state but also valence excited states, by selectively exciting valence electrons to unoccupied orbitals [28, 29, 30]. Original contribution to TR-NEXAFS is provided in Chapter 5.

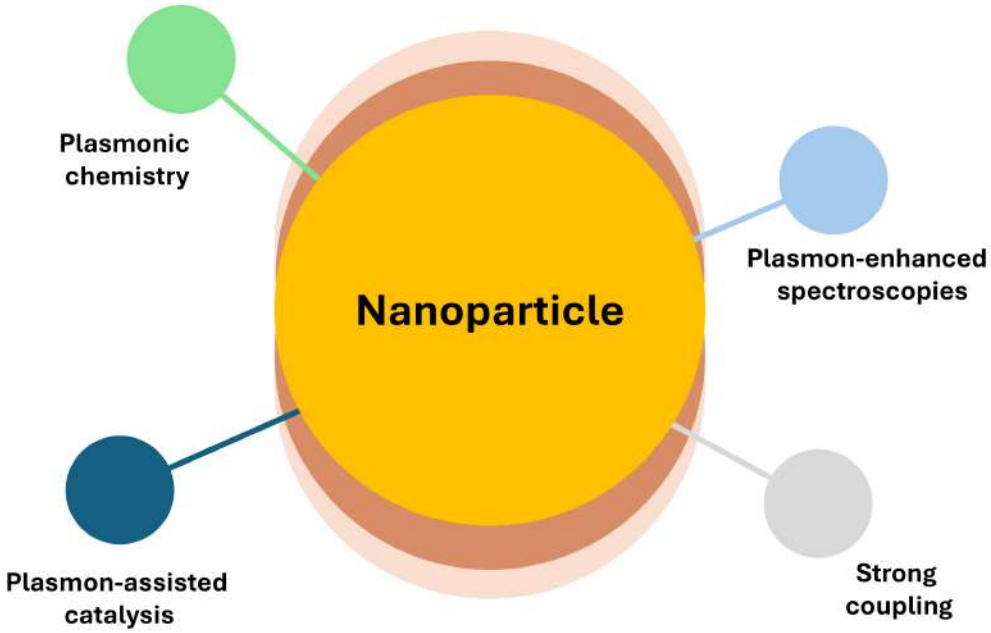

FIGURE 1.2: Schematic overview of the field of molecular nanoplasmonics.

1.3 Nanoplasmonics

When moving from molecules to systems at the nanoscale, light-matter interaction acquires qualitatively new features [31]. In specific metal nanostructures, the collective oscillations of valence electrons-known as plasmons-dominate the optical response. When they are confined to the surface of metallic nanoparticles (NPs), they are called localized surface plasmon resonances (LSPRs) [32]. Excitation of these modes produces extraordinary effects, including enhanced absorption and scattering, as well as the confinement of light below the diffraction limit [1]. Such capabilities have enabled nanoscale manipulation of light in ways inaccessible to bulk systems.

Plasmon decay further enriches the physics of these systems, producing energetic carriers and local heating through electron-electron and electron-phonon scattering processes [33]. These mechanisms can profoundly influence chemical pathways, driving new types of reactions through plasmon-mediated effects [32, 34]. This concept has given rise to the field of plasmonic chemistry, where plasmonic excitations are exploited to stimulate and control chemical transformations in potentially more efficient and sustainable ways [35].

Interesting phenomena occur when we place a molecular system close to plasmonic NPs. The convergence of molecular excitations with plasmonic modes defines the emerging field of molecular nanoplasmonics [36] (Figure 1.2). When molecules

are placed near metallic nanostructures and irradiated by light, their intrinsic properties can be profoundly reshaped by coupling to NP LSPRs. Experiments have shown that this interaction alters molecular absorption spectra and chemical reactivity [37, 38, 39, 40, 41, 42, 43, 44, 45], revealing a powerful route for tailoring matter through optical means.

The strength and nature of these effects are highly sensitive to the nanostructure geometry, size, and composition. By engineering these parameters, one can deliberately tune the molecular response, a feature that has motivated extensive exploration of NP designs in search of novel plasmon–induced functionalities. At the heart of this process lies the excitation of LSPRs [46, 47, 48]. Beyond amplifying local electromagnetic fields, LSPRs release substantial energy upon decay, providing an additional handle for driving chemical and physical processes [49, 50, 51, 52]. Molecular nanoplasmonics has grown into a rich research domain, encompassing diverse plasmon–assisted phenomena and experimental strategies. These include surface–enhanced Raman spectroscopy [53, 54], plasmon–modified fluorescence [39, 55], high–harmonic generation [56, 57, 58, 59], plasmon–induced CD [60, 61] and plasmon–driven photochemistry [62, 63]. Together, these advances highlight the transformative potential of NP-molecule interactions: by bridging the physics of nanoplasmonics with the chemistry of molecular systems, researchers are developing new strategies for controlling light, matter and energy at the smallest scales. Details regarding the application to plasmon–enhanced ECD and plasmon–assisted photocatalysis can be found respectively in Subsection 1.3.1 and 1.3.2.

The field of molecular nanoplasmonics encompasses a broad range of applications, exploiting the strong and localized electromagnetic fields generated by plasmonic nanostructures to manipulate molecular properties and processes [53, 64, 65]. Thanks to the computational developments carried out in recent years within our group in Trieste, we have been able to investigate in a systematic and predictive way the influence of an external NP on molecular systems [66, 67, 68, 69, 70]. In particular, our work has focused on two main areas: spectroscopy and photocatalysis.

On the one hand, plasmonic NPs can strongly modify and enhance molecular spectroscopic signals by amplifying the local electromagnetic field experienced by the molecule, as in the case of plasmon–enhanced ECD [61] (see Section 3.3 of Chapter 3). On the other hand, the interaction between molecules and the plasmonic near field can significantly alter excited–state dynamics and reactivity, enabling plasmon–assisted photocatalysis, where plasmonic effects are harnessed to modulate chemical transformations at the nanoscale [71] (see Chapter 4).

1.3.1 Plasmon-enhanced ECD

One of the most striking plasmonic effects is the remarkable amplification of otherwise weak molecular signals, as in the case of the aforementioned SERS. A similar

principle applies to chiroptical responses: the inherently weak CD signal of chiral molecules can be strongly enhanced when they interact with plasmonic nanostructures. This enhancement makes detection feasible even at very low concentrations [72, 73, 74, 75] Modulation of the CD signal by plasmonic NPs has been extensively investigated due to the relevance of the spectroscopic techniques related to this property in chemistry and physics. Plasmonic systems exhibiting chiroptical activity can be broadly classified into three categories: NPs with intrinsic structural chirality [76, 77, 78, 79, 80, 81], achiral NPs interacting with a chiral molecular system [61, 64, 82, 83, 84, 85, 86, 87, 88, 89, 90, 91], and chiral superstructures formed by assemblies of otherwise achiral NPs [92, 93, 94, 95, 96, 97]. In the last years many experimental works have investigated the enhanced sensitivity and response of chiral molecules in presence of NPs [98, 99, 100, 101, 102, 103, 104, 105]. Concurrently, a number of theoretical works have studied this interaction, mostly using a dipole–like description of the chiral molecule within a master equation [61, 106, 107, 64, 105, 82, 83, 84, 73, 85, 86, 108, 60, 87, 109, 110, 90, 111].

In my investigation, I focus on systems where an achiral NP interacts with a chiral molecule, producing characteristic modifications in the molecular CD spectrum. Such interactions can either enhance existing molecular peaks or generate new spectral features at the plasmonic resonance [61]. The enhancement mechanism arises from the combined action of the external field and the NP induced field, with its effectiveness depending on polarization and the energy difference between molecular excitations and the plasmonic frequency. The degree of CD enhancement can span a very broad range - from only a few units up to several thousand - depending on multiple factors. Key parameters include the intrinsic properties of the chiral molecule, the size, geometry, and material of the NP, as well as the spatial orientation of the molecule with respect to the NP [98, 99, 100, 101, 102, 103, 104, 105]. The methodology developed within our group in Trieste enables us to move beyond the conventional dipole–like representation of the molecule, allowing for a more accurate description of its interaction with an external NP. By combining electronic dynamics simulations of the molecular system with a simplified yet effective representation of the NP, we are able to investigate how the presence of the NP modifies the ECD response of the molecular system. This approach provides direct access to the ECD spectra in the coupled system.

1.3.2 Plasmon-mediated photocatalysis

Photocatalysis represents a transformative area of chemistry and materials science, exploiting light energy to drive chemical transformations. In essence, a photocatalyst absorbs photons, undergoes electronic excitation, and subsequently transfers

this energy to adsorbed molecules, thereby initiating a catalytic process. This mechanism underpins a wide range of applications, including environmental remediation, solar–to–chemical energy conversion, and the design of novel functional materials.

The heterogeneous photocatalytic process is inherently complex, involving multiple interdependent steps such as adsorption, photoexcitation, charge separation, and bond breaking/formation [112, 113]. Its efficiency is strongly influenced by external factors, including the chemical nature of the substrate, pH, temperature, and the presence of oxygen or other reactive species [114, 115]. The ability to manipulate chemical processes has expanded significantly through the interaction of target molecular systems with nanostructures. Plasmon–driven photocatalysis represents a striking example, demonstrating how the integration of nanostructured components can unlock new pathways and enhance chemical reactivity in ways unattainable by conventional approaches. [65, 116, 117, 118, 119, 120]. Once a plasmon is excited, the collective oscillation of conduction electrons undergoes decay through Landau damping, generating electron–hole pairs that effectively store the plasmon energy. These carriers rapidly thermalize, resulting in a hot Fermi–Dirac distribution of electrons and holes at temperatures higher than that of the surrounding lattice. The excess carrier energy is subsequently dissipated to the lattice through electron–phonon scattering, leading to heating effects [121, 122, 123, 33, 124]. Such hot–carrier dynamics are not only relevant to energy dissipation but also play a crucial role in modifying chemical reactivity. In the proximity of a metallic nanostructure, photochemical reactions can be enhanced or altered by the generation and transfer of hot carriers into adsorbed molecules [34]. Over the past decade, both experimental and theoretical studies have shed light on the mechanisms behind hot–carrier formation and transfer [125, 126, 52].
Two main pathways for carrier transfer can be distinguished:

1. Indirect transfer, in which hot carriers are first generated within the nanostructure and subsequently injected into molecular orbitals.

2. Direct transfer, where the plasmon decay itself drives an electronic transition from metal states into the unoccupied orbitals of the molecule.

In Fig. 1.3, a scheme of the carrier transfer mechanism is reported. In the field of photocatalysis, these processes are exploited to build hybrid systems which enhance the formation rate of the reaction product. Nanostructures with well–known plasmonic features such as Ag, Au and Al are exploited as light harvesters, and coupled to smaller transition–metal clusters (e.g., Pd, Pt, Fe, Ru), which are already widely employed as efficient catalysts in heterogeneous reactions. These conventional transition–metal systems exhibit highly favorable electronic properties, making them exceptionally effective at adsorbing molecules and promoting surface chemical transformations, while also offering improved selectivity compared to

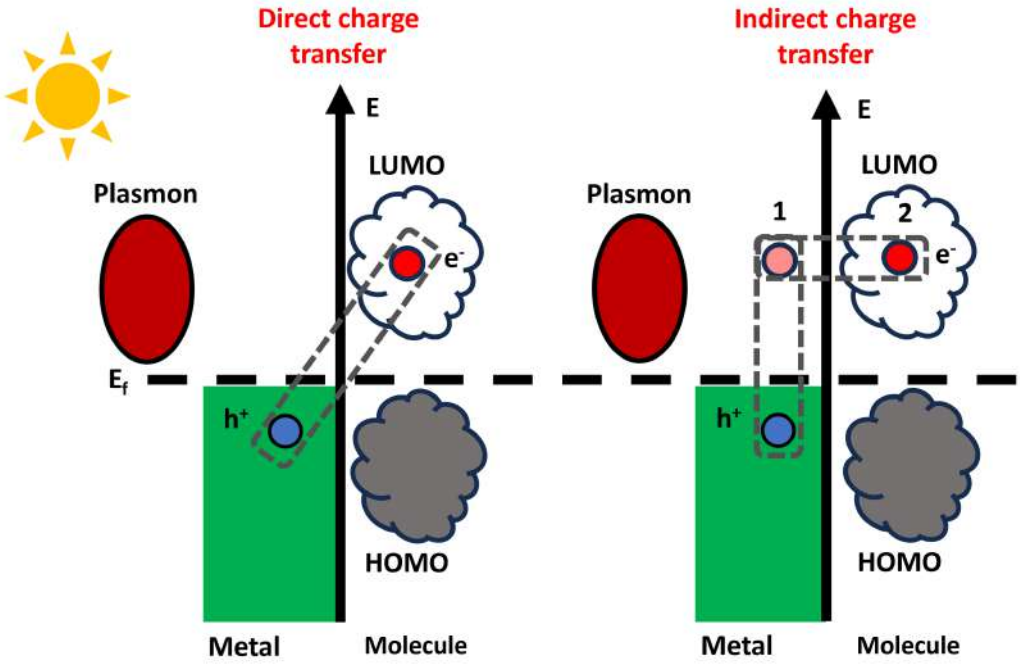

FIGURE 1.3: Scheme of the carrier transfer mechanism between a metal surface and a molecular system.

purely thermal processes. Their main limitation, however, lies in their weak interaction with light, which hinders their ability to enhance (photo)catalytic performance. Conversely, plasmonic metals display only modest intrinsic catalytic activity, yet they are capable of sustaining LSPRs with large optical cross–sections. This property enables them to generate intense electromagnetic field enhancements in their immediate surroundings, providing a powerful means of coupling light with catalytic processes [36, 127, 128, 32, 66, 129, 130]. Combining these two systems to form "antenna–reactor" complex allows us to get the best out of the two subsystem [71, 131]. The plasmonic nanoantenna serves as a light–harvesting unit that amplifies absorption in the nearby catalytically active reactor. When exposed to an external electromagnetic field, the antenna generates a strong optical near field that induces polarization in the reactor particle, effectively exciting a plasmon within it. The decay of this induced plasmon leads to the generation of hot carriers, which enable access to alternative reaction pathways that are otherwise energetically unfavorable. This process reduces activation barriers while simultaneously enhancing reaction selectivity.

It is important to emphasize how complex it is to identify a plasmon–mediated photocatalytic process in which hot carriers play a role from one in which the production rate is enhanced by photothermal effects.

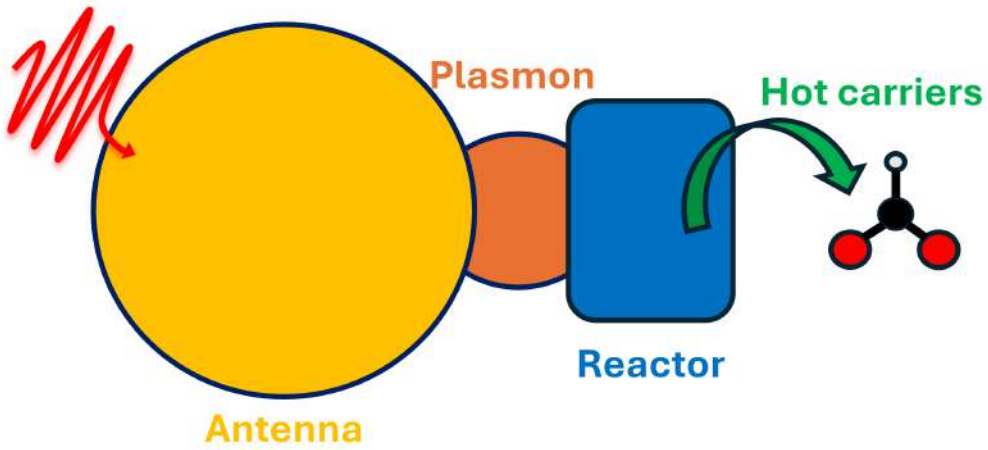

FIGURE 1.4: Schematic representation of the antenna–reactor complex.

1.4 Outline

This thesis is structured to first present the theoretical methodologies and their implementations (Chapter 2), followed by the results of my research (Chapters 3–5). Each chapter reports the work related to the most important topics of my thesis. They are written reporting scientific articles (published, submitted, or in preparation) related to the corresponding topic. To ensure clarity, every article is preceded by a short introduction where I also outline my personal contributions to the work.

Chapter 3 presents a detailed study on my investigation on chirality. This topic has been addressed in different ways:

- **Laser–Induced Charge Migration**: in this work I investigated the interaction between chiral light and endohedral fullerenes. This study was carried out under the supervision of Professor Jean Christophe Tremblay, during my stay at the Université de Lorraine in Metz, France.
- **Time–Resolved ECD**: this work presents preliminary results from a collaborative project with Professor Ali Hassanalis group at ICTP in Trieste. Here, we combined non-adiabatic molecular dynamics (NAMD) with TR-ECD spectroscopy to follow the photodynamics of a molecular motor during its photoisomerization process.
- **Plasmon effects in molecular ECD**: this work explores plasmon-enhanced ECD, where we examined how the presence of an external NP modifies the ECD spectra of chiral molecules.

Chapters 4 is devoted to the analysis of plasmon-assisted photocatalysis. Based on the work of Ref. [132], we modeled an antenna–reactor complex made by a Au nanorod tipped with Pd. This system has been observed to enhance the production of H_2 in the formic acid dehydrogenation reaction [132]. In this chapter two works devoted to the analysis of this system are reported:

- Simulating the reactor: in this work I report the investigation on the electron dynamics of the catalytic system, i.e. Pd, emphasizing the influence of the topology of the metal cluster and the key electronic processes triggered by light in the molecular system.
- Role of the Au nanorod: this section extends this study by introducing a plasmonic nanorod into the catalytic system. Here, we investigated how the plasmonic effect modifies the electronic dynamics and demonstrated that the enhanced photocatalytic activity can be directly attributed to the presence of the nanorod.

Chapter 5 (**Probing fast internal conversion in gas-phase thymine via TR-NEXAFS**) introduces a study on TR-NEXAFS spectroscopy. Using a time-domain computational approach within the theory of open quantum systems, we computed the excited–state spectra of gas–phase thymine, thus probing its fast internal conversion.

In Chapter 6 I sum up all the relevant findings from this thesis.

Chapter 2

Theoretical framework

In this chapter, we introduce the theoretical and computational methods employed to simulate real–time electron dynamics in molecular and composite systems. We begin in Section 2.1.1 with the description of the TDSE, which provides the fundamental framework for modeling photoinduced processes, and its stochastic extension (Section 2.1.2) for treating open quantum systems. An alternative density–matrix approach, based on the Liouville-von Neumann equation, is also presented (Section 2.1.3).

In Section 2.2, we describe the polarizable continuum model for NPs (PCM–NP), which accounts for the electromagnetic response of nanostructures. Both frequency–domain and time–domain formulations are reviewed, highlighting their role in coupling quantum systems to plasmonic environments.

Section 2.3 discusses how the TDSE is coupled to PCM-NP, yielding a real–time quantum/classical framework for simulating molecules in the presence of NPs. The equilibration procedure and computational workflow are outlined.

In Section 2.4, we present the computational tools used to interpret electronic dynamics. In particular, we describe the evaluation of absorption and ECD from real–time propagation, the computation of time–dependent projected density of states (ΔPDOS) for tracking charge populations and transient electronic density to track electronic motions along the dynamics.

Finally, Section 2.5 reports the computational details of the simulations, with emphasis on the AMS-WaveT interface that was developed and extended during this project. Key implementations include the calculation of transition potentials, transition dipole moments among excited states, and MPI parallelization strategies to enable large-scale simulations.

2.1 Real–Time Electron Dynamics

2.1.1 TDSE

In the length gauge, TDSE can be expressed as:

$$i\frac{d}{dt}\left|\Psi(t)\right\rangle = \hat{H}(t)\left|\Psi(t)\right\rangle, \tag{2.1}$$

where $|\Psi(t)\rangle$ represents the time-evolving wavefunction, while $\hat{H}(t)$ denotes the time-dependent Hamiltonian operator.

The Hamiltonian is typically partitioned into a field–free contribution and a time–dependent interaction term:

$$\hat{H}(t) = \hat{H}_0 + \hat{H}_F(t), \tag{2.2}$$

with $\hat{H}_0$ corresponding to the Hamiltonian of the isolated system and $\hat{H}_F(t)$ describing the coupling to an external field. Within the semiclassical approximation, the molecule interacts with a classical electromagnetic pulse. The interaction term coupling $\hat{H}_F(t)$ is given by

$$\hat{H}_F(t) = -\vec{\hat{\mu}} \cdot \vec{F}(t), \tag{2.3}$$

with $\vec{\hat{\mu}}$ the electric dipole operator and $\vec{F}(t)$ the electric field, as mentioned in the Introduction. In this formulation, field-free $\hat{H}_0$ is identified with the electronic Hamiltonian $\hat{H}_{el}$ of the molecule in the absence of an external perturbation.

The wavefunction in Eq. 2.1 can be expanded in terms of the N_{states} eigenstates of $\hat{H}_0$ as

$$\left|\Psi(t)\right\rangle = \sum_{\lambda=0}^{N_{\text{states}}-1} C_\lambda(t)\left|\lambda\right\rangle, \tag{2.4}$$

where $C_\lambda(t)$ are the time-dependent expansion coefficients and $|\lambda\rangle$ denote the eigenstates of $\hat{H}_0$. Substituting this expansion into Eq. 2.1 leads to a matrix formulation of the TDSE:

$$i\frac{d\mathbf{C}(t)}{dt} = \mathbf{H}(t)\mathbf{C}(t), \tag{2.5}$$

with $\mathbf{C}(t)$ the coefficient vector and $\mathbf{H}(t)$ the matrix representation of the Hamiltonian at time t. The Hamiltonian matrix elements are given by

$$\left\langle\lambda'\right|\hat{H}(t)\left|\lambda\right\rangle = E_\lambda\delta_{\lambda'\lambda} - \sum_\gamma F_\gamma(t)\left\langle\lambda'\right|\hat{\mu}_\gamma\left|\lambda\right\rangle, \tag{2.6}$$

where E_λ are the eigenenergies of $\hat{H}_0$, and $\gamma = x, y, z$ labels the Cartesian components of the transition dipole moment.

The external electric field is modeled classically as

$$\vec{F}(t) = F_0\hat{n}f(t)g(\omega), \tag{2.7}$$

where F_0 is the peak amplitude, $\hat{n}$ is a unit vector that specifies the direction of polarization, $f(t)$ is an envelope function and $g(\omega)$ characterizes the frequency profile. In case of a kick pulse, g is simply a constant.

Even though the approach can be generally coupled to any level of theory for the electronic structure, in all works presented here we used a singly–excited ansatz:

$$|\lambda\rangle = d_0|\psi_0\rangle + \sum_{i}^{\text{occ}} \sum_{a}^{\text{vir}} d_{i,\lambda}^{a} |\psi_i^a\rangle, \tag{2.8}$$

where $|\psi_0\rangle$ denotes the ground-state Slater determinant, and $|\psi_i^a\rangle = \hat{a}_a^\dagger \hat{a}_i |\psi_0\rangle$ represents a singly-excited configuration obtained by promoting an electron from an occupied orbital i to a virtual orbital a. The coefficients d_0 and $d_{i,\lambda}^a$ are expansion parameters that specify the electronic structure of $|\lambda\rangle$. The algebraic expression of Eq. 2.5 is then propagated according to a second-order Euler algorithm [133, 134].

The electronic dynamics simulations are carried out using the WaveT code [135], which has recently been interfaced with the Amsterdam Modeling Suite (AMS) [136]. More details on the interface and computational procedures are provided in Section 2.5.

2.1.2 Stochastic Schrödinger equation

WaveT implements the theory of open quantum systems [137] via the Stochastic Schrödinger Equation (SSE) [138]. The theory of open quantum systems provides a framework to include environmental effects on the system degrees of freedom. In the Markovian limit, the environment equilibrates much faster than the system, and its correlation function reduces to a Dirac delta [138].

The corresponding SSE is

$$i\frac{d}{dt}|\Psi_S(t)\rangle = \hat{H}_S(t)|\Psi_S(t)\rangle \sum_{q}^{M} l_q(t)\hat{S}_q|\Psi_S(t)\rangle - \frac{i}{2}\sum_{q}^{M}\hat{S}_q^\dagger \hat{S}_q|\Psi_S(t)\rangle, \tag{2.9}$$

where $\Psi_S(t)$ is the time-dependent system wavefunction and $\hat{H}_S(t)$ is the system Hamiltonian described in Eq. 2.2, the $\hat{S}_q$ operators describe system–environment interactions, and $l_q(t)$ are white–noise fluctuations. The non–Hermitian term accounts for dissipation, while the stochastic term models fluctuations.

The reduced density matrix of the system is defined by tracing out the environment (E) degrees of freedom from the full density matrix $\hat{\rho}(t)$

$$\hat{\rho}_S(t) = \text{Tr}_E \hat{\rho}(t), \tag{2.10}$$

and can be recovered as the ensemble average of N_{traj} stochastic trajectories:

$$\hat{\rho}_S(t) = \frac{1}{N_{\text{traj}}} \sum_j |\Psi_{S,j}(t)\rangle\langle\Psi_{S,j}(t)|. \tag{2.11}$$

In the limit of numerous SSE trajectories, the density matrix converges to that from the Lindblad equation [139]. Diagonal and off-diagonal elements define populations and coherences, respectively.

System–environment coupling is described through channels q, identified in our approach with system states λ. In WaveT three different interaction channels are implemented [134, 140, 141, 135, 142], i.e. radiative and nonradiative decay, and pure dephasing.
We focus here only on the nonradiative decay, which has been used in Chapter 5 to mimic internal conversion and consequent population transfer in time–resolved NEXAFS. The relaxation operator we have employed is

$$\hat{S}_\lambda^{nr} = \sqrt{\Gamma_\lambda^{nr}}|0\rangle\langle\lambda|, \tag{2.12}$$

with Γ_λ^{nr} being the decay rate from experiments or nonadiabatic nuclear dynamics. Even though a vibronic basis and corresponding Γ_λ^{nr} operators have been introduced [141], here we assume the degrees of freedom of the system are the pure electronic ones.

SSE propagation is implemented via the quantum jump algorithm [143, 144, 145] and details are provided in Refs [134, 140, 141].

2.1.3 Liouville-von Neumann equation

An alternative approach to modeling ultrafast electron dynamics is through the Liouville-von Neumann equation for many-body systems. In my work at the Université de Lorraine in Metz, under the supervision of Professor Tremblay, we applied this method to investigate laser-induced phenomena in endofullerene systems (see Section 3.1 in Chapter 3).

Within this framework, ultrafast electron dynamics is described using a hybrid time-dependent density functional theory/configuration interaction (TDDFT/CI) approach [146, 147].

The time-dependent state of an N-electron system is described by its reduced density matrix $\hat{\rho}_S(t)$, which evolves according to the Liouville-von Neumann equation [148]:

$$\partial_t\hat{\rho_S}(t) = -\frac{i}{\hbar}\left[\hat{H}_0, \hat{\rho_S}(t)\right] + \frac{i}{\hbar}\left[\hat{\mu}\cdot\vec{F}(t), \hat{\rho}_S(t)\right] - \left[\hat{W}, \hat{\rho}_S(t)\right]_+ . \tag{2.13}$$

Here, $\hat{H}_0$ denotes the electronic Hamiltonian in the clamped–nuclei approximation, as reported in Section 2.1.1. The operator $\hat{W}$ is a complex absorbing potential that accounts for electron loss through single ionization into the continuum. The coupling with the external electric field $\vec{F}(t)$ via the dipole operator $\hat{\mu}$ is introduced semiclassically. For a circularly polarized laser pulse with duration T and frequency ω, the field is expressed as

$$\vec{F}(t) = \sum_{\gamma=\{x,y,z\}} F_0^{(\gamma)} \sin^2(\pi t/T) \cos(\omega t + \varphi_\gamma)\hat{n}_\gamma \tag{2.14}$$

where $F_0^{(\gamma)}$ indicates the field amplitude along the direction $\hat{n}_\gamma$, and φ_γ represents the phase of the α component.

Within the hybrid TDDFT/CI framework, the spin-free, time-dependent N–electron density matrix is expanded in terms of N_{states} stationary singly excited many-body states, $|\lambda\rangle \equiv \lambda(\mathbf{r}^N)$, where $\mathbf{r}$ denotes electron coordinates in real space. Thus, the density matrix is written as

$$\hat{\rho}_S(t) = \sum_{\lambda=0}^{N_{\text{states}}} \sum_{\lambda'=0}^{N_{\text{states}}} \rho_{\lambda'\lambda,S}(t)\, e^{-i(E_\lambda^{(N)} - E_{\lambda'}^{(N)})t/\hbar} |\lambda\rangle\langle\lambda'| \,, \tag{2.15}$$

where $E_\lambda^{(N)}$ is the energy of state λ with N electrons. The field-free Hamiltonian is diagonal in the pseudo–CI basis. Each excited eigenstate $\lambda_m(\mathbf{r}^N)$ is expressed as a superposition of singly excited configuration state functions, as described in Eq. 2.8. A configuration state function corresponds to promoting one electron from an occupied orbital i into a virtual orbital a, relative to the KohnSham reference state. The transition amplitudes $d_{i,\lambda}^a$ are obtained from linear–response TDDFT. These are extracted from standard quantum chemistry outputs and post–processed with the open–source package detCI@ORBKIT [149]. Contributions with magnitude $|d_{i,\lambda}^a| < 10^{-3}$ are discarded before renormalization.

The absorbing potential $\hat{W}$ is expressed as a sum over projectors onto the pseudo–CI eigenstates:

$$\hat{W} = \sum_\lambda \frac{I_\lambda}{2} |\lambda\rangle\langle\lambda| \,, \tag{2.16}$$

where I_λ denotes the ionization rate of state λ. To characterize the coupling strength with the continuum, we follow the phenomenological model introduced in Refs. [150, 151, 146], defining

$$I_\lambda = \begin{cases} \frac{\sqrt{2(E_\lambda^{(N)} - E_{\text{ion}})}}{d} & \text{if } E_\lambda^{(N)} \geq E_{\text{ion}} \\ 0 & \text{otherwise} \end{cases} . \tag{2.17}$$

The ionization energy E_{ion} is obtained for each system as

$$E_{\text{ion}} = E_0^{(N)} - E_0^{(N-1)} \tag{2.18}$$

where $E_0^{(N)}$ is the ground-state energy of the N-electron system and $E_0^{(N-1)}$ is the ground-state energy of the $N-1$ system. The parameter d, interpreted as an escape length, is fixed to $1\,a_0$ in all calculations [150].

By substituting Eq. (2.15) into Eq. (2.13), we obtain the algebraic form

$$\frac{d\rho_{\lambda'\lambda,S}(t)}{dt} = \frac{i}{\hbar}\sum_{k=0}^{N_{\text{states}}} \vec{F}(t)\cdot\left(\mu_{\lambda' k}\rho_{k\lambda,S}(t) - \rho_{\lambda' k,S}(t)\mu_{k\lambda}\right) - \frac{1}{2}(I_{\lambda'} + I_{\lambda})\rho_{\lambda'\lambda,S}(t) \tag{2.19}$$

where the dipole matrix elements $\mu_{\lambda' k}$ are evaluated numerically using ORBKIT [152, 147, 149]. Equation (2.19) is integrated with an adaptive Runge-Kutta method using preconditioning [153]. The last term introduces an average ionization rate between two states, which results both in dephasing (exponential decay of off-diagonal terms of $\hat{\rho}_S(t)$) and in ionization loss (exponential decay of populations above threshold). Consequently, population is not conserved, and the norm deficit quantifies ionization.

2.2 PCM-NP

To describe the polarization dynamics of a NP, represented as a continuum medium interacting with a quantum system, we employ the TDPlas library [133, 135]. This code allows for the evaluation and propagation of the degrees of freedom associated with the NP polarization. The central approach implemented in TDPlas is based on the Polarizable Continuum Model (PCM) method extended to treat NPs [154, 155].

PCM is widely regarded as the standard approach in many computational frameworks for coupling a quantum-mechanical description of a molecular system with a continuum representation of its environment. [156, 157]. In the past three decades, it has been extensively refined and extended to describe diverse molecular processes and environments. [158, 159]. This approach has been adapted over the years also to account for metallic or dielectric NPs [160, 161, 162]. In this framework, the NP is represented as a homogeneous body, with its electromagnetic response to an external potential $\mathbf{V}(\omega)$ expressed in terms of induced apparent surface charge densities distributed over its surface. The numerical implementation follows the Boundary Element Method (BEM), which partitions the NP surface into small surface elements, or tesserae. Each tessera carries a polarization charge positioned at its geometric center, thus providing a discrete representation of the NP electromagnetic response.

Within this description, the field–free Hamiltonian is updated with respect to the previous Section and becomes

$$\hat{H}_0 = \hat{H}_{el} + \mathbf{q}^{\mathrm{GS}} \cdot \hat{\mathbf{V}} \tag{2.20}$$

where $\mathbf{q}^{\mathrm{GS}}$ denotes the polarization charges equilibrated with the molecular electronic ground state and $\hat{H}_{el}$ is the electronic Hamiltonian for the isolated molecular system (for a bare molecule $\hat{H}_0 \equiv \hat{H}_{el}$). The operator $\hat{\mathbf{V}}$ is associated with the molecular electrostatic potential calculated at the position of the charges on the NP surface. It accounts for both nuclear and electronic contributions, evaluated at the tessellation nodes where the polarization charges are located.

The equilibrium polarization charges are obtained from the electrostatic potential of the electronic ground state as

$$\mathbf{q}^{\mathrm{GS}} = \mathbf{Q}(0) \langle 0| \hat{\mathbf{V}} |0\rangle \tag{2.21}$$

where $\mathbf{Q}(0)$ is the BEM response matrix which can be expressed as

$$\mathbf{Q}(0) = -\mathbf{S}^{-1} \left(2\pi \frac{\epsilon_0 + 1}{\epsilon_0 - 1} + \mathbf{DA} \right)^{-1} (2\pi \mathbb{I} + \mathbf{DA}) \,. \tag{2.22}$$

Here, $\mathbf{S}$ and $\mathbf{D}$ are BEM matrices related to the Calderon projectors [161], $\mathbf{A}$ is diagonal with entries corresponding to tesserae areas, and ϵ_0 is the static dielectric constant. In practice, both $\hat{H}_0$ and the polarization charges must be determined self–consistently. This can be achieved either by an independent quantum chemistry calculation or by means of a preparatory WaveT/TDPlas run (see Section 2.3), which allows one to equilibrate the polarization charges not only with the ground state but also with other eigenstates of $\hat{H}_0$.

2.2.1 Frequency-domain formulation

In the quasi–static limit (neglecting retardation effects and spatial dependence of the pulse, which is a robust assumption for NP size of the order of few or tens of nm interacting with a UV–Vis light), the polarization charges in frequency space are expressed as

$$\mathbf{q}(\omega) = \mathbf{Q}(\omega)\mathbf{V}(\omega), \tag{2.23}$$

where the frequency–dependent response matrix is

$$\mathbf{Q}(\omega) = -\mathbf{S}^{-1} \left(2\pi \frac{\epsilon(\omega) + 1}{\epsilon(\omega) - 1} + \mathbf{DA} \right)^{-1} (2\pi \mathbb{I} + \mathbf{DA}) \,. \tag{2.24}$$

The array $\mathbf{V}(\omega)$ contains the external and reaction fields evaluated on the NP surface at frequency ω, while $\epsilon(\omega)$ is the dielectric function of the metal, which may

be parametrized by models such as Drude-Lorentz [133, 163, 164] or fitted to experimental data [69], as shown in Section 2.2.2.

2.2.2 Time-domain formulation

To couple the real–time evolution of a molecular wavefunction with the polarization dynamics of the NP, one must derive a practical equation of motion for the surface charges in the time domain from the following:

$$\mathbf{q}(t) = \int_{-\infty}^{+\infty} dt' \mathbf{Q}(t-t')\mathbf{V}(t'), \tag{2.25}$$

which is obtained as the Fourier transform of Eq. 2.23. Depending on how $\epsilon(\omega)$ is modeled, TDPlas employs two different strategies:

Model dielectric function (Drude–Lorentz or Debye). In this case, it is convenient to recast the BEM response matrix (Eq. 2.22) in a diagonal form by rewriting $\mathbf{S}^{-1/2}\mathbf{D}\mathbf{A}\mathbf{S}^{1/2}$ into $\mathbf{T}\Lambda\mathbf{T}^{\dagger}$. After some algebra, we can obtain a version of this equation in a diagonal representation which is written as

$$\mathbf{Q}(\omega) = -\mathbf{S}^{-1/2}\mathbf{T}\mathbf{K}(\omega)\mathbf{T}^{\dagger}\mathbf{S}^{-1/2}, \tag{2.26}$$

with kernel elements:

$$K_p(\omega) = \frac{2\pi + \lambda_p}{2\pi\frac{\epsilon(\omega)+1}{\epsilon(\omega)-1} + \lambda_p}, \tag{2.27}$$

here λ_p are the eigenvalues collected in Λ. The full derivation is reported in Ref [163]. Substituting $\epsilon(\omega)$ with an equation of the frequency, such as the Drude-Lorentz (DL), allows us to obtain the frequency-dependent kernel function

$$\epsilon(\omega) = 1 + \frac{\Omega_p^2}{\omega_0^2 - \omega^2 - i\gamma\omega}, \tag{2.28}$$

where Ω_p^2 is the squared bulk metal plasma frequency, ω_0 is the frequency of the bound oscillator and γ is a damping parameter. One can Fourier transform the kernel into the time domain and insert it into Eq. 2.25, leading to

$$\mathbf{q}(t) = -\int_{-\infty}^{+\infty} dt' \mathbf{S}^{-1/2}\mathbf{T}\mathbf{K}(t-t')\mathbf{T}^{\dagger}\mathbf{S}^{-1/2}\mathbf{V}(t'). \tag{2.29}$$

By differentiating Eq. 2.29, one finally arrives at the explicit equation of motion for the charges [133]:

$$\ddot{\mathbf{q}}(t) = -\gamma\dot{\mathbf{q}}(t) - \mathbf{Q}_{\omega}\mathbf{q}(t) + \mathbf{Q}_f\mathbf{V}(t), \tag{2.30}$$

with

$$\begin{aligned}\mathbf{Q}_\omega &= \mathbf{S}^{-1/2}\mathbf{T}(\omega_0^2 + \tfrac{\gamma}{4})(\omega)\mathbf{T}^\dagger\mathbf{S}^{-1/2},\\ \mathbf{Q}_f &= -\mathbf{S}^{-1/2}\mathbf{T}\frac{(2\pi+\Lambda)\Omega_p^2}{4\pi}\mathbf{T}^\dagger\mathbf{S}^{-1/2}.\end{aligned} \tag{2.31}$$

TDPlas integrates Eq. 2.30 using a velocity–Verlet scheme, which guarantees numerical stability. The complete derivation is reported in Ref. [133].

General dielectric function. When $\epsilon(\omega)$ cannot be represented by a simple analytical model, the response matrix cannot be diagonalized in the same way. Instead, the dielectric contribution is isolated in a scalar function

$$\mathbf{q}(\omega) = \frac{1}{2\pi} f(\omega)\mathbf{F}(\omega), \tag{2.32}$$

with

$$\mathbf{F}(\omega) = -\left[\mathbf{A}\mathbf{D}^*\mathbf{q}(\omega) + \mathbf{S}^{-1}(2\pi\mathbf{I} + \mathbf{D}\mathbf{A})\mathbf{V}(\omega)\right]. \tag{2.33}$$

The function $f(\omega)$ is then fitted with a sum of Drude-Lorentz-like poles,

$$f(\omega) = \frac{\epsilon(\omega)-1}{\epsilon(\omega)+1} \simeq \sum_{p=1}^{N} \frac{A_p}{\omega_p^2 - \omega^2 - i\gamma_p\omega}, \tag{2.34}$$

where the number N of the DL terms is defined by the number of the poles of the function $f(\omega)$. In this way the total charge is expressed as $\mathbf{q}(\omega) = \sum_p \mathbf{q}_p(\omega)$. Each pole contributes

$$\left(\omega_p^2 - \omega^2 - i\gamma_p\omega\right)\mathbf{q}_p(\omega) = \frac{A_p}{2\pi}\mathbf{F}(\omega). \tag{2.35}$$

After Fourier transformation, the time–domain equations read

$$\ddot{\mathbf{q}}_p(t) = -\omega_p^2\mathbf{q}_p(t) - \gamma_p\dot{\mathbf{q}}_p(t) + \frac{A_p}{2\pi}\mathbf{F}(t), \tag{2.36}$$

with the total polarization charge obtained as $\mathbf{q}(t) = \sum_p \mathbf{q}_p(t)$.

A comprehensive discussion of this formulation, including numerical strategies for propagation, is reported in Ref. [69]. At this point we can include in the time–dependent Hamiltonian from Eq. 2.2 the time–evolution of surface charges as:

$$\hat{H}(t) = \hat{H}_0 - \vec{\hat{\mu}}\cdot\vec{F}(t) + \mathbf{q}(t)\cdot\hat{\mathbf{V}} \tag{2.37}$$

where $\hat{\mathbf{V}}$ is the molecular electrostatic potential already introduced in Eq. 2.20.

Two main polarization effects are needed to correctly describe the time–dependent charges: one that includes the interaction with the external potential ($\mathbf{q}_{ref}$) and one that describes the interaction with the molecular potential ($\mathbf{q}_{pol}$).

$$\mathbf{q}(t) = \mathbf{q}_{ref}(t) + \mathbf{q}_{pol}(t) \tag{2.38}$$

The derivation of these two sets of charges follows directly the procedure outlined above, with the only difference being in the perturbation term present in Eq. 2.33.

This general approach has been applied in the works reported in this thesis, in particular in the works regarding plasmon–enhanced ECD (Section 3.3 of Chapter 3) and plasmon–assisted photocatalysis (Section 4.2 of Chapter 4) where the presence of an explicit gold nanostructure has been included in the electronic dynamics calculation.

2.3 Coupling TDSE with PCM-NP

In the last Section we introduced how, within the PCM framework, the polarization response of the nanostructure can be coupled to a quantum–mechanical description of the molecular electronic degrees of freedom (or of a selected active region). This multiscale scheme is denoted as the real–time PCM for nanostructures (RT–PCM–NP), and it is inherently time–dependent since it relies on solving the TDSE in real time. Details regarding this procedure are presented in Section 2.5.

TDPlas and WaveT are coupled by an interface to include the effect of a NP on the electronic dynamics of a molecular system. This interface is responsible for tasks such as reading and initializing the environmental parameters, and handling the mutual coupling between the quantum subsystem and the classical environment. My contribution lies instead in the coupling of WaveT/TDPlas with the AMS quantum-chemistry software, allowing us to extract all the information from the standard quantum chemistry outputs to generate the input files for the electronic dynamics calculations.

A key advantage of the methodology lies in its generality: the propagation of the TDSE does not depend on the details of the electronic–structure approach used for the isolated (field–free) problem. The computational workflow can be summarized in two steps: (i) choosing a basis set to represent the time–dependent wavefunction $|\Psi(t)\rangle$; (ii) propagating the TDSE in this space under the influence of both the nanostructure—treated at the PCM level through the BEM—and the external electromagnetic pulse.

In this framework, the TDSE maintains the formal structure of Eq. 2.1, with a time dependent Hamiltonian given by Eq. 2.37

Before the real–time propagation in presence of the NP, it is possible to obtain the equilibrated wavefunction with the NP in two possible ways: either as a post–processing step after the quantum–chemistry calculation [165, 67], or directly embedded within the electronic–structure code [140, 134]. In this thesis, we restrict our attention to the first approach, to which I have contributed directly. The equilibration

procedure reported below is general and common to both strategies; what differs is only the practical implementation used to obtain the equilibrated wavefunction.

The expansion of the NP–free wavefunction is the one presented in Eq. 2.4. The eigenstates of that expression do not contain any information regarding the external NP and for this reason they will be referenced as λ_{vac}.

The post processing step to include the light–off polarization with the NP correspond to a self–consistent equilibration which precedes the real–time propagation. This involves:

1. Selecting the subset of $|\lambda\rangle_{\text{vac}}$ states to define the active space of Eq. 2.4;
2. Minimizing the total energy of the coupled quantum (QM)/classical system. At this stage the nanostructure is assigned a set of equilibrium polarization charges $\mathbf{q}_{\text{eq}}^{GS}$, starting from the QM ground state. A new ground state can thus be written as $|0\rangle_{\text{eq}} = \sum_{\lambda'} a_{\lambda'}^{0} \, |\lambda^{'}\rangle_{\text{vac}}$;
3. With the equilibrium charges frozen, the operator $\hat{\mathbf{V}}_{\text{BEM}}$ defines a modified Hamiltonian which is diagonalized in the active space. This yields a new set of equilibrated excited states $|\lambda\rangle_{\text{eq}} = \sum_{\lambda'} a_{\lambda'}^{\lambda} \, |\lambda^{'}\rangle_{\text{vac}}$, together with their eigenenergies. These equilibrated states, along with the ground–state charges, form the starting point for TDSE propagation under the time–dependent Hamiltonian in Eq. 2.37.

The wavefunction expansion becomes

$$|\Psi(t)\rangle = \sum_{\lambda} C_{\lambda}^{\text{eq}}(t) \, |\lambda\rangle_{\text{eq}} \,, \tag{2.39}$$

with the relation between the two coefficient sets given by $C_{\lambda}^{\text{vac}}(t) = \sum_{\lambda'} a_{\lambda}^{\lambda^{'}} C_{\lambda'}^{\text{eq}}(t)$.

Once equilibration is established, one can define the transition electrostatic potential between two equilibrated states $|\lambda_{eq}^{'}\rangle$ and $|\lambda_{eq}\rangle$ at tessera T as

$$V_{\text{BEM}}^{\lambda_{\text{eq}}^{'},\lambda_{\text{eq}}}(\mathbf{R}_t) = \langle \lambda_{\text{eq}}^{'} | \frac{1}{|\mathbf{R}_t - \mathbf{r}|} | \lambda_{\text{eq}} \rangle + V_{nuc}(\mathbf{R}_t) \, \delta_{\lambda_{\text{eq}}^{'},\lambda_{\text{eq}}}, \tag{2.40}$$

where $V_{nuc}(\mathbf{R}_t)$ is the nuclear contribution at the tessera position $\mathbf{R}_t$.

The resulting time–dependent coefficients obtained from the electronic dynamics encode the effect of the NP on the molecular response. In Section 2.4, we will show how these coefficients can be exploited to compute observables such as absorption and ECD spectra, as well as ΔPDOS, thereby revealing the impact of the nanostructure on the systems properties and the transient electronic density and its time derivative which can be used to visualize the motions of electrons and holes over time.

2.4 Tools for dynamics analysis

A variety of theoretical and computational tools have been developed in the group to analyze the outcomes of electronic dynamics simulations [133, 166, 167]. In this chapter, I introduce the most relevant methods that I have employed throughout this thesis. I begin by describing the procedure used to compute electronic absorption and ECD spectra from the electron dynamics (Section 2.4.1). Subsequently, I present the ΔPDOS descriptor which enables us to monitor the time evolution of density of states (Section 2.51). Transient electronic density and its time derivative are then presented for the analysis of the electronic dynamics results from the propagation of the density matrix via the Liouville–Von Neumann equation, as described in Section 2.1.3.

2.4.1 Electronic absorption and ECD

By propagating TDSE in real time under the influence of an explicit electromagnetic field, one can evaluate the ECD spectra of molecular systems [166, 167, 67]. In order to calculate the absorption and ECD spectra, it is necessary to calculate the induced electric and magnetic dipole moments, $\Delta\vec{\mu}(t)$ and $\Delta\vec{m}(t)$:

$$\Delta\vec{\mu}(t) = \vec{\mu}(t) - \vec{\mu}(0), \tag{2.41}$$

and

$$\Delta\vec{m}(t) = \vec{m}(t) - \vec{m}(0). \tag{2.42}$$

Here, $\vec{\mu}(t)$ and $\vec{m}(t)$ denote the electric and magnetic dipole moments at a given time t, while $\vec{\mu}(0)$ and $\vec{m}(0)$ correspond to their initial values at $t = 0$. From the propagation of the TDSE in the electronic state basis we can calculate the time–dependent electric and magnetic dipole moment as:

$$\vec{\mu}(t) = \sum_{\lambda'\lambda} C^*_{\lambda'}(t)\, C_\lambda(t)\ \langle\lambda'|\,\vec{\hat{\mu}}\,|\lambda\rangle\,, \tag{2.43}$$

and

$$\vec{m}(t) = \sum_{\lambda'\lambda} C^*_{\lambda'}(t)\, C_\lambda(t)\ \langle\lambda'|\,\vec{\hat{m}}\,|\lambda\rangle\,, \tag{2.44}$$

where $\langle\lambda'|\,\vec{\hat{\mu}}\,|\lambda\rangle$ and $\langle\lambda'|\,\vec{\hat{m}}\,|\lambda\rangle$ represent the transition electric and magnetic dipole moments.

The full matrix of transition dipole moments is determined, also including the elements connecting two excited states. A derivation of these transition moments can be found in Refs. [167, 67] and details of their implementation in our codes in Section 2.5.

With the induced electric and magnetic dipole moments at hand, the absorption spectrum is obtained from

$$P_{nl}^{\mathrm{ABS}}(\omega) = \frac{1}{2\pi F_n^0(\omega)} \int_0^{+\infty} \Delta\overline{\mu}_l(t)\, e^{i(\omega+i\Gamma)t}\, dt, \tag{2.45}$$

while the ECD spectrum is given by

$$P_{nl}^{\mathrm{ECD}}(\omega) = -\frac{i}{2\pi\omega F_n^0(\omega)} \int_0^{+\infty} \Delta m_l(t)\, e^{i(\omega+i\Gamma)t}\, dt. \tag{2.46}$$

In these expressions, $\Delta\overline{\mu}_l(t)$ and $\Delta m_l(t)$ denote the lth components of the induced electric and magnetic dipole moments, respectively. The factor Γ acts as a damping parameter that introduces an exponential decay of the excited-state population. $F_n^0(\omega)$ corresponds to the Fourier transform of the nth component of the external electric field, whose general form is provided in Eq. 2.7.

Eqs. 2.45–2.46 make it possible to follow how each polarization component of $\vec{F}$ influences the time evolution of the associated electric or magnetic transition dipole moment, and thereby the absorption or ECD response. After separately computing the three Cartesian components (i.e., xx, yy, and zz), rotationally averaged quantities are obtained to enable comparison with experimental measurements:

$$\overline{P}^{\mathrm{ABS}}(\omega) = \frac{1}{3}\left(P_{xx}^{\mathrm{ABS}}(\omega) + P_{yy}^{\mathrm{ABS}}(\omega) + P_{zz}^{\mathrm{ABS}}(\omega)\right) \tag{2.47}$$

and

$$\overline{P}^{\mathrm{ECD}}(\omega) = \frac{1}{3}\left(P_{xx}^{\mathrm{ECD}}(\omega) + P_{yy}^{\mathrm{ECD}}(\omega) + P_{zz}^{\mathrm{ECD}}(\omega)\right). \tag{2.48}$$

The calculation of ECD and absorption spectra have been employed in the works reported in Section 3.2 for the evaluation of the ECD and absorption spectra along the photoisomerization process of the molecular motor both in the ground and first excited state and Section 3.3 in Chapter 3 for the evaluation of the effect of the presence of a gold nanosphere on the ECD spectra of chiral molecules. In the work reported in Chapter 5, an original computational procedure and theoretical methods for the calculation of NEXAFS spectra from valence–excited state is instead reported.

2.4.2 Time-dependent ΔPDOS

The study of electron dynamics is carried out using a one–electron descriptor available as one of the post-processing analysis tools, namely the differential projected density of states (ΔPDOS) [166].
Starting from the wavepacket in the ground state at the initial time, i.e., $|\Psi(t=0)\rangle$ (in this project ΔPDOS has been used only to characterize closed-system dynamics, even though it was extended to the SSE framework [142]), the initial projected density of states $\mathrm{PDOS}_{ini}(\epsilon)$ is defined as

$$\mathrm{PDOS}_{ini}(\epsilon) = \sum_{i}^{occ} w_i \langle 0|\, \hat{n}_i \,|0\rangle\, L_\eta(\epsilon - \quad \epsilon_i) = \tag{2.49}$$
$$2\sum_{i}^{occ} w_i L_\eta(\epsilon - \epsilon_i)$$

Here, $\hat{n}_i$ is the number operator, while $L(\epsilon - \epsilon_i)$ denotes a Lorentzian function centered at the orbital energy ϵ_i with broadening parameter η. The coefficient w_i corresponds to the Mulliken or Löwdin weight assigned to the ith molecular orbital. If the system is partitioned into non–overlapping fragments, such that each atom belongs exclusively to a single fragment, the Mulliken or Löwdin weight for orbital i in fragment K is expressed as

$$w_i^K = \sum_{\alpha(K),\beta} d^i_{\alpha(K)} S_{\alpha(K),\beta}\, d^i_\beta, \tag{2.50}$$

where α indexes the basis functions of atoms in fragment K, while β runs over all basis functions. $S_{\alpha(K),\beta}$ is the overlap matrix element between basis functions, and $d^i_{\alpha(K)}$ and d^i_β are the coefficients of the orbital expansion in the atomic orbital basis.

The time-dependent ΔPDOS, defined as $\mathrm{PDOS}(\epsilon, t) - \mathrm{PDOS}_{ini}(\epsilon)$, can be written as

$$\Delta\mathrm{PDOS}_K(t,\epsilon) = -\sum_{i}^{occ} w_i^K \mathrm{Re}\left[\sum_{M,L} C^*_\lambda(t) C_{\lambda'}(t) \sum_{a}^{vir} d^{a*}_{i,\lambda} d^a_{i,\lambda'}\right] \; L_\eta(\epsilon - \epsilon_i) \tag{2.51}$$
$$+\sum_{a}^{vir} w_a^K \mathrm{Re}\left[\sum_{\lambda',\lambda} C^*_\lambda(t) C_{\lambda'}(t) \sum_{i}^{occ} d^{a*}_{i,\lambda} d^a_{i,\lambda'}\right] L_\eta(\epsilon - \epsilon_i),$$

In Eq. 2.51, $d^a_{i,\lambda'}$ ($d^a_{i,\lambda}$) are the coefficients of the orbital expansion for states $|\lambda'\rangle$ and $\langle\lambda|$, respectively (see Eq. 2.8). L_η denotes a Lorentzian function centered at ϵ_i with width η, included to smooth the distribution. The Mulliken (or Löwdin, as in Ref. [68]) weights w_i^K are applied consistently with the chosen fragmentation scheme. Further technical details can be found in Ref. [166]. The index K indicates the fragment (an atom or group of atoms) with respect to which charge populations are evaluated.

Integrating over the energy range allows us to obtain the time–dependent charge (electron and hole) population with respect to the initial condition[68, 142]

$$\text{electron population} = \frac{1}{2}\int_{-\infty}^{+\infty} [\Delta\mathrm{PDOS}_K(t,\epsilon) + |\Delta\mathrm{PDOS}_K(t,\epsilon)|] d\epsilon \tag{2.52}$$

and

$$\text{hole population} = \frac{1}{2}\int_{-\infty}^{+\infty} [\Delta\text{PDOS}_K(t,\epsilon) + |\Delta\text{PDOS}_K(t,\epsilon)|]\, d\epsilon. \tag{2.53}$$

This kind of analysis was applied in particular for the works reported in Chapter 4 regarding photocatalysis, in order to to follow the time–evolution of electrons and holes during the dynamics with and without the presence of the gold nanorod.

2.4.3 Transient electronic density

From the evaluation of the electronic density matrix it is possible to exctract many information regarding the electronic processes of the quantum system. This quantity is strictly linked to many different observables, which allows us to describe the electronic processes occurring during the simulation.

We can find a direct link with the flux density by recasting the dynamics into a one-electron quantum continuity equation:

$$\partial_t \rho_S(t) = -\nabla \cdot \vec{j}(t) \tag{2.54}$$

where $\vec{j}(t)$ is the flux density.

Exploiting the structure of the many–body wavefunction, as it is expressed in Eq. 2.8, allows us to obtain to simple one-electron integrals between molecular orbitals which are evaluated with detCI@ORBKIT toolbox [152, 147, 149].

From the one–electron density matrix, one can evaluate the transient electronic density $\Delta\rho_S$ and its time derivative $\partial_t\rho_S$. $\Delta\rho_S$ allows us to directly see and monitor the evolution of the electron density in respect to the initial density value. The visualization of this quantity allows us to gain direct insight in the motion of the electrons and holes as we have shown in the work reported in Section 3.1 of Chapter 3. The second quantity instead is directly linked to the flux density by the continuity equation. The time derivative of the electronic density, $\partial_t\rho_S$, measures how the probability of finding the electron at a given point changes in time; physically, it reflects the local balance between probability flowing into and out of that region, as dictated by the continuity equation. In the work reported in Section 3.1 in Chapter 3, it is reported a clear example of how these quantities provide relevant information regarding the evolution of the electronic motions in molecular systems.

2.5 AMS-WaveT interface

A central part of my PhD research has been devoted to the development of new computational tools to extend the capabilities of existing electronic structure and

real–time dynamics codes. In particular, I worked on the interface code that connects AMS [136] with WaveT, enabling simulations that combine the accuracy of TDDFT electronic excitations with the real–time propagation of quantum states. This method relies on propagating the electronic wavefunction in the basis of electronic states. Consequently, the quantities obtained from the AMS quantum chemistry output (dipoles and potentials, which are originally computed in the atomic basis) must be transformed into this basis. The AMS-WaveT interface performs this transformation.

The work described in this Section represents the core of my technical contributions: I implemented (i) the calculation of transition potentials to account for the effect of a NP on molecular excitations (first strategy described in Section 2.3), (ii) the computation of transition dipole moments among excited states, which are essential for simulating advanced spectroscopies such as absorption and ECD, as seen in Section 3.2 of Chapter 3 and Chapter 5 and (iii) introduced an MPI parallelization version of the interface to treat large systems in presence of the NP.

In Figure 2.1, I report a schematic overview of the computational workflow required to perform a WaveT simulation starting from an AMS TDDFT calculation. As of the latest release (v.2025), AMS [167, 67, 66] can be coupled directly to WaveT. This connection is managed through a custom interface, composed of two in-house codes, which extracts the relevant information from AMS outputs and formats it into the input required for WaveT. In particular, the interface enables the calculation of coupling matrix elements of one-operators in the $|\lambda\rangle$ state space [4].

Within AMS, the eigenstates consist of the Kohn-Sham DFT ground state and the $(N_{\text{states}} - 1)$ excited states obtained via linear-response TDDFT, within the singly-excited configuration ansatz [166], as expressed in Eq. 2.8. Since WaveT propagates the electronic wavefunction in a chosen $|\lambda\rangle$ basis, we must provide as inputs the unperturbed energies E_λ and the electric dipole moment matrix elements $\langle\lambda|\,\vec{\hat{\mu}}\,|\lambda'\rangle$ from Eq. 2.6. While excitation energies are easily available from most quantum chemistry codes, transition dipole moments are not always directly accessible. For this reason, we developed an interface code that bridges AMS and WaveT, automating the extraction and transformation of these quantities.

During a standard AMS TDDFT run, all relevant information - such as excitation coefficients, transition dipole moments, and transition potentials - is stored in the output files `adf.rkf/TAPE21` and `TAPE15`. These files are sufficient to run the AMS-WaveT interface. The code `read_adf.f90` extracts the excitation coefficients and reformulates them in the molecular orbital basis, while the code `write_wavet.f90` rewrites these quantities in the state space, generating the input files required by WaveT.

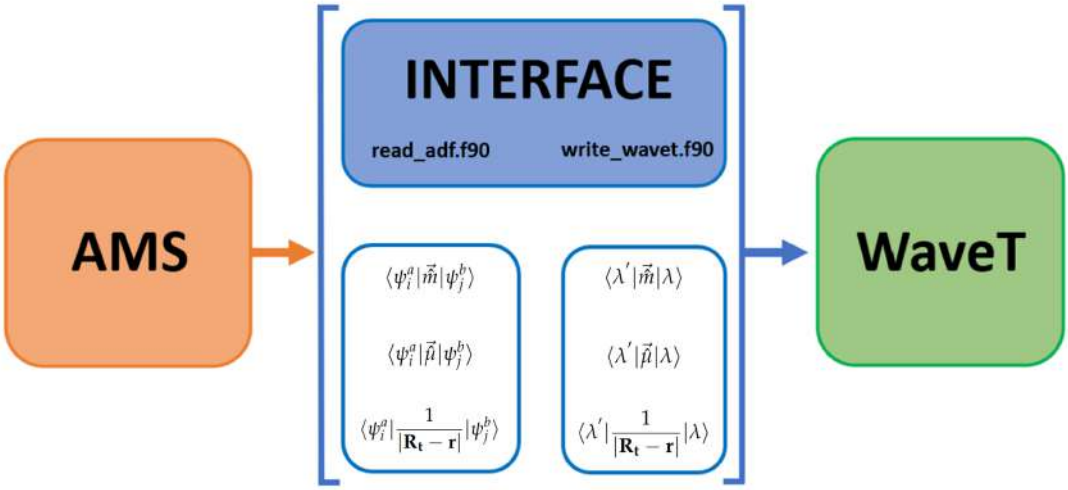

FIGURE 2.1: Schematic representation of the AMS/WaveT computational procedure.

2.5.1 Transition potential

The calculation of the transition potential in AMS in the atomic orbital basis is performed by a subroutine that I specifically implemented. All the information regarding this calculation are then stored in `TAPE15` which can be read by the interface. `read_adf.f90` extracts the information from the `TAPE15` file and rewrites the electronic and nuclear transition electrostatic potential (see Eq. 2.40) in the molecular orbital basis. The output files generated by this code for the transition potential are `potmat.dat` and `potmat_nuc.dat`, which correspond to the electronic and nuclear contribution of the transition potential in the molecular orbital basis. Then, `write_wavet.f90` reads the output of the first interface code and rewrites these quantities in terms of excitation $(\mathbf{X}^{\lambda(\lambda')} + \mathbf{Y}^{\lambda(\lambda')})$ and deexcitation $(\mathbf{X}^{\lambda(\lambda')} - \mathbf{Y}^{\lambda(\lambda')})$ in the space of the singly-excited configurations as:

$$\langle\lambda|\,\hat{V}_{\mathrm{BEM}}\,|0\rangle = (\mathbf{X}^{\lambda} + \mathbf{Y}^{\lambda}) \cdot \mathbf{P}_{\mathrm{BEM}}(\mathbf{R}_t) \tag{2.55}$$

and

$$\begin{aligned}\langle\lambda|\,\hat{V}_{\mathrm{BEM}}(\mathbf{R}_t)\,|\lambda'\rangle = \tfrac{1}{2}[&(\mathbf{X}^{\lambda} + \mathbf{Y}^{\lambda}) \cdot \mathbf{P}_{\mathrm{BEM}}(\mathbf{R}_t) \cdot (\mathbf{X}^{\lambda'} + \mathbf{Y}^{\lambda'}) + \\ &(\mathbf{X}^{\lambda} - \mathbf{Y}^{\lambda}) \cdot \mathbf{P}_{\mathrm{BEM}}(\mathbf{R}_t) \cdot (\mathbf{X}^{\lambda'} - \mathbf{Y}^{\lambda'})],\end{aligned} \tag{2.56}$$

where $\mathbf{P}_{\mathrm{BEM}}(\mathbf{R}_t)$, is the matrix representation of the operator corresponding to the external potential, as expressed in Eq. 2.40. In Eq. 2.55 and 2.56 we reported the contribution related to ground state–excited states transitions and to the excited states – excited states, respectively.

To include the calculation of the transition potential in AMS in the atomic orbital basis, it is necessary first to perform a TDPlas calculation, which provides the spatial distribution of surface charges on the NP. The relevant information is stored in the `cavity.inp` file, from which we extract a `.xyz` file containing the coordinates of the charges. Another possible way is to build the mesh of the nanostructure with GMSH – an open-source software for mesh generation and geometry modeling – and with an interface obtain the necessary file to perform a TDPlas run. By activating the `Nanoparticle` section and the `TransitionPotential` flag in the AMS input, the program reads the `.xyz` file and evaluates the transition potential accordingly. The procedure is summarized in Figure 2.2.

An illustrative fragment of the Fortran implementation of Eqs. 2.55 and 2.56 is reported below, where the terms highlighted in green represent the product between excitation terms $(\mathbf{X}^{\lambda}+\mathbf{Y}^{\lambda})*(\mathbf{X}^{\lambda'}+\mathbf{Y}^{\lambda'})$ and in red between deexcitation terms $(\mathbf{X}^{\lambda}-\mathbf{Y}^{\lambda})*(\mathbf{X}^{\lambda'}-\mathbf{Y}^{\lambda'})$. The loop runs over the number of tesserae (nts), the number of states (ntoten) with the variables `is` and `js` and over the occupied and virtual molecular orbitals with the variables `i` and `ia`. The matrix `potmat` represents the transition potential in the basis of the molecular orbitals. `tddfteig` and `tddfteig1` represent respectively the matrix of excitation and deexcitation terms extracted from the output of the AMS calculation.

```
GS-EX

do ints=1,nts
    do is=1,ntoten
        kk = cont(1,is+1)
        do i=1,kocc
            do ia=1,kvirt
                potmut(kk,ints) = potmut(kk,ints) +&
                    &tddfteig(ia,i,is)*potmat(i,kocc+ia,ints)
            enddo
        enddo
    enddo
enddo

EX-EX

do ints=1,nts
    do is=1,ntoten
       do js=is,ntoten
          kk = cont(is+1,js+1)
          do i=1,kocc
             do ia=1,kvirt
                potmut(kk,ints) = potmut(kk,ints) +
                   tddfteig(ia,i,is)*tddfteig(ia,i,js)*&
```

```
                    &(potmat(kocc+ia,kocc+ia,ints)-potmat(i,i,ints))
                    potmut1(kk,ints) = potmut1(kk,ints) +
                        tddfteig1(ia,i,is)*tddfteig1(ia,i,js)*&
                    &(potmat(kocc+ia,kocc+ia,ints)-potmat(i,i,ints))
                    ...
                enddo
            enddo
        enddo
    enddo
enddo
```

This calculation in `write_wavet.f90` allows us to obtain the input file `ci_pot.inp` which contains the information regarding the transition potential in the electronic state basis. This file is then read by WaveT.

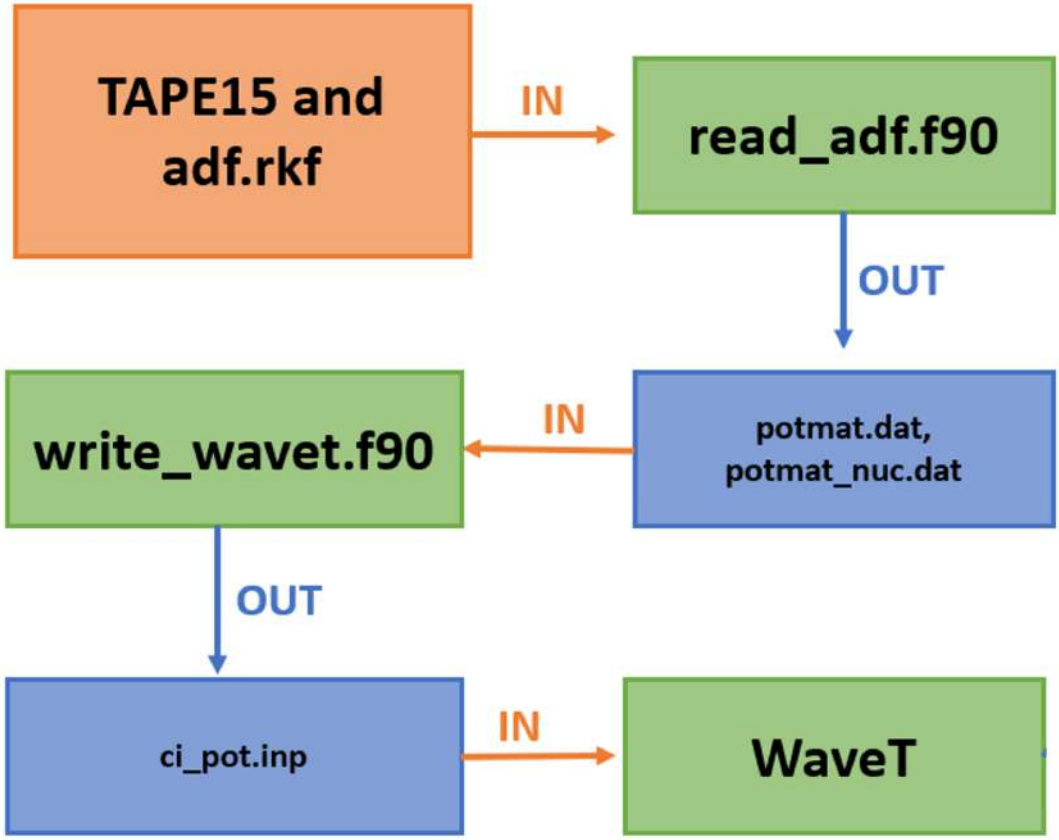

FIGURE 2.2: Representation of the computational procedure for the extraction of the information regarding the transition potential from AMS. The square in red represents the input files from AMS, the green squares the codes and in blue the output files.

2.5.2 Transition-dipole moments among excited states

Another implementation was the calculation of transition dipole moments among excited states in a general manner. This feature is particularly important for simulating absorption and ECD spectra.

The γ-th electric component of the transition dipole is written as:

$$\langle\lambda|\,\hat{\mu}_\gamma\,|\lambda'\rangle = \tfrac{1}{2}[(\mathbf{X}^\lambda + \mathbf{Y}^\lambda)\cdot\mathbf{D}_\gamma\cdot(\mathbf{X}^{\lambda'} + \mathbf{Y}^{\lambda'}) + (\mathbf{X}^\lambda - \mathbf{Y}^\lambda)\cdot\mathbf{D}_\gamma\cdot(\mathbf{X}^{\lambda'} - \mathbf{Y}^{\lambda'})]. \tag{2.57}$$

and the γ-th magnetic component as:

$$\langle\lambda|\,\hat{m}_\gamma\,|\lambda'\rangle = \tfrac{1}{2}[(\mathbf{X}^\lambda + \mathbf{Y}^\lambda)\cdot\mathbf{M}_\gamma\cdot(\mathbf{X}^{\lambda'} - \mathbf{Y}^{\lambda'}) + (\mathbf{X}^\lambda - \mathbf{Y}^\lambda)\cdot\mathbf{M}_\gamma\cdot(\mathbf{X}^{\lambda'} + \mathbf{Y}^{\lambda'})]. \tag{2.58}$$

Here, $\gamma = x, y, z$ and $\mathbf{D}_\gamma$, $\mathbf{M}_\gamma$ are the operator matrices in the molecular orbital basis.

We report here an example of how in the interface we compute the transition dipole moments among excited states in the case of the electric and magnetic dipole moments, following equation 2.57 and 2.58.

```
1   do is=1,ntoten
2     do js=is,ntoten
3        kk = cont(is+1,js+1)
4        do i=1,kocc
5           do ia=1,kvirt
6              dmut(1,kk) = dmut(1,kk) +
                  tddfteig(ia,i,is)*tddfteig(ia,i,js)*&
7             &(dipmatx(kocc+ia,kocc+ia)-dipmatx(i,i))
8              dmut(2,kk) = dmut(2,kk) +
                  tddfteig(ia,i,is)*tddfteig(ia,i,js)*&
9             &(dipmaty(kocc+ia,kocc+ia)-dipmaty(i,i))
10             dmut(3,kk) = dmut(3,kk) +
                  tddfteig(ia,i,is)*tddfteig(ia,i,js)*&
11            &(dipmatz(kocc+ia,kocc+ia)-dipmatz(i,i))
12             ...
13          enddo
14       enddo
15    enddo
16  enddo
17
18  do is=1,ntoten
19    do js=is,ntoten
20       kk = cont(is+1,js+1)
```

```
        do i=1,kocc
           do ia=1,kvirt
              dmut1(1,kk) = dmut1(1,kk)
                 +tddfteig1(ia,i,is)*tddfteig1(ia,i,js)*&
              &(dipmatx(kocc+ia,kocc+ia)-dipmatx(i,i))
              dmut1(2,kk) = dmut1(2,kk) +
                 tddfteig1(ia,i,is)*tddfteig1(ia,i,js)*&
              &(dipmaty(kocc+ia,kocc+ia)-dipmaty(i,i))
              dmut1(3,kk) = dmut1(3,kk) +
                 tddfteig1(ia,i,is)*tddfteig1(ia,i,js)*&
              &(dipmatz(kocc+ia,kocc+ia)-dipmatz(i,i))
              ...
           enddo
        enddo
     enddo
  enddo

dmut = 0.5d0*(dmut + dmut1)
```

We report here only a part of the nested loop which runs over the same variables of the transition potential and also the nature of the product among excitation coefficients is the same. `dipmatx`, `dipmaty`, `dipmatz` are matrices containing the transition dipole moments in the molecular orbital basis for the x, y and z directions.

For the magnetic dipole, the operator is antisymmetric, so mixed excitation-deexcitation terms must be included. The relevant parts of the implementation are:

```
  do is=1,ntoten
     do js=is,ntoten
        kk = cont(is+1,js+1)
          do i=1,kocc
             do ia=1,kvirt
                lmut(1,kk) = lmut(1,kk) +
                   tddfteig(ia,i,is)*tddfteig1(ia,i,js)*&
                &(lmatx(kocc+ia,kocc+ia)-lmatx(i,i))
                ...
             enddo
          enddo
       enddo
  enddo

  do is=1,ntoten
     do js=is,ntoten
        kk = cont(is+1,js+1)
          do i=1,kocc
             do ia=1,kvirt
```

```
                    lmut1(1,kk) = lmut1(1,kk) +
                        tddfteig1(ia,i,is)*tddfteig(ia,i,js)*&
                    &(lmatx(kocc+ia,kocc+ia)-lmatx(i,i))
                    ...
                enddo
            enddo
        enddo

lmut=0.5d0*(lmut + lmut1)
```

In this case the part in green corresponds to the product between excitation and deexcitation elements $(\mathbf{X}^{\lambda} + \mathbf{Y}^{\lambda}) * (\mathbf{X}^{\lambda'} - \mathbf{Y}^{\lambda'})$ and in red between deexcitation and excitation elements $(\mathbf{X}^{\lambda} - \mathbf{Y}^{\lambda}) * (\mathbf{X}^{\lambda'} + \mathbf{Y}^{\lambda'})$. The details of the nested loops and the variables involved are the same we reported for the electric dipole moment. In this case `lmatx`, `lmaty`, `lamtz` represent the magnetic transition dipole moment in the molecular orbital basis for the x, y and z directions.

The calculation of the transition dipole moments allows us to obtain two input files for WaveT: `ci_mut.inp` and `ci_lt.inp`. These two files, respectively, contain the electric and magnetic transition dipole moments.

2.5.3 MPI parallelization

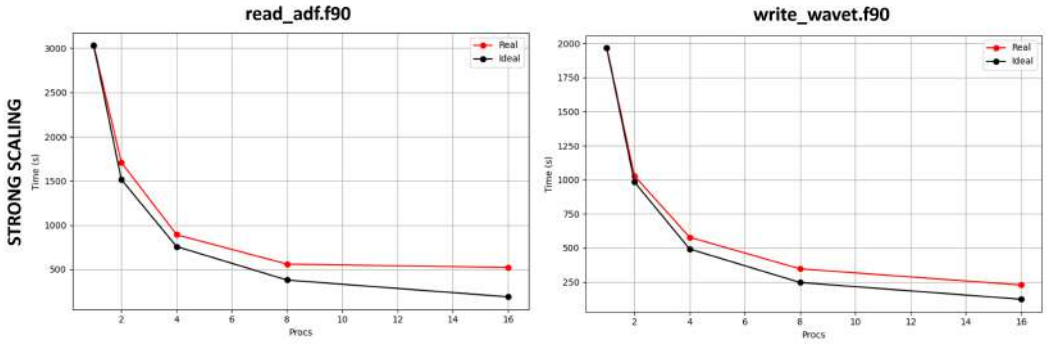

FIGURE 2.3: Strong scaling performance of the MPI-parallelized codes. Red lines correspond to the measured execution times, while black lines indicate the theoretical scaling behavior.

An MPI parallelization in both `read_adf.f90` and `write_wavet.f90` has been implemented. In particular, the calculation of transition potentials involves an outer loop running over the number of tesserae. For large systems - for instance, when metallic systems are modeled as a QM system and the TDDFT calculation produces thousands of excitations - this procedure rapidly becomes computationally demanding and impractical to run. To address this issue, I developed an MPI–parallel version of the interface, which distributes the most expensive parts of the calculation

across multiple processors. This implementation significantly reduces the execution time of the transition potential evaluation, making it feasible to investigate metallic systems with hundreds or even thousands of excitations. Thanks to this development, the range of accessible systems has been substantially expanded, allowing realistic NP-molecule hybrid simulations that would otherwise be prohibitively costly. To evaluate the performance of the MPI parallelization, I performed strong scaling tests on the two code of the interface, namely `read_adf.f90` and `write_wavet.f90`. The results are reported in Figure 2.3. The case test is the tetrahelicene molecule with 40 excited states, coupled to a NP with 360 tesserae.
The execution time is calculated in this way:

```
call system_clock(st,rate)
.
.
.
call system_clock(current)

write(*,*) 'Elapsed time: ', real(current-st)/real(rate)
```

where the command `call system_clock(st,rate)` is called before the input–reading operation and the command `call system_clock(current)` is called after the output–writing operation. The division of the computation time for the variable `rate` allows to extract the elapsed time in seconds.

In strong scaling tests the total workload is kept fixed and distributed among an increasing number of processes. Both routines exhibit a substantial reduction in the execution time when the number of processes is increased, following closely the theoretical scaling trend. This confirms that the MPI implementation is effective in parallelizing the most computationally expensive parts of the code, enabling simulations that would otherwise be prohibitively time–consuming.

Overall, these benchmarks demonstrate that the parallelization is successful: strong scaling shows excellent improvements in the performance with a behavior closely resembling the ideal situation. In practice, this allows the study of systems with thousands of excitations with feasible computational cost, significantly broadening the applicability of the method.

Chapter 3

Investigating Chirality

3.1 Laser Induced Charge Migration

In this chapter, I present the work conducted at the Université de Lorraine in Metz under the supervision of Prof. Jean-Christophe Tremblay. This collaboration sought to combine the expertise of both groups in studying light–matter interactions, with a particular focus on endohedral fullerenes, materials of considerable interest due to their promising applications in molecular electronics.

The broader objective of the project was to explore carbon peapods and understand how the behavior of endohedral fullerenes is modified inside carbon nanotubes. As a first step, we investigated the electronic dynamics of these systems under the influence of chiral light, and in particular circularly polarized light. Such fields induce a circular motion of electrons when interacting with a laser pulse, reflecting the transfer of angular momentum from light to the molecular system.

As model systems, we considered pristine fullerene (C_{60}), fullerene encapsulating a magnesium atom ($Mg@C_{60}$), and fullerene encapsulating a chloride anion ($Cl^{-}@C_{60}$). Interestingly, we found that changing the encapsulated atom profoundly modified the nature of the electronic response. To explore this, we first performed TDDFT calculations to characterize the electronic structure of the three systems. From these results, we selected excitations below the ionization threshold to target in our real–time electronic dynamics simulations. From the quantum chemistry output we extracted the information regarding the excitation energies and coefficients to build a library of transition dipole moment to use for the electronic dynamic simulation. These calculations were carried out using a in–house code. These calculations were then analyzed through several postprocessing tools, including the transient electronic density and its time derivative, described in Chapter 2 in Section 2.4.3.

In pristine fullerene, angular momentum transfer caused a pronounced depopulation of the ground state and selective population of excited states, leading to significant charge separation and the emergence of a rotating dipole. For $Mg@C_{60}$, electron density variations were mainly localized around the magnesium atom, producing a weaker induced dipole but more spatially confined excitations. In contrast,

$Cl^{-}@C_{60}$ exhibited minimal angular momentum transfer, with an almost isotropic charge distribution consistent with the charge–transfer nature of its excitations.

In this work, I performed all calculations and analyses. I also contributed substantially to the interpretation of results, the writing of the corresponding sections of the paper and to the final editing of the manuscript.

This works is present in literature as Biancorosso, L., Coccia, E., & Tremblay, J. C. (2024). "Laser-Induced Circular Charge Migration in Endohedral Fullerenes in the Presence of Ionization". *J.Phys. Chem. C*, **129**, p. 464.

THE JOURNAL OF PHYSICAL CHEMISTRY C
A JOURNAL OF THE AMERICAN CHEMICAL SOCIETY

pubs.acs.org/JPCC Article

Laser-Induced Circular Charge Migration in Endohedral Fullerenes in the Presence of Ionization

Leonardo Biancorosso,* Emanuele Coccia, and Jean Christophe Tremblay*

Cite This: J. Phys. Chem. C 2025, 129, 464−472 Read Online

ACCESS | Metrics & More | Article Recommendations | Supporting Information

ABSTRACT: In this study, we explore the behavior of endohedral fullerenes and examine how different doping species influence the ultrafast photoinduced electronic dynamics. We analyzed a reference fullerene (C_{60}) and two endohedral fullerenes with Cl^- and Mg atoms inside the cage using electronic dynamics calculations. By applying circularly polarized light, we observed the transfer of angular momentum from the light to the electron density in these systems. The optical properties and specific excitations were determined through quantum chemical calculations, which formed the basis of our analysis. In the C_{60} reference system, excitation led to a significant rotation of the electron density and the formation of a large rotating dipole. For the Mg@C60 system, the electron density changes were mostly localized around the Mg atom, resulting in a smaller induced dipole but more localized excitations. In the $Cl^-@C_{60}$ system, minimal angular momentum transfer was observed with an isotropic distribution of charges due to the charge-transfer nature of the excitations. The distinct behaviors observed in these systems highlight the diverse phenomena that can arise and represent a significant step toward developing novel molecular devices.

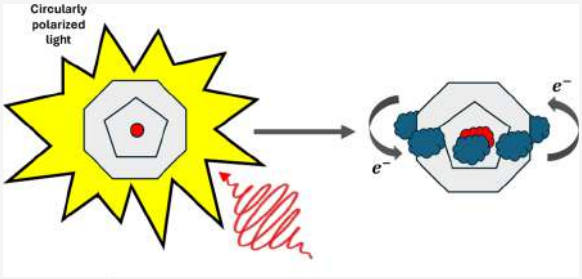

INTRODUCTION

The peculiar structure of fullerene has triggered the imagination of scientists since its discovery.[1] The unique and different properties of this molecular system made fullerene the leading character in various fields such as molecular electronics,[2−4] material science,[5,6] optics,[7,8] and many others.[9−11] Insertion and trapping of atomic and molecular species within the fullerene cavity has been advocated as a simple and flexible approach to modulate the electronic properties of these systems.[12,13] This has led the way to an increasing number of studies on possible applications of these endohedral systems.[14,15] In this context, the symmetry and regularity of the structures have made them the perfect test case for new theoretical methods, trying to unravel their vast and different electronic and structural behaviors.[16] For this reason, several theoretical methods have been employed to study the structures of endohedral fullerenes, and they have proved to provide reliable theoretical estimates of their structure and physical properties.[13,17−19]

In previous studies, a lot of effort has been put into the determination of the formation energies of the system and polarizabilities of different endohedral systems.[20,21] It has been shown that the different properties depend heavily on the endohedral species and on the dimensions of the fullerene cage. Further, the effects of confinement and of electron correlations on the relative time delay between the 3s and 3p photoemissions of Ar confined endohedrally in buckminsterfullerene C_{60} were studied by electron dynamics within the time-dependent local density approximation.[22] Similarly, the current-induced dynamics in endohedral fullerene molecular junctions was studied from a structural and a dynamical perspective.[23] In this particular case, the authors addressed the case of Au−Li@C_{60}−Au conductance junctions subjected to resonant current. This revealed a coupled two-dimensional dynamics in which the C_{60} bounces against the gold electrode and the Li atom instead undergoes large amplitude oscillations at a higher frequency.[23] Vibrationally induced electron relaxation in endofullerene Mg@C_{60} was studied using nonadiabatic molecular dynamics simulations.[24] It was found that after initial local photoexcitation of the Mg heteroatom electronic relaxation from the center to the outer C_{60} shell can be mediated by vibrations within a picosecond. Further, a slowdown of the electron relaxation process due to the presence of large gaps in the spectrum of excited electronic states was also observed. Yet, the few-femtosecond dynamics is found to be essentially a pure electronic charge migration. All these previous studies demonstrate the great influence of endohedral species on the static and dynamic behavior of the overall system, while the effect of ionization upon photoexcitation has not been addressed.

Received: September 19, 2024
Revised: November 19, 2024
Accepted: December 9, 2024
Published: December 17, 2024

https://doi.org/10.1021/acs.jpcc.4c06331
J. Phys. Chem. C 2025, 129, 464−472

In the present work, we investigate how doping can be used to tune the ionization potential of C_{60} and how this affects ultrafast photoinduced electron dynamics. Two endohedral fullerenes with the Cl^- anion and a Mg, placed at the center of the cage, are chosen and compared with the reference fullerene system from static and dynamical perspectives. Ultrafast charge migration is triggered by circularly polarized light in order to transfer angular momentum to the transient electron density of the target.[25] Similar pulses have been proposed to create and probe long-lived molecular magnets in the presence of strong dephasing,[26,27] for which the Jahn−Teller distortion was also shown to affect the dynamics.[28,29] Here, we assess the potential of endohedral fullerenes as short-lived photoinduced molecular magnets in the presence of ionization loss.

All dynamical simulations are performed using the hybrid time-dependent functional theory/configuration interaction methodology.[30,31] In this approach, energies and pseudo-configuration interaction singles (CIS) eigenvectors obtained from a reference time-dependent density functional theory (TDDFT) calculation in linear response are used as a basis for the many-electron dynamics. From the knowledge of the many-body wave packet, electron dynamics can be imaged using either transient electronic current density maps or the time-derivative of the instantaneous electron density,[32,33] also known as electron flow. The latter is directly related to the measurable time-resolved X-ray scattering signal,[34] and a related quantity was independently proposed by others to visualize electron dynamics.[35] These intuitive tools reveal the mechanism of ultrafast charge migration after photoexcitation using an angular momentum bearing light.

In Section 2, we provide a theoretical description of the methods employed and the computational details of the calculations. The results and the discussion are presented in Section 3, and Conclusions are given in Section 4.

MODELS AND METHODS

Ultrafast electron dynamics is simulated within the hybrid TDDFT/configuration interaction (CI) framework.[30,33] Similar methods for electron dynamics that provide a balance between computational efficiency and numerical accuracy have also been proposed over the years.[36−38] The time-dependent state of an N-electron system is described by its reduced density matrix, $\hat{\rho}(t)$. It evolves according to the many-body Liouville−von Neumann equation

$$\partial_t \hat{\rho}(t) = -\frac{i}{\hbar}[\hat{H}_0, \hat{\rho}(t)] + \frac{i}{\hbar}[\boldsymbol{\mu}\cdot\vec{F}(t), \hat{\rho}(t)] - [\hat{W}, \hat{\rho}(t)]_+ \tag{1}$$

Here, $\hat{H}_0$ is the field-free electronic Hamiltonian in the clamped-nuclei approximation. The operator $\hat{W}$ is a complex absorbing potential that accounts for the loss of electrons to the continuum through single ionization. The interaction between an external electric field $\vec{F}(t)$ and the molecular dipole $\hat{\boldsymbol{\mu}}$ is treated semiclassically. In the following, the circularly polarized field associated with a laser pulse of duration T and frequency ω will take the generic form

$$\vec{F}(t) = \sum_{q=\{x,y,z\}} F_0^{(q)} \sin^2(\pi t/T)\cos(\omega t + \varphi_q)\mathbf{e}_q \tag{2}$$

where $F_0^{(q)}$ is the field amplitude along direction $\mathbf{e}_q$, and φ_q is the phase of a given component.

In the hybrid TDDFT/CI method, the spin-free time-dependent N-electron reduced density matrix is represented using a linear combination of N_{states} stationary singly excited many-body excited states, $|\Phi_m\rangle \equiv \Phi_m(\mathbf{r}^N)$, where $\mathbf{r}$ is a vector describing the position of an electron in real space. The density matrix thus takes the form

$$\hat{\rho}(t) = \sum_{m=0}^{N_{\text{states}}}\sum_{n=0}^{N_{\text{states}}} \rho_{mn}(t) e^{-i(E_m^{(N)} - E_n^{(N)})t/\hbar} |\Phi_m\rangle\langle\Phi_n| \tag{3}$$

where $E_{m(n)}^{(N)}$ is the energy of state $m(n)$ with N electrons. The field-free electronic Hamiltonian is diagonal on the basis of these pseudo-CI eigenfunctions. The lowest-lying excited eigenstates, $\Phi_m(\mathbf{r}^N)$, of the many-body electronic Hamiltonian, are themselves expressed as linear combinations of singly excited configuration state functions

$$\Phi_m(\mathbf{r}^N) = \sum_{ar} D_{a,m}^r \Phi_a^r(\mathbf{r}^N) \tag{4}$$

The configuration state functions are defined by transferring an electron from occupied orbital a to virtual orbital r, with respect to the Kohn−Sham ground state $\Phi_0(\mathbf{r}^N)$. The transition amplitudes $D_{a,m}^r$ are obtained from TDDFT in linear response. These can be extracted directly from the output of standard quantum chemistry programs and postprocessed using the open-source program package detCI@ORBKIT.[39] All contributions below $|D_{a,m}^r| < 10^{-3}$ are discarded prior to renormalization.

The absorbing potential $\hat{W}$ is chosen as a sum of projectors on pseudo-CI eigenfunctions

$$\hat{W} = \sum_m \frac{I_m}{2} |\Phi_m\rangle\langle\Phi_m| \tag{5}$$

where I_m is the ionization rate of state m. To measure the coupling strength to the continuum, we adapt the phenomenological model used in refs 30, 40, and 41 and define the ionization rates of state m as

$$I_m = \begin{cases} \dfrac{\sqrt{2\left(E_m^{(N)} - E_{\text{ion}}\right)}}{d} & \text{if } E_m^{(N)} \geq E_{\text{ion}} \\ 0 & \text{else} \end{cases} \tag{6}$$

The first ionization energy, E_{ion}, is calculated for each system as

$$E_{\text{ion}} = E_0^{(N)} - E_0^{(N-1)} \tag{7}$$

where $E_0^{(N)}$ is the energy of the ground state of the N-electron system, while $E_0^{(N-1)}$ denotes the ground state energy of the $N-1$ electron system. The parameter d is interpreted as an escape length, and it is set to $1a_0$ in all simulations.[40]

Substituting ansatz (4) into eq 1 yields the following algebraic equation

$$\frac{d\rho_{mn}(t)}{dt} = \frac{i}{\hbar}\sum_{k=0}^{N_{\text{states}}} \vec{F}(t)\cdot(\boldsymbol{\mu}_{mk}\rho_{kn}(t) - \rho_{mk}(t)\boldsymbol{\mu}_{kn}) - \frac{1}{2}(I_m + I_n)\rho_{mn}(t) \tag{8}$$

The dipole matrix elements, $\boldsymbol{\mu}_{mk}$ are computed by numerical integration using ORBKIT[32,33,39] and eq 8 is integrated directly using a preconditioned adaptive step size Runge−Kutta algorithm.[42] The last term in eq 8 takes the form of an

https://doi.org/10.1021/acs.jpcc.4c06331
J. Phys. Chem. C 2025, 129, 464−472

average ionization rate between two states, leading both to pure dephasing (i.e., an exponential decay of the off-diagonal element of the reduced density matrix) and to ionization loss (i.e., an exponential decay of the population of states above the ionization threshold). As a consequence, the electronic population is not conserved in the simulations, and the loss-of-norm gives a measure of ionization loss.

To visualize the electron dynamics in the various systems, we use the transient electronic density, $\Delta\rho(\mathbf{r})$ and its time-derivative, $\partial_t\rho(\mathbf{r})$, which are defined as

$$\Delta\rho(\mathbf{r}) = \sum_k \int d\mathbf{r}^N \mathrm{Tr}[\delta(\mathbf{r}-\mathbf{r}_k)(\hat{\rho}(t)-\hat{\rho}(0))] \tag{9}$$

$$\partial_t\rho(\mathbf{r}) = \sum_k \int d\mathbf{r}^N \mathrm{Tr}[\delta(\mathbf{r}-\mathbf{r}_k)\partial_t\hat{\rho}(t)] \tag{10}$$

These can be computed using the coefficients obtained by numerical integration of eq 8 and substituting them into the density matrix eq 4. All required integrals are then computed using detCI@ORBKIT.[32,33,39] Further, we report the expectation value of the dipole moment operator to track the evolution of the system in the oscillating field. In the pseudo-CI eigenfunction basis, this takes the form

$$\langle\boldsymbol{\mu}\rangle(t) = \sum_{k=0}^{N_{\mathrm{states}}}\sum_{j=0}^{N_{\mathrm{states}}} \boldsymbol{\mu}_{kj}\rho_{jk}(t) \tag{11}$$

The expectation value of the dipole moment $\langle\boldsymbol{\mu}\rangle(t)$ is the convolution of all transition dipole moments over the instantaneous state of the system defined by $\hat{\rho}(t)$.

In this work, the 200 lowest-lying excited states of each system are computed using the range-separated functional ωB97XD.[43] The carbon atoms are represented using a 6-31G basis and the heteroatoms with 6-311G++ basis sets, as implemented in Gaussian16.[44] The selection of functionals and basis sets was aimed at providing a good description of the optical properties exhibited by the chosen systems. Although the choice of a small double-ζ basis may lead to under-polarization of the carbon atoms, this would lead to a quantitative change in the simulations presented here but not a quantitative change. Nuclear motion is typically much slower than electron dynamics, and the nuclei are kept frozen throughout this work. All many-electron dynamical simulations are performed using in-house codes.[41,42,45−47] Matplotlib[48] is used to illustrate the transient electronic densities, the molecular orbitals, and all molecular structures.

RESULTS AND DISCUSSION

The results can be categorized into two main subsections: electronic structure and electron dynamics. The quantum chemistry analysis provides a comprehensive overview of the optical properties of these three systems and the electron dynamics reports on simulations of photoinduced circular charge migration, highlighting potential applications as molecular magnets.

Electronic Structure. The lower parts of the absorption spectra computed using linear response TDDFT are shown in Figure 1 for C_{60}, Mg@C_{60}, and Cl^-@C_{60}, respectively, from top to bottom. Ionization energies calculated using eq 7 are shown as vertical dashed lines. The general appearance of the three spectra is similar, with a small absorption peak at lower energy and two dominant bands between 150 and 220 nm.

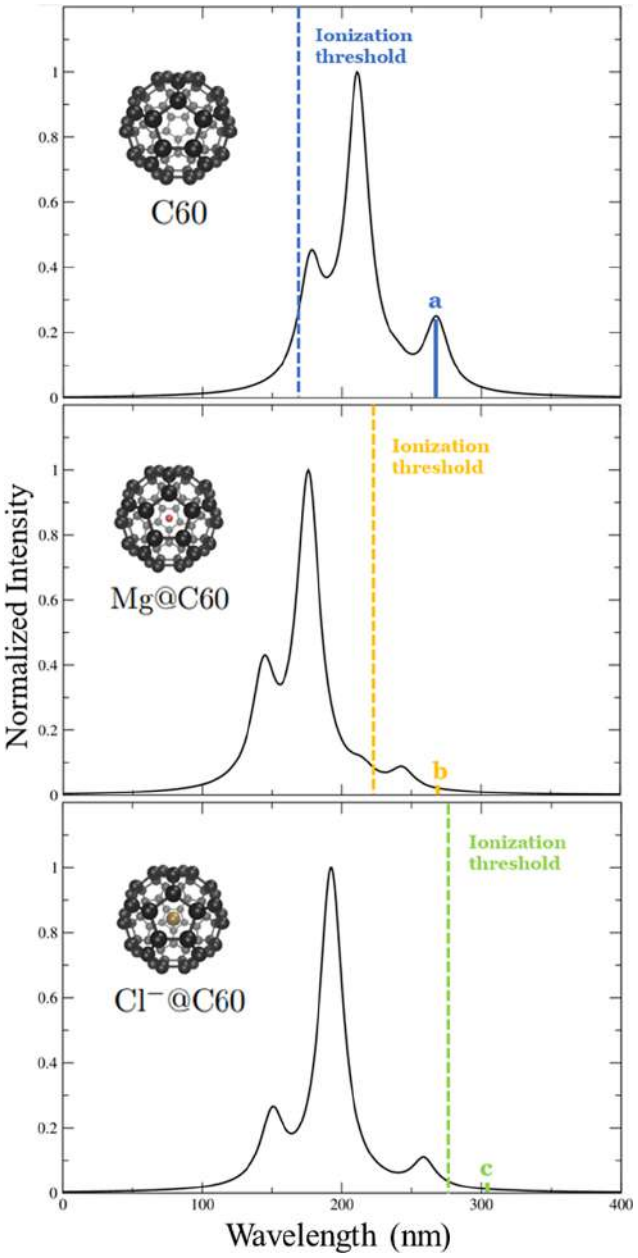

Figure 1. Absorption spectra of the three systems under analysis, namely, buckminsterfullerene (C_{60}), endohedral Mg (Mg@C_{60}), and e Cl^- (Cl^-@C_{60}). Vertical dashed lines indicate the ionization thresholds calculated using eq 7. Solid lines labeled a/b/c mark the target states for the dynamics. All bands are convoluted using Lorentzian functions with fwhm = 0.1 eV.

The main difference is that the largest peaks are found above the ionization threshold in both endohedral species.

In C_{60}, the ionization energy falls within the range of 7.6−7.8 eV[49,50] and all reported states in the top panel of Figure 1 are below this threshold. In Mg@C_{60}, the inclusion of the Mg atom in the carbon cage decreases the ionization energy of the system to 6.05 eV, also much below the ionization potential for free-standing Mg at about 7.6 eV.[51,52] This is indicative of a hybridization effect that stabilizes the endohedral system at the expense of destabilizing the highest occupied molecular orbital. Similarly, in Cl^-@C_{60}, the ionization energy decreases to 4.41 eV, indicative of the anion-like behavior of the system, where

https://doi.org/10.1021/acs.jpcc.4c06331
J. Phys. Chem. C 2025, 129, 464−472

the negative charge significantly influences the optical properties. Interestingly, the electron affinity of free-standing Cl is about 2.5 eV,[53] which indicates that the chlorine anion is strongly stabilized when encapsulated in C_{60}. This is in line with previous findings from static DFT calculations, which showed that C_{60} behaves like a large ion upon intake of various charged species.[13,54]

One aim of the static characterization is to identify states below the ionization threshold that can be photoexcited to transfer the angular momentum and induce circular charge migration. The energy of the selected excitations is labeled a/b/c in Figure 1 for the three systems, respectively. A list of all bright states below the ionization threshold is given for each system in the Supporting Information. For the pristine C_{60} system, all excitations correspond to CAGE−CAGE transitions. To minimize electron loss to the continuum upon photoexcitation, the lowest bright state of symmetry T_{1u} is retained as a target for the dynamics. It corresponds predominantly to a transition from 5-fold H_u to 3-fold T_{1g} orbitals, as can be seen from Figure 2a. This orbital transition

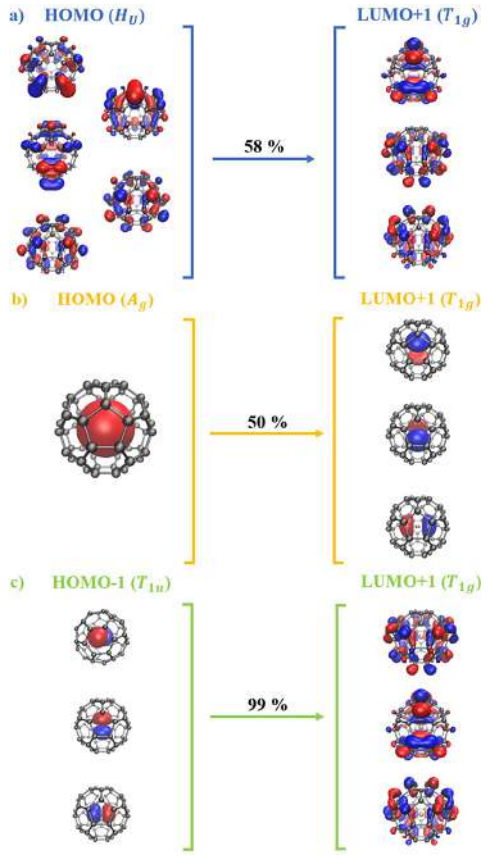

Figure 2. Dominant orbital transition character for selected excitations in (a) C_{60} at 270 nm, (b) Mg@C_{60} at 285 nm, and (c) Cl^-@C_{60} at 322 nm. Initial orbital on the left; final orbital on the right. The percentage associated with each transition is also reported.

corresponds to a redistribution of the electrons among the π-system of the C_{60} cage. The CAGE−CAGE character of all three peaks in the C_{60} spectrum is largely preserved in the other two systems, albeit with some slight energy shifts.

In Mg@C_{60}, the presence of the heteroatom opens the possibility to observe local transitions in the center of the C_{60} cage. Indeed, the HOMO of symmetry A_g involved in the excitation labeled 'b' (see central panel of Figure 1) is fully localized on the Mg atom, and the final orbital for the transition (LUMO+1, symmetry T_{1g}) is also localized on the central atom. Figure 2b shows that this transition determines about 50% of this target state, while many other higher local transitions also contribute a little to the character. Little hybridization with the orbitals localized on the endofullerene cage is observed. Yet, the lowest bright CAGE−CAGE transition is much reduced and its energy is blue-shifted, and it is likely responsible for some transfer of intensity to the ATOM−ATOM transition. The atom-like behavior observed in the Mg@C_{60} system is distinctive and absent in the other systems under examination.

For Cl^-@C_{60}, the ionization threshold greatly diminishes the range of excitations that can be photoexcited without the loss of electrons to the continuum. While the CAGE−CAGE transitions are still visible in the spectrum, they all appear above the ionization threshold for this system. A novel type of excitation emerges below the ionization threshold, denoted by the label 'c' in Figure 1. This low-intensity excitation is attributed to the transition with strong charge transfer character between orbitals localized on the Cl^- ion and those centered on the π-system of the fullerene cage (see Figure 2). In the following, it is termed the ATOM−CAGE transition.

Electron Dynamics. The results of the electron dynamics simulations are reported for the three systems in Figure 3. The transient populations and dipole moments are displayed in the left and right panels, respectively. In each case, the pulse duration is set to 20 fs, and the laser frequency $\hbar\omega$ in eq 2 is chosen to be resonant with the selected excitation. The amplitude $F_0^{(q)}$ and polarization direction (yz-plane) of the laser fields are chosen to maximize the population of the target state (labeled 'a', 'b', and 'c' in Figure 1 in panel a). The population dynamics of C_{60} reveals an almost complete depopulation of the ground state, while the target state is selectively populated at about 95% by the end of the simulation. Only the marginal population of other, nonresonant states is observed at intermediate times, which stems from the response of the electronic density when the oscillating field is on. The strong quantitative population transfer to the target state is made possible because the transition dipole moments that mediate the transition in the yz-plane are large. No electron loss is observed under the simulation conditions because the frequency is far from the ionization threshold and the intensity of the laser pulse ($I = 0.43 \times 10^{12}$ W/cm^2, $F_{q0} = 1.27 \times 10^9$ V/m) remains moderate. By the end of the pulse, a circularly rotating wave packet composed of two states is created. This can be observed from the right panel of Figure 3a, which shows the expectation values of the dipole moment in the yz-plane as a function of time. This rotating dipole could potentially be detected directly in an experimental setup with suitable time resolution.[55] The rotation period of the dipole is determined by the frequency of the circularly polarized pulse, which effectively transfers its angular momentum to the wave packet. The direction of charge migration can be simply inverted by using clockwise circular polarization (see panels b and c, for example). The field and dipole rotate at the same frequency because the electronic wave packet created after the pulse is essentially a superposition of the ground state and an angular-momentum bearing state. This can be represented conceptually as $|\psi\rangle = e^{-i\tilde{E}_0 t/\hbar}(C_0|0\rangle + C_e e^{-i\omega_{0e}t}|e\rangle)$, with $\{C_0, C_e\}$ a complex coefficient containing the phase information from the

https://doi.org/10.1021/acs.jpcc.4c06331
J. Phys. Chem. C 2025, 129, 464−472

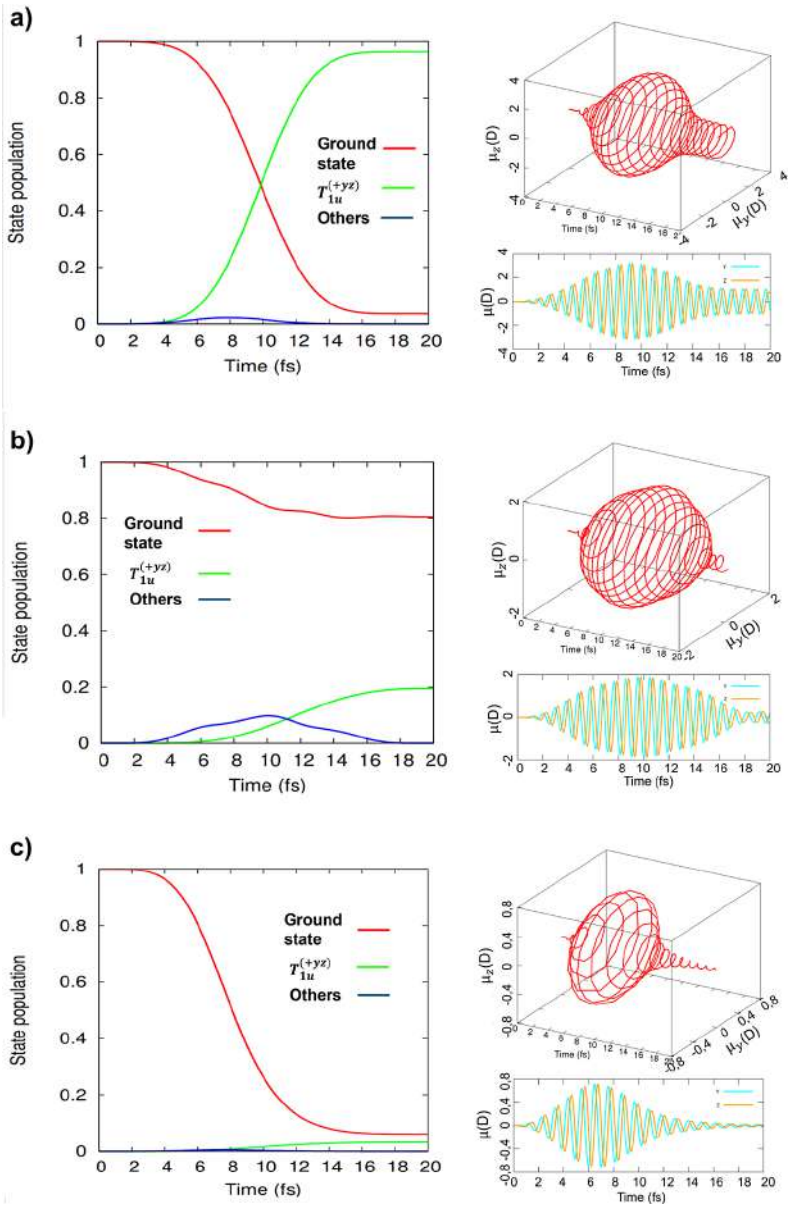

Figure 3. Population dynamics (left panels) and time-dependent dipole moments (right panels) for laser excitation of C_{60}, $Mg@C_{60}$, and $Cl^{-}@C_{60}$, respectively, from top to bottom. In each case, a pulse of duration T = 20 fs is used to trigger the dynamics, and the laser frequency is set resonant with the selected excitation. Laser parameters for panel (a) $\hbar\omega$ = 4.63 eV and $F_{q0} = 1.27 \times 10^9$ V/m, panel (b) $\hbar\omega$ = 4.34 eV and $F_{q0} = 3.63 \times 10^9$ V/m, and panel (c) $\hbar\omega$ = 3.84 eV and $F_{q0} = 3.63 \times 10^9$ V/m. Target state population in green, ground state population in red, and population of all other states in blue.

laser excitation. The frequency ω_{0e} corresponds precisely to that of the resonant transition excited by the laser, which explains why the field and dipole oscillate at the same frequency. Further, it was shown that there is no dephasing between the field and dipole in a dissipative system when laser excitation occurs at the resonance frequency,[47] which explains why they are also in phase during the pulse.

In panel b, the population dynamics of $Mg@C_{60}$ is reported for a laser pulse tuned to excite selectively the ATOM−ATOM transition in magnesium (label 'b' in Figure 1). The population of the target state is much lower (about 20%) due to the small transition dipole moments, which require a larger pulse intensity to obtain a larger depopulation of the ground state and a consequent population of the target states. Despite competition from the bright CAGE−CAGE transition at 240 nm, excitation of the ATOM−ATOM transition remains very selective. Since the pulse intensity is larger than for the C_{60} excitation ($I = 0.1 \times 10^{13}$ W/cm^2, $F_{q0} = 3.63 \times 10^9$ V/m), the electronic response is much larger during the pulse, as can be seen from the blue line that reaches in excess of 10% population at intermediate times.

The stronger electronic response leads to a loss of excitation selectivity when increasing the field amplitude. Furthermore, using a more intense field leads to a larger depopulation of the ground state at the expense of an increased ionization loss without improving transfer efficiency to the target state. The dipole moment reveals, in part, the strong electronic response of the system, which has a more regular amplitude when the field is on. By the end of the pulse, the amplitude of the rotating dipole moment becomes very small compared to the

https://doi.org/10.1021/acs.jpcc.4c06331
J. Phys. Chem. C 2025, 129, 464−472

pristine C_{60} simulation. This is due to the fact that charge is being displaced on a much smaller distance in the ATOM−ATOM transition and that charge migration occurs on a very small radius around the central Mg atom compared with the cage dimensions. Hence, circular charge migration will not lead to a strong fluctuation of the dipole moment, despite the fact that the laser pulse effectively transfers a significant amount of angular momentum to the electronic system.

A very different behavior is observed for the $Cl^-@C_{60}$ system, whose population dynamics is depicted in Figure 3c. In this case, the population of the target state is accompanied by a strong bleach of the ground state. Yet, only about 5% of the population reaches the target and 7% remains in the ground state by the end of the pulse. For the selected ATOM−CAGE transition, the strong charge transfer character leads to small transition dipoles. It is thus necessary to use much stronger fields ($F_0^{(q)} = 3.63 \times 1 \times 10^9$ V/m) to excite the system. Yet, an electronic response is barely observed throughout the dynamics. In such intense fields ($I = 0.1 \times 10^{13}$ W/cm^2), the dynamics is typically subject to strong dynamical broadening and multiphoton processes. The former allows exciting transitions that are not strictly resonant with the field frequency. Since the selected ATOM−CAGE transition is just below the ionization threshold, dynamic broadening enables direct ionization. The high field intensity also opens the possibility of two-photon ionizations, which further increases the photoionization probability. In fact, even for this high-intensity laser, the Keldysh parameter is about 15 which confirms the strong preference for multiphoton processes over tunnel ionization.[56] The increased propensity of $Cl^-@C_{60}$ to release electrons upon photoexcitation at low energies would make it an excellent candidate for sensor applications. The wave packet created by the field reveals an interesting dipole moment profile. After an initial rise due to the electronic response of the system and the partial population of the target state, the magnitude of the dipole moment decreases exponentially to a vanishingly small value at the end of the pulse. While this exponential decay can be understood by the population loss to the ionization continuum, the origin of the remaining small dipole moment cannot be explained on the basis of simple geometrical arguments as in the two previous scenarios.

The interaction with circularly polarized laser pulses results in complex and rich electron dynamics in all three systems under investigation. The rotation of the dipole in the plane of the pulse polarization (yz) is an indication of the successful transfer of the angular momentum to the electronic density upon photoexcitation. Yet, the dipole moment is too coarse to capture the subtleties of charge migration in such systems. To this end, the top panels of Figure 4 show the difference in electronic density, eq 9, for the last period of the dynamics in photoexcited C_{60}, when the field becomes vanishingly small. Regions of density increase are depicted in orange and those of density depletion are shown in cyan. The four snapshots span the period defined by the field frequency, $T = 2\pi/\omega = 0.88$ fs. At t_0, the system excitation to the target excited state leads to electron−hole separation on the cage and along the y-direction, causing the induced dipole observed in Figure 3a. The three following snapshots, respectively, at delay times of $T/4$, $T/2$, and $3T/4$, demonstrate the circular charge migration about the x-axis. This picture is confirmed by the time-derivative of the instantaneous density depicted in the bottom panels. In the first snapshot, the density is found to increase on

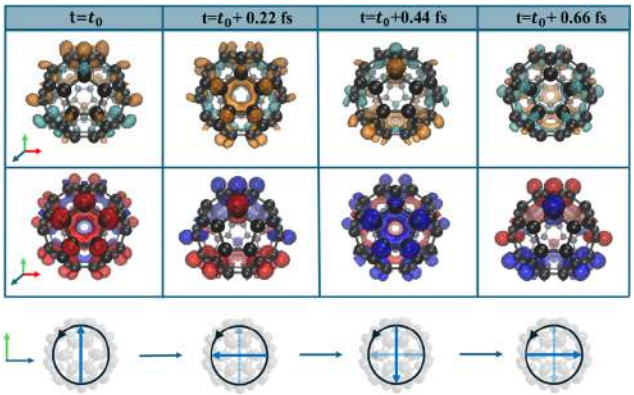

Figure 4. Transient electronic density ($\Delta\rho(\mathbf{r})$) and its time-derivative ($\partial_t\rho(\mathbf{r})$) for charge migration in the photoexcited C_{60} system are presented in the first and second rows, respectively. The laser pulse parameters are given in Figure 3. The orientation is chosen such that the x-axis points to the right and the y-axis to the top, with the z-axis sticking out of the paper. Positive/negative isovalues are presented in orange/cyan and red/blue for the difference density and for its time-derivative, respectively. The time t_0 is chosen to cover the last period of field-free charge migration. Bottom panel: cartoon representation of the charge migration mechanism projected in the yz-plane. The length of the arrow correlates with the magnitude and position of the expectation value of the dipole moment.

the five-membered ring along the positive z-axis (red isocontours) and is depleted at the back of the C_{60} cage. It is very similar to the charge distribution (top panel) that is observed at the next time step, i.e., at t_0 + 0.22 fs. The pattern repeats itself for the subsequent time steps, indicating that the difference density can be predicted directly from its time-derivative at the previous time step. It should be noted that this finding is only strictly correct for a wave packet behaving like a two-level system, as is the case here. Placing the positive and negative charges approximately on the cage further allows for estimating the degree of charge separation in the wave packet. For a C_{60} of radius of 3.52429 Å and a dipole magnitude of about 1D, this amounts to an effective charge separation of mere ∼0.03 e. This can be rationalized by the fact that although the negative charge is mostly localized on a five-membered ring at a given instance, the positive charges are more spread on the whole cage. Despite the small charge separation achieved by laser excitation, the magnitude of the rotating dipole is large because of the relatively important distance of the charge separation imposed by the C_{60} cage.

The top panels of Figure 5 show snapshots of the difference density in the $Mg@C_{60}$ case for each quarter of the charge migration period of duration $T = 2\pi/\omega = 1.02$ ps. The snapshots confirm that the electron−hole pair is created around the central Mg atom. This is to be expected from the LOCAL−LOCAL character of the orbital transitions associated with the targeted excited state (see Figure 2b). Yet, important differences are observed on the cage, which is also found to undergo circular charge migration. This is a consequence of the hybridization between the atomic orbitals of the Mg center and the molecular orbitals of the C_{60} cage. Since the target state becomes only about 20% populated by the end of the pulse, the amount of charge separation is small. Further, the electron−hole pair is predominantly localized close to the central atom, which implies a small charge separation distance and a small dipole magnitude as a

https://doi.org/10.1021/acs.jpcc.4c06331
J. Phys. Chem. C 2025, 129, 464−472

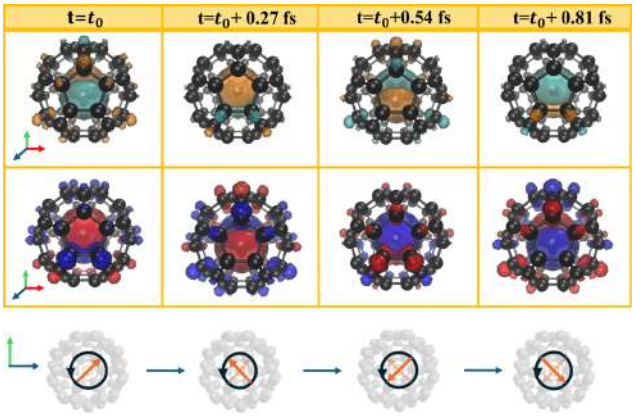

Figure 5. Same as Figure 4 but for charge migration in photoexcited Mg@C_{60}.

consequence—about half of what is observed in C_{60} (see Figure 3b). The time-derivative of the density is found again to be a good predictor of the difference density at the subsequent time step, but it appears to be more sensitive. Indeed, the features of electron dynamics on the C_{60} cage are more prominent, and they reveal that the charge migration from the atom rotating about itself is localized in the π-system of the cage. These results show that electron dynamics can reveal subtle features that are barely observable from static calculations.

The situation with Cl^-@C_{60} differs significantly from that of the other two cases. The induced dipole, shown in Figure 3c, becomes vanishingly small at the end of the pulse, despite some populations reaching the target state and bearing the signature of photon-to-electron angular momentum transfer. The targeted excited states, in this case, are characterized by an ATOM−CAGE transition involving an initial Cl^- orbital and final cage orbitals. This behavior is evident from the snapshots of the difference density in the top panels of Figure 6. The

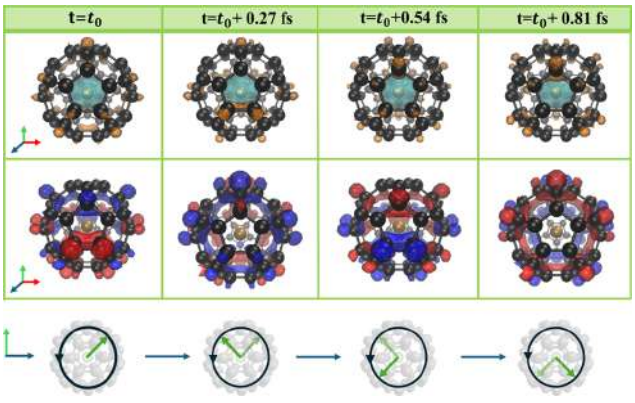

Figure 6. Same as Figure 4 but for charge migration in photoexcited Cl^-@C_{60}.

holes remain mostly localized on the Cl atom at the center with a well-defined spherical symmetry. The changes in electron density occur primarily on the cage rather than the central atom, but the changes registered are small. The rotational behavior, clearly observed in the other two systems, is not easily recognizable here. The almost isotropic distribution of the electron effectively leads to a vanishing small dipole in the wave packet created by the ATOM−CAGE transition in endohedral Cl^-@C_{60}. Nonetheless, the signatures of circular charge migration—and of angular momentum transfer—are more readily observed from the time-derivative of the electron density (bottom panels of Figure 6). The four snapshots reveal that during the rotation period of duration $T = 2\pi/\omega = 1.02$ ps the charge migration is observed only around the cage and in the space away from the central atom. Contrary to the two previous cases, there is no correspondence between the time-derivative of the electron density and the difference density at the subsequent snapshot, indicating more intricate dynamics dominated by the quasi-spherical character of the ATOM−CAGE transition.

■ CONCLUSIONS

In this study, we investigated how doping C_{60} with different atomic species affects its ultrafast photoinduced electron dynamics. We focused on two types of endohedral fullerenes—one with a Cl^- anion and another with a Mg atom—and compared their behaviors to a reference fullerene system. The systems were excited by using circularly polarized light, which transfers angular momentum to their electron densities. To understand these dynamics, we analyzed and visualized changes in the electron density and its time-derivative. We started with quantum chemistry analysis to determine key properties and select specific excitations for our electronic dynamics calculations. The behavior of the endofullerenes was found to be distinctly influenced by the nature of the encaged species: the Cl^- system exhibits characteristics typical of an anion, while the Mg system retains features reminiscent of the free atom. Through our calculations and imaging, we observed diverse electronic behaviors across the three systems. In the case of the pristine fullerene, the transfer of angular momentum resulted in significant depopulation of the ground state and selective excitation of target excited states, leading to substantial charge separation and the formation of a rotating dipole. For the Mg-doped endofullerene, similar angular momentum transfer was noted with electron density variations concentrated around the Mg atom. Conversely, the Cl^-@C_{60} system showed minimal angular momentum transfer and a negligible induced dipole. In this case, changes in electron density were primarily localized on the fullerene cage rather than on the Cl^- ion, leading to an isotropic distribution of electrons and holes. This isotropic distribution accounts for the low induced dipole and the nature of charge migration observed in the system. Our results indicate that doping fullerene with Cl^- and Mg significantly alters the electronic dynamics compared to the pristine fullerene system, leading to a wide range of distinct behaviors. The subtleties of the ultrafast electron dynamics could be directly observed by time-resolved X-ray scattering[26,34,57−59] or by monitoring the time-dependent dipole moment.[55]

A fascinating route for future research would be to explore how incorporating these doped fullerene systems within a larger nanostructure, such as a carbon peapod, would affect their electronic dynamics. This could provide insights into the interactions between the doped fullerenes and the encapsulating nanostructure, potentially revealing new physical properties or emergent behaviors due to the confined environment. Investigating these effects could not only deepen our understanding of the fundamental physics involved but also pave the way for developing novel nanodevices with tailored electronic properties.

https://doi.org/10.1021/acs.jpcc.4c06331
J. Phys. Chem. C 2025, 129, 464−472

■ ASSOCIATED CONTENT

Supporting Information

The Supporting Information is available free of charge at https://pubs.acs.org/doi/10.1021/acs.jpcc.4c06331.

Coordinate files for all optimized structures and list of bright-state characters (PDF)

■ AUTHOR INFORMATION

Corresponding Authors

Leonardo Biancorosso − *Dipartimento di Scienze Chimiche e Farmaceutiche, Università di Trieste, 34127 Trieste, Italy;* orcid.org/0009-0002-2180-5898; Email: leonardo.biancorosso@phd.units.it

Jean Christophe Tremblay − *CNRS-Université de Lorraine, LPCT, 57070 Metz, France;* orcid.org/0000-0001-8021-7063; Email: jean-christophe.tremblay@univ-lorraine.fr

Author

Emanuele Coccia − *Dipartimento di Scienze Chimiche e Farmaceutiche, Università di Trieste, 34127 Trieste, Italy;* orcid.org/0000-0003-3389-0989

Complete contact information is available at: https://pubs.acs.org/10.1021/acs.jpcc.4c06331

Notes

The authors declare no competing financial interest.

■ ACKNOWLEDGMENTS

The authors acknowledge the Erasmus+ Traineeship grant 2022-1-IT02-KA131-HED-000064396 for the funding.

■ REFERENCES

(1) Smalley, R. E. Discovering the fullerenes (Nobel lecture). *Angew. Chem., Int. Ed.* **1997**, *36*, 1594−1601.
(2) Martin, C. A.; Ding, D.; Sørensen, J. K.; Bjørnholm, T.; van Ruitenbeek, J. M.; van der Zant, H. S. Fullerene-based anchoring groups for molecular electronics. *J. Am. Chem. Soc.* **2008**, *130*, 13198−13199.
(3) Pinzon, J. R.; Villalta-Cerdas, A.; Echegoyen, L. Fullerenes, carbon nanotubes, and graphene for molecular electronics. In *Unimolecular and Supramolecular Electronics I: Chemistry and Physics Meet at Metal-Molecule Interfaces*; Springer, 2012; pp 127−174.
(4) Guldi, D. M.; Illescas, B. M.; Atienza, C. M.; Wielopolski, M.; Martín, N. Fullerene for organic electronics. *Chem. Soc. Rev.* **2009**, *38*, 1587−1597.
(5) Wudl, F. Fullerene materials. *J. Mater. Chem.* **2002**, *12*, 1959−1963.
(6) Nierengarten, J.-F.; Guttiérez-Nava, M.; Zhang, S.; Masson, P.; Oswald, L.; Bourgogne, C.; Rio, Y.; Accorsi, G.; Armaroli, N.; Setayesh, S. Fullerene-containing macromolecules for materials science applications. *Carbon* **2004**, *42*, 1077−1083.
(7) Kataura, H.; Maniwa, Y.; Abe, M.; Fujiwara, A.; Kodama, T.; Kikuchi, K.; Imahori, H.; Misaki, Y.; Suzuki, S.; Achiba, Y. Optical properties of fullerene and non-fullerene peapods. *Appl. Phys. A: Mater. Sci. Process.* **2002**, *74*, 349−354.
(8) Kamanina, N. V. *Organic nanophotonics*; Springer, 2003; pp 177−192.
(9) Collavini, S.; Delgado, J. L. Fullerenes: the stars of photovoltaics. *Sustainable Energy & Fuels* **2018**, *2*, 2480−2493.
(10) Friedl, J.; Lebedeva, M. A.; Porfyrakis, K.; Stimming, U.; Chamberlain, T. W. All-fullerene-based cells for nonaqueous redox flow batteries. *J. Am. Chem. Soc.* **2018**, *140*, 401−405.
(11) Chai, Y.; Liu, X.; Wu, B.; Liu, L.; Wang, Z.; Weng, Y.; Wang, C. In situ switching of photoinduced electron transfer direction by regulating the redox state in fullerene-based dyads. *J. Am. Chem. Soc.* **2020**, *142*, 4411−4418.
(12) Popov, A. A.; Yang, S.; Dunsch, L. Endohedral fullerenes. *Chem. Rev.* **2013**, *113*, 5989−6113.
(13) Cioslowski, J. Endohedral chemistry: Electronic structures of molecules trapped inside the C_{60} cage. *J. Am. Chem. Soc.* **1991**, *113*, 4139−4141.
(14) Chandler, H. J.; Stefanou, M.; Campbell, E. E.; Schaub, R. Li@C60 as a multi-state molecular switch. *Nat. Commun.* **2019**, *10*, 2283.
(15) Jeon, I.; Shawky, A.; Lin, H.-S.; Seo, S.; Okada, H.; Lee, J.-W.; Pal, A.; Tan, S.; Anisimov, A.; Kauppinen, E. I.; et al. Controlled redox of lithium-ion endohedral fullerene for efficient and stable metal electrode-free perovskite solar cells. *J. Am. Chem. Soc.* **2019**, *141*, 16553−16558.
(16) Ali, E.; Madjet, M. E.-A.; De, R.; Frauenheim, T.; Chakraborty, H. S. Ultrafast nonadiabatic electron dynamics in photoexcited C60: A comparative study among DFT exchange-correlation functionals. **2023**, *arXiv preprint arXiv:2306.16386*.
(17) Saroj, A.; Ramanathan, V.; Mishra, B. K.; Panda, A. N.; Sathyamurthy, N. Improved estimates of host-guest interaction energies for endohedral fullerenes containing rare gas atoms, small molecules, and cations. *ChemPhysChem* **2022**, *23*, No. e202200413.
(18) Chakraborty, D.; Chattaraj, P. K. Bonding, reactivity, and dynamics in confined systems. *J. Phys. Chem. A* **2019**, *123*, 4513−4531.
(19) De Proft, F.; Van Alsenoy, C.; Geerlings, P. Ab initio study of the endohedral complexes of C60, Si60, and Ge60 with monoatomic ions: Influence of electrostatic effects and hardness. *J. Phys. Chem.* **1996**, *100*, 7440−7448.
(20) Sabirov, D. S.; Bulgakov, R. Polarizability exaltation of endofullerenes X@ C n (n= 20, 24, 28, 36, 50, and 60; X is a noble gas atom). *JETP letters* **2010**, *92*, 662.
(21) Li, M.; Zhao, R.; Dang, J.; Zhao, X. Theoretical study on the stabilities, electronic structures, and reaction and formation mechanisms of fullerenes and endohedral metallofullerenes. *Coord. Chem. Rev.* **2022**, *471*, No. 214762.
(22) Dixit, G.; Chakraborty, H. S.; Madjet, M. E.-A. Time delay in the recoiling valence photoemission of ar endohedrally confined in c 60. *Phys. Rev. Lett.* **2013**, *111*, No. 203003.
(23) Jorn, R.; Zhao, J.; Petek, H.; Seideman, T. Current-driven dynamics in molecular junctions: endohedral fullerenes. *ACS Nano* **2011**, *5*, 7858−7865.
(24) Madjet, M. E.-A.; Ali, E.; Carignano, M.; Vendrell, O.; Chakraborty, H. S. Ultrafast Transfer and Transient Entrapment of Photoexcited Mg Electron in Mg@ C 60. *Phys. Rev. Lett.* **2021**, *126*, No. 183002.
(25) Picón, A.; Benseny, A.; Mompart, J.; de Aldana, J. V.; Plaja, L.; Calvo, G. F.; Roso, L. Transferring orbital and spin angular momenta of light to atoms. *New J. Phys.* **2010**, *12*, No. 083053.
(26) Tremblay, J. C.; Pohl, V.; Hermann, G.; Dixit, G. Time-resolved imaging of correlation-driven charge migration in light-induced molecular magnets by X-ray scattering. *Faraday Discuss.* **2021**, *228*, 82−103.
(27) Sun, S.; Yong, H.; Chen, F.; Mukamel, S. Coherent ring-current migration of Mg-phthalocyanine probed by time-resolved X-ray circular dichroism. *Chem. Sci.* **2022**, *13*, 10327−10335.
(28) Nandipati, K. R.; Vendrell, O. On the generation of electronic ring currents under vibronic coupling effects. *J. Chem. Phys.* **2020**, *153*, 224308.
(29) Nandipati, K. R.; Sasmal, S.; Vendrell, O. Inverse optically-induced ring currents in ring-shaped molecules. *J. Phys. Chem. Lett.* **2024**, *15*, 5034−5040.
(30) Klinkusch, S.; Tremblay, J. C. Resolution-of-identity stochastic time-dependent configuration interaction for dissipative electron dynamics in strong fields. *J. Chem. Phys.* **2016**, *144*, 184108.
(31) Hermann, G.; Tremblay, J. C. Ultrafast photoelectron migration in dye-sensitized solar cells: Influence of the binding mode and many-body interactions. *J. Chem. Phys.* **2016**, *145*, 174704.

(32) Pohl, V.; Hermann, G.; Tremblay, J. C. An open-source framework for analyzing N-electron dynamics. I. Multideterminantal wave functions. *J. Comput. Chem.* **2017**, *38*, 1515−1527.
(33) Hermann, G.; Pohl, V.; Tremblay, J. C. An open-source framework for analyzing N-electron dynamics. II. Hybrid density functional theory/configuration interaction methodology. *J. Comput. Chem.* **2017**, *38*, 2378−2387.
(34) Hermann, G.; Pohl, V.; Dixit, G.; Tremblay, J. C. Probing electronic fluxes via time-resolved x-ray scattering. *Phys. Rev. Lett.* **2020**, *124*, No. 013002.
(35) Langkabel, F.; Albrecht, P. A.; Bande, A.; Krause, P. Making optical excitations visible−An exciton wavefunction extension to the time-dependent configuration interaction method. *Chem. Phys.* **2022**, *557*, No. 111502.
(36) Coccia, E.; Troiani, F.; Corni, S. Probing quantum coherence in ultrafast molecular processes: An ab initio approach to open quantum systems. *J. Chem. Phys.* **2018**, *148*, 204112.
(37) Hoerner, P.; Lee, M. K.; Schlegel, H. B. Angular dependence of strong field ionization of N_2 by time-dependent configuration interaction using density functional theory and the Tamm-Dancoff approximation. *J. Chem. Phys.* **2019**, *151*, No. 054102.
(38) Coccia, E.; Luppi, E. Time-dependent ab initio approaches for high-harmonic generation spectroscopy. *J. Phys.: Condens. Matter* **2022**, *34*, No. 073001.
(39) *Orbkit download link*. https://github.com/orbkit/orbkit (accessed October 2020).
(40) Klinkusch, S.; Saalfrank, P.; Klamroth, T. Laser-induced electron dynamics including photoionization: A heuristic model within time-dependent configuration interaction theory. *J. Chem. Phys.* **2009**, *131*, 114304.
(41) Tremblay, J. C.; Klinkusch, S.; Klamroth, T.; Saalfrank, P. Dissipative many-electron dynamics of ionizing systems. *J. Chem. Phys.* **2011**, *134*, No. 044311.
(42) Tremblay, J. C.; Carrington, T., Jr. Using preconditioned adaptive step size Runge-Kutta methods for solving the time-dependent Schrödinger equation. *J. Chem. Phys.* **2004**, *121*, 11535.
(43) Chai, J.-D.; Head-Gordon, M. Long-range corrected hybrid density functionals with damped atom−atom dispersion corrections. *Phys. Chem. Chem. Phys.* **2008**, *10*, 6615−6620.
(44) Frisch, M. J.; Trucks, G. W.; Schlegel, H. B.; Scuseria, G. E.; Robb, M. A.; Cheeseman, J. R.; Scalmani, G.; Barone, V.; Petersson, G. A.; Nakatsuji, H. *Gaussian 16, Revision A. 03*; Gaussian. Inc.: Wallingford, CT, 2016,.
(45) Tremblay, J. C.; Klamroth, T.; Saalfrank, P. Time-dependent configuration-interaction calculations of laser-driven dynamics in presence of dissipation. *J. Chem. Phys.* **2008**, *129*, No. 084302.
(46) Tremblay, J. C.; Saalfrank, P. Guided locally-optimal control of quantum dynamics in dissipative environments. *Phys. Rev. A* **2008**, *78*, No. 063408.
(47) Tremblay, J. C.; Krause, P.; Klamroth, T.; Saalfrank, P. The effect of energy and phase relaxation on dynamic polarizability calculations. *Phys. Rev. A* **2010**, *81*, No. 063420.
(48) Hunter, J. D. Matplotlib: A 2D graphics environment. *Comput. Sci. Eng.* **2007**, *9*, 90−95.
(49) Baba, M. S.; Narasimhan, T. L.; Balasubramanian, R.; Mathews, C. Ionization and fragmentation of C60: an electron impact ionization study. *J. Phys. Chem.* **1995**, *99*, 3020−3032.
(50) Muigg, D.; Scheier, P.; Becker, K.; Märk, T. Measured appearance energies of fragment ions produced by electron impact on. *J. Phys. B: At. Mol. Opt. Phys.* **1996**, *29*, 5193.
(51) Rauh, E.; Ackermann, R. First ionization potentials of some refractory oxide vapors. *J. Chem. Phys.* **1974**, *60*, 1396−1400.
(52) Rauh, E.; Ackermann, R. The first ionization potentials of the transition metals. *J. Chem. Phys.* **1979**, *70*, 1004−1007.
(53) Bowen, K.; Liesegang, G.; Sanders, B.; Herschbach, D. Electron attachment to molecular clusters by collisional charge transfer. *J. Phys. Chem.* **1983**, *87*, 557−565.
(54) Cioslowski, J.; Fleischmann, E. D. Endohedral complexes: atoms and ions inside the C_{60} cage. *J. Chem. Phys.* **1991**, *94*, 3730−3734.
(55) Yachmenev, A.; Yurchenko, S. N. Detecting chirality in molecules by linearly polarized laser fields. *Phys. Rev. Lett.* **2016**, *117*, No. 033001.
(56) Keldysh, L. V. *Selected Papers of Leonid V Keldysh*; World Scientific, 2024; pp 47−55.
(57) Giri, S.; Tremblay, J. C.; Dixit, G. Imaging charge migration in chiral molecules using time-resolved x-ray diffraction. *Phys. Rev. A* **2021**, *104*, No. 053115.
(58) Giri, S.; Tremblay, J. C.; Dixit, G. Probing the effect of molecular structure saddling on ultrafast charge migration via time-resolved x-ray diffraction. *Phys. Rev. A* **2022**, *106*, No. 033120.
(59) Tremblay, J. C.; Blanc, A.; Krause, P.; Giri, S.; Dixit, G. Probing Electronic Symmetry Reduction during Charge Migration via Time-Resolved X-Ray Diffraction. *ChemPhysChem* **2023**, *24*, No. e202200463.

https://doi.org/10.1021/acs.jpcc.4c06331
J. Phys. Chem. C 2025, 129, 464−472

3.2 Time–Resolved ECD

We present a combined spectroscopic and structural analysis of the photoisomerization dynamics of a molecular motor (9-(2,4,7-trimethyl-2,3-dihydro-1H-inden-1-ylidene)-9H-fluorene). Inspired by the work of Miròn *et al.* [168] and Vicario *et al.* [169], we intend to follow the photoisomerization process, with pump in S_1, through a computational protocol which allows us to combine the methods developed in our group with the ones in the group of Ali Hassanali at ICTP in Trieste.

This family of motors undergoes unidirectional 360° rotation via a four-step cycle consisting of two photochemical isomerizations followed by two thermal helix inversions, with the rate of rotation governed by the activation energy of the thermal steps [170] (Figure 3.1). Structural modifications that increase steric hindrance slow rotation, whereas reducing steric congestion-such as replacing six–membered rings with five–membered ones-accelerates it [171]. This approach has enabled the design of the fastest light–driven molecular motors to date and continues to guide the optimization of their dynamic behavior [169]. The first generation of molecular motors was formed by symmetric biphenanthrylidenes [172]. Based on that model, many different modification have been made to increase the speed of rotation[171, 173, 174, 175]. The new class of molecular motor is based on a 5-membered upper half ring and a fluorene lower half [169]. Its molecular structures is shown in Figure 3.1. The mechanism of photoisomerization initiates with a photon-induced excitation [170, 176], which promotes the molecule to an excited electronic state and triggers a rotation around the dihedral angle. This process leads to the formation of an unstable ground-state intermediate (M) through a conical intersection (CI). Subsequently, thermal energy drives a helix inversion, resulting in the formation of a stable conformer (P). Representation of this process is reported in Figure 3.1. The photon-induced step is of primary importance, as it provides the necessary energy to activate the molecular motor and constitutes the central focus of this study.

In the work of Miron et al. [168], the photo-isomerization process was investigated in detail, yielding particularly insightful results. Upon excitation of the molecular motor in its initial configuration, the authors observed the formation of two distinct conformers: one corresponding to the photo-isomerized product (the M isomer) and another whose conformation closely resembles that of the reactant (the P isomer).

Using the NAMD simulations of from Ref. [168], we intend to simulate ECD and absorption spectra along these trajectories, trying to correlate the spectral features of the molecular structures with the evolution of the dihedral angle that drives isomerization. By doing so, we apply a time-resolved methodology for ECD calculations, effectively simulating a TR-ECD experiment (see Section 3.2 of Chapter 1).

Following the classification in the reference work of Miron et al., two distinct classes of trajectories were identified. Active trajectories display the expected decrease of the dihedral angle and converge to the M isomer of the photoproduct [168] (see Figure 3.8). In contrast, non-active trajectories, characterized by persistently large dihedral angles, fail to isomerize and remain structurally close to the initial configuration (P isomer formation in the ground state S_0, see Figure 3.8). This distinction is clearly reflected in the simulated ECD spectra, which exhibit high sensitivity to the conformational diversity emerging during the dynamics, whereas the absorption spectra remain comparatively featureless. These findings underscore the utility of ECD spectroscopy as a probe of isomer–specific pathways and structural variability in photoactive systems. Although preliminary, the results already highlight meaningful trends. Despite the approximate nature of both the clustering procedure and the trajectory sampling frequency, the simulations demonstrate the potential of computational spectroscopy to complement ultrafast experiments by offering mechanistic insight into the interplay between electronic responses and conformational dynamics in light–driven molecular machines. It is important to note that the theoretical methodology employed here is not suited for an accurate description of the electronic structure near conical intersections. Nonetheless, it still enables the extraction of valuable semiquantitative information from the simulations.

Supervised by E. Coccia, M. Monti and A. Hassanali I performed the electronic dyanmics simulations on the selected geometries and performed the geometrical and spectroscopical analysis. NAMD simulations were computed by G. D. Miron. M. Monti and G. D. Miron currently work in the group of Ali Hassanali at ICTP in Trieste.

3.2.1 Methods

Nonadiabatic Molecular Dynamics

NAMD simulations were carried out using the DFTB method [177] as implemented in the open-source packages DFTB+ [178] and SHARC [179]. The computational strategy follows the approach established by Miron *et al.* [168], which combines the analytical evaluation of the nonadiabatic coupling vectors (NACVs) between the ground and excited states with the pseudo–wavefunction formalism for computing NACVs among excited states. For details of the NACV implementation within the DFTB framework, the reader is referred to Ref. [168].

In the present work, the Tamm–Dancoff approximation (TDA) was employed. This approximation is well known to produce results comparable to Casida formalism while avoiding the numerical instabilities that often arise near conical intersections [180].

The photoinduced dynamics were simulated using the trajectory surface hopping (TSH) algorithm [181], along the ground state S_0 and a few excited states (see below). Within this scheme, nuclear motion is treated classically using forces derived from a single potential energy surface. At each time step, the probability of a nonradiative transition is evaluated, and a stochastic algorithm determines whether the system continues on the current surface or hops to another.

Because the photophysical relaxation of the system occurs on fast timescales (femtoseconds to picoseconds), the trajectory evolution is strongly dependent on the initial conditions. To achieve reliable convergence, an ensemble of trajectories must therefore be propagated. Additionally, a decoherence correction was applied following the method proposed by Granucci and Persico [182].

Electronic dynamics calculation: TDSE

To calculate the ECD spectra of the molecular motor, both in the ground and first excited state, we performed electronic dynamics simulations based on the TDSE. We reported the computational and methodological details of this kind of calculation in Section 2.1.1 of Chapter 2.

Calculation of Excited State Spectra

The ground S_0 and the first-excited S_1 are explicitly considered, i.e. $|C_{S_1}(t=0)|^2 = 1$ or $|C_{S_0}(t=0)|^2 = 1$ and calculations have been carried out on the corresponding molecular geometries. In other words, to get an excited-state spectrum, the initial condition for TDSE propagation is to have the system in that excited state, e.g. $|C_{S_1}(t=0)|^2 = 1$ to get a signal from S_1.

The calculation of excited–state spectra relies on the implementation of excited–excited magnetic and electric transition dipole moment elements. The methodology used to compute ECD spectra–described in Section 2.4, Subsection 2.4.1 of Chapter 2–is directly applicable to the excited–state spectra as well. Specifically, the spectra are obtained through the Fourier transform of the induced electric and magnetic dipole moment (see Eqs. 2.41 and 2.42). In this case, the time evolution involves transition dipole moments between excited states (see Eqs. 2.43 and 2.44), since the initial condition of the simulation places the system in an excited state rather than in the ground state. The computational details for evaluating these transition dipole moments within our interface are provided in Section 2.5 of Chapter 2. Once these quantities are available, the procedure to compute excited–state spectra is identical to that used for the ground–state case, as discussed in Section 2.4.1. To extract rotationally averaged spectra for each geometry, we employ Eq. 2.48. The calculation of the average spectra at each time t of the simulation can be calculated as:

$$\overline{P}^{\mathrm{X}}_{tot}(t) = \frac{\sum_i^N \overline{P}^{\mathrm{X}}_i(t)}{N} \tag{3.1}$$

where $\overline{P}_i(t)$ is the rotationally–averaged spectrum (with X=ABS or ECD) at a certain time t of the simulation for trajectory i and $\mathrm{P}_{tot}(t)$ is the full average spectrum at a certain time t, averaging over N trajectories.

In order to compare computed spectra with the experimental data, we must weight the theoretical spectra according to the experimentally determined excited–state population. This approach allows us to reproduce the observed spectral trends from pump probe experiments. The spectrum calculated at time t for the ith-trajectory is written as

$$\overline{P}^{\mathrm{X}}_{\mathrm{tot}}(t) = \frac{\sum_i^N \mathrm{pop} \times \overline{P}^{\mathrm{X}}_i(t) + (1 - \mathrm{pop}) \times \overline{P}^{\mathrm{X}}_{\mathrm{GS},i}(t = 0)}{N} \tag{3.2}$$

where $\overline{P}_{\mathrm{tot}}(t)$ is the full rotationally–averaged spectrum at a certain time t of the simulation. This spectra includes contributions from both the ground state (GS) and the target excited state. $\overline{P}_i(t)$ is the rotationally averaged spectrum computed at time t for trajectory i and pop is the experimentally measured excited–state population. $\overline{P}_{\mathrm{GS},i}$ represents the rotationally–averaged ground state spectrum at $t = 0$ of trajectory i. This weighting procedure accounts for the fraction of molecules that remain in the ground state after the photoexcitation but still contribute to the overall recorded spectrum.

All simulations were performed with the `WaveT` code, interfaced with AMS. Details on the computational setup can be found in Section 2.5.

3.2.2 Computation Details

The simulation workflow starts with optimizing the molecular geometry in vacuum, making use of the rational optimizer provided in DFTB+. Once the geometry optimization is complete, frequency calculations are carried out to obtain the vibrational frequencies and normal modes of the system. From these results, 200 random initial configurations (positions and velocities) are sampled from the Wigner distribution at 300 K. For each of these initial conditions, a TD-DFTB calculation was performed, considering the first 10 excited states. NAMD simulations were then executed within the NVE ensemble, using a 0.5 fs timestep. Hopping events were identified based on the NACVs, as described in the previous Section, with a decoherence correction parameter of 0.1 Hartree applied. Each simulation was propagated for 1 ps.

For the electronic dynamics, geometries from the 50 trajectories randomly chosen were sampled every 100 fs. On these selected structures, TDDFT calculations were performed at the CAM-B3LYP/TDA level with a TZ basis set, incorporating 100 excited states. Subsequently, electronic dynamics simulations of 100 fs were carried

out with a timestep of $\delta t = 1$ as. An external field was applied along the x, y, and z directions, and the resulting spectra were averaged across these orientations. The field parameters were chosen as FWHM = 94 as and an intensity of $I = 10^2$ W/cm^2.

3.2.3 Results

Figure 3.1 shows the ECD spectra of the initial configuration of the molecular rotor under study (9-(2,4,7-trimethyl-2,3-dihydro-1H-inden-1-ylidene)-9H-fluorene) - denoted as GS-and the corresponding photoproduct. Both spectra were calculated with WaveT in the electronic ground state. We extracted two geometries from the NAMD simulations, associated with the initial (labeled GS) and final configuration (labeled PHOTO PROD) of the photoisomerization process that we reported in Figure 3.1. We performed on these two structures electron-dynamics simulations with WaveT and extracted the ground state spectra to compare with the experimental data [169]. The comparison between theoretical and experimental spectra is reported in Figure 3.1: the two structures show an inverted ECD signal. Computed spectra capture the main features of the experimental ones, though failing in reproducing the peak at around 240 nm.

We then moved on to the analysis of the trajectories produced via NAMD. At selected time steps along the dynamics (0, 100, 200, , 1000 fs), we extracted molecular geometries and carried out electronic dynamics calculations on each geometry.

The molecular system initially evolves in the first excited state (S_1) and subsequently relaxes to the ground state (S_0), enabling the isomerization process. Across randomly-chosen 50 trajectories among the ensemble of the 200 ones carried out by NAMD, the average $S_1 \rightarrow S_0$ decay time was found to be 587.0 $\pm$ 103.4 fs for the analyzed trajectories (588.1 $\pm$ 100.1 fs for all trajectories). After obtaining the spectra at each step for every trajectory, we computed the ECD spectra by averaging over the full set of 50 trajectories. We must specify that that with the methods at hand it is not possible to accurately study the absorption and ECD spectra of geometries close to the CI but, nonetheless, we can extract valuable semiquantitative information from our simulations.

Figures 3.2 and 3.3 present the averaged absorption and ECD spectra across the various time steps of the dynamics, obtained using Eq. 3.2.

On their own, these averaged spectra provide only limited insight into the photoisomerization process. However, a few trends are already visible. In the ECD spectra, we can see a negative peak that over the time of the dynamics tends to shift at lower energies and then disappear when the system in average goes from S_1 to S_0. In the absorption spectra, for example, the signal at longer wavelengths (above 500 nm) decreases significantly as the dynamics progress, as it is reported in Figure 3.4, whereas at early times absorption peaks are clearly present in this region. This

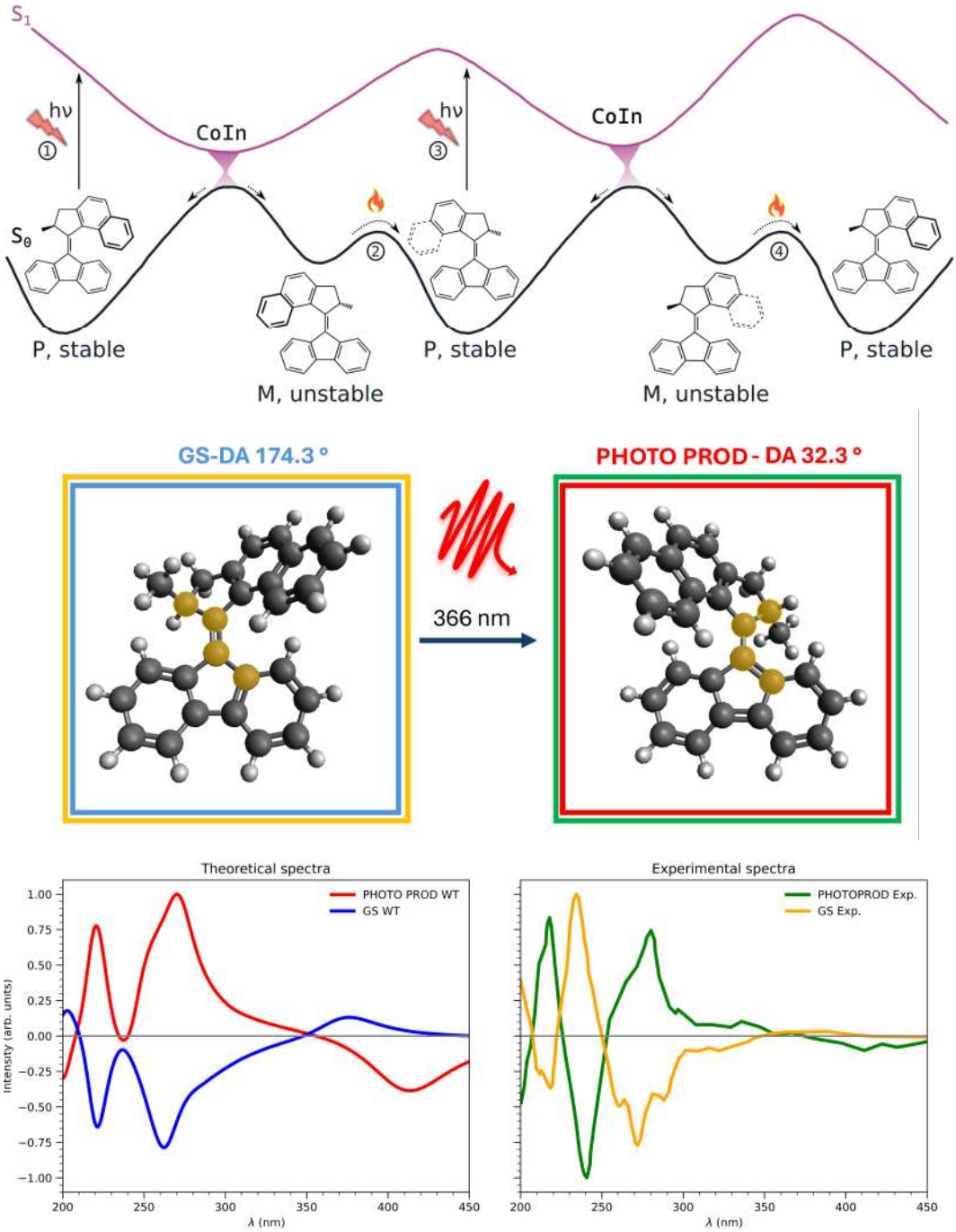

FIGURE 3.1: Top: schematic overview of the four-step cycle underlying the molecular motor mechanism (adapted from Ref. [168]). Middle: molecular structures corresponding to the initial configuration of the cycle (P isomer, stable) and the final configuration of the photoisomerization process (M isomer, unstable) involved in the first step of the cycle. DA = dihedral angle (atoms highlighted). Bottom: left panel shows the computed ECD spectra of the initial configuration (blue box) and the photoproduct (red box). Right panel presents digitized experimental ECD spectra of the same species, adapted from Ref. [169].

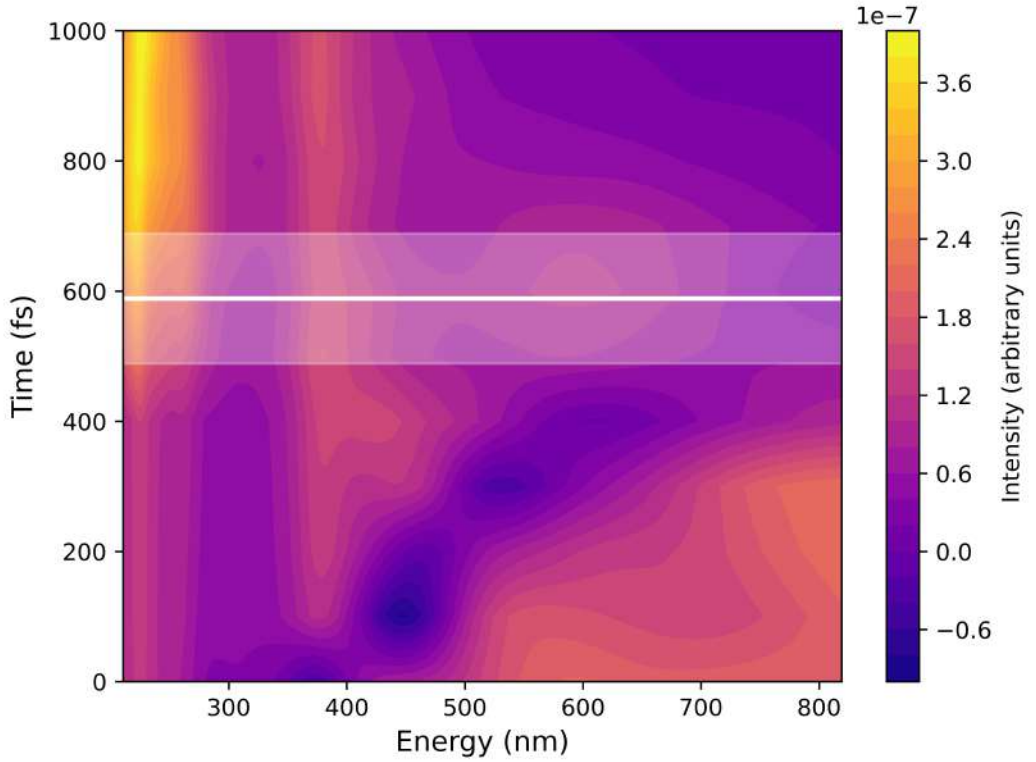

FIGURE 3.2: Average time-resolved absorption spectra. White horizontal line and the light bands are the CI and the corresponding error.

descending trend well agrees with the transient absorption spectra obtained experimentally in Ref. [183].

To better quantify the changes, I performed a simple statistical analysis. The spectra reported below are all obtained using Eq. 3.1 in order to highlight the spectral contributions of the geometries involved in the photoisomerization process without the GS contribution in background. Figure 3.5 illustrates the ECD spectra at 100, 700, and 1000 fs. The panels show both the frequency distribution of spectral features across trajectories (left) and the averaged spectra with associated standard deviations (right). At time 100 fs, the standard deviation is very small, indicating that nearly all trajectories exhibit the same spectral features. In contrast, at 700 fs and 1000 fs, the variance increases markedly, with much broader deviations around the averaged spectrum. This reflects the growing diversity of conformations and configurations of the molecular motor along the dynamics. Once the system relaxes from S_1 to S_0, the resulting structures vary significantly from trajectory to trajectory, and this variability is clearly imprinted in the ECD response.

Interestingly, while the ECD spectra reveal a large trajectory–to–trajectory variability, the absorption spectra show a much smaller degree of fluctuation at large times, as shown in Figure 3.6. As expected, ECD is a more sensitive probe of the conformational diversity emerging during the photoisomerization process.

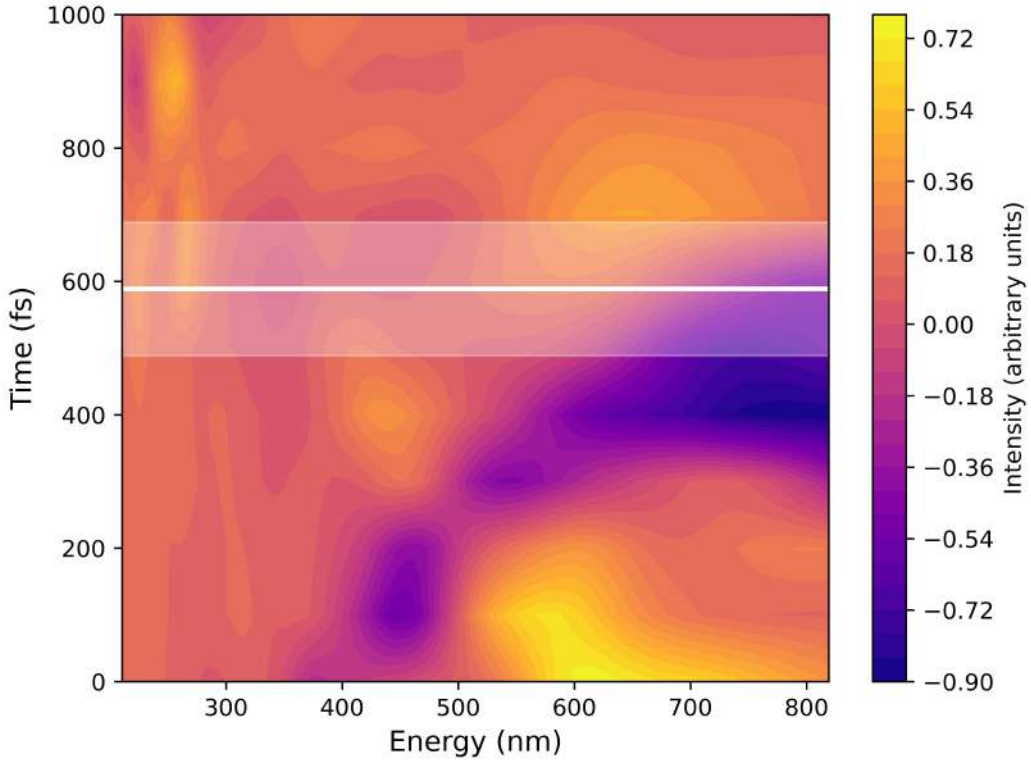

FIGURE 3.3: Average time-resolved ECD spectra. White horizontal line and the light bands are the CI and the corresponding error.

In order to correlate the spectral variations with the molecular dynamics, I analyzed the evolution of the dihedral angle directly involved in the isomerization of the molecular motor, inspired by the work of Ref. [168].

Figure 3.8 shows the trend observed across the first 50 trajectories. The dihedral angle was defined using the atoms most directly participating in the photoisomerization reaction: the two carbon atoms linking the rotor structure to the base and two carbon atoms respectively in the rotor and at the base connected with the two atoms linking the structures (Figure 3.1). The choice of these atoms follows the analysis of Miron et al. [168]. As expected, the angle starts from a high initial value around 180° and progressively decreases along the course of the reaction.

The average trend of the dihedral angle is consistent with the isomerization mechanism: initially high values gradually decrease as the system relaxes. However, the associated standard deviation increases significantly along the dynamics. At early steps the standard deviation is nearly zero, meaning that all trajectories share very similar geometrical features. At later stages, however, the variance becomes large, reflecting strong deviations from the expected isomerization pathway.

To rationalize the photodynamics, the trajectories were divided into two classes: active (A) and non-active (NA). We define a trajectory as NA if, at any time, its dihedral angle deviates by more than $\pm 100°$ from the expected mean value. In contrast,

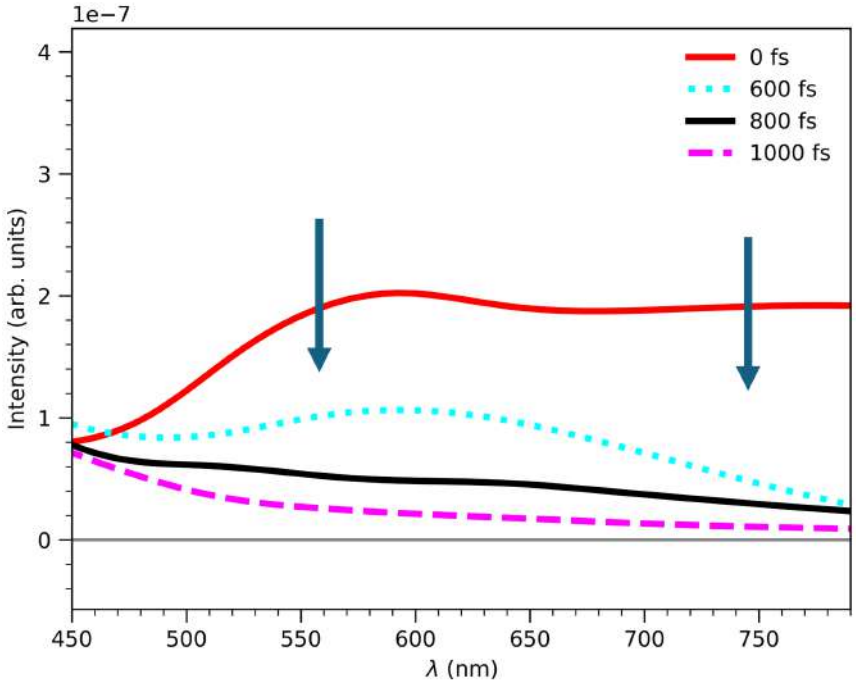

FIGURE 3.4: Reported descending trend for the absorption spectra calculated at four different time along the simulations.

active trajectories remain within this threshold, thus following the anticipated isomerization pathway. This classification is similar to what was previously done in this system by Miron and coworkers [168].

As illustrated in Figure 3.8, A trajectories exhibit a regular evolution of the dihedral angle, consistent with the expected isomerization and the formation of the M isomer. This isomer should be unstable and heating should bring to the formation of the more stable P isomer which present geometrical features similar to the reactant [169]. Conversely, NA trajectories display large deviations, leading to geometries with high dihedral angles. In Ref. [168], a similar distinction was drawn between structures characterized by small ($20 - 70^{\circ}$) and large ($100 - 180^{\circ}$) dihedral angles, corresponding to isomers M and P, respectively. The present A trajectories follow the M-like pathway, yielding geometries consistent with the M isomer.

The geometries obtained at the end of the NA trajectories are instead similar to reactant, showing the failure of the photoisomerization process. Quantitatively, 54.9% of the first 50 trajectories were classified as A. Extending the analysis to all 200 trajectories yields a comparable fraction (57.3%), confirming that the initial subset already provides a representative picture of the system dynamics.

Having established this classification, we then compared the chiroptical response of the two sets. In particular, we analyzed ECD and absorption spectra averaged over A and NA trajectories. This allows us to connect the structural partitioning (A vs. NA) with distinct spectroscopic fingerprints.

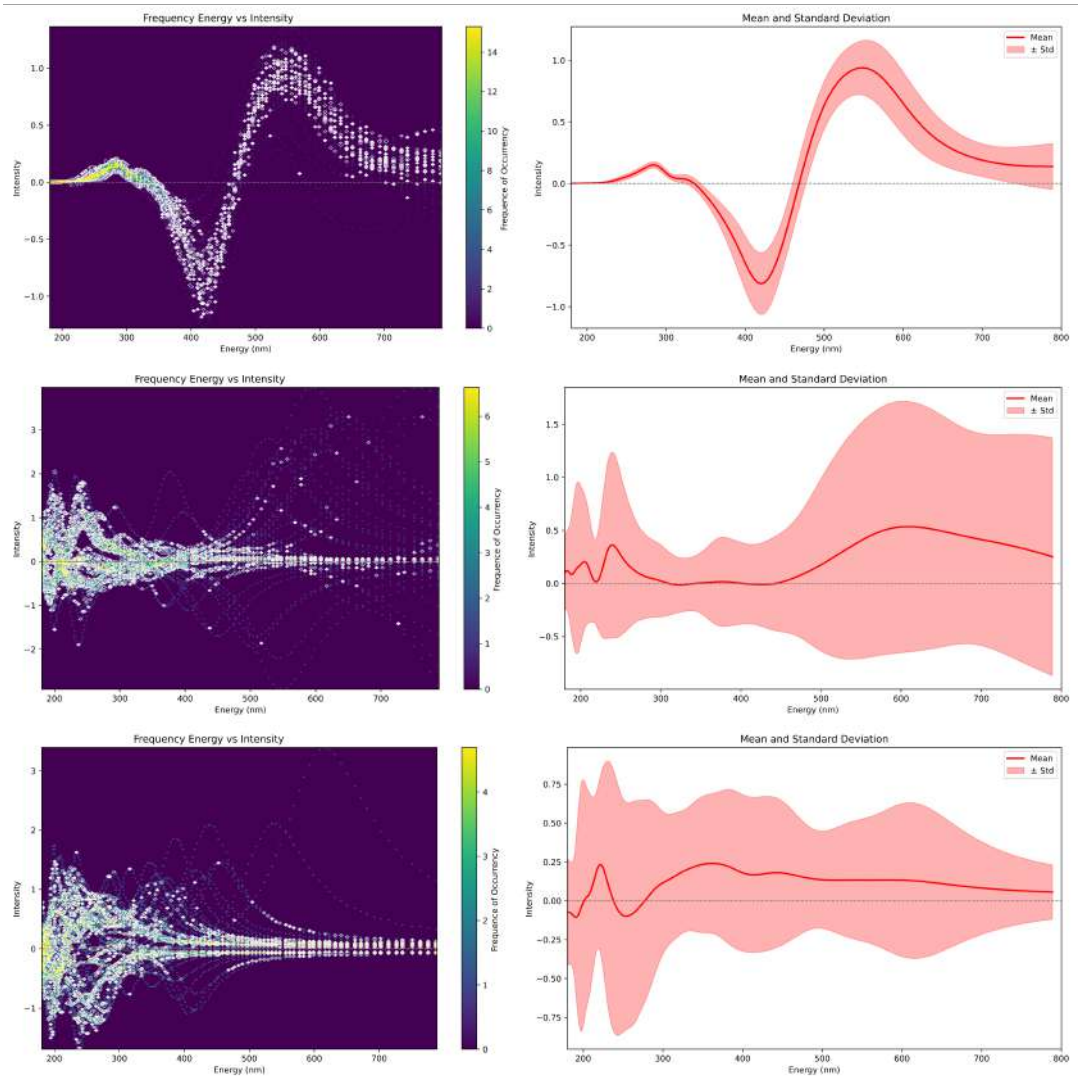

FIGURE 3.5: Left panels: frequency of occurrence for every analyzed trajectory. Right panels: average and standard deviation for the ECD spectra at 100, 700 and 1000 fs.

At early times (100 fs, Figure 3.9, top row), the ECD spectra of the two classes are nearly identical. This is consistent with the fact that the dihedral angle distribution is still narrow at this stage, resulting in geometries that are effectively indistinguishable.

At later times (700-1000 fs, Figure 3.9, middle and bottom rows), the difference becomes evident. A trajectories develop sharp positive ECD peaks in the 200-500 nm region, while NA trajectories lack these features and instead show a strong absorption beyond 500 nm, with a distinct peak around 600 nm. This divergence mirrors the structural separation: as the dihedral angle distribution broadens, the geometries sampled by A and NA trajectories become increasingly different, and so do their spectral signatures.

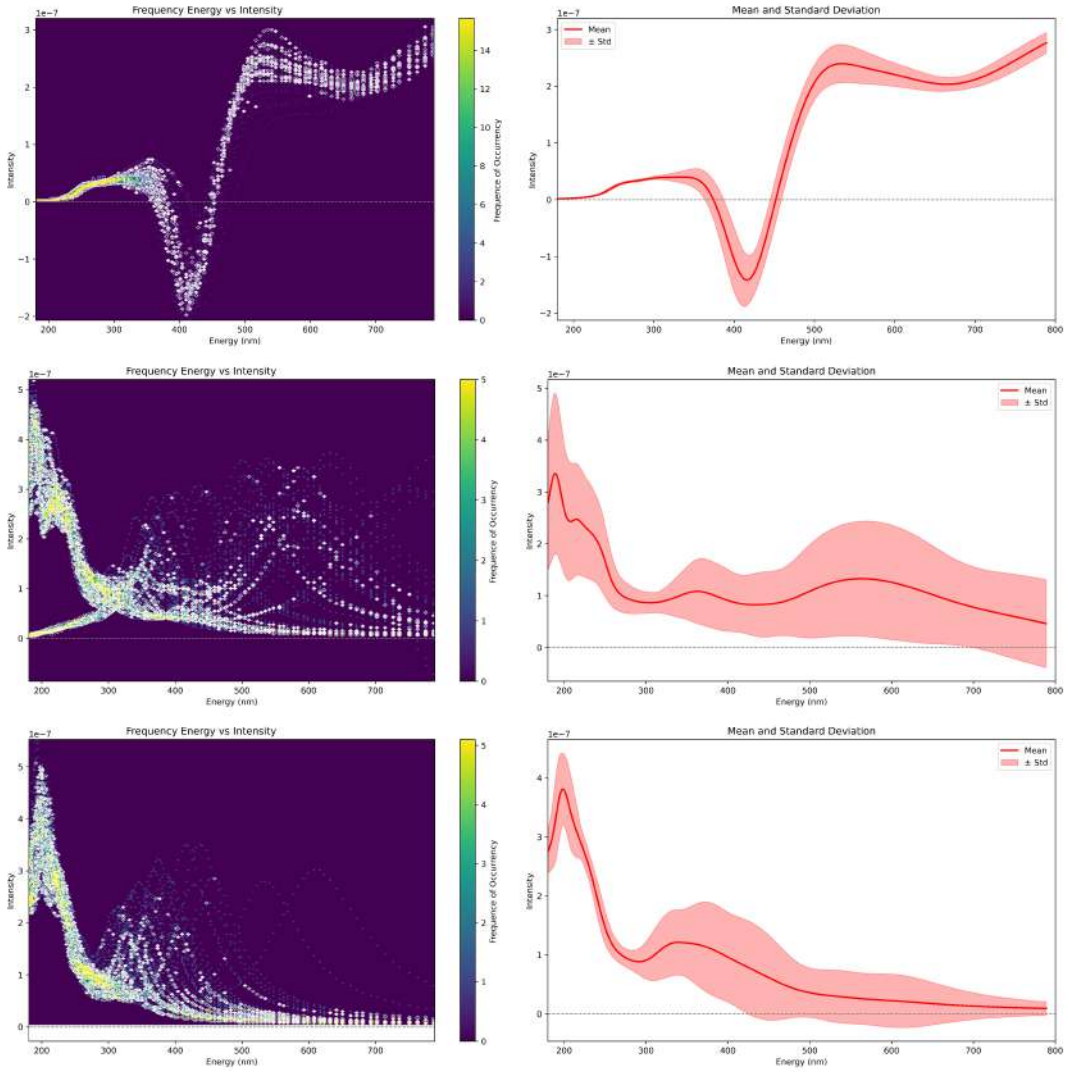

FIGURE 3.6: Left panels: frequency of occurrence for every analyzed trajectory. Right panels: average and standard deviation for the absorption spectra at 100, 700 and 1000 fs.

At 1000 fs the differences are striking. A trajectories display strong ECD absorption between 200 and 500 nm, while NA trajectories instead exhibit two negative peaks and broad bands beyond 500 nm. Interestingly, the ECD features of NA trajectories closely resemble those of the starting configuration, suggesting limited or absent isomerization.

As it is possible to see from Figure 3.10, absorption spectra alone do not capture these distinctions. Small differences are present at 700 and 1000 fs, in contrast to the large variations observed in the ECD spectra. These spectra are more sensitive to the variation of the average electronic state of the system than to the geometrical variations. This data confirm ECD spectroscopy as a more sensitive probe of geometrical diversity and reaction pathways.

Keeping this in mind, it is possible to analyze the evolution of the ECD signal

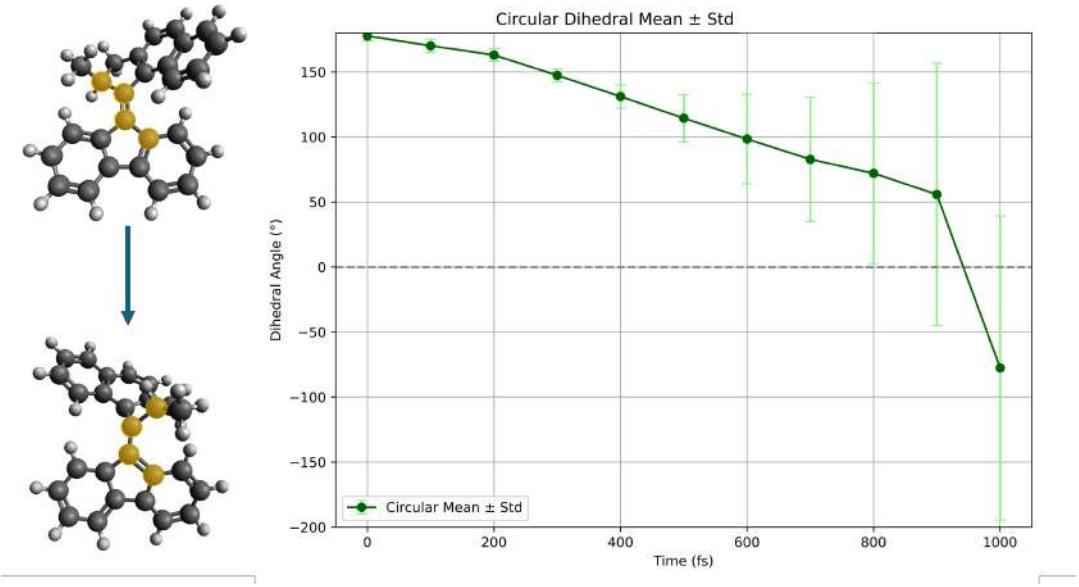

FIGURE 3.7: Dihedral angle as a function of time for the 50 analyzed trajectories.

of A trajectories. In Figure 3.11, I reported the average ECD spectra between 500 and 800 fs of the A trajectories. The evolution of the ECD highlights two diagnostic peaks at 210 and 270 nm that emerge around 600 fs and grow in intensity until 700 fs. Beyond this time, the peaks broaden and evolve into a positive band by 800 fs, reflecting structural variations along the dynamics.

These two diagnostic peaks can be directly associated with the optimized photoproduct spectrum (Figure 3.1), thereby marking the onset of photoproduct formation. Their temporal coincidence with the passage through the conical intersection (around 588 fs, green marker) indicates that immediately following the nonadiabatic transition, the system already adopts the characteristic geometry of photoproduct isomer M. Beyond 700 fs, the ECD response undergoes further evolution: the sharp peaks are replaced by broader features, reflecting subsequent conformational relaxation. The disappearance of the diagnostic signals after 700 fs is attributed to room-temperature dynamics, where the excess energy stored in the photoproduct is dissipated through geometrical fluctuations, resulting in a broadening of the overall positive response. We further underline that only a multiconfigurational method is able to correctly describe the electronic structure of these geometries around the CI, nonetheless with our methodology we can still extract valuable information from these spectra.

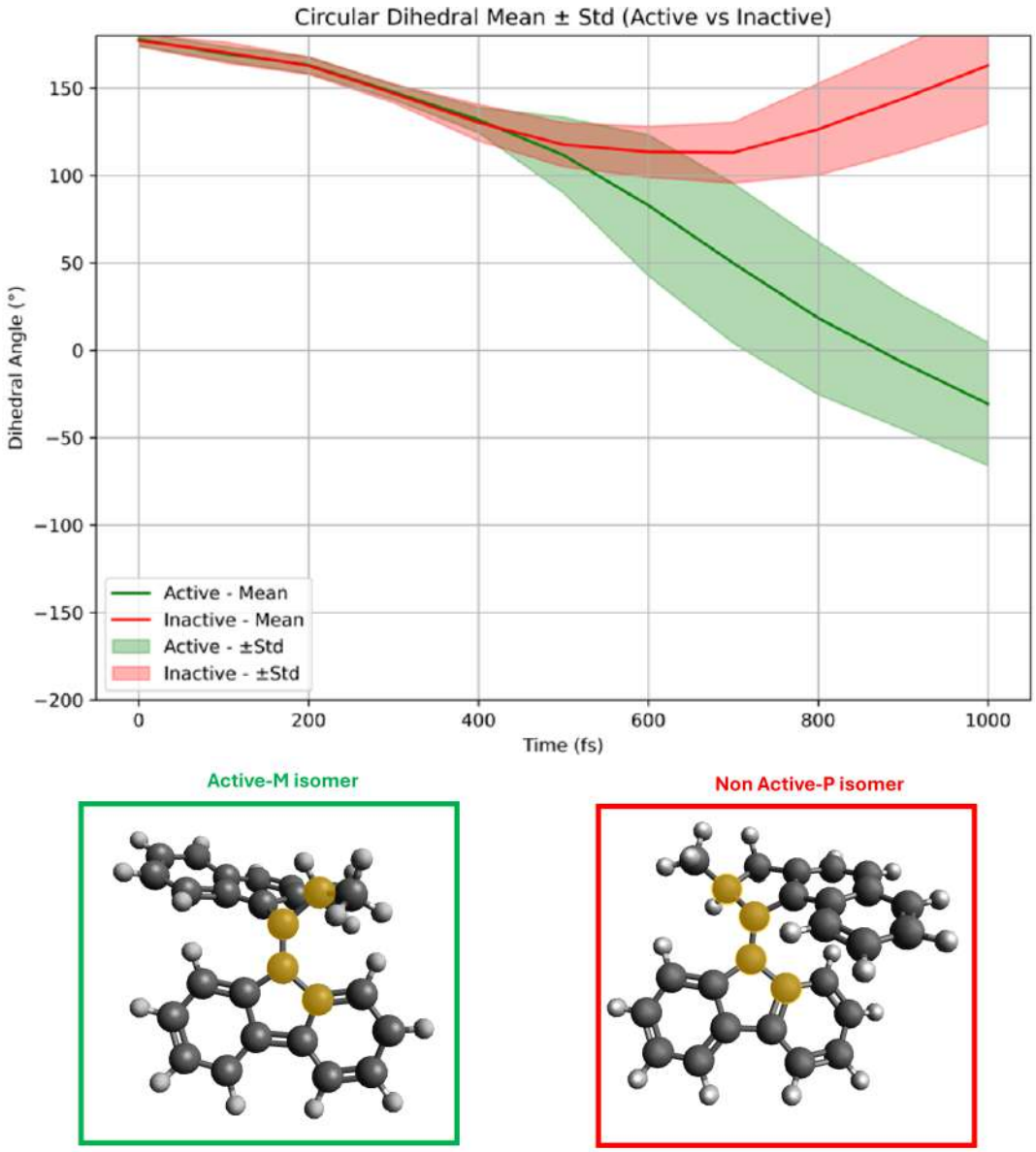

FIGURE 3.8: Dihedral angle analysis from A and NA trajectories. On the bottom, examples of geometries at 1000 fs from an A (left) and a NA (right) trajectory.

3.2.4 Conclusions

In this study, we investigated the evolution of ECD and absorption spectra during the photoisomerization dynamics of a molecular motor (9-(2,4,7-trimethyl-2,3-dihydro-1H-inden-1-ylidene)-9H-fluorene). By combining spectral simulations with a detailed analysis of the key dihedral angle, we were able to directly connect structural rearrangements with spectroscopic signatures. This integrated approach allowed us to follow the dynamics not only in terms of energetic relaxation, but also through the conformational pathways leading to different isomeric outcomes.

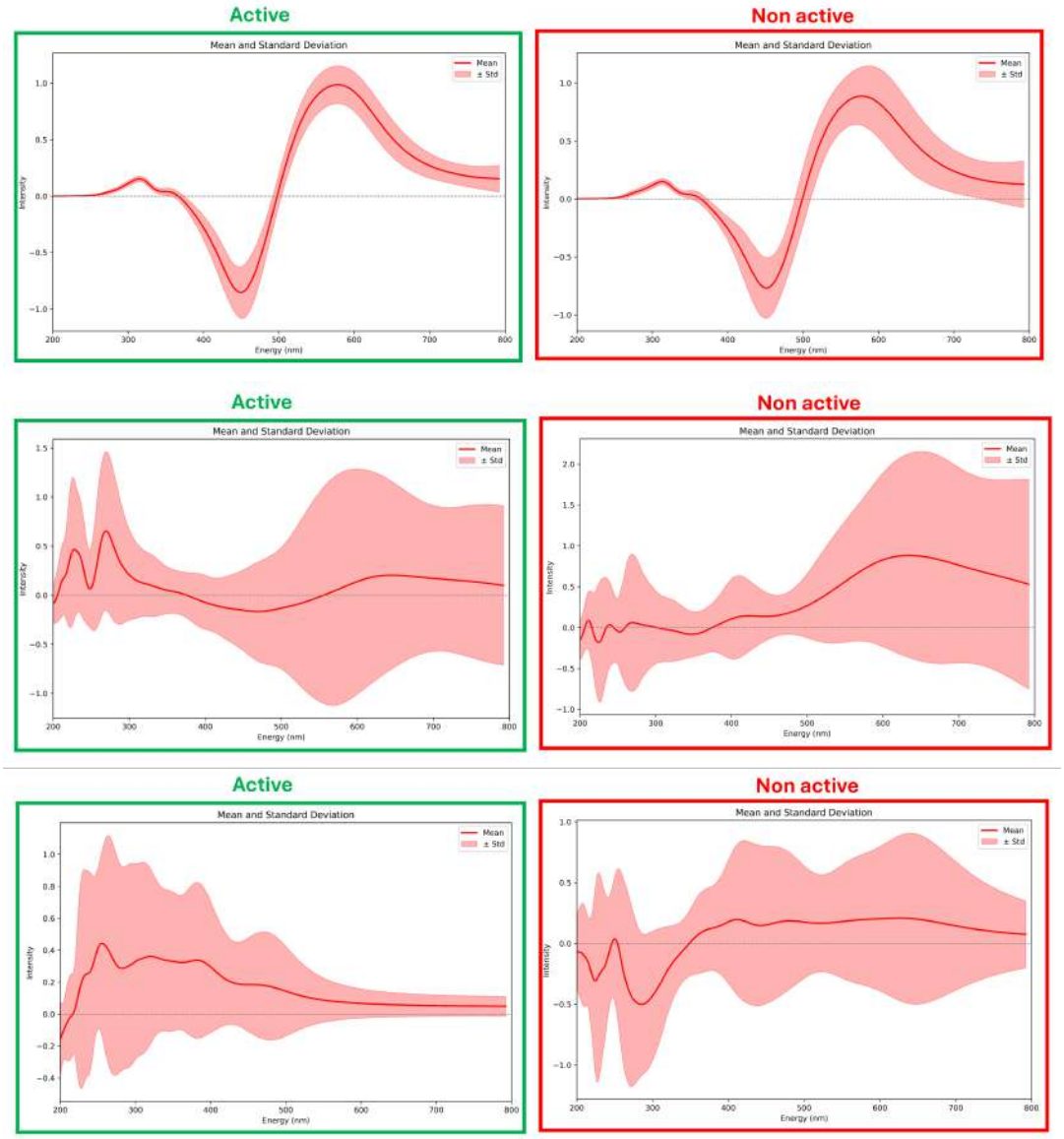

FIGURE 3.9: Average ECD spectra and standard deviation for A (left) and NA (right) trajectories at 100 fs (top row), 700 fs (middle row) and 1000 fs (bottom row).

Our analysis revealed the presence of two main classes of trajectories. A trajectories follow the expected decrease of the dihedral angle and converge toward the M isomer of the photoproduct. By contrast, NA trajectories, characterized by persistently large DA values fail to isomerize entirely, remaining close in structure to the initial configuration. This distinction is reflected most clearly in the ECD spectra. While absorption spectra remain comparatively insensitive to these differences, ECD spectra reveal pronounced divergences between the various pathways, particularly at longer times, thus providing a sensitive probe of the conformational diversity of the system.

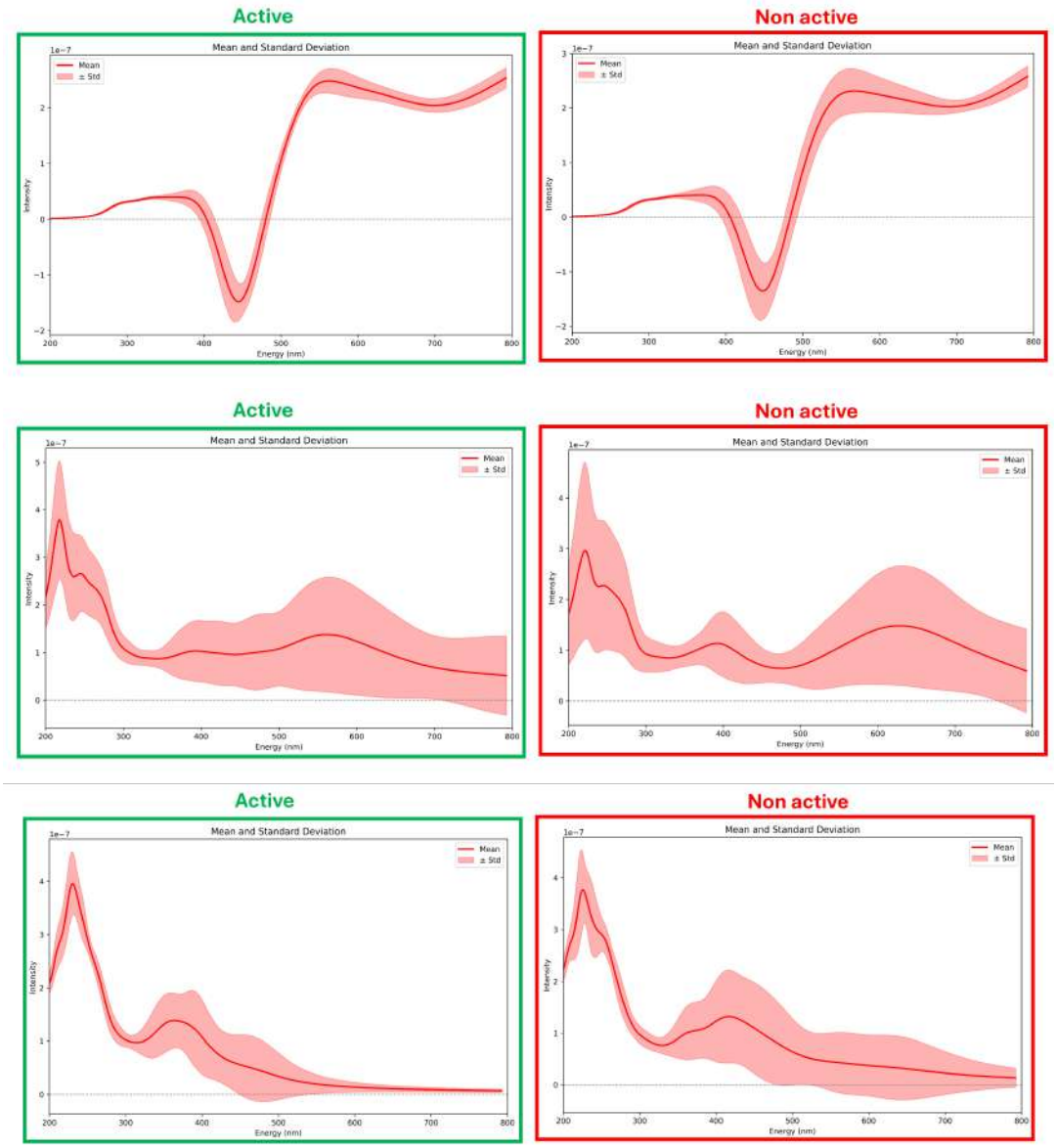

FIGURE 3.10: Average ABS spectra and standard deviation for A (left) and Na (right) trajectories at 100 fs (top row), 700 fs (middle row) and 1000 fs (bottom row).

From a methodological perspective, the workflow we employed proved both robust and scalable. The high consistency between results obtained from an initial subset of 50 trajectories and the full analysis over 200 trajectories confirms the reliability of the approach.

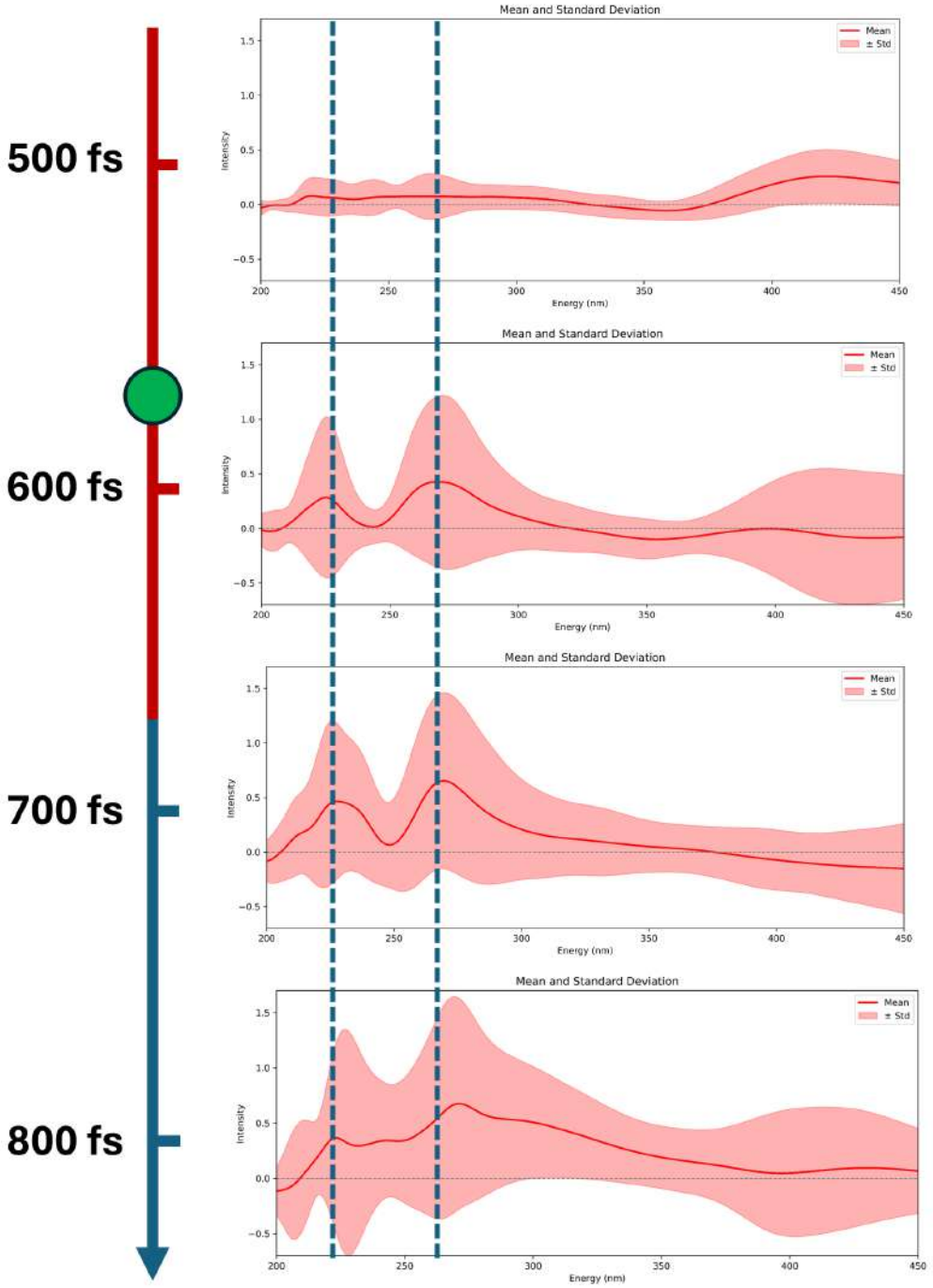

FIGURE 3.11: Evolution of the ECD signal of active trajectories between 500 fs and 800 fs. In red is reported the time window in which, on average, the system descends from S_0 to S_1. In green, $t = 588$ fs, the average descent time. The two vertical dashed lines refer to the position of the two diagnostic peaks of the photoproduct.

3.3 Plasmon effects in molecular ECD

In this work, we showed the results regarding the the development of the methodology I described in Chapter 2 to include the presence of a plasmonic NP in the electron-dynamics calculation of a target molecular system. Our primary goal was to examine whether the presence of a plasmonic NP alters key molecular properties such as the ECD spectrum of chiral molecule close to it. In particular, we focus on how plasmonic effects modify the ECD response of two molecules, peridinin (PID) and methyloxirane (MOX), when placed in proximity to a metallic NP. This approach, as also stated in Chapter 2, goes beyond the conventional dipole-like representation of the chiral target by providing a realistic description of the molecular electronic structure and dynamics under the combined influence of an external pulse and the polarization induced in a nearby NP.

Our simulations reveal that PID exhibits a plasmon-induced enhancement of its ECD signal when the NP is positioned at a distance of 1 nm and the external pulse is polarized perpendicularly to the molecular axis. Notably, the feature around 4.2 eV shows an enhancement factor of about 20 under these conditions, while the peak at 2.9 eV undergoes both a change in sign and an increase in absolute intensity. By contrast, no significant enhancement is observed when the polarization is parallel to the molecular axis, regardless of the NP–molecule distance. These findings identify PID as a plasmon-sensitive molecule, provided that the plasmon resonance (here at 2.5 eV) is close to the molecular excitations and that the system geometry allows a constructive contribution of the induced field.

In comparison, MOX shows no appreciable plasmonic enhancement, even at the shortest separation considered (1 nm). This difference can be rationalized in terms of the energy alignment between plasmonic and molecular excitations, as well as the coupling between the external pulse and the molecular electric and magnetic transition dipole moments. When the plasmon–molecule energy gap is too large, as in the case of MOX, plasmonic effects remain negligible. For PID, however, the close resonance between its lowest excitations and the NP plasmon leads to a remarkable enhancement of the ECD signal, which decreases with increasing NP–molecule distance due to the weakening of the induced field.

In this work I did all the analysis and calculations. The implementation of the features in AMS and the interface code between AMS and WaveT were done by me, assisted by Pierpalo D'Antoni. I contributed to the interpretation of results, the writing of the corresponding sections of the paper and to the final editing of the manuscript.

This work is present in literature as Biancorosso, L., DAntoni, P., Corni, S., Stener, M., & Coccia, E. (2024). "Time-dependent quantum/continuum modeling of plasmon-enhanced electronic circular dichroism." *J. Chem. Phys.* , **161** p. 214104

RESEARCH ARTICLE | DECEMBER 03 2024

Time-dependent quantum/continuum modeling of plasmon-enhanced electronic circular dichroism

L. Biancorosso ; P. D'Antoni ; S. Corni ; M. Stener ; E. Coccia

J. Chem. Phys. 161, 214104 (2024)
https://doi.org/10.1063/5.0235531

The Journal of Chemical Physics ARTICLE pubs.aip.org/aip/jcp

Time-dependent quantum/continuum modeling of plasmon-enhanced electronic circular dichroism

Cite as: J. Chem. Phys. 161, 214104 (2024); doi: 10.1063/5.0235531
Submitted: 28 August 2024 • Accepted: 13 November 2024 •
Published Online: 3 December 2024

L. Biancorosso,[1] P. D'Antoni,[1] S. Corni,[2,3] M. Stener,[1] and E. Coccia[1,a)]

AFFILIATIONS

[1] Dipartimento di Scienze Chimiche e Farmaceutiche, Università di Trieste, Via L. Giorgieri 1, 34127 Trieste, Italy
[2] Dipartimento di Scienze Chimiche, Università di Padova, Via F. Marzolo 1, 35131 Padova, Italy
[3] Istituto Nanoscienze-CNR, Via Campi 213/A, 41125 Modena, Italy

[a)] **Author to whom correspondence should be addressed:** ecoccia@units.it

ABSTRACT

In this work, we present a multiscale real-time approach to study the plasmonic effects of a metal nanoparticle (NP) on the electronic circular-dichroism (ECD) spectrum of a chiral molecule interacting with it. The method is based on the time-evolution of the molecule's time-dependent wavefunction, expanded in the eigenstates of a perturbed Hamiltonian. A quantum description of the molecular system is coupled to a classical representation of the NP via a continuum model. The method is applied to methyloxirane and peridinin at various distances (1, 3, and 5 nm) with respect to a gold NP surface. While no remarkable effect is observed for methyloxirane at any studied distance, an enhancement appears when the peridinin lies at 1 nm and the pulse is linearly polarized perpendicularly to the molecular axis, with the ECD signal centered at 4.1 eV increased by a factor of around 20. These results are rationalized looking at the gap between the plasmonic peak of the NP at around 2.5 eV and the molecular excitations: the smaller the gap between molecular and plasmonic excitations, the larger the plasmonic enhancement of the ECD signal. Moreover, ECD peaks are selectively enhanced due to the favorable coupling between the pulse polarization and the combined effect of electric and magnetic dipole moments. This approach allows one to go through the electronic structure and dynamics of chiral molecules for obtaining a realistic description of plasmon-mediated ECD spectra, e.g., paving the way to applications to molecules of biological relevance interacting with nanostructures of experimental interest.

I. INTRODUCTION

The optical properties of a molecule can be dramatically modified by close metal nanoparticles (NPs) in the presence of an external electromagnetic perturbation.[1–6] Plasmonic effects from NPs are exploited to enhance weak molecular signals, with surface enhanced Raman scattering (SERS), namely being the most known plasmon-assisted spectroscopy:[7–10] the Raman signal is enhanced by several orders of magnitude thanks to the plasmonic response, making SERS an extremely sensitive technique.

In addition, the optical properties of chiral molecules can be enhanced by the coupling with plasmons. Among them, circular dichroism (CD) is central in many chemico-physical applications, being used to assign the absolute configuration of chiral compounds by distinguishing the response of the enantiomers of chiral molecules when interacting with left- and right-circularly polarized light.[11–18]

Plasmonic NPs with chiroptical properties can be classified into the following three classes:[19] (i) plasmonic systems with intrinsic chirality;[20–28] (ii) achiral plasmonic NPs coupled to a chiral molecule;[29–47] and (iii) chiral arrangement of achiral plasmonic NPs.[48–53] In this work, we focus on the second class of systems. The presence of the NP can affect the CD signal by determining two types of specific responses: enhancement of one or more molecular peak(s); promoting the appearance of a peak in correspondence to the plasmonic resonance.

The first feature is strictly related to the induced field generated by the NP, to its nature and shape, to the polarization direction of the

The Journal of Chemical Physics ARTICLE pubs.aip.org/aip/jcp

pulse, and to the energy gap between plasmon resonance and molecular excitations. The origin of this enhancement is the molecular response with respect to a total perturbation due to the external pulse and the induced field generated by the polarized NP.[30,54] Biological chiral molecules can be characterized by an absorption close to plasmon resonance, which is typically around 1–2.5 eV, permitting resonant coupling between the molecular and plasmon modes.

The second mechanism is interpreted as a chirality transfer to the NP, which then acquires a CD signal. In addition, this optical response depends on the geometry and shape of the NP. This second feature prevails when the molecular excitations are far from the plasmonic resonance.[30]

The enhanced sensitivity and response of chiral molecules in the presence of NPs have been thoroughly investigated in many experimental works,[35,55–61] and plenty of theoretical literature was dedicated to a dipole-like description of the chiral molecule,[30–43,45,46,57,62–65] usually within a master equation for the quantum states of the molecule. The magnitude of the enhancement in CD, which can vary from a few units to thousands, depends on several conditions, such as the nature of the chiral molecule, the size, shape, and nature of the NP, and the possible alignment of the molecule.[35,41,47,55–61,63] Giant enhancement of the order of 10^4 is usually due to magnetic and/or quadrupolar contributions.[63]

Modeling the plasmonic-enhanced CD spectrum within the quantum-chemistry framework, beyond a dipole-like representation of the molecule, is a fundamental step to support experimentalists in the prediction and rationalization of the recorded data. It is a challenging task for theory because a large and complex system, generically composed of a NP and a molecule, has to be properly simulated.

Limiting the discussion to the electronic CD (ECD), as an example, a full quantum real-time approach has been proposed in Ref. 66, applied to nanoscale metal–organic clusters.

We propose here to extend the recently published approach by some of the authors[67] based on the propagation of a time-dependent Schrödinger equation (TDSE) in the presence of an explicit electromagnetic field in length gauge[68,69] to account for the possible plasmonic effects of a metal NP on the ECD spectrum of a chiral molecule. The presented multiscale method is characterized by a quantum description of the chiral moiety, whereas the NP is treated according to a polarizable continuum model extended to nanoparticles (PCM-NPs).[6,70,71] Generally, one can compute the ECD spectrum by using the response of the time-dependent induced magnetic dipole to an electric-field perturbation or the response of the time-dependent electric dipole to a magnetic-field perturbation.[18] Here, we use the time-dependent magnetic dipole moment of the chiral molecule, which is computed on the basis of the molecular eigenstates of an effective Hamiltonian, accounting for the presence of the NP. Propagating TDSE in the state space permits to separate the electronic-structure problem from TDSE propagation, at variance with methods based on the direct time evolution of molecular orbitals.[72–74] Since the magnetic response of the NP is not included in the theory by construction, the computed plasmon-assisted spectra reported in this work only present molecular peaks possibly augmented by the plasmon. Details are given in Sec. II.

Molecular plasmonics has also been theoretically explored by parametrized quantum approaches based on density functional tight binding[75–77] for studying the absorption properties of large metal clusters[75,77] and the effect of quantum tunneling in the efficiency of electron energy transfer in a plasmonic chain composed of silver clusters.[76]

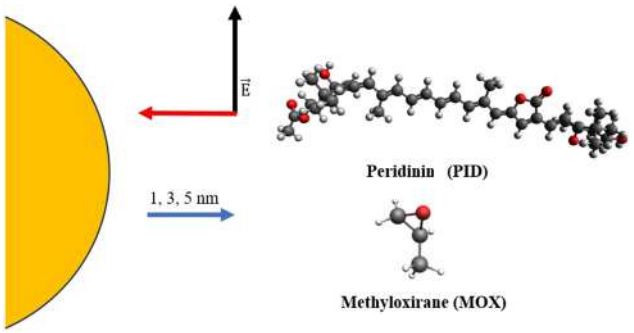

FIG. 1. Sketch representation of the NP + molecule (MOX and PID) system. The distance between the NP surface and the molecule is also reported (see Fig. 2 and main text for details). Code color: carbon black; oxygen red; hydrogen white; gold yellow.

In this article, we compute the ECD spectra of methyloxirane (MOX) and peridinin chromophore (PID) at various distances from an Au spherical NP of a radius of 2.5 nm (Fig. 1) to test the ability of our method to reproduce possible large plasmonic enhancements. We use density functional theory (DFT) and TDDFT for MOX and PID. MOX has been used to study surface-enhanced Raman optical activity,[78,79] while chiral properties of PID molecules have been studied both theoretically and experimentally in the context of the peridinin-chlorophyll-a protein (PCP),[80–83] and the enhancement of the optical properties of PCP in the presence of metal nanoparticles has been reported.[84–86]

The choice of MOX and PID in this work has been performed to answer these questions: can we discriminate by our approach "plasmon-sensitive" and "plasmon-insensitive" chiral molecules? Is this sensitiveness an absolute property of composite systems? Can we rationalize the possible plasmon enhancement of the ECD signal by analyzing the electron structure and dynamics of the spectroscopic target?

The goal is to verify the reliability of our method for understanding the microscopic reason of plasmon-induced changes in the ECD spectrum, such as enhancement and quenching of the signal, by means of a quantum description of the spectroscopic target.

The article is organized as follows: theory is presented in Sec. II; computational details are collected in Sec. III; results are shown and discussed in Sec. IV; conclusions are reported in Sec. V.

II. THEORY

A. Real-time propagation

In this work, we model the real-time magnetic response of the chiral molecule to an external electric field in the presence of a plasmonic NP. Our multiscale approach couples the nanostructure polarization based on the polarizable continuum model (PCM) to a quantum representation of the electronic degrees of freedom of the chiral molecule. We name the method hereafter time-dependent

The Journal of Chemical Physics ARTICLE pubs.aip.org/aip/jcp

PCM-NP (TD-PCM-NP). Theory is formulated in time domain using the TDSE; atomic units are used.

The computational protocol is articulated in three main steps: (i) defining the basis for the time-dependent wavefunction $|\Psi(t)\rangle$; (ii) propagating TDSE in the state space in the presence of the nanostructure, treated at PCM level via the boundary-element method (BEM),[6,87] and of the external pulse; (iii) computing the plasmon-modified ECD spectrum.[67] Within BEM, the NP surface is discretized by a set N_T of (typically) triangular tesserae, on which apparent charges are located.[6] The time evolution of these charges describes the NP polarization induced by the external pulse and by the mutual interaction with the time-dependent electronic density of the quantum target.

TDSE in length gauge for TD-PCM-NP reads as

$$i\frac{d}{dt}|\Psi(t)\rangle = \hat{H}(t)|\Psi(t)\rangle, \tag{1}$$

with $\hat{H}(t)$ being the time-dependent Hamiltonian

$$\hat{H}(t) = \hat{H}_0 - \vec{\hat{\boldsymbol{\mu}}}\cdot\vec{E}_{ext}(t) + \mathbf{q}(t)\cdot\hat{\mathbf{V}}_{\mathrm{BEM}}. \tag{2}$$

where $\vec{\hat{\boldsymbol{\mu}}}$ is the dipole operator of the molecule, $\vec{E}_{ext}(t)$ is the external pulse, $\mathbf{q}(t)$ are the BEM charges,[71,88] and $\hat{\mathbf{V}}_{\mathrm{BEM}}$ is the operator associated with the molecular electrostatic potential calculated at the position of the charges on the NP surface. Both $\mathbf{q}(t)$ and $\hat{\mathbf{V}}_{\mathrm{BEM}}$ are vectors with N_T elements. $\hat{H}_0$ is the field-free electronic Hamiltonian

$$\hat{H}_0 = \hat{H}_{el} + \mathbf{q}_{GS}\cdot\hat{\mathbf{V}}_{\mathrm{BEM}}, \tag{3}$$

where $\hat{H}_{el}$ is the electronic Hamiltonian of the bare molecule, and the charges $\mathbf{q}_{GS}$ are obtained by a self-consistent calculation for the quantum ground-state (GS) in the presence of the polarizable NP.[89]

The time evolution of the charges in Eqs. (1) and (2) is obtained by the time-dependent PCM formulation in the integral equation formalism (IEF-PCM),[71,90] combined with a description of the dielectric function of the medium $\varepsilon(\omega)$ based on fitting the experimental data.[91] In the frequency domain, the charges $\mathbf{q}(\omega)$ are defined as[91]

$$\mathbf{q}(\omega) = \frac{1}{2\pi}f(\omega)\mathbf{F}(\omega), \tag{4}$$

with

$$f(\omega) = \frac{\varepsilon(\omega)-1}{\varepsilon(\omega)+1}, \tag{5}$$

and

$$\mathbf{F}(\omega) = -\left[\mathbf{A}\mathbf{D}^{*}\mathbf{q}(\omega) + \mathbf{S}^{-1}(2\pi\mathbf{I}+\mathbf{D}\mathbf{A})\mathbf{V}(\omega)\right], \tag{6}$$

being $\mathbf{A}$ a diagonal matrix with elements equal to the area of the tesserae, $\mathbf{D}$ and $\mathbf{S}$ matrices containing the Calderon projectors, $\mathbf{I}$ is the identity, and $\mathbf{V}$ the electrostatic potential.[91] The function $f(\omega)$ is fitted by a series of N Drude–Lorentz terms

$$f(\omega) = \frac{\varepsilon(\omega)-1}{\varepsilon(\omega)+1} \simeq \sum_{p=1}^{N}\frac{A_p}{\omega_p^2-\omega^2-i\gamma_p\omega}, \tag{7}$$

where A_p is related to the plasma frequency of the metal, γ_p is the relaxation time, and ω_p is the oscillator frequency.[71] Equation (7) allows one to rewrite the surface charges as a sum of pole-dependent charges

$$\mathbf{q}(\omega) = \sum_{p=1}^{N}\mathbf{q}_p(\omega), \tag{8}$$

and for each $\mathbf{q}_p(\omega)$ in Eq. (8), a time-dependent equation is then defined

$$\ddot{\mathbf{q}}_p(t) = -\omega_p^2\mathbf{q}_p(t) - \gamma_p\dot{\mathbf{q}}_p(t) + \frac{A_p}{2\pi}\mathbf{F}(t), \tag{9}$$

with $\mathbf{F}(t)$ being the Fourier transform of $\mathbf{F}(\omega)$. We refer to the original works (in particular Ref. 91 for this implementation) for further details.

In Eq. (1), $|\Psi(t)\rangle$ is defined as a linear combination of the N_{states} eigenstates of the effective field-free Hamiltonian $\hat{H}_0$, also containing the ground-state polarization of the molecule and the NP,

$$|\Psi(t)\rangle = \sum_{M=0}^{N_{\mathrm{states}}-1} C_M(t)|M\rangle, \tag{10}$$

where $C_M(t)$ are time-dependent coefficients, and $|M\rangle$ is the Mth eigenstate of the system, with eigenvalue E_M. The initial guess for the self-consistent calculation is provided by the eigenstates of H_{el}. In this work, such eigenstates are the Kohn–Sham DFT ground state and the (N_{states}-1) TDDFT eigenstates in the singly excited ansatz,[92,93] i.e.,

$$|M\rangle = \sum_{i}^{occ}\sum_{a}^{vir} d_{i,M}^{a}|\Phi_i^a\rangle, \tag{11}$$

where $|\Phi_i^a\rangle$ is the singly excited Slater determinant, with an electron promoted from the occupied orbital i to the virtual one a, while $d_{i,M}^{a}$ are the amplitudes of the expansion for the state $|M\rangle$.

The $|M\rangle$ states and the polarization charges, after the self-consistent step, are the starting point for the propagation of TDSE, according to Eq. (1). Without the NP, the Hamiltonian reduces to $\hat{H}(t) = \hat{H}_{el} - \vec{\hat{\boldsymbol{\mu}}}\cdot\vec{E}_{ext}(t)$, and the basis for $|\Psi(t)\rangle$ is simply given by the set of eigenstates of $\hat{H}_{el}$. From this point on, we no longer distinguish between eigenstates of the isolated molecule or of the molecule close to the NP, which will simply be referred to as $|M\rangle$ or $|L\rangle$.

Using TDDFT eigenstates within Casida's assignment ansatz[94] in TDSE propagation is an approach widely applied in several fields, such as, e.g., photochemistry,[95,96] high-harmonic generation spectroscopy,[97,98] Raman spectroscopy,[99] and strong-field ionization.[92] It is an alternative approach to real-time TDDFT (RT-TDDFT), which is undoubtedly a valuable tool for studying electronic dynamics in molecules and plasmonic systems.[72,73,100–106] However, the accuracy of photoinduced dynamics computed at the RT-TDDFT level could be affected by the choice of functional and the fact that the adiabatic approximation is typically used; this could lead to well-documented artifacts in the literature,[108–110] resulting in difficulty in correctly assigning the physical nature of the observed features in the dynamics itself, as in the case of a molecule close to an NP. On the other hand, a TDSE-based method is general since

The Journal of Chemical Physics ARTICLE pubs.aip.org/aip/jcp

time propagation can be coupled to different levels of theory for the electronic structure, not limited to TDDFT eigenstates.[89,111,112]

In order to simulate a kick pulse, the external electric field $\vec{E}_{ext}(t)$ is given by a narrow linear Gaussian function

$$\vec{E}_{ext}(t) = \vec{E}_{max} t \exp\left(-\frac{(t-t_0)^2}{2\sigma^2}\right), \tag{12}$$

where t_0 is the center and σ the amplitude of the Gaussian function, respectively, and $\vec{E}_{max}$ is the maximum amplitude of the field. The choice of the pulse prevents numerical artifacts possibly affecting the Fourier transform of the time-dependent signal.

B. Excited-excited matrix elements in TDDFT

TD-PCM-NP, originally developed to study electron dynamics within molecular plasmonics,[110] has been extended here to the calculation of ECD spectra modified by plasmonic effects, using an in-house interface between the AMS package[112] and the WaveT code for propagation.[110] Such an interface has been recently proposed,[67,93] allowing one to simulate ECD spectra of isolated molecules using TDSE and DFT/TDDFT for the description of the molecular target. We emphasize here the novel implementation in the interface regarding the computation of a matrix element between excited states of a one-electronic operator $\hat{A}$ within DFT and TDDFT. Although the results reported in this paper concern a linear response, i.e., the pulse intensity is low enough, the dynamics were carried out using a full approach, that is, considering the entire matrix in the space of states, $\langle L|\hat{A}|M\rangle$. The need for the full DFT/TDDFT matrix comes from the practical solution of TDSE in Eq. (1) in the electronic basis

$$i\frac{\partial \mathbf{C}(t)}{\partial t} = \mathbf{H}(t)\mathbf{C}(t), \tag{13}$$

with the matrix representation at time t of $\hat{H}(t)$ in the basis of the eigenstates reading as

$$\begin{aligned}\mathbf{H}(t)_{LM} &= \langle L|\hat{H}(t)|M\rangle \\ &= E_M\delta_{LM} - \vec{E}_{ext}(t)\langle L|\vec{\hat{\mu}}|M\rangle + \mathbf{q}(t)\langle L|\hat{\mathbf{V}}_{\mathrm{BEM}}|M\rangle.\end{aligned} \tag{14}$$

From the inspection of Eq. (14), one sees that $\langle L|\vec{\hat{\mu}}|M\rangle$ and $\langle L|\hat{\mathbf{V}}_{\mathrm{BEM}}|M\rangle$ are ingredients in TDSE propagation. The full matrix for the magnetic dipole moment is required to compute the ECD spectrum, as specified in Sec. II C.

The molecular electrostatic potential $\hat{\mathbf{V}}_{BEM}$ in the basis of eigenstates $|M\rangle$, i.e., $\langle L|\hat{\mathbf{V}}_{BEM}|M\rangle$, which for each tessera T, is given by

$$\langle L|\hat{V}_{\mathrm{BEM}}(\mathbf{s}_T)|M\rangle = \langle L|\frac{1}{|\mathbf{s}_T - \mathbf{r}|}|M\rangle + V_{nuc}(\mathbf{s}_T)\delta_{LM}, \tag{15}$$

where $V_{nuc}(\mathbf{s}_T)$ is the nuclear contribution at the position $\mathbf{s}_T$ of the Tth tessera, and $\mathbf{r}$ is the electronic coordinate. Dependence of V_{BEM} and V_{nuc} on $\mathbf{s}_T$ is made explicit in Eq. (15). Further details about the nature of the charges $\mathbf{q}(t)$ are given in Ref. 71.

The approach proposed here to compute $\langle L|\hat{A}|M\rangle$, where $\hat{A}$ is an one-electron operator, is based on the frequency-dependent linear density matrix response[113–118]

$$\rho_M^{(1)} = \sum_{ia}\left[X_{i,M}^a\phi_i\phi_a^* + Y_{i,M}^a\phi_i^*\phi_a\right], \tag{16}$$

with $\rho_M^{(1)}$ being an element of the tensor space F, $N_{occ}xN_{vir} \otimes N_{vir}xN_{occ}$, with units tensors $\phi_i\phi_a^*$ and $\phi_i^*\phi_a$, being ϕ_i and ϕ_a occupied and virtual molecular orbitals. N_{occ} (N_{vir}) is the number of occupied (virtual) molecular orbitals. Starting from this formal definition one can arrange the terms $X_{i,M}^a\phi_i\phi_a^*$ and $Y_{i,M}^a\phi_i^*\phi_a$ in two arrays $\boldsymbol{\chi}^M$ and $\boldsymbol{\Upsilon}^M$ such that $\chi_i^{M,a} = X_{i,M}^a\phi_i\phi_a^*$ and $\Upsilon_i^{M,a} = Y_{i,M}^a\phi_i^*\phi_a$. We remark that $X_{i,M}^a$ and $Y_{i,M}^a$ in Eq. (16) are the elements of the usual TDDFT vectors $\mathbf{X}^M$ and $\mathbf{Y}^M$.[113,116] One can then write

$$\langle L|\hat{A}|M\rangle = \begin{pmatrix}\boldsymbol{\chi}^L & \boldsymbol{\Upsilon}^L\end{pmatrix}\begin{pmatrix}\hat{A} & 0\\ 0 & \hat{A}\end{pmatrix}\begin{pmatrix}\boldsymbol{\chi}^M\\ \boldsymbol{\Upsilon}^M\end{pmatrix}, \tag{17}$$

and, explicitly, one obtains

$$\langle L|\hat{A}|M\rangle = \sum_{ij}\sum_{ab}\left[X_{j,L}^{b*}X_{i,M}^a\langle ib|\hat{A}|aj\rangle + Y_{j,L}^{b*}Y_{i,M}^a\langle aj|\hat{A}|ib\rangle\right]. \tag{18}$$

where indices i and j run over occupied orbitals while indices a and b run over virtual ones.

If the operator $\hat{A}$ is symmetric, such as the electric dipole moment $\vec{\hat{\mu}}$ and the electrostatic potential $\hat{V}_{\mathrm{BEM}}(\mathbf{s}_T)$, then

$$\langle L|\hat{A}|M\rangle = \sum_{ij}\sum_{ab}\left[\langle ib|\hat{A}|aj\rangle\left(X_{j,L}^{b*}X_{i,M}^a + Y_{j,L}^{b*}Y_{i,M}^a\right)\right], \tag{19}$$

$$= \mathbf{X}^L\cdot\mathbf{A}\cdot\mathbf{X}^M + \mathbf{Y}^L\cdot\mathbf{A}\cdot\mathbf{Y}^M, \tag{20}$$

where the matrix $(\mathbf{A})_{ia,\,jb} = \langle ib|\hat{A}|aj\rangle$ has been defined. If the operator $\hat{A}$ is antisymmetric, such as the magnetic dipole moment $\vec{\hat{m}}$,[116,117] then

$$\langle L|\hat{A}|M\rangle = \sum_{ij}\sum_{ab}\left[\langle ib|\hat{A}|aj\rangle\left(X_{j,L}^{b*}X_{i,M}^a - Y_{j,L}^{b*}Y_{i,M}^a\right)\right], \tag{21}$$

$$= \mathbf{X}^L\cdot\mathbf{A}\cdot\mathbf{X}^M - \mathbf{Y}^L\cdot\mathbf{A}\cdot\mathbf{Y}^M. \tag{22}$$

According to Slater–Condor rules, the term $\langle ib|\hat{A}|aj\rangle$ simplifies to $\langle a|\hat{A}|b\rangle\delta_{ij} - \langle i|\hat{A}|j\rangle\delta_{ab}$, thus recovering the usual expressions in the molecular basis.[93]

In terms of excitation ($\mathbf{X}^{I(M)} + \mathbf{Y}^{I(M)}$) and deexcitation ($\mathbf{X}^{I(M)} - \mathbf{Y}^{I(M)}$), expressions in Eqs. (20) and (22) become, once the specific operators are made explicit

$$\begin{aligned}\langle L|\hat{V}_{\mathrm{BEM}}(\mathbf{s}_T)|M\rangle = \frac{1}{2}\big[&(\mathbf{X}^L + \mathbf{Y}^L)\cdot\mathbf{P}_{\mathrm{BEM}}(\mathbf{s}_T)\cdot(\mathbf{X}^M + \mathbf{Y}^M)\\ &+ (\mathbf{X}^L - \mathbf{Y}^L)\cdot\mathbf{P}_{\mathrm{BEM}}(\mathbf{s}_T)\cdot(\mathbf{X}^M - \mathbf{Y}^M)\big],\end{aligned} \tag{23}$$

$$\begin{aligned}\langle L|\hat{\mu}_\alpha|M\rangle = \frac{1}{2}\big[&(\mathbf{X}^L + \mathbf{Y}^L)\cdot\mathbf{D}_\alpha\cdot(\mathbf{X}^M + \mathbf{Y}^M) + (\mathbf{X}^L - \mathbf{Y}^L)\\ &\times\mathbf{D}_\alpha\cdot(\mathbf{X}^M - \mathbf{Y}^M)\big],\end{aligned} \tag{24}$$

The Journal of Chemical Physics ARTICLE pubs.aip.org/aip/jcp

and

$$\langle L|\hat{m}_\alpha|M\rangle = \frac{1}{2}\left[(\mathbf{X}^L + \mathbf{Y}^L)\cdot\mathbf{M}_\alpha\cdot(\mathbf{X}^M - \mathbf{Y}^M) + (\mathbf{X}^L - \mathbf{Y}^L) \times \mathbf{M}_\alpha\cdot(\mathbf{X}^M + \mathbf{Y}^M)\right], \quad (25)$$

where $\alpha = x, y$, or z indicates the Cartesian component of the dipole, and being $\mathbf{D}_\alpha$, $\mathbf{M}_\alpha$, and $\mathbf{P}_{\mathrm{BEM}}(\mathbf{s}_T)$ the matrix representations of the corresponding operators. $\mathbf{P}_{\mathrm{BEM}}(\mathbf{s}_T)$ in Eq. (23) refers to the matrix representation of $\hat{V}_{\mathrm{BEM}}(\mathbf{s}_T)$ (one single tessera at position $\mathbf{s}_T$) in the molecular space, while $\hat{\mathbf{V}}_{\mathrm{BEM}}$ in Sec. II A is the vector representation of the potential operator with respect to the number of tesserae.

C. Computing the ECD spectrum

The induced magnetic dipole $\Delta\vec{m}(t)$ is defined as the difference between the time-dependent magnetic moment $\vec{m}(t)$ at time t and that at initial time $(t = 0)$, $\vec{m}(0)$, with $\vec{m}(t)$ provided by

$$\vec{m}(t) = \sum_{L,M} C_L^*(t)C_M(t)\langle L|\vec{\hat{m}}|M\rangle, \quad (26)$$

with $\langle L|\vec{\hat{m}}|M\rangle$ given by Eq. (25). The ECD spectrum is computed as the imaginary part of the following:[67,119]

$$P_{nl}^{ECD}(\omega) = -\frac{i}{2\pi\omega\vec{E}_{ext,n}(\omega)}\int_0^{+\infty} -\Delta\vec{m}_l(t)e^{i(\omega+i\Gamma)t}dt. \quad (27)$$

In Eq. (27), $\vec{E}_{ext,n}(\omega)$ is the Fourier transform of the nth component of the electric field of the external pulse, $\Delta\vec{m}_l(t)$ is the lth component of the induced magnetic dipole, and Γ is a damping parameter.[119,120]

III. COMPUTATIONAL DETAILS

Ground-state geometry of MOX and PID have been taken from Refs. 67 and 121, respectively. The time-domain ECD calculations have been performed with the WaveT package,[111] whose interface with AMS has been recently proposed for the electric and magnetic transition dipole moments.[67,93] Excitation energies and transition dipole moments are provided by the TDDFT calculation using the B3LYP functional and TZP basis set for MOX and CAM-B3LYP and TZP basis set for PID, and then employed as input parameters for the real-time propagation. For both MOX and PID, 150-fs dynamics have been carried out with a time step δt of 0.7 as. 20 (MOX) and 10 (PID) electronic excited states have been considered for the wavefunction expansion of Eq. (10). The equilibration procedure related to the effective Hamiltonian $\hat{H}_{NP}$ is implemented in WaveT.[89]

The external field is characterized by a maximum intensity equal to 10^4 W/cm^2 and a full width half maximum of 94 as for the Gaussian envelope [see Eq. (12)]. The value of the damping parameter Γ in Eq. (27) is 400 au for all the cases. The ECD spectrum in Eq. (27) has been computed with a post-processing tool implemented in WaveT, using the TDSE dynamics as input.

NP has a radius of 2.5 nm; 2704 tesserae have been used to discretize the NP surface. In our computed spectra, n and l components of Eq. (27) coincide.

IV. RESULTS AND DISCUSSION

In the present work, we have studied plasmonic effects of the NP on the ECD spectra of MOX and PID at various distances and pulse polarizations through the time-dependent multiscale method reported in Sec. II. The shortest distance selected for our simulations is 1 nm because we want to simulate a purely plasmon-driven physical effect by excluding any interaction of chemical type. Distances of 1 nm could be experimentally prepared by using, e.g., a molecular spacer.

We have rationalized the MOX and PID responses in terms of coupling between plasmon and molecular excitations, electric selection of excited states during the dynamics, interplay between electric and magnetic dipole moments, coupling with the pulse polarization, and the role of the induced field. Of course, all these ingredients are closely connected to each other; our theory and simulations have allowed us to dissect the role of each of them and, therefore, it represents an original approach to chiral plasmonics.

Since our methodology is not able, by construction, to determine plasmon peaks in the CD spectrum, our attention is exclusively focused on the possible enhancement of molecular peaks. In order

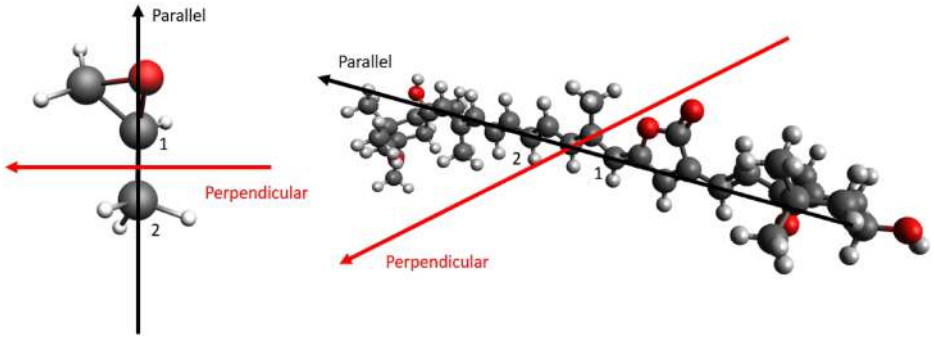

FIG. 2. Pulse polarization directions used in this work. MOX: "Parallel" is along the carbon–carbon bond; "perpendicular" is orthogonal to it. PID: "parallel" is parallel to the carbon chain; "perpendicular" is perpendicular to it. In both cases, "parallel" and "perpendicular" refer to the relative orientation with respect to the NP surface. Carbon atoms labeled as 1 and 2 define the two reference atoms, whose middle point is used for defining the distance with respect to the NP (see text). Components of the pulse polarization unit vector are: MOX "parallel" (−0.918, 0.092, −0.386); MOX "perpendicular" (0.100, 0.995, 0.000); PID "parallel" (−0.979, −0.183, −0.094); PID "perpendicular" (−0.146, 0.930, −0.289).

The Journal of Chemical Physics ARTICLE pubs.aip.org/aip/jcp

to verify the reliability of the approach, we have selected two chiral molecules with different electronic and optical properties: MOX and PID (Fig. 1). In this context, we define the enhancement (quenching) at a given energy in the spectrum corresponding to an ECD peak when the ratio between the ECD signal with and without the NP is larger (smaller) than 1. For both molecules, the distance between the NP and the molecule is defined as the distance between the NP surface and the middle point of the vector connecting the reference carbon atoms (labeled 1 and 2), as shown in Fig. 2. We consider the pulse polarization to be tangential to the NP surface when it is parallel to the vector connecting these two atoms (labeled "Parallel"), while it is perpendicular to the NP surface when orthogonal to this vector (labeled "Perpendicular").

First, we have studied the NP effect on the ground state of MOX and PID before irradiating the system. The variation ΔE of the ground-state energy (formally a free-energy, but for metal nanoparticle polarization the entropic contribution is negligible) as a function of the NP distance is reported in Fig. 1 of the supplementary material. ΔE is defined as the difference between the ground-state energy of the bare molecule (Vac) and the ground-state energy of the molecule in the presence of the NP,

$$\Delta \mathrm{E} = E_{GS}^{Vac} - E_{GS}^{NP}. \tag{28}$$

ΔE accounts for both electronic and nuclear contributions to the electrostatic term in the ground-state energy. At 3 and 5 nm, the effect of the presence of the NP on the stabilization of the GS energy is minimal, while at 1 nm for both MOX and PID, a stabilization by 50 mKcal/mol is observed.

In Fig. 2 of the supplementary material, the differential projected density of states $\Delta\mathrm{PDOS}(t=0,\varepsilon)$[93] for the ground state of PID at 1 nm from the NP surface, i.e., at time $t = 0$, is reported

$$\Delta\mathrm{PDOS}(t=0,\varepsilon) = \mathrm{PDOS}^{NP}(t=0,\varepsilon) - \mathrm{PDOS}^{Vac}(t=0,\varepsilon). \tag{29}$$

The $\Delta\mathrm{PDOS}(t=0,\varepsilon)$ describes how the population of the molecular orbitals in the electronic ground state varies when the molecule interacts with the NP. In the PID case, HOMO-1 is largely depopulated in favor of LUMO and LUMO+1 at 1 nm, as shown in Fig. 2 of the supplementary material. This effect is completely negligible when PID is between 3 and 5 nm from the NP surface.

We then moved to rationalize the changes in the ECD spectrum due to the presence of the NP by looking first at the linear absorption spectra of the NP, MOX, and PID, reported in Fig. 3. Absorption spectra of MOX and PID have been computed by directly Fourier transforming the time-dependent induced electric dipole with no damping factor. The NP spectrum [panel (a) of Fig. 3] is computed as the imaginary part of the polarizability.[88] The plasmonic peak is clearly evident at around 2.5 eV. Using the same frequency scale, absorption spectra of bare MOX [panel (b) of Fig. 3] and bare PID [panel (c) of Fig. 3] for the two pulse polarization directions are also reported.

Excitation energies of MOX and PID after equilibration with the NP (see Sec. II) are not strongly modified with respect to the bare-molecule values, as seen in Tables 1–4 (MOX) and 9–12 (PID) of the supplementary material.

Values of Cartesian components of the electric and magnetic transition dipole moments for isolated MOX and PID and close to the NP are reported in Tables 1–16 of the supplementary material, together with their projection along the parallel and perpendicular direction (see Fig. 3). For the sake of simplicity, only the first ten transitions from the ground state are shown, even though simulations have been carried out including the full transition dipole matrices.

Electric and magnetic transition dipole moments of MOX and PID do not vary appreciably from the values of the isolated molecule when the NP is added at any distance (Tables 1–8 in the supplementary material). In Figs. 3 and 4 of the supplementary material, the absorption spectra of MOX and PID are reported in the presence of the NP. While MOX optical response is unaffected by the interaction with NP (as suggested by the behavior of the transition dipole moments in Tables 1–8 of the supplementary material), PID spectra show some appreciable differences, especially when the target molecule is placed at 1 nm from the NP. With a parallel pulse polarization, the very intense peak at 2.9 eV is partially quenched, while the other peaks do not significantly change with the variation of the distance. With a perpendicular pulse polarization, instead we observe an enhancement of the peak at 4.1 eV. These findings are due to the interaction between PID and NP during the dynamics. The latter result, indeed, is a peak enhancement of plasmonic nature: the corresponding transition dipoles alone are not sufficiently large to explain this intensity, which is instead easily understood if we consider the increase in the population of excited states due to the field induced by the NP, which adds up positively to the external one.[54,71] Indeed, the time-dependent population $|C_M(t)|^2$ of the excited states $(M > 0)$ is in the order of 10^{-8} for PID with a parallel pulse at all distances. For PID with perpendicular polarization at 1 nm, the population of the first three low-lying excitations is in the order 10^{-10}–10^{-11}, whereas the values of the populations without NP are in the range of 10^{-12}–10^{-13}. This result is clear evidence of the plasmonic effect on the electron dynamics, which in turn affects the PID optical response. However, plasmonic effects on a linear absorption spectrum are also not automatically observed in the ECD spectrum at the same frequencies, since in the latter case the magnetic transition dipole moment comes into play. The absolute value of the population depends on the applied pulse intensity.

With these caveats in mind, peak positions in panels (b) and (c) of Fig. 3 can be used to be compared with the 2.5 eV plasmon. Considering both parallel and perpendicular pulse polarizations, MOX excited states are more than 4 eV higher than the plasmon energy, while the lowest PID excited states are much closer to the plasmon resonance.

This preliminary analysis of the absorption spectra of MOX and PID is crucial to understand the ECD spectra collected here. Indeed, according to the theory reported in Ref. 30, enhancement is only expected when molecule and plasmon are in resonance or the gap is small enough. Moreover, the coupling between pulse polarization and molecular excitation and the geometric configuration of the composite system directly affect the intensity of the optical response of the chiral molecule.

Comparison of ECD spectra of bare MOX is reported in Fig. 4: spectra obtained with parallel and perpendicular pulse polarizations show different features, but the intensity of peaks is characterized by the same order of magnitude. The effect of the NP is encoded in the spectra collected in Fig. 5. The general result is that the enhancement related to the induced field of the plasmonic excitation is not observed due to the gap between the electronic excitations of MOX

The Journal of Chemical Physics ARTICLE pubs.aip.org/aip/jcp

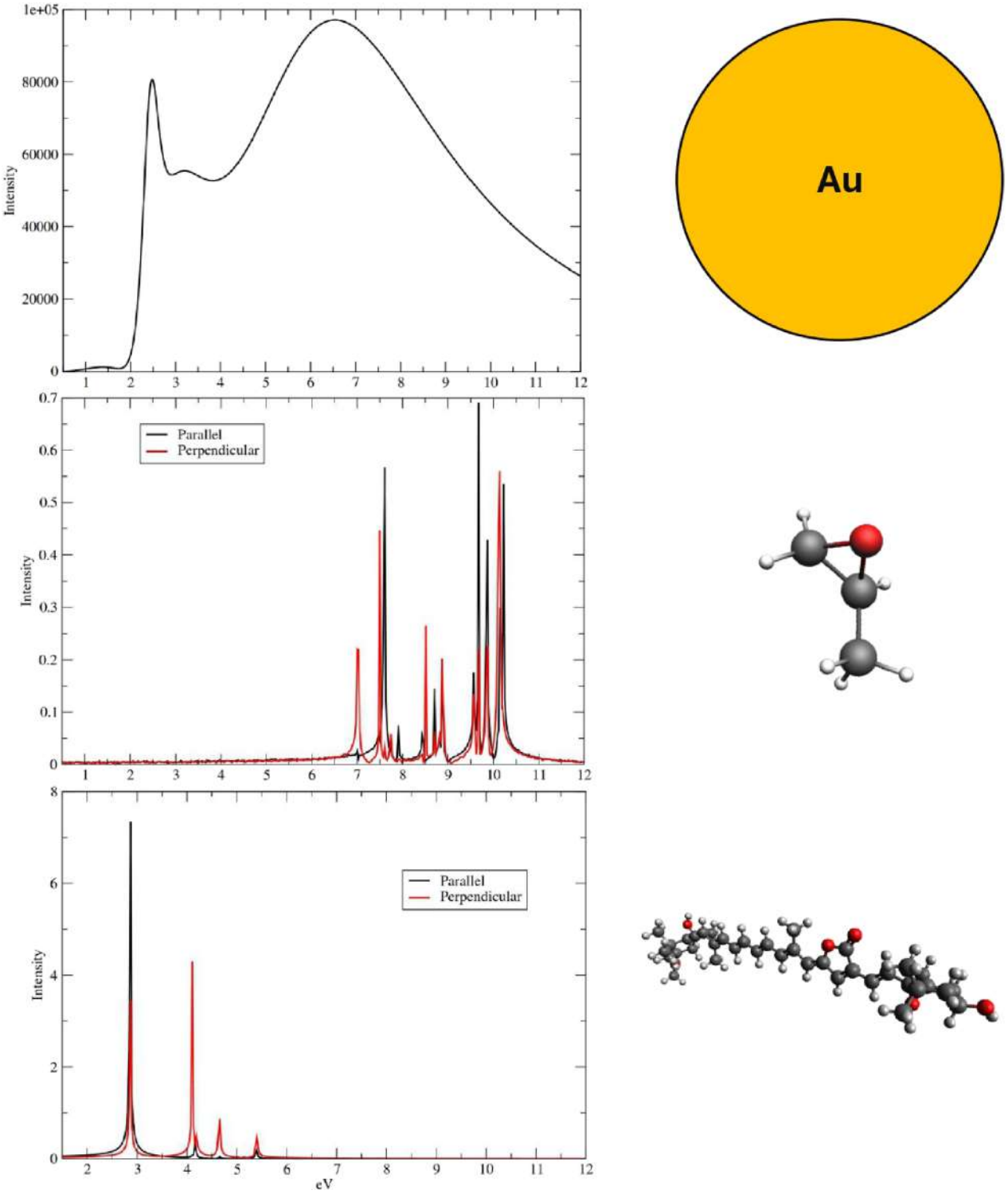

FIG. 3. (a) Absorption spectrum of the Au spherical NP of a radius of 2.5 nm, (b) absorption spectra of isolated MOX, and (c) PID. MOX and PID spectra are normalized to unity.

The Journal of Chemical Physics ARTICLE pubs.aip.org/aip/jcp

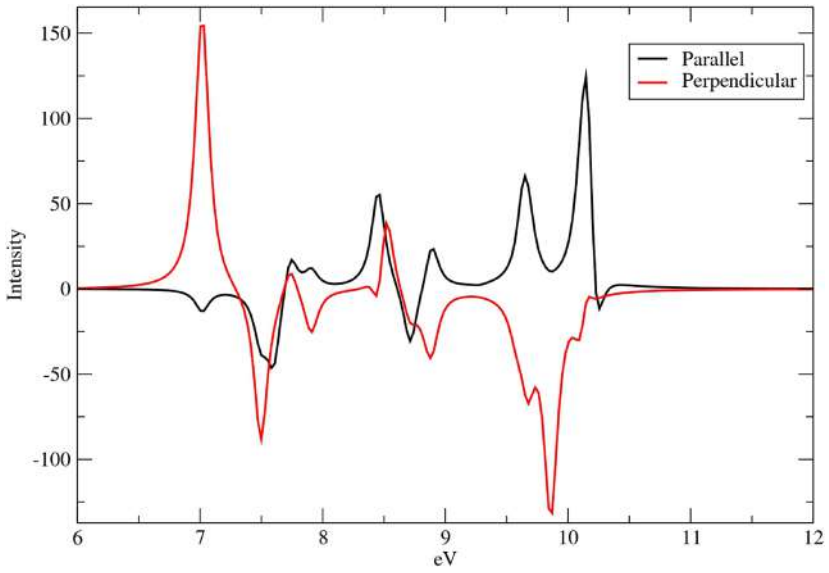

FIG. 4. ECD spectra of bare MOX with parallel and perpendicular pulse polarization with respect to the NP surface.

and the plasmon of the NP, making MOX insensitive to the gold NP of this size at the selected distances. Indeed, the difference between the plasmonic peak and the lowest MOX excitation is more than 4 eV, as already pointed out.

It is worth mentioning that the modulation of the bare-molecule ECD spectra is due to the combined effect of electric and magnetic dipole moments: the excited states playing a role are selected by the electric interaction in Eq. (2), thus affecting the time-dependent coefficients $C_M(t)$; such coefficients are responsible for the amplitude of the time-dependent magnetic moments, together with the magnetic transition dipole moments [see Eq. (26)]. In the presence of the NP, also the (possible) induced field has to be considered.

In detail, ECD spectra at 1, 3, and 5 nm are practically superimposed to the bare-molecule one for the parallel polarization, while tiny differences are found only at 1 nm for the perpendicular polarization, consistent with the change of the magnetic transition dipole moments. The spectra of the isolated molecule calculated compare pretty well with the reference ones in the literature, as it was also reported in Ref. 67.

In conclusion, no plasmonic enhancement is observed in the ECD spectra of MOX when distances of 1, 3, and 5 nm from the NP surface are considered.

The same computational protocol has been applied to PID. Parallel and perpendicular ECD spectra of the bare molecule of Fig. 6 are clearly distinguishable, but with different intensities. The

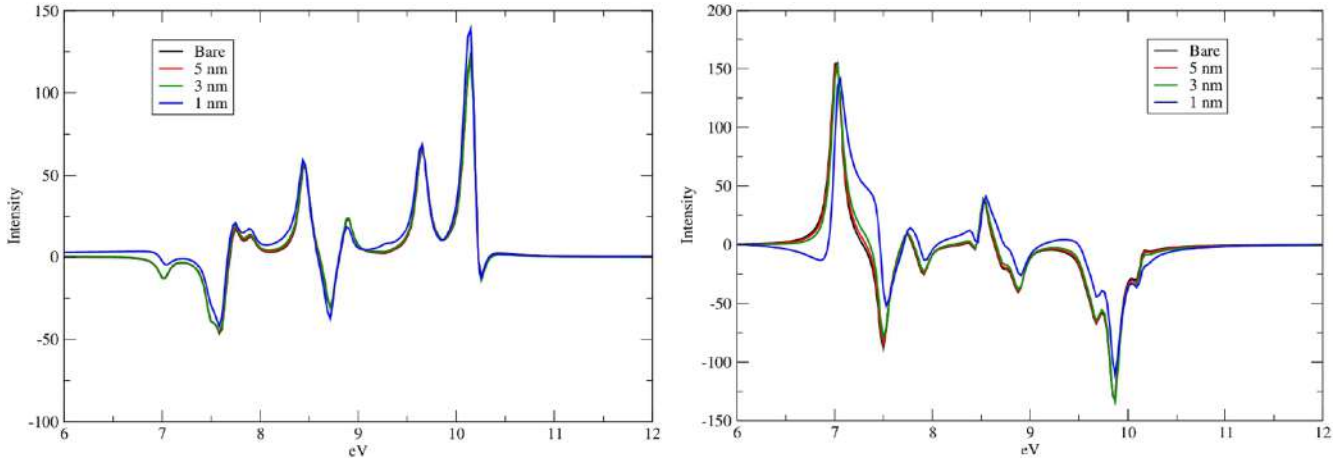

FIG. 5. ECD spectra of MOX at a distance *d* of 1, 3, and 5 nm from the NP surface for both pulse polarization directions, parallel (left panel) and perpendicular (right panel). Bare-molecule spectra are also reported for comparison.

The Journal of Chemical Physics ARTICLE pubs.aip.org/aip/jcp

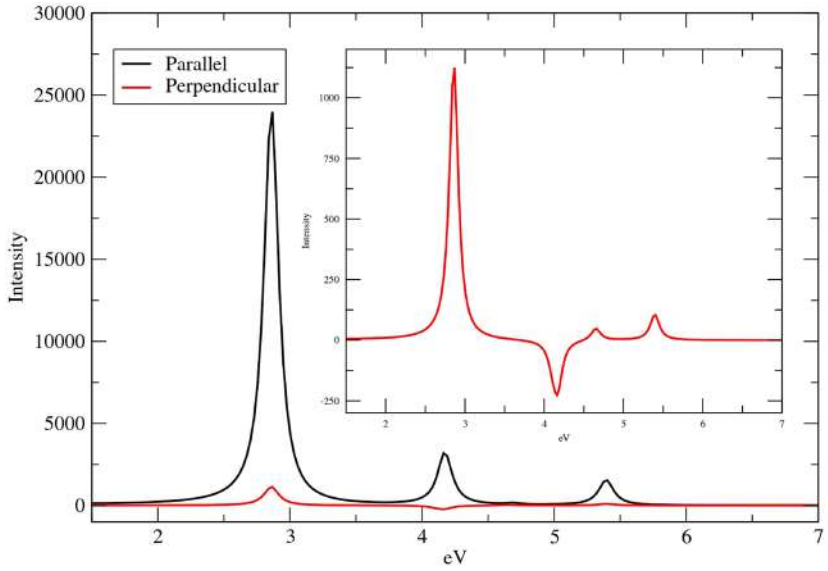

FIG. 6. ECD spectra of the bare PID with parallel and perpendicular pulse polarization with respect to the NP surface.

parallel spectrum shows an intense positive peak at around 2.9 eV and two other positive peaks centered at 4.2 and 5.4 eV. The perpendicular spectrum is much less intense, and it is mainly characterized by a positive peak at around 2.9 eV and a negative peak at 4.2 eV, whereas two other small and positive peaks appear at 4.6 and 5.4 eV.

Parallel and perpendicular ECD responses of PID behave in a totally different way when the gold NP is added, as shown in Fig. 7. In the parallel polarization spectra, shown in the left panel of Fig. 7, we observe at 1 nm a contained enhancement of the peak at 2.9 eV, whereas the other two peaks are unaffected. An analysis of the population of the excited states shows that the population of the first excited state (whose excitation is centered at 2.9 eV) at 1 nm is comparable to the ones at 3 and 5 nm and without NP. For this reason we do not observe important variations in the spectra at any distance.

ECD spectra calculated with the perpendicular polarization, reported in the panel of Fig. 7 (right), instead show a general much more intense response of PID with NP at 1 nm. In detail, a large enhancement of the structure centered at around 4.2 eV for the molecule at 1 nm is observed. The factor of this enhancement is around 20, which indicates a significant influence of the induced field. This interpretation is also supported by the value of the populations of the low-lying excited states, which are defined as $p_M = |C_M(t)|^2$, with C_M (t) given by Eq. (10). For this particular excitation, the increase in the population p_M is equal to a factor 10^3 at 1 nm with respect to the bare-molecule population for the

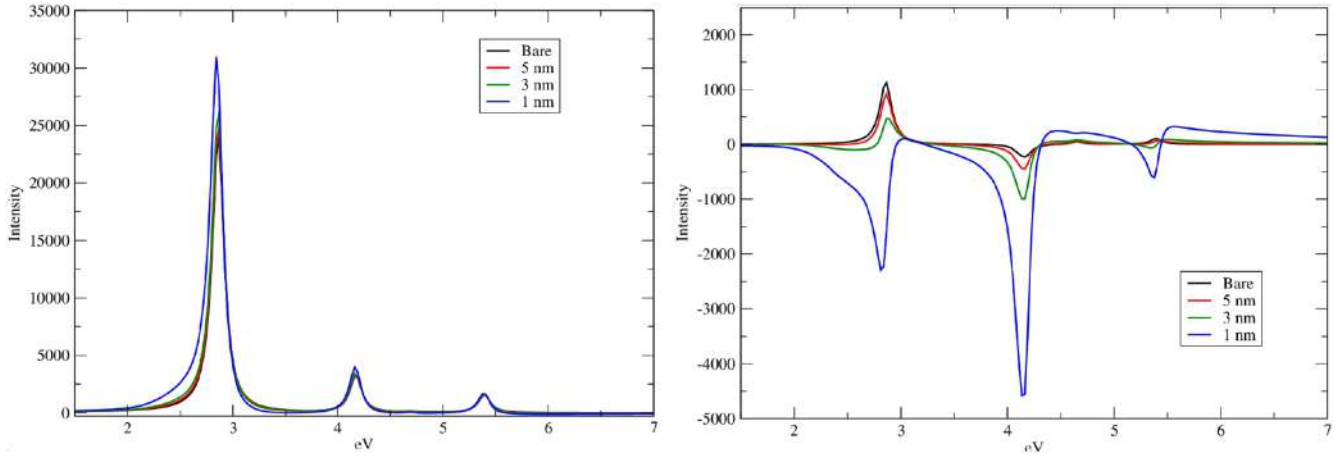

FIG. 7. ECD spectra of PID at a distance *d* of 1, 3, and 5 nm from the NP surface for both pulse polarization directions, parallel (left) and perpendicular (right). Bare-molecule spectra are also reported for comparison.

The Journal of Chemical Physics ARTICLE pubs.aip.org/aip/jcp

same electronic state, which justifies the observed enhancement. The peak centered at 2.9 eV shows an enhancement of the peak as well, consequent to an increase of the population at 1 nm of a factor 10^3, but also a sign inversion in the intensity of the peak, which "hides" the enhancement in absolute value. The trend that brings to the sign inversion is already present at both 3 and 5 nm, for which one observes a decrease in the intensity of the peak if compared to the molecule without NP. Only at 1 nm to we observe a negative peak, though. A similar trend, characterized by an inversion of sign, can also be observed for the peak centered at 5.4 eV, although less pronounced. The observed sign flip could be interpreted in terms of a change of the induced density of the molecules due to the plasmonic field.

Enhancement observed for PID with perpendicular pulse polarization is robust against the value of the damping parameter Γ in Eq. (27). Indeed, the enhancement factor of the peak at 4.17 eV remains unchanged when a value of 200 or 600 a.u. is used, as reported in Fig. 5 of the supplementary material. Increasing the Γ value, e.g., 400 or 600 a.u., reduces the artifact of the smoothing procedure; for this reason, we are confident that the most accurate ECD spectra for PID with perpendicular pulse are those reported in Fig. 7 (Γ = 400 a.u.) and that in the left panel of Fig. 5 of the supplementary material (Γ = 600 a.u.).

By summarizing, the NP effect on PID is much more pronounced because of the smaller gap with the plasmon. However, a large enhancement of the ECD signal is only found for the perpendicular configuration. To the best of our knowledge, no experimental work has been dedicated to aligned PID molecules with Au NPs; therefore, we cannot get a direct comparison with published data. However, a large but not giant enhancement, as that found for PID, is in line with a pure electric dipole-driven mechanism.[30]

V. CONCLUSIONS

In this work, we have extended the TD-PCM-NP multiscale approach to the calculation of ECD spectra of chiral molecules close to a metal NP. We have studied the ECD response of MOX and PID in the presence of a spherical gold NP at various configurations. MOX and PID are described at the quantum level of theory, while the NP is a classically described continuous medium, whose polarization is simulated via the time evolution of BEM apparent surface charges. ECD spectra have been computed by Fourier transforming the molecular time-dependent magnetic dipole moment using TDSE based on B3LYP/TZP and CAM-B3LYP/TZP TDDFT calculations. This approach goes beyond a dipole-like representation of the chiral target, providing a realistic description of the electronic structure and dynamics of the molecule under the influence of an external pulse and of the coupled NP polarization.

We observe a large plasmonic-induced enhancement of the ECD signal for PID with the NP at 1 nm when the pulse is polarized perpendicularly to the molecular axis. In particular, the signal at around 4.2 eV is strongly affected by plasmonic effects; the enhancement factor is 20 at 1 nm. The peak at 2.9 eV is characterized by a change of sign and by an enhancement in absolute value.

Instead, no appreciable enhancement is observed when the pulse polarization is parallel to the axis at any of the considered distances. PID can therefore be defined as a plasmon sensitive molecule when the plasmon peak is located at 2.5 eV and the system configuration results in a positive contribution of the induced field, as in the perpendicular case.

Moreover, MOX shows no appreciable enhancement when the NP is close to it, up to the shortest distance investigated, i.e., 1 nm.

These results are easily rationalized in terms of the gap between plasmonic and molecular excitation and of the coupling of the pulse with the electric and magnetic dipoles of the molecule. If the gap is too large, plasmon effects are negligible, as in the case of MOX; instead, since the PID lowest excitations are close to the NP plasmon, the effect of the induced plasmon field is remarkable and determines an enhancement approximately of a factor 20 with a pulse polarization perpendicular to the NP surface. This effect decreases with the distance between NP and PID, as the amplitude of the induced field decreases.

This method paves the way to a quantum-chemistry systematic investigation of plasmon-assisted ECD molecular spectra, also of biological relevance, and to propose novel routes for experiments.

SUPPLEMENTARY MATERIAL

See the supplementary material for ground-state energy variation of MOX and PID in the presence of the NP. Differential PDOS for the ground state of MOX and PID, with and without NP. Electric and magnetic transition dipole moments for MOX and PID. Absorption spectra of MOX and PID as a function of the distance with the NP surface. ECD spectra for PID with Γ = 200 and 600 a.u.

ACKNOWLEDGMENTS

Financial support from ICSC—Centro Nazionale di Ricerca in High Performance Computing, Big Data, and Quantum Computing, funded by the European Union—NextGenerationEU is gratefully acknowledged.

AUTHOR DECLARATIONS

Conflict of Interest

The authors have no conflicts to disclose.

Author Contributions

L. Biancorosso: Data curation (lead); Investigation (lead); Methodology (equal); Software (equal); Visualization (equal); Writing – original draft (equal); Writing – review & editing (equal). **P. D'Antoni**: Methodology (equal); Software (equal); Writing – review & editing (equal). **S. Corni**: Formal analysis (equal); Methodology (equal); Software (equal); Writing – review & editing (equal). **M. Stener**: Formal analysis (equal); Methodology (equal); Software (equal); Writing – review & editing (equal). **E. Coccia**: Conceptualization (equal); Funding acquisition (equal); Investigation (equal); Methodology (equal); Software (equal); Supervision (equal); Validation (equal); Writing – original draft (equal); Writing – review & editing (equal).

The Journal of Chemical Physics ARTICLE pubs.aip.org/aip/jcp

DATA AVAILABILITY

The data that support the findings of this study are available from the corresponding author upon reasonable request.

REFERENCES

[1] J. Gersten and A. Nitzan, "Spectroscopic properties of molecules interacting with small dielectric particles," J. Chem. Phys. **75**, 1139 (1981).
[2] R. P. Van Duyne, "Molecular plasmonics," Science **306**, 985 (2004).
[3] L. Novotny and B. Hecht, *Principles of Nano-Optics* (Cambridge University Press, Cambridge, 2012).
[4] A. Lauchner, A. E. Schlather, A. Manjavacas, Y. Cui, M. J. McClain, G. J. Stec, F. J. García de Abajo, P. Nordlander, and N. J. Halas, "Molecular plasmonics," Nano Lett. **15**, 6208 (2015).
[5] A. J. Wilson and K. A. Willets, "Molecular plasmonics," Annu. Rev. Anal. Chem. **9**, 27 (2016).
[6] B. Mennucci and S. Corni, "Multiscale modelling of photoinduced processes in composite systems," Nat. Rev. Chem. **3**, 315 (2019).
[7] D. Cialla, A. März, R. Böhme, F. Theil, K. Weber, M. Schmitt, and J. Popp, "Surface-enhanced Raman spectroscopy (SERS): Progress and trends," Anal. Bioanal. Chem. **403**, 27 (2012).
[8] S. Schlücker, "Surface-enhanced Raman spectroscopy: Concepts and chemical applications," Angew. Chem., Int. Ed. **53**, 4756 (2014).
[9] A. B. Zrimsek, N. Chiang, M. Mattei, S. Zaleski, M. O. McAnally, C. T. Chapman, A. I. Henry, G. C. Schatz, and R. P. Van Duyne, "Single-molecule chemistry with surface- and tip-enhanced Raman spectroscopy," Chem. Rev. **117**, 7583 (2017).
[10] P. Lafiosca, L. Nicoli, L. Bonatti, T. Giovannini, S. Corni, and C. Cappelli, "QM/classical modeling of surface enhanced Raman scattering based on atomistic electromagnetic models," J. Chem. Theory Comput. **19**, 3616 (2023).
[11] N. Berova, L. D. Bari, and G. Pescitelli, "Application of electronic circular dichroism in configurational and conformational analysis of organic compounds," Chem. Soc. Rev. **36**, 914–931 (2007).
[12] P. Lazzeretti, "General connections among nuclear electromagnetic shieldings and polarizabilities," Adv. Chem. Phys. **75**, 507 (1989).
[13] P. Lazzeretti, "Electric and magnetic properties of molecules," in *Handbook of Molecular Physics and Quantum Chemistry* (John Wiley & Sons, 2003), Vol. 3, p. 53.
[14] C. Diedrich and S. Grimme, "Systematic investigation of modern quantum chemical methods to predict electronic circular dichroism spectra," J. Phys. Chem. A **107**, 2524 (2003).
[15] T. D. Crawford, "*Ab initio* calculation of molecular chiroptical properties," Theor. Chem. Acc. **115**, 227 (2006).
[16] T. D. Crawford, M. C. Tam, and M. L. Abrams, "The current state of *ab initio* calculations of optical rotation and electronic circular dichroism spectra," J. Phys. Chem. A **111**, 12057 (2007).
[17] I. Warnke and F. Furche, "Circular dichroism: Electronic," Wiley Interdiscip. Rev.: Comput. Mol. Sci. **2**, 150 (2012).
[18] S. S. Andrews and J. Tretton, "Physical principles of circular dichroism," J. Chem. Educ. **97**, 4370 (2020).
[19] N. S. S. Nizar, M. Sujith, K. Swathi, C. Sissa, A. Painelli, and K. G. Thomas, "Emergent chiroptical properties in supramolecular and plasmonic assemblies," Chem. Soc. Rev. **50**, 11208 (2021).
[20] C. Gautier and T. Bürgi, "Chiral gold nanoparticles," ChemPhysChem **10**, 483 (2009).
[21] Z. Fan and A. O. Govorov, "Chiral nanocrystals: Plasmonic spectra and circular dichroism," Nano Lett. **12**, 3283 (2012).
[22] M. Hentschel, M. Schäferling, X. Duan, H. Giessen, and N. Liu, "Chiral plasmonics," Sci. Adv. **3**, e1602735 (2017).
[23] W. Ma, L. Xu, A. F. de Moura, X. Wu, H. Kuang, C. Xu, and N. A. Kotov, "Chiral inorganic nanostructures," Chem. Rev. **117**, 8041 (2017).
[24] G. Zheng, J. He, V. Kumar, S. Wang, I. Pastoriza-Santos, J. Pérez-Juste, L. M. Liz-Marzán, and K.-Y. Wong, "Discrete metal nanoparticles with plasmonic chirality," Chem. Soc. Rev. **50**, 3738 (2021).
[25] E. S. A. Goerlitzer, A. S. Puri, J. J. Moses, L. V. Poulikakos, and N. Vogel, "The beginner's guide to chiral plasmonics: Mostly harmless theory and the design of large-area substrates," Adv. Opt. Mater. **9**, 2100378 (2021).
[26] S. Wang, X. Liu, S. Mourdikoudis, J. Chen, W. Fu, Z. Sofer, Y. Zhang, S. Zhang, and G. Zheng, "Chiral Au nanorods: Synthesis, chirality origin, and applications," ACS Nano **16**, 19789 (2022).
[27] S. Both, M. Schäferling, F. Sterl, E. A. Muljarov, H. Giessen, and T. Weiss, "Nanophotonic chiral sensing: How does it actually work?," ACS Nano **16**, 2822 (2022).
[28] W. Wu and M. Pauly, "Chiral plasmonic nanostructures: Recent advances in their synthesis and applications," Mater. Adv. **3**, 186 (2022).
[29] J.-M. Ha, A. Solovyov, and A. Katz, "Postsynthetic modification of gold nanoparticles with calix[4]arene enantiomers: Origin of chiral surface plasmon resonance," Langmuir **25**, 153 (2009).
[30] A. O. Govorov, Z. Fan, P. Hernandez, J. M. Slocik, and R. R. Naik, "Theory of circular dichroism of nanomaterials comprising chiral molecules and nanocrystals: Plasmon enhancement, dipole interactions, and dielectric effects," Nano Lett. **10**, 1374 (2010).
[31] A. O. Govorov, "Plasmon-induced circular dichroism of a chiral molecule in the vicinity of metal nanocrystals. Application to various geometries," J. Phys. Chem. C **115**, 7914 (2011).
[32] J. M. Slocik, A. O. Govorov, and R. R. Naik, "Plasmonic circular dichroism of peptide-functionalized gold nanoparticles," Nano Lett. **11**, 701 (2011).
[33] N. A. Abdulrahman, Z. Fan, T. Tonooka, S. M. Kelly, N. Gadegaard, E. Hendry, A. O. Govorov, and M. Kadodwala, "Induced chirality through electromagnetic coupling between chiral molecular layers and plasmonic nanostructures," Nano Lett. **12**, 977 (2012).
[34] F. Lu, Y. Tian, M. Liu, D. Su, H. Zhang, A. O. Govorov, and O. Gang, "Discrete nanocubes as plasmonic reporters of molecular chirality," Nano Lett. **13**, 3145 (2013).
[35] B. M. Maoz, Y. Chaikin, A. B. Tesler, O. Bar Elli, Z. Fan, A. O. Govorov, and G. Markovich, "Amplification of chiroptical activity of chiral biomolecules by surface plasmons," Nano Lett. **13**, 1203 (2013).
[36] H. Zhang and A. O. Govorov, "Giant circular dichroism of a molecule in a region of strong plasmon resonances between two neighboring gold nanocrystals," Phys. Rev. B **87**, 075410 (2013).
[37] T. Wu, J. Ren, R. Wang, and X. Zhang, "Competition of chiroptical effect caused by nanostructure and chiral molecules," J. Phys. Chem. C **118**, 20529 (2014).
[38] R. Y. Wang, P. Wang, Y. Liu, W. Zhao, D. Zhai, X. Hong, Y. Ji, X. Wu, F. Wang, D. Zhang, W. Zhang, R. Liu, and X. Zhang, "Experimental observation of giant chiroptical amplification of small chiral molecules by gold nanosphere clusters," J. Phys. Chem. C **118**, 9690 (2014).
[39] T. J. Davis and D. E. Gomez, "Interaction of localized surface plasmons with chiral molecules," Phys. Rev. B **90**, 235424 (2014).
[40] D. Zhai, P. Wang, R. Y. Wang, X. Tian, Y. Ji, W. Zhao, L. Wang, H. Wei, X. Wu, and X. Zhang, "Plasmonic polymers with strong chiroptical response for sensing molecular chirality," Nanoscale **7**, 10690 (2015).
[41] M. C. di Gregorio, A. Ben Moshe, E. Tirosh, L. Galantini, and G. Markovich, "Chiroptical study of plasmon–molecule interaction: The case of interaction of glutathione with silver nanocubes," J. Phys. Chem. C **119**, 17111 (2015).
[42] T. Levi-Belenkova, A. O. Govorov, and G. Markovich, "Orientation-sensitive peptide-induced plasmonic circular dichroism in silver nanocubes," J. Phys. Chem. C **120**, 12751 (2016).
[43] W. Zhang, T. Wu, R. Wang, and X. Zhang, "Surface-enhanced circular dichroism of oriented chiral molecules by plasmonic nanostructures," J. Phys. Chem. C **121**, 666 (2017).
[44] S. Lee, J.-H. Kang, S. Yoo, and Q.-H. Park, "Robust numerical evaluation of circular dichroism from chiral medium/nanostructure coupled systems using the finite-element method," Sci. Rep. **8**, 8406 (2018).
[45] W. Wang, F. Wu, Y. Zhang, W. Wei, W. Niu, and G. Xu, "Boosting chiral amplification in plasmon-coupled circular dichroism using discrete silver nanorods as amplifiers," Chem. Commun. **57**, 7390 (2021).
[46] A. Carone, P. Mariani, A. Desert, M. Romanelli, J. Marcheselli, M. Garavelli, S. Corni, I. Rivalta, and S. Parola, "Insight on chirality encoding from small thiolated molecule to plasmonic Au@Ag and Au@Au nanoparticles," ACS Nano **16**, 1089 (2022).

The Journal of Chemical Physics ARTICLE pubs.aip.org/aip/jcp

[47]M. Venturi, R. Adhikary, A. Sahoo, C. Ferrante, I. Daidone, F. Di Stasio, A. Toma, F. Tani, H. Altug, A. Mecozzi, M. Aschi, and A. Marini, "Plasmon-enhanced circular dichroism spectroscopy of chiral drug solutions," J. Chem. Phys. **159**, 154703 (2023).
[48]J. George and K. G. Thomas, "Surface plasmon coupled circular dichroism of Au nanoparticles on peptide nanotubes," J. Am. Chem. Soc. **132**, 2502 (2010).
[49]X. Shen, C. Song, J. Wang, D. Shi, Z. Wang, N. Liu, and B. Ding, "Rolling up gold nanoparticle-dressed DNA origami into three-dimensional plasmonic chiral nanostructures," J. Am. Chem. Soc. **134**, 146 (2012).
[50]M. J. Urban, P. K. Dutta, P. Wang, X. Duan, X. Shen, B. Ding, Y. Ke, and N. Liu, "Plasmonic toroidal metamolecules assembled by DNA origami," J. Am. Chem. Soc. **138**, 5495 (2016).
[51]X. Lan, X. Lu, C. Shen, Y. Ke, W. Ni, and Q. Wang, "Au nanorod helical superstructures with designed chirality," J. Am. Chem. Soc. **137**, 457 (2015).
[52]J. George, S. Kar, E. S. Anupriya, S. M. Somasundaran, A. D. Das, C. Sissa, A. Painelli, and K. G. Thomas, "Chiral plasmons: Au nanoparticle assemblies on thermoresponsive organic templates," ACS Nano **13**, 4392 (2019).
[53]J. Lu, Y. Xue, K. Bernardino, N.-N. Zhang, W. R. Gomes, N. S. Ramesar, S. Liu, Z. Hu, T. Sun, A. F. de Moura, N. A. Kotov, and K. Liu, "Enhanced optical asymmetry in supramolecular chiroplasmonic assemblies with long-range order," Science **371**, 1368 (2021).
[54]E. Coccia and S. Corni, "Role of coherence in the plasmonic control of molecular absorption," J. Chem. Phys. **151**, 044703 (2019).
[55]Y. Zhao, A. N. Askarpour, L. Sun, J. Shi, X. Li, and A. Alù, "Chirality detection of enantiomers using twisted optical metamaterials," Nat. Commun. **8**, 14180 (2017).
[56]I. Lieberman, G. Shemer, T. Fried, E. M. Kosower, and G. Markovich, "Plasmon-resonance-enhanced absorption and circular dichroism," Angew. Chem., Int. Ed. **47**, 4855 (2008).
[57]M. L. Nesterov, X. Yin, M. Schäferling, H. Giessen, and T. Weiss, "The role of plasmon-generated near fields for enhanced circular dichroism spectroscopy," ACS Photonics **3**, 578 (2016).
[58]L. A. Warning, A. R. Miandashti, L. A. McCarthy, Q. Zhang, C. F. Landes, and S. Link, "Nanophotonic approaches for chirality sensing," ACS Nano **15**, 15538–15566 (2021).
[59]I. Carmeli, I. Lieberman, L. Kraversky, Z. Fan, A. O. Govorov, G. Markovich, and S. Richter, "Broad band enhancement of light absorption in photosystem I by metal nanoparticle antennas," Nano Lett. **10**, 2069–2074 (2010).
[60]T. R. Leite, L. Zschiedrich, O. Kizilkaya, and K. M. McPeak, "Resonant plasmonic–biomolecular chiral interactions in the far-ultraviolet: Enantiomeric discrimination of sub-10 nm amino acid films," Nano Lett. **22**, 7343–7350 (2022).
[61]W. Ma, H. Kuang, L. Xu, L. Ding, C. Xu, L. Wang, and N. A. Kotov, "Attomolar DNA detection with chiral nanorod assemblies," Nat. Commun. **4**, 2689 (2013).
[62]B. M. Maoz, R. van der Weegen, Z. Fan, A. O. Govorov, G. Ellestad, N. Berova, E. W. Meijer, and G. Markovich, "Plasmonic chiroptical response of silver nanoparticles interacting with chiral supramolecular assemblies," J. Am. Chem. Soc. **134**, 17807 (2012).
[63]T. Wu, W. Zhang, R. Wang, and X. Zhang, "A giant chiroptical effect caused by the electric quadrupole," Nanoscale **9**, 5110 (2017).
[64]L. M. Kneer, E.-M. Roller, L. V. Besteiro, R. Schreiber, A. O. Govorov, and T. Liedl, "Circular dichroism of chiral molecules in DNA-assembled plasmonic hotspots," ACS Nano **12**, 9110 (2018).
[65]S. Adhikari and M. Orrit, "Optically probing the chirality of single plasmonic nanostructures and of single molecules: Potential and obstacles," ACS Photonics **9**, 3486 (2022).
[66]E. Makkonen, T. P. Rossi, A. H. Larsen, O. Lopez-Acevedo, P. Rinke, M. Kuisma, and X. Chen, "Real-time time-dependent density functional theory implementation of electronic circular dichroism applied to nanoscale metal–organic clusters," J. Chem. Phys. **154**, 114102 (2021).
[67]M. Monti, M. Stener, and E. Coccia, "Electronic circular dichroism from real-time propagation in state space," J. Chem. Phys. **158**, 084102 (2023).
[68]J. Mattiat and S. Luber, "Electronic circular dichroism with real time time dependent density functional theory: Propagator formalism and gauge dependence," Chem. Phys. **527**, 110464 (2019).
[69]J. Mattiat and S. Luber, "Comparison of length, velocity, and symmetric gauges for the calculation of absorption and electric circular dichroism spectra with real-time time-dependent density functional theory," J. Chem. Theory Comput. **18**, 5513 (2022).
[70]S. Corni and J. Tomasi, "Enhanced response properties of a chromophore physisorbed on a metal particle," J. Chem. Phys. **114**, 3739–3751 (2001).
[71]S. Pipolo and S. Corni, "Real-time description of the electronic dynamics for a molecule close to a plasmonic nanoparticle," J. Phys. Chem. C **120**, 28774 (2016).
[72]N. Tancogne-Dejean, M. J. T. Oliveira, X. Andrade, H. Appel, C. H. Borca, G. Le Breton, F. Buchholz, A. Castro, S. Corni, A. A. Correa, U. De Giovannini, A. Delgado, F. G. Eich, J. Flick, G. Gil, A. Gomez, N. Helbig, H. Hübener, R. Jestädt, J. Jornet-Somoza, A. H. Larsen, I. V. Lebedeva, M. Lüders, M. A. L. Marques, S. T. Ohlmann, S. Pipolo, M. Rampp, C. A. Rozzi, D. A. Strubbe, S. A. Sato, C. Schäfer, I. Theophilou, A. Welden, and A. Rubio, "Octopus, a computational framework for exploring light-driven phenomena and quantum dynamics in extended and finite systems," J. Chem. Phys. **152**, 124119 (2020).
[73]T. P. Rossi, M. Kuisma, M. J. Puska, R. M. Nieminen, and P. Erhart, "Kohn-Sham decomposition in real-time time-dependent density-functional theory: An efficient tool for analyzing plasmonic excitations," J. Chem. Theory Comput. **13**, 4779 (2017).
[74]S. A. Fischer, C. J. Cramer, and N. J. Govind, "Excited state absorption from real-time time-dependent density functional theory," J. Chem. Theory Comput. **11**, 4294 (2015).
[75]S. D'Agostino, R. Rinaldi, G. Cuniberti, and F. Della Sala, "Density functional tight binding for quantum plasmonics," J. Phys. Chem. C **122**, 19756 (2018).
[76]N. V. Ilawe, M. B. Oviedo, and B. M. Wong, "Effect of quantum tunneling on the efficiency of excitation energy transfer in plasmonic nanoparticle chain waveguides," J. Mater. Chem. C **6**, 5857 (2018).
[77]N. Asadi-Aghbolaghi, R. Rüger, Z. Jamshidi, and L. Visscher, "TD-DFT+TB: An efficient and fast approach for quantum plasmonic excitations," J. Phys. Chem. C **124**, 7946 (2020).
[78]T. Wu, X. Zhang, R. Wang, and X. Zhang, "Strongly enhanced Raman optical activity in molecules by magnetic response of nanoparticles," J. Phys. Chem. C **120**, 14795 (2016).
[79]X. Ren, W. Lin, Y. Fang, F. Ma, and J. Wang, "Raman optical activity (ROA) and surface-enhanced ROA (SE-ROA) of (+)-(R)-methyloxirane adsorbed on a Ag_{20} cluster," RSC Adv. **7**, 34376–34381 (2017).
[80]F. J. Kleima, M. Wendling, E. Hofmann, E. J. Peterman, R. van Grondelle, and H. van Amerongen, "Peridinin chlorophyll a protein: Relating structure and steady-state spectroscopy," Biochemistry **39**, 5184–5195 (2000).
[81]T. Polívka, R. G. Hiller, and H. A. Frank, "Spectroscopy of the peridinin–chlorophyll-a protein: Insight into light-harvesting strategy of marine algae," Arch. Biochem. Biophys. **458**, 111–120 (2007).
[82]D. Carbonera, G. Giacometti, U. Segre, E. Hofmann, and R. G. Hiller, "Structure-based calculations of the optical spectra of the light-harvesting peridinin–chlorophyll–protein complexes from *Amphidinium carterae* and *Heterocapsa pygmaea*," J. Phys. Chem. B **103**, 6349–6356 (1999).
[83]M. Pilch and M. Pawlikowski, "Circular dichroism (CD) study of peridinin–chlorophyll a protein (PCP) complexes from marine dinoflagellate algae: The tetramer approach," J. Chem. Soc., Faraday Trans. **94**, 227–232 (1998).
[84]I. Kaminska, J. Bohlen, S. Mackowski, P. Tinnefeld, and G. P. Acuna, "Strong plasmonic enhancement of a single peridinin–chlorophyll a–protein complex on DNA origami-based optical antennas," ACS Nano **12**, 1650–1655 (2018).
[85]M. K. Schmidt, A. O. Govorov, and S. Mackowski, "Plasmon induced modifications of the Förster energy transfer in reconstituted peridinin-chlorophyll-protein photosynthetic complex," MRS Online Proc. Libr. **1286**, 324 (2010).
[86]N. Czechowski, P. Nyga, M. K. Schmidt, T. H. Brotosudarmo, H. Scheer, D. Piatkowski, and S. Mackowski, "Absorption enhancement in peridinin–chlorophyll–protein light-harvesting complexes coupled to semicontinuous silver film," Plasmonics **7**, 115–121 (2012).
[87]U. Hohenester and A. Trügler, "MNPBEM: A Matlab toolbox for the simulation of plasmonic nanoparticles," Comput. Phys. Commun. **183**, 370 (2012).
[88]G. Dall'Osto, E. Coccia, C. A. Guido, and S. Corni, "Investigating ultrafast two-pulse experiments on single DNQDI fluorophores: A stochastic quantum approach," Phys. Chem. Chem. Phys. **22**, 16734 (2020).

The Journal of Chemical Physics ARTICLE pubs.aip.org/aip/jcp

[89]M. Marsili and S. Corni, "Electronic dynamics of a molecular system coupled to a plasmonic nanoparticle combining the polarizable continuum model and many-body perturbation theory," J. Phys. Chem. C **126**, 8768 (2022).
[90]S. Corni, S. Pipolo, and R. Cammi, "Equation of motion for the solvent polarization apparent charges in the polarizable continuum model: Application to real-time TDDFT," J. Phys. Chem. A **119**, 5405 (2015).
[91]G. Dall'Osto, G. Gil, S. Pipolo, and S. Corni, "Real-time dynamics of plasmonic resonances in nanoparticles described by a boundary element method with generic dielectric function," J. Chem. Phys. **153**, 184114 (2020).
[92]P. Hoerner, M. K. Lee, and B. Schlegel, "Angular dependence of strong field ionization of N_2 by time-dependent configuration interaction using density functional theory and the Tamm-Dancoff approximation," J. Chem. Phys. **151**, 054102 (2019).
[93]P. Grobas Illobre, M. Marsili, S. Corni, M. Stener, D. Toffoli, and E. Coccia, "Time-resolved excited-state analysis of molecular electron dynamics by TDDFT and Bethe–Salpeter equation formalisms," J. Chem. Theory Comput. **17**, 6314 (2021).
[94]M. E. Casida, "Time-dependent density functional response theory for molecules," in *Recent Advances in Density Functional Methods: (Part I)* (World Scientific, 1995), pp. 155–192.
[95]E. Tapavicza, I. Tavernelli, and U. Rothlisberger, "Trajectory surface hopping within linear response time-dependent density-functional theory," Phys. Rev. Lett. **98**, 023001 (2007).
[96]E. Tapavicza, I. Tavernelli, U. Rothlisberger, C. Filippi, and M. E. Casida, "Mixed time-dependent density-functional theory/classical trajectory surface hopping study of oxirane photochemistry," J. Chem. Phys. **129**, 124108 (2008).
[97]E. Luppi and M. Head-Gordon, "Computation high-harmonic generation spectra H_2 and N_2 in intense laser pulses using quantum chemistry methods and time-dependent density functional theory," Mol. Phys. **110**, 909 (2012).
[98]C. F. Pauletti, E. Coccia, and E. Luppi, "Role of exchange and correlation in high-harmonic generation spectra of H_2, N_2, and CO_2: Real-time time-dependent electronic-structure approaches," J. Chem. Phys. **154**, 014101 (2021).
[99]G. Dall'Osto and S. Corni, "Time resolved Raman scattering of molecules: A quantum mechanics approach with stochastic Schroedinger equation," J. Phys. Chem. A **126**, 8088 (2022).
[100]F. Ding, W. Liang, C. T. Chapman, C. M. Isborn, and X. Li, "On the gauge invariance of nonperturbative electronic dynamics using the time-dependent Hartree-Fock and time-dependent Kohn-Sham," J. Chem. Phys. **135**, 164101 (2011).
[101]P. Wopperer, P. M. Dinh, P.-G. Reinhard, and E. Suraud, "Electrons as probes of dynamics in molecules and clusters: A contribution from time dependent density functional theory," Phys. Rep. **562**, 1 (2015).
[102]B. Peng, D. B. Lingerfelt, F. Ding, C. M. Aikens, and X. Li, "Real-time TDDFT studies of exciton decay and transfer in silver nanowire arrays," J. Phys. Chem. C **119**, 6421 (2015).
[103]J. J. Goings, P. J. Lestrange, and X. Li, "Real-time time-dependent electronic structure theory," Wiley Interdiscip. Rev.: Comput. Mol. Sci. **8**, e1341 (2018).
[104]A. Parise, A. Alvarez-Ibarra, X. Wu, X. Zhao, J. Pilmé, and A. de la Lande, "Quantum chemical topology of the electron localization function in the field of attosecond electron dynamics," J. Phys. Chem. Lett. **9**, 844 (2018).
[105]X. Li, N. Govind, C. Isborn, A. E. DePrince III, and K. Lopata, "Real-time time-dependent electronic structure theory," Chem. Rev. **120**, 9951 (2020).
[106]M. Jacobs, J. Krumland, A. M. Valencia, and C. Cocchi, "Pulse-induced dynamics of a charge-transfer complex from first principles," J. Phys. Chem. A **127**, 8794 (2023).
[107]S. Raghunathan and M. Nest, "Critical examination of explicitly time-dependent density functional theory for coherent control of dipole switching," J. Chem. Theory Comput. **7**, 2492 (2011).
[108]M. R. Provorse and C. M. Isborn, "Electron dynamics with real-time time-dependent density functional theory," Int. J. Quantum Chem. **116**, 739 (2016).
[109]F. Bedurke, T. Klamroth, and P. Saalfrank, "Many-electron dynamics in laser-driven molecules: Wavefunction theory vs. density functional theory," Phys. Chem. Chem. Phys. **23**, 13544 (2021).
[110]E. Coccia, J. Fregoni, C. A. Guido, M. Marsili, S. Pipolo, and S. Corni, "Hybrid theoretical models for molecular nanoplasmonics," J. Chem. Phys. **153**, 200901 (2020).
[111]E. Coccia and E. Luppi, "Time-dependent *ab initio* approaches for high-harmonic generation spectroscopy," J. Phys.: Condens. Matter **34**, 073001 (2021).
[112]R. Rüger, M. Franchini, T. Trnka, A. Yakovlev, E. van Lenthe, P. Philipsen, T. van Vuren, B. Klumpers, and T. Soini, *AMS 2022.1, SCM, Theoretical Chemistry* (Vrije Universiteit, Amsterdam, The Netherlands, 2022).
[113]R. McWeeny, *Methods of Molecular Quantum Mechanics* (Academic Press, 2016).
[114]F. Furche, R. Ahlrichs, C. Wachsmann, E. Weber, A. Sobanski, F. Vögtle, and S. Grimme, "Circular dichroism of helicenes investigated by time-dependent density functional theory," J. Am. Chem. Soc. **122**, 1717 (2000).
[115]F. Furche, "On the density matrix based approach to time-dependent density functional response theory," J. Chem. Phys. **114**, 5982 (2001).
[116]J. Autschbach, T. Ziegler, S. J. A. van Gisbergen, E. J. Baerends, and E. J. Baerends, "Chiroptical properties from time-dependent density functional theory. I. Circular dichroism spectra of organic molecules," J. Chem. Phys. **116**, 6930 (2002).
[117]J. Autschbach and T. Ziegler, "Calculating molecular electric and magnetic properties from time-dependent density functional response theory," J. Chem. Phys. **116**, 891 (2002).
[118]J. Autschbach, S. Patchkovskii, T. Ziegler, S. van Gisbergen, and E. Jan Baerends, "Chiroptical properties from time-dependent density functional theory. II. Optical rotations of small to medium sized organic molecules," J. Chem. Phys. **117**, 581 (2002).
[119]S. Pipolo, S. Corni, and R. Cammi, "The cavity electromagnetic field within the polarizable continuum model of solvation: An application to the real-time time dependent density functional theory," Comput. Theor. Chem. **1040–1041**, 112 (2014).
[120]D. Varsano, L. A. Espinosa-Leal, X. Andrade, M. A. L. Marques, R. di Felice, and A. Rubio, "Towards a gauge invariant method for molecular chiroptical properties in TDDFT," Phys. Chem. Chem. Phys. **11**, 4481 (2009).
[121]S. Knecht, C. M. Marian, J. Kongsted, and B. Mennucci, "On the photophysics of carotenoids: A multireference DFT study of peridinin," J. Phys. Chem. B **117**, 13808–13815 (2013).

Chapter 4

Antenna-reactor complex for plasmon-mediated photocatalysis

In this work, I computationally investigated plasmon-mediated photocatalysis, focusing in particular on the electronic processes that occur within the catalyst and the adsorbed molecular system. The methodology I have developed during my PhD enables me to study the electronic behavior of molecular systems in the presence of an external NP. A particularly relevant system in this context is the so–called antenna-reactor complex [71, 65, 131, 32], as mentioned in the Introduction. This hybrid structure typically combines a plasmonic NP-commonly made of metals such as Au, Ag, or Al-with a catalytic nanostructure based on metals like Pd or Pt, which are highly efficient catalysts. Numerous experimental studies have shown that the presence of plasmonic NPs can significantly enhance both the selectivity and yield of the catalyzed reaction, making these systems highly attractive for a wide range of applications [184, 132].

Our system of interest was the formic acid dehydrogenation reaction on Pd, a process of considerable industrial relevance as it produces molecular hydrogen from formic acid and has been extensively investigated experimentally [184, 132]. As a first step, we examined the catalytic system in the absence of NPs. The adsorbed species consisted of the formate intermediate, bound in a bridge-like configuration on the Pd surface, along with atomic hydrogen. Then, we explicitly introduced the optical response of a gold nanorod, as shown experimentally [132]. In our study, we focus on the antenna-reactor configuration described in Ref. [132], consisting of a gold nanorod that acts as the antenna, with Pd layers deposited on its tip to form the catalytic reactor. The reaction of interest is the dehydrogenation of formic acid, which produces molecular hydrogen. We used the adsorbed $HCOO^*$) and H^* moieties, since they correspond tothe reaction intermediate.

4.1 Simulating the Pd reactor

As a first step, we analyzed the electronic behavior of the catalyst-adsorbate system in the absence of the NP. For the laser excitation, we chose the frequency corresponding to the plasmonic resonance of the gold nanorod, which will later be included in the simulations. To model the catalyst, we considered different Pd(111) surface topologies: two–layer clusters with nine and sixteen atoms per layer (2L3 and 2L4), and a three-layer cluster with nine atoms per layer (3L3).

Across all systems, we observed a net transfer of negative charge from the Pd layers to both $HCOO^*$ and H^*. In the 2L3 and 2L4 cases, the transferred charge was mainly localized on the oxygen atoms of $HCOO^*$, consistent with a photoinduced direct mechanism. In contrast, the 3L3 system displayed more complex dynamics: the initial direct process was followed, at around 50 fs, by an indirect mechanism involving hole injection into $HCOO^*$. To characterize these processes, we tracked the time evolution of charge populations using ΔPDOS and its energy integral, analyzing contributions from the Pd layers, the $HCOO^*$ species (both as a whole and at the atomic level), and the adsorbed hydrogen.

This project highlighted the main electronic behaviour observed with this system in absence of NP, in the next Section we included in the simulation a metal plasmonic NP.

In this work I did all the analysis and calculations, and contributed to the interpretation of the results and to the writing of the paper. This work is present in literature as Biancorosso, L., and E. Coccia. (2025) "Study of the Photoinduced Charge Injection in the Reaction Intermediate of the Dehydrogenation of Formic Acid on Palladium." *J. Comp. Chem.* **46** p. e70087.

Journal of Computational Chemistry

WILEY

Journal of COMPUTATIONAL CHEMISTRY

RESEARCH ARTICLE OPEN ACCESS

Study of the Photoinduced Charge Injection in the Reaction Intermediate of the Dehydrogenation of Formic Acid on Palladium

L. Biancorosso | E. Coccia

Dipartimento di Scienze Chimiche e Farmaceutiche, Università di Trieste, Trieste, Italy

Correspondence: E. Coccia (ecoccia@units.it)

Received: 14 January 2025 | **Revised:** 6 March 2025 | **Accepted:** 11 March 2025

Keywords: photocatalysis | real-time methods | time-dependent Schroedinger equation

ABSTRACT

The production rate of hydrogen from formic acid on palladium is enhanced in the presence of an Au nanorod by irradiating the system at its plasmon frequency. Taking inspiration from this, we study here the effect of the shape of the Pd cluster (from Pd(111)) on the photoinduced charge injection into the HCOO moiety and adsorbed H, which are the reaction intermediates of the dehydrogenation of formic acid, upon irradiation with a pulse with a carrier frequency equal to the plasmon resonance of a (not included) Au nanorod. We simulate the electron/hole dynamics at frozen nuclei by propagating the time-dependent Schrödinger equation in the space of time-dependent density-functional-theory pseudo-eigenstates in the tight-binding approximation. We have taken into account a cluster with two layers of Pd and 3×3 and 4×4 atoms per layer (2L3 and 2L4, respectively) or with three layers and 3×3 atoms per layer (3L3). For all the systems, a net negative charge on HCOO has been found, according to a photoinduced direct charge-transfer mechanism. For 3L3, an indirect charge-transfer mechanism, occurring after 50 fs and inducing a hole injection into HCOO, has also been found. Moreover, we also used a tailored pulse to populate the antibonding molecular orbital localized on the C-H bond for 3L3.

1 | Introduction

The depletion of fossil fuels and their environmental harm have spurred research into sustainable, eco-friendly energy alternatives. Solutions like solar cells, biomass conversion, and green fuels are being extensively explored and used [1–4]. Among these, hydrogen stands out as a clean fuel meeting both sustainability and environmental requirements [5, 6]. However, challenges in its storage and transportation persist.

Formic acid HCOOH (FA) emerges as a promising, safe and abundant hydrogen reservoir [7–12]. HCOOH decompositon (FAD) becomes a key reaction in catalysis and energy storage, particularly in hydrogen production [13–17]. This reaction occurs through two main pathways: Dehydrogenation, which produces carbon dioxide (CO_2) and hydrogen (H_2), and dehydration, which provides carbon monoxide (CO) and water (H_2O) [18–21]. The two pathways are energetically competitive, and many efforts have been made for improving the selectivity of the reaction towards hydrogen production [22, 23]. The mechanism through which FAD brings to the formation of H_2 and CO_2 is a crucial step which has been thoroughly investigated by theory [21–29]. To study this reaction, methods based on the exploration of the potential energy surface of FAD have been largely employed [30–32]. These studies have simulated the thermal catalytic reaction in gas-phase [23, 27–29], in a solvent like water [22], for example, on small Pd clusters [25] and single atom-Pd catalyst [24]. According to these studies, the reaction intermediate of the dehydrogenation route is the HCOO moiety which is adsorbed on the surface of Pd along with H.

The ability of plasmonic nanoparticles (NPs) to absorb and control light can greatly enhance the photocatalytic performances [33–40]. This result may be explained in terms of the decay of localized surface plasmon resonances, that is, collective electron excitations which in turn decay rapidly in electron-hole hot pairs [41–48]. In plasmon-mediated photocatalysis, one exploits the multicomponent nature of the experimental setup to enhance production rate and selectivity in reactions [49–60]. The idea is to couple plasmonic nanostructures with (smaller) transition metal ones with well-known catalytic properties. The combination of plasmonic and catalytic metal nanostructures in proximity, forming a strongly coupled "antenna reactor" complex [57, 61], is therefore a natural solution to obtain the best of the two components. The plasmonic nanoantenna is used to harvest light and directly enhance absorption in the nearby catalytically active reactor. Upon interaction with the external electromagnetic field, the plasmonic antenna induces an optical polarization in the reactor particle through its near field, thus driving a plasmon in the reactor. The plasmon decay produces hot carriers in the reactor, which in turn permits the exploration of new reaction pathways [44, 62].

In the context of the photocatalytic H_2 generation from FA [34], an example of antenna-reactor setup is provided by Zheng et al. [63], with a tipped Au nanorod with Pd used to investigate the FAD. The observed hydrogen production rate matched levels typically achieved at high temperatures, with a distinct plasmonic effect playing a key role. In addition, the authors reported an increase in selectivity toward the dehydrogenation pathway.

Theory is essential to interpret experiments and elucidate the mechanisms driving plasmon-mediated photocatalytic reactions [64, 65]. Since such mechanisms are based on ultrafast processes (the plasmon decay), to understand plasmonic effects on photocatalysis we must use time-resolved methods in the femtosecond (fs) timescale [66–69]. Building on the work in Reference [63]., here we focus on the effect of different Pd clusters and pulse frequencies on the photoinduced charge distribution of the target system. To study the FAD that produces CO_2 and H_2, the chosen targets are the HCOO species and the hydrogen atom adsorbed on different Pd(111) clusters serving as catalytic centers. We used real-time first-principle methods based on the propagation of the time-dependent Schrödinger equation (TDSE) for the electronic degrees of freedom interacting with an explicit pulse, at frozen nuclei [70]. In general, the importance of nuclear motion in plasmon decay in metal nanoclusters has been theoretically pointed out over the years [71–74]. The goal is to first investigate the effect of plasmonic frequency on the reactor in the presence of HCOO and H: How does the reactor itself, without plasmon dynamics, react to the plasmon frequency? Indeed, the results of this work represent a preliminary but necessary study to simulate the dynamics of hot carriers in the full multiscale system. The next step, in future work, will be to consider the Au nanorod in time-resolved simulations with an explicit pulse, to represent the experimental conditions in Reference [63]. We have also studied the photoinduced dynamics in the case of a tailored pulse which facilitates the FAD towards hydrogen production.

In Section 2, the theoretical framework is presented, while we collect the computational details in Section 3. The results are reported and discussed in Section 4, and the conclusions are given in Section 5.

2 | Theory

Photoinduced electron dynamics is simulated by propagating the TDSE which is given in atomic units and length gauges by

$$i\frac{d}{dt}|\Psi(t)\rangle = \hat{H}(t)|\Psi(t)\rangle \tag{1}$$

$|\Psi(t)\rangle$ is the time-dependent wavefunction while $\hat{H}(t)$ is the time-dependent Hamiltonian, which is composed of a field-free electronic Hamiltonian $\hat{H}_0$ and a coupling term between the electric dipole operator $\hat{\mu}$ and the electric field $\vec{E}_{ext}(t)$ from and external pulse

$$\hat{H}(t) = \hat{H}_0 - \vec{\hat{\mu}} \cdot \vec{E}_{ext}(t) \tag{2}$$

The time-dependent $|\Psi(t)\rangle$ is defined as a linear combination of the N_{states} eigenstates of the field-free Hamiltonian $\hat{H}_0$

$$|\Psi(t)\rangle = \sum_{M=0}^{N_{states}-1} C_M(t)|M\rangle \tag{3}$$

with $C_M(t)$ being the time-dependent coefficients of the expansion and $|M\rangle$ is the Mth eigenstate of the system. In the space of these eigenstates, one can rewrite the TDSE as

$$i\frac{d\mathbf{C}(t)}{dt} = \mathbf{H}(t)\mathbf{C}(t) \tag{4}$$

where $\mathbf{C}(t)$ is the vector of the expansion coefficients and $\mathbf{H}(t)$ is the matrix representation at time t of the time-dependent Hamiltonian, that is, $\mathbf{H}_{LM} = \langle L|\hat{H}(t)|M\rangle$ which is diagonal for the field-free part of the eigenenergies E_M and contains the transition electric dipole moments between states,

$$\langle L|\hat{H}(t)|M\rangle = E_M\delta_{LM} - \sum_{\gamma} F_\gamma(t)\langle L|\vec{\hat{\mu}}\,|M\rangle \tag{5}$$

where $\gamma = x, y, z$ indicates the three coordinates of the transition electric dipole moment.

To describe the excited states, we use approximated time-dependent density functional theory eigenvectors with tight binding (TD-DFT+TB) [75] within a configuration-interaction singles ansatz [76], as implemented in the Amsterdam Modeling Suite (AMS) [77]:

$$|M\rangle = \sum_{i}^{occ}\sum_{a}^{vir} d_{i,M}^{a}\left|\Phi_i^a\right\rangle \tag{6}$$

where $\left|\Phi_i^a\right\rangle$ is the singly excited Slater determinant with an electron promoted from the occupied molecular orbital (MO) i to the virtual one a, and $d_{i,M}^{a}$ are the amplitudes for the

expansion of the excited state $|M\rangle$. In TD-DFT+TB, a DFT ground-state calculation provides the molecular orbitals for the subsequent linear-response calculation with tight-binding approximations [75].

The external electric field $\vec{E}_{ext}(t)$ is given by

$$\vec{E}_{ext}(t) = \vec{E}_{max} \exp\left(-\frac{(t-t_0)^2}{2\sigma^2} \right) \sin(\omega t) \tag{7}$$

where t_0 is the center and σ the amplitude of the Gaussian envelope function, $\vec{E}_{max}$ is the maximum amplitude of the field, and ω is the pulse frequency.

Analysis of the electron dynamics is performed using the time-dependent projected density of states (PDOS(t,ϵ)) [78], which is defined as the expectation of the value of the number operator $\hat{n}$ to the wavefunction $|\psi(t)\rangle$. Specifically, we compute the differential PDOS at time t (ΔPDOS), which refers to the initial condition at $t = 0$

$$\Delta\mathrm{PDOS}_K(t,\epsilon) = -\sum_i^{occ} w_i^K \mathrm{Re}\left[\sum_{M,L} C_L^*(t) C_M(t) \sum_a^{vir} d_{i,L}^{a*} d_{i,M}^a \right] F_\eta(\epsilon - \epsilon_i) \tag{8}$$

$$+ \sum_a^{vir} w_a^K \mathrm{Re}\left[\sum_{M,L} C_L^*(t) C_M(t) \sum_i^{occ} d_{i,L}^{a*} d_{i,M}^a \right] F_\eta(\epsilon - \epsilon_i) \tag{9}$$

In Equation (9), $d_{i,M}^a$ ($d_{i,L}^a$) are the linear coefficients of the expansion for state $|M\rangle$ ($\langle L|$) and F_η is a Lorentzian function centered on the MO energies ϵ_i, with width η, used to obtain a smooth profile. Mulliken weights w_i^K are used in the fragmentation of the studied system. Details are found in Reference [78]. The subscript/superscript K refers to the fragment, that is, the single atom or group of atoms, to which one computes the charge population.

The time-dependent charge (electron and hole) population to the initial condition is defined as [64, 65]

$$\text{electron population} = \frac{1}{2} \int_{-\infty}^{+\infty} [\Delta\mathrm{PDOS}_K(t,\epsilon) + |\Delta\mathrm{PDOS}_K(t,\epsilon)|] d\epsilon \tag{10}$$

and

$$\text{hole population} = \frac{1}{2} \int_{-\infty}^{+\infty} \left[\Delta\mathrm{PDOS}_K(t,\epsilon) - |\Delta\mathrm{PDOS}_K(t,\epsilon)|\right] d\epsilon \tag{11}$$

3 | Computational Details

We studied the electron/hole dynamics for the three systems given in Figure 1: 3L3 with 27 Pd atoms (a), 2L4 with 32 Pd atoms (b), and 2L3 with 18 Pd atoms (c). The notation ALB refers to A layers and $B \times B$ Pd atoms per layer. Structures of the three systems in Figure 1 have been extracted from a geometry optimization of a slab of Pd(111) with HCOO and H adsorbed on top of it. All calculations were performed using the projector augmented wave method [79], as implemented in VASP software [80]. The PBE functional [81] with the van der Waals correction proposed by Grimme [82] was used for the geometry relaxation. Electron smearing of $\sigma = 0.1$ eV was used with the Methfessel–Paxton scheme [83]. The Brillouin zone was sampled by using the Monkhorst–Pack scheme, with an employed k-mesh of $3 \times 3 \times 2$ [84]. In addition, a plane-wave basis set with a cutoff energy of 520 eV was used. A large vacuum of 14.5 Å was used to avoid spurious interactions. All structures were optimized until the Helmann–Feynman forces (that acting on each atom) were less than 0.01 eV/Å. The single unit cell is the one shown in Figure 1d). In the calculation, the first two layers have been left free to reorganize, while the third layer was left in the crystalline position of the Pd(111) surface. From this initial slab, we extracted three finite systems: A cluster with three layers (3L3), two clusters with two layers, that is, $2(3\times3)$ (2L3) and $2(4\times4)$ (2L4) (Figure 1). The geometries obtained after the optimization are in good agreement with the literature reference [85] (see Table S1 in Supporting Information (SI)). Cartesian coordinates are also reported in SI. In all cases, the system, that is, Pd layers + HCOO + H, is neutral.

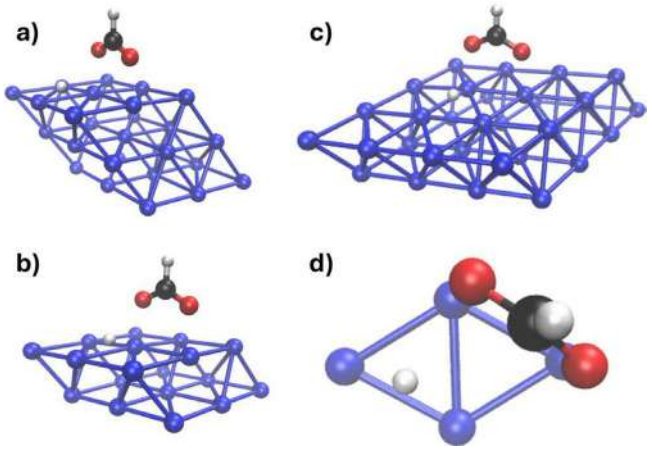

FIGURE 1 | Structures analyzed and studied. HCOO and H are adsorbed of $3(3\times3)$ (a), $2(3\times3)$ (b), $2(4\times4)$ (c), and Pd (111) surface. (d) Top view of the adsorption site of HCOO and H on the surface unit.

Real-time calculations were carried out using the WaveT package [86], interfaced with AMS for extracting electric transition dipole moments [66, 70, 78]. Excitation energies and transition dipole moments, calculated using TD-DFT+TB [75] with the RPBE functional [87] combined with Grimme corrections, and DZ basis set for all three systems, served as inputs for real-time propagation. For each system, 100-fs dynamics were simulated with a time-step δt of 1 as. Wavefunction expansion in Equation (3) includes 1,808, 4,000, and 5,500 excited states for the 2L3, 3L3, and 2L4 systems, respectively, covering excitations up to 6 eV for 2L3, 6.4 eV for 3L3 and 6.3 eV for 2L4. In Figure 2 the absorption spectra of the three systems along with the plasmonic frequency of a model Au nanorod (13.2 nm of length, 3 nm of diameter) is reported (Figure S1 of the SI). The Au nanorod is modeled using the polarizable continuum model; details are found in References [66, 86].

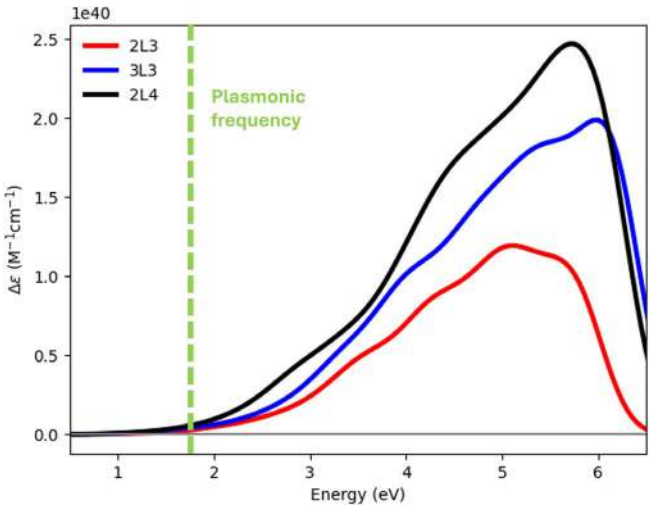

FIGURE 2 | Absorption spectra of the 2L3, 3L3, and 2L4 systems. The green dashed line corresponds to the plasmonic frequency of the Au nanorod.

The applied external field $\vec{E}_{ext}(t)$ of Equation (7) has a peak intensity of 10^2 W/cm2 and a full-width half maximum (FWHM) of 21 fs for the Gaussian envelope. This choice for FWHM is based on the fact that an ultrafast pulse simulates approximately the effect of a CW light with a coherence length of few μm, as typically used in the experiments [65]. In all cases, the pulse is linearly polarized as perpendicular to the Pd layers. Two frequencies were selected for the electronic dynamics simulation: The plasmonic frequency (P1) of the Au nanorod (length of 13.2 nm, diameter of 3 nm) at 681 nm (1.82 eV, see Figure 1 in SI) and a frequency (P2, for the 3L3 system only) that populates the anti-bonding MOs facilitating the C–H bond breaking. The P1 frequency has been computed by means of the boundary element method (BEM) coupled to the polarizable continuum model [86]; details of the BEM calculation are given in the caption of Figure S1 of the SI.

In all the cases, the system is initially in the ground state, that is, $|C_0(0)|^2 = 1$. Nuclei were kept frozen along the dynamics.

4 | Results and Discussion

The goal is not to characterize the time-evolution of a plasmonic response, but simply to observe the effect of the plasmonic frequency of a gold nanorod (the P1 frequency), which has not been explicitly included in the simulations, on the photoinduced electron dynamics in Pd clusters interacting with HCOO and H species.

Electron-dynamics simulations were performed on the systems of Figure 1, which include the intermediates, that is, HCOO and H, of the dehydrogenation reaction of FA. 2L3, 2L4 and 3L3 geometrical features closely match those reported in literature [27, 85]. Specifically, the bridge-like adsorption configuration of HCOO on the Pd surface and the preference of H to adsorb at the hcp site are consistent with the results of published computational works [27, 85]. HCOO was identified to be the main intermediate of the reaction pathway [22, 27, 85], ultimately leading to the formation of CO_2 and H_2. The rationale behind the choice of 2L3, 2L4, and 3L3 clusters is based on exploring the number of layers and Pd atoms for converged results in terms of electron dynamics in a finite-size system.

Starting from these geometries, TD-DFT+TB calculations were carried out using AMS as a preliminary step before performing the electron/hole dynamics by means of WaveT [66, 68]. Post-processing tools [64, 65, 78] allow us to analyze the electron/hole dynamics in terms of charge transfer processes among the various components of the system. Quantities such as ΔPDOS [65, 78] (Equation (9)) and its energy integrals (Equations (10) and (11)), along with the evolution of electron and hole populations over time, were computed to describe the dynamics of the target systems.

In Figure 3, the time-evolution of the net charge of the Pd cluster (left panel) and of the HCOO+H species (right panel) is shown for 2L3, 2L4, and 3L3. The P1 pulse, that is, the pulse with the plasmonic frequency, is also reported as a reference. The net charge is defined as the difference between the hole (Equation (11), K = Pd cluster or HCOO+H) and electron (Equation (10)) population: A positive (negative) value indicates a defect (accumulation) of electrons.

A net electron injection into HCOO and H is observed regardless of the specific shape of the Pd cluster. Charge separation is more efficient with 3L3, while 2L3 and 2L4 are characterized by a very similar profile up to around 45 fs, after the maximum of the pulse. At larger times, charge separation in 2L4 is smaller than that in 2L3. Intriguingly, the amount of charge separation does not follow simply the number of Pd atoms, but it rather seems to be a function of the number of layers and, in general, of the topology of the Pd cluster.

Of course, the sum of the net charge on Pd, HCOO, and H is zero, because no other source or sink of charge is present in the simulations.

From Figure 3, one observes that the pulse maximum is at around 35 fs, while it ends at around 60 fs. In the next subsections, we report and discuss the results of the dynamics in terms of the charge of defined fragments, emphasizing differences and similarities between 2L3, 2L4, and 3L3. Plus, for 3L3 only, we also show the charge population induced by the P2 pulse.

4.1 | 2L3 and 2L4

From now on, the charge population is represented as a percentage, which is calculated by dividing the value of the electron/hole population of the fragment over time by the maximum value of the electron/hole population of the full system (Pd cluster + HCOO + H); the percent net charge is then calculated from the percent populations of negative and positive charge. If not explicitly stated, the P1 pulse was used in the calculations.

The three panels of Figure 4 report the time-evolution of the photoinduced charge population of Pd atoms, for the 2L3 system. P1 pulse has been used. In the top panel, the results are displayed for the full Pd cluster, whereas in the bottom panels, the

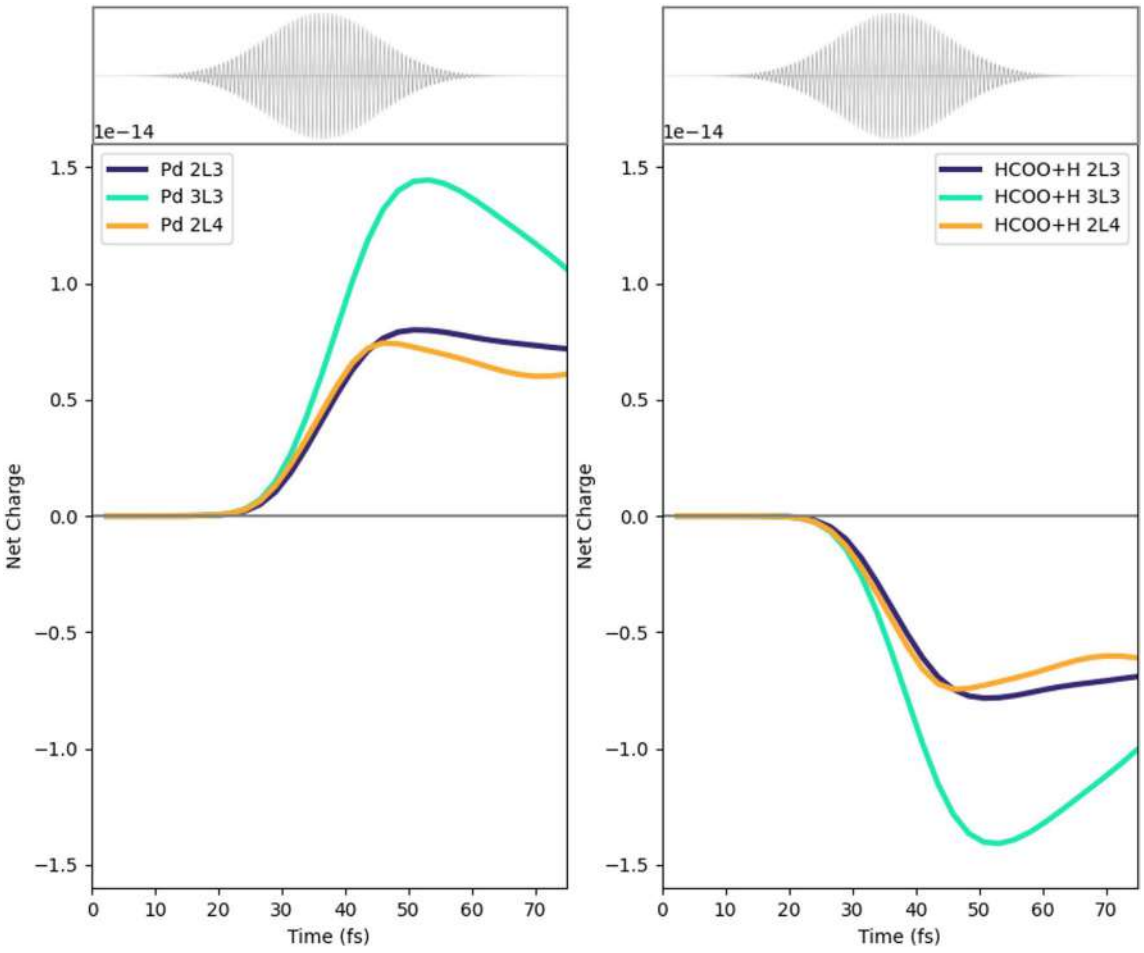

FIGURE 3 | Left panel: Time-evolution of the net charge of the Pd cluster for the three analyzed systems (2L3, 3L3, and 2L4) with the P1 pulse. Right panel: Time-evolution of the net charge of the HCOO species for the three analyzed systems with the P1 pulse.

data regarding the lower (dark blue) and upper (orange) layers are displayed. The lower layer is slightly negatively charged at times at which the pulse is already very small or zero, indicating that it is not a direct photoinduced process. The upper layer has a net positive charge that arises between 30 and 40 fs; moreover, the net charge is also larger than the one in the lower layer. These two findings give evidence that electronic charge has been directly transferred from the upper PD layer to the adsorbed species due to the pulse. A net positive charge in the Pd cluster is also observed in Figure S2 of the SI for the 2L4 case. Here, both layers are slightly positively charged according to a direct photoinduced mechanism [65]. Increasing the size of the Pd layer appears to have minimal impact on the overall electron and hole populations of the system, with only minor variations observed in the behavior of single layers.

In Figure 5, the charge populations of the HCOO moiety are reported. The top panel displays the electron and hole population of the entire HCOO fragment, revealing an excess of electrons, that is, the net charge is negative. This negative charge arises from an electron injection process, with electrons being transferred from the upper Pd layer to the molecular species, as already stated. The bottom three panels of Figure 5describe the charge population of the carbon atom (left), two oxygen atoms (middle), and hydrogen (right) of HCOO. The negative charge in HCOO is mainly concentrated on the two oxygen atoms, which interact with the positively charged Pd atoms of the upper layer. A similar result is found for 2L4 (Figure S3 of the SI), even though the percentage of negative charge on C and H is larger in this case.

The HCOO charge populations observed in 2L3 and 2L4 can also be rationalized by inspecting the ΔPDOS (Equation (9)) of the fragment before ($t = 0$) and after (at around 65 fs) the pulse (Figures S4 and S5 of the SI, respectively). This quantity shows how the populations of the molecular orbitals are changed at a given time to the initial orbital population, that is, $t = 0$. Negative peaks indicate the depopulation of the corresponding orbital, whereas the positive peak indicates an increase in the population. ΔPDOS of the HCOO before and after the pulse is reported in Figures S4 and S5 of the SI along with the occupied and virtual molecular orbitals that are involved in the excitation. The occupied ones are mostly centered on the Pd atoms (indicating a strong interaction between Pd atoms and adsorbed species), whereas the virtual ones also involve HCOO (especially the oxygen atoms) and H species. This is an ulterior proof of the fact that the P1 pulse is moving electrons from the Pd layers to the molecular species.

Of course, we are interested in the charge population on HCOO from a photocatalytic point of view, but still, we also analyzed the time-evolution of the photoinduced charge on the hydrogen atom. For all systems, the net charge in H is about two orders of

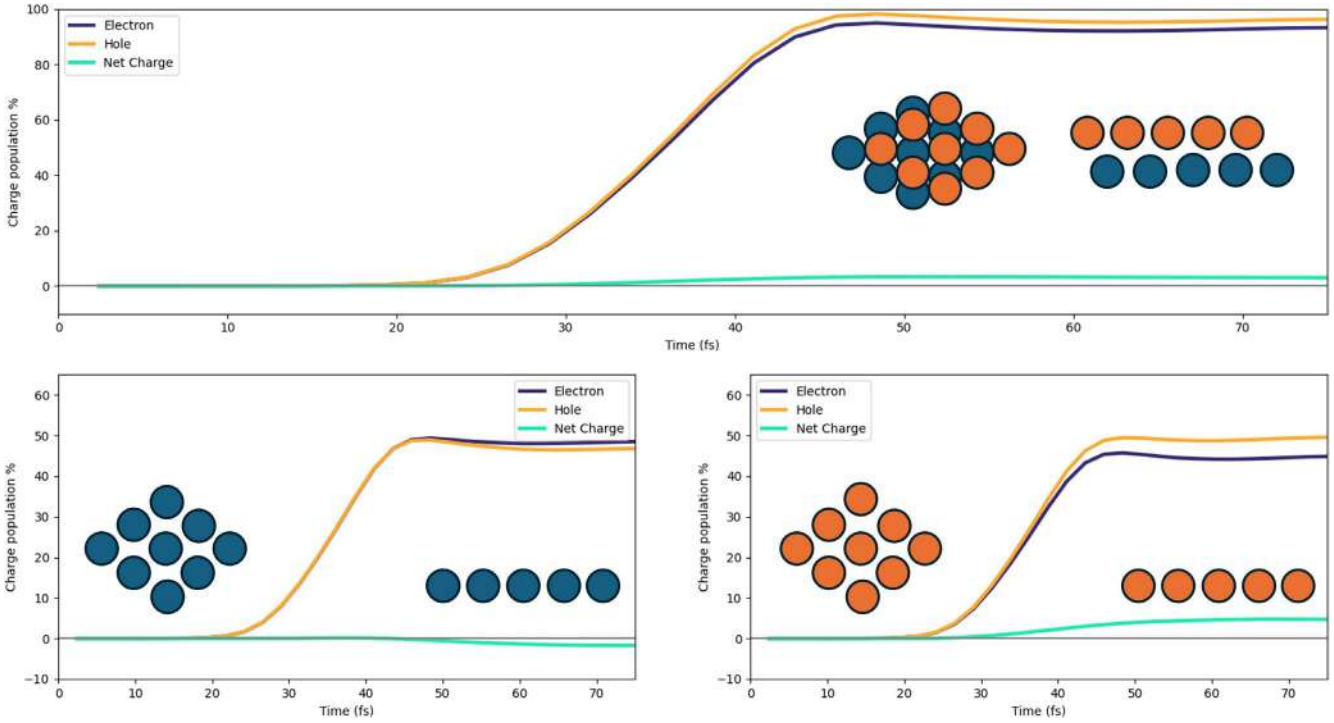

FIGURE 4 | Upper panel: Time-evolution of the photoinduced charge populations (electron, hole, and net) of the full Pd cluster in the 2L3 system with P1 pulse. Bottom panels: Time-evolution of the photoinduced charge populations (electron, hole, and net) of the bottom layer (left) and upper layer (right).

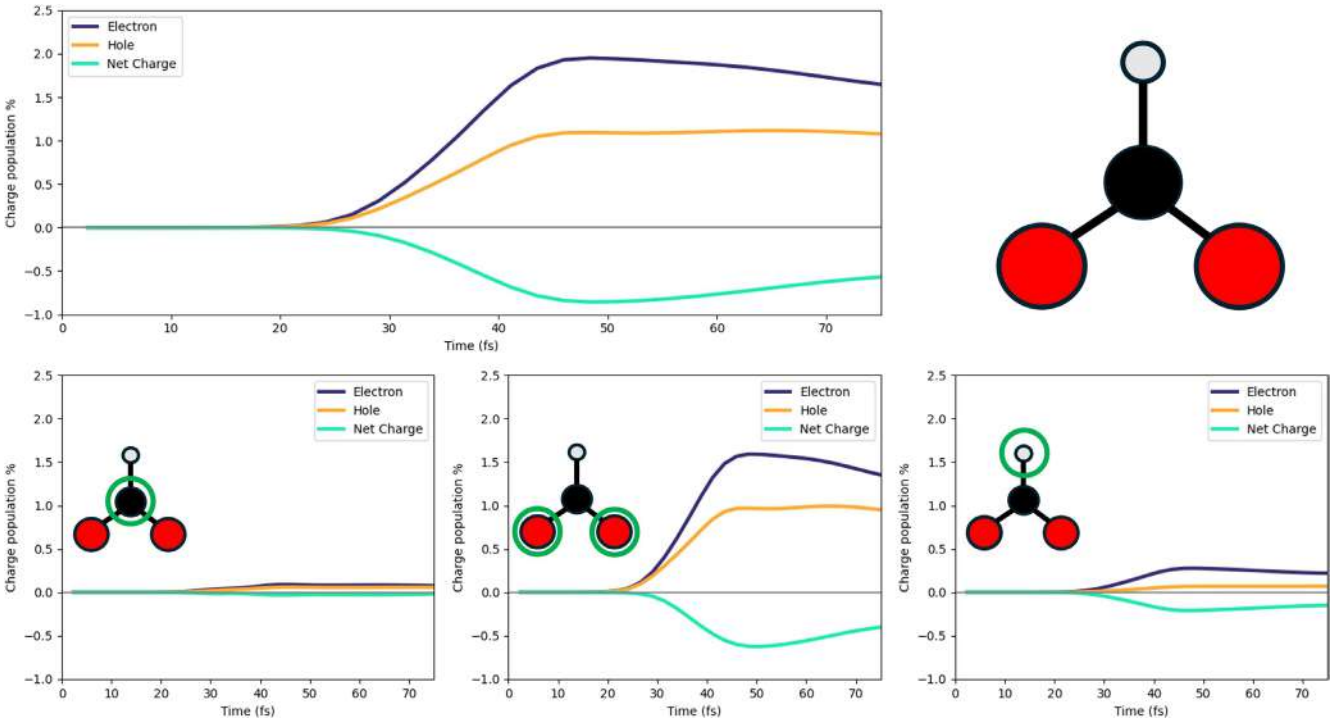

FIGURE 5 | Upper panel: Time-evolution of the photoinduced charge populations (electron, hole, and net) of the HCOO fragment in the 2L3 system with P1 pulse. Bottom panels: On the left, the time-evolution of the photoinduced charge populations (electron, hole, and net) of the carbon atom; in the middle, the same for the oxygen atoms; on the right, the same for the hydrogen atom of HCOO.

magnitude larger than in HCOO. The time-dependent electron and hole populations of the adsorbed H atom for 2L3 and 2L4 are reported in Figures S6 and S7 of the SI, respectively. In both cases, the H atom acquires a negative net charge.

Another piece of information that we can extract from real-time simulations is how the surface charges of the slab are modified due to the interaction with the pulse. Indeed, surface-charge heterogeneity is considered one of the main factors determining

the enhancement observed in plasmon-assisted photocatalysis [63]. In Figure 6, the net charge population of the Pd atoms in proximity to the HCOO and H is reported. Pd atoms that interact with HCOO are reported in green, in blue the ones that interact with H, and in purple two other neighbor Pd atoms. The Pd atoms belong to the upper layer. The Pd pair which interacts with HCOO and the close purple pair tends to acquire a net negative charge, whereas the one interacting with H is positively charged. Different slopes in the time profile suggest the presence of different mechanisms of charge injection. The same analysis has been performed for 2L4, as shown in Figure S8 of the SI. Differently from 2L3, the only spot negatively charged is given by the two Pd atoms interacting with HCOO. Also, the absolute value of the charges of the 2L4 system is smaller than the ones of the 2L3 case.

In conclusion, we can infer that increasing the size of the Pd layer does not affect the type of charge injection into HCOO. However, the internal dynamics of the Pd cluster have been observed to depend on the number of Pd atoms per layer.

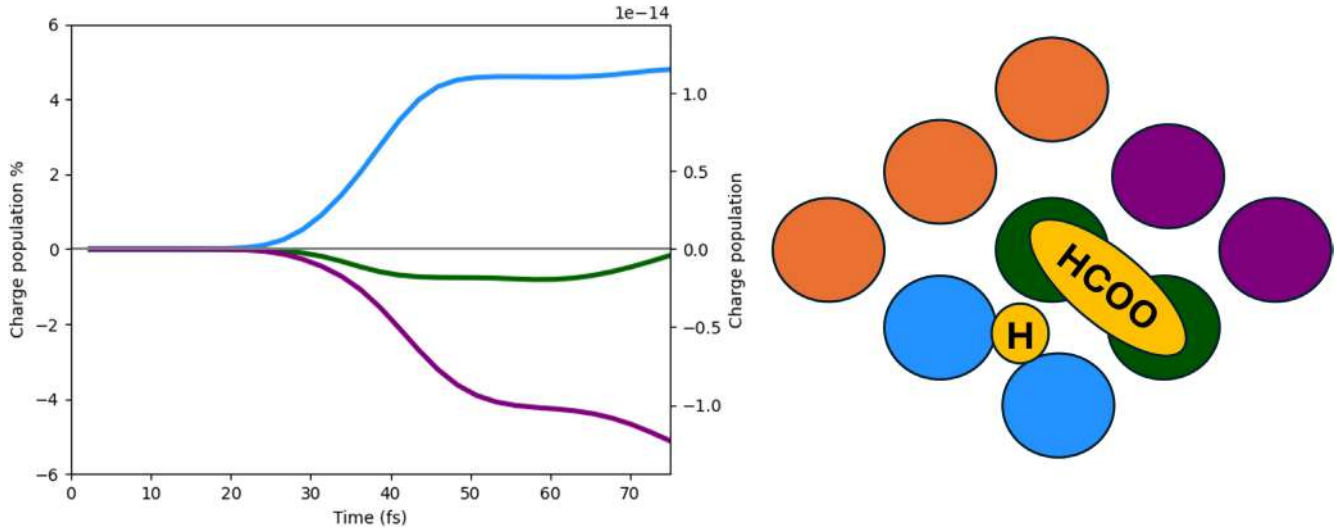

FIGURE 6 | Time-evolution of the photoinduced net charge of the Pd atoms of the upper layer interacting with the molecular species in the 2L3 system with P1 pulse.

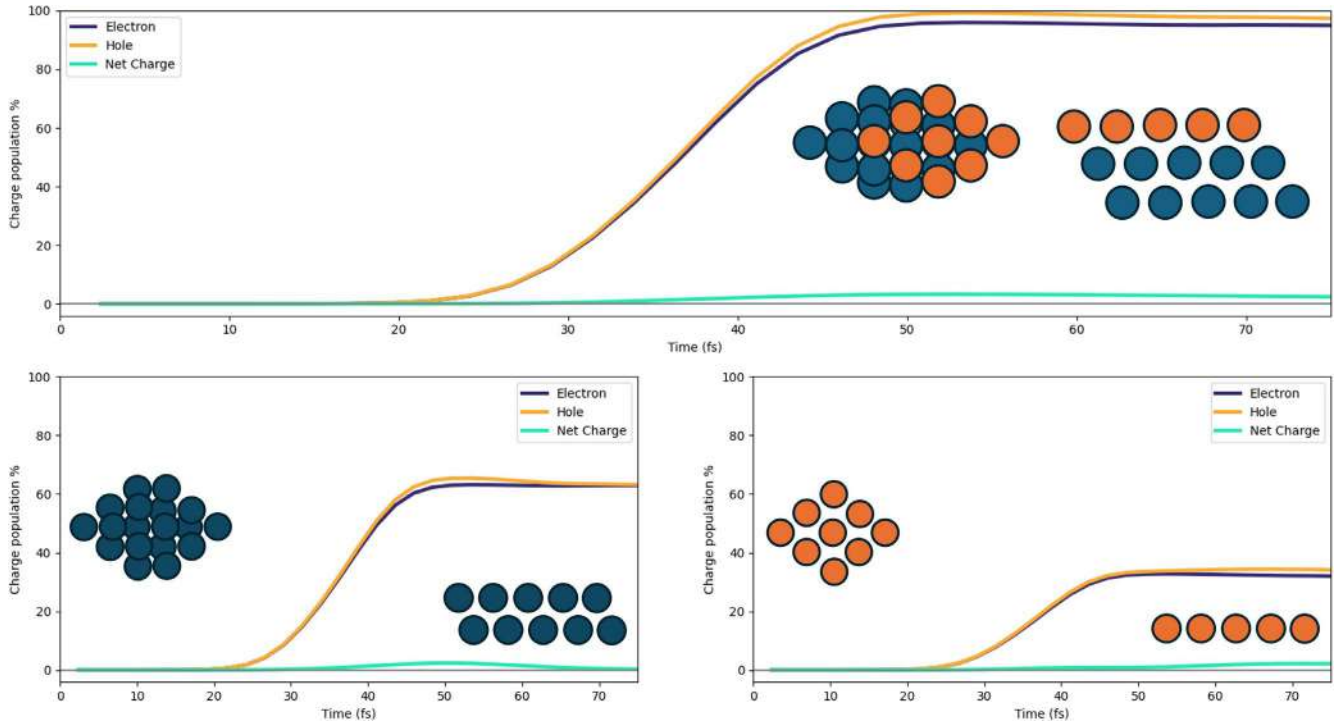

FIGURE 7 | Upper panel: Time-evolution of the photoinduced charge populations (electron, hole, and net) of the Pd cluster in the 3L3 system with P1 pulse. Bottom panel: Time-evolution of the photoinduced charge populations (electron, hole, and net) of the two lower Pd layers (left) and upper one (right).

4.2 | 3L3

In the 3L3 system, three Pd layers are explicitly considered. In Figure 7, the charge populations of the Pd cluster are reported, as we did for 2L3 and 2L4. Also, in this case, a net positive charge, generated by a direct photoinduced process, is present on the fragment due to the transfer of electrons from Pd to the molecular species adsorbed on top of the upper layer. The two bottom panels of Figure 7show the charge population of the upper layer (right) and two lower layers (left). In the left bottom panel, we can observe that the excess of hole population decreases after 60 fs, and a consequent hole excess on the upper layer tends to arise, indicating an indirect, that is, not mediated by light, charge transfer [64, 65]. This indirect charge-transfer mechanism also involves HCOO. We compare in Figure 8 the net charge of the lower Pd layers, upper Pd layer, and HCOO, in absolute terms. The decrease of the net charge of the lower Pd layers starting at 50 fs, that is, at the tail of the pulse, coincides with an increase of the net charge of the lower Pd layer and with the delayed change of sign of the HCOO net charge, occurring at

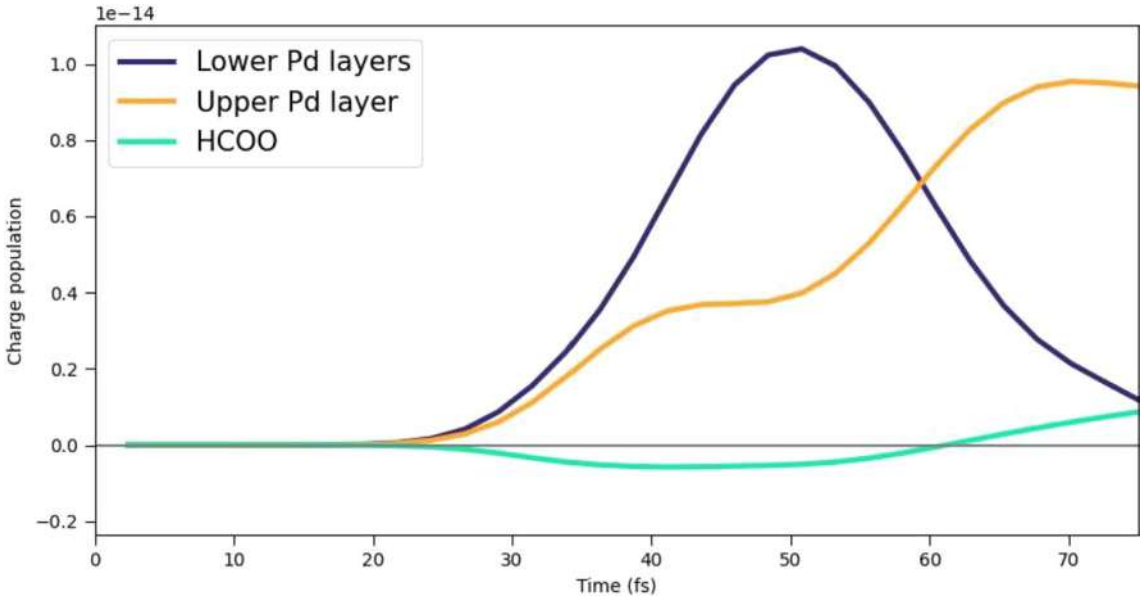

FIGURE 8 | Time-evolution of the net charge of the lower Pd layers, upper Pd layer, and HCOO.

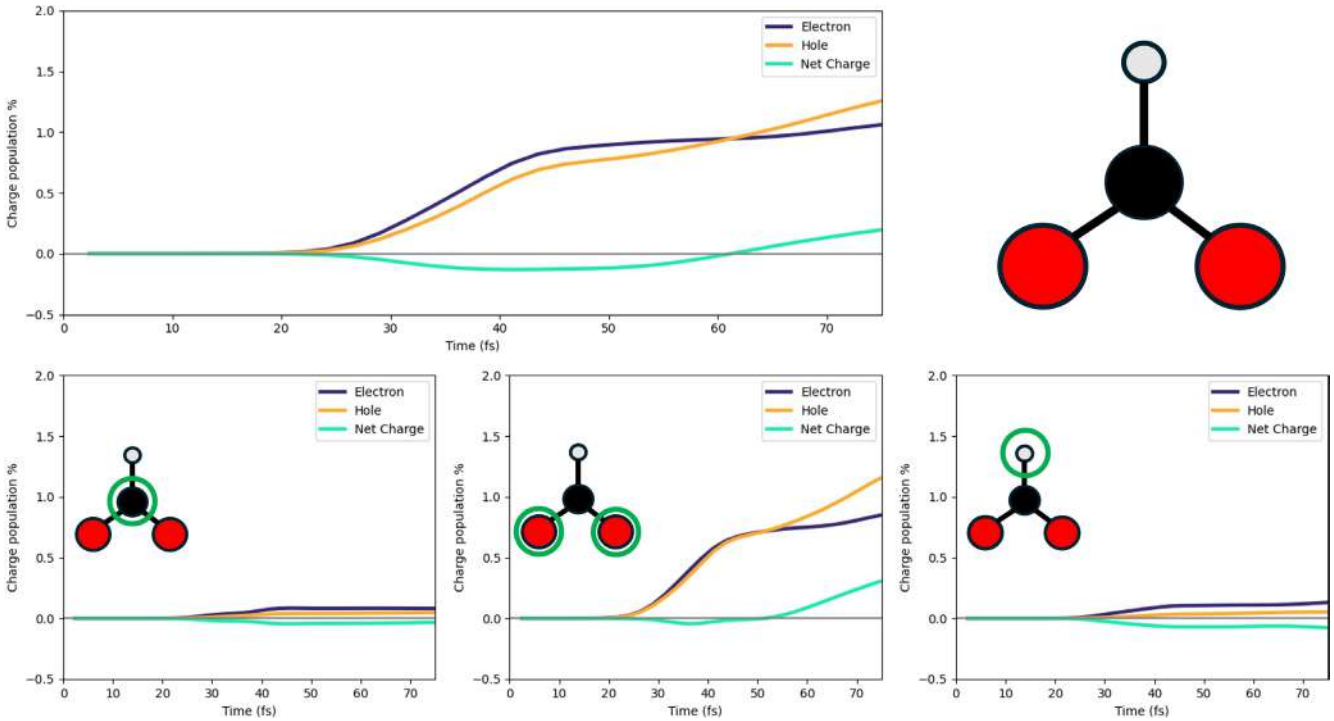

FIGURE 9 | Upper panel: Time-evolution of the photoinduced charge populations (electron, hole, and net) of the HCOO fragment in the 3L3 system with P1 pulse. Bottom panels: On the left, the time-evolution of the photoinduced charge populations (electron, hole, and net) of the carbon atom; in the middle, the same for the oxygen atoms; on the right, the same for the hydrogen atom of HCOO.

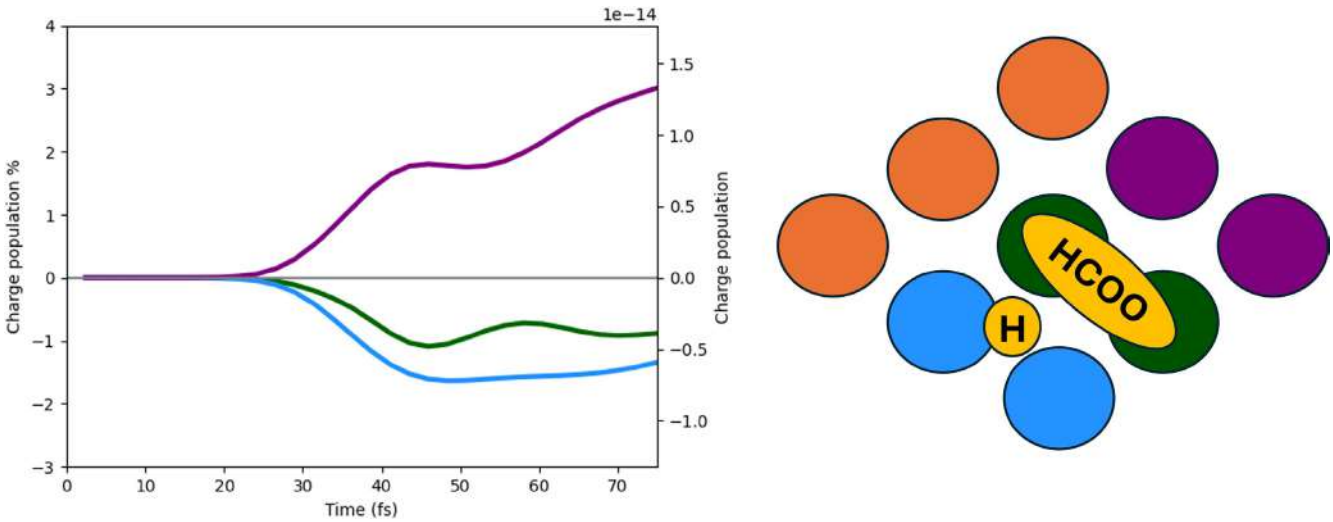

FIGURE 10 | Time-evolution of the photoinduced charge populations (electron, hole, and hole) of the Pd atoms of the upper layer interacting with the molecular species in the 3L3 system with P1 pulse. Green: Pd pairs interacting with HCOO. Blue: Pd pairs interacting with H. Purple: Pd pairs not interacting with any molecular species.

60 fs. These data are interpreted as a hole transfer from the lower Pd layers to the upper Pd layer and HCOO.

The net charge of HCOO is also given as a percentage in the upper panel of Figure 9. Atoms of HCOO involved in the indirect charge transfer, and therefore in the sign flip of the net charge, are the O atoms, which strongly interact with the Pd ones of the upper layer, as argued from the lower panels of Figure 9. Indeed, while C and H atoms of HCOO acquire a small negative charge upon irradiation holding along the dynamics, O atoms are characterized by a transient negative charge between 30 and 40 fs approximately, and then a hole injection on them is observed.

Analysis of the ΔPDOS and the molecular orbitals involved in the dynamics (Figure S9 of the SI) allows one to further confirm this interpretation. In this case, the ΔPDOS at 45.97 fs has been reported as well, together with the data at 65.50 fs and those at the beginning of the dynamics ($t = 0$). In this way, one can observe changes in the orbitals occupation before ($t < 50$ fs) and after ($t > 50$ fs) the hole injection. Table S2 in SI reports the values of the ratio (65.50 fs)/45.97 fs) of the absolute value of ΔPDOS peaks. These ratio values are around 1, that is, no change in the dynamics occurs before and after 50 fs, except for the occupied orbitals labeled "4" and "5". These two orbitals, which maintain a strong oxygen character, become increasingly depopulated at 65.50 fs, with a correspondingly higher value of the ratio (2.09 for "4", 1.63 for "5"). This indicates that the depopulation of these orbitals does not contribute to the population of the virtual orbitals projected on the HCOO fragment.

Charge separation in the upper layer of Pd atoms also occurs in the 3L3 case, as shown in Figure 10. The pairs of Pd atoms interacting with the adsorbed species become negatively charged. Interestingly, this analysis also gives evidence of the indirect mechanism at times greater than 50 fs, with a change in the time profile of the pair interacting directly with HCOO and the adjacent pair without adsorbates.

The evolution of the electron, hole, and net charge populations of the adsorbed H atom is reported in Figure S10 of the SI. A negative charge is accumulated on H, in greater amounts than in the case of 2L3 and 2L4.

In percentage, the photoinduced charge population in HCOO is greater in the 2L3 case, as evident from Figures 5 and 9, and Figure S3 of the SI. This result can be interpreted in terms of the greater tendency of electrons to escape when the number of Pd atoms is reduced, as precisely in the 2L3 case.

It is interesting to point out that in light-off conditions the system is already polarized, with HCOO being negatively charged, as shown in Table S3 of the SI; this result is obtained for each of the systems studied.

The P1 pulse frequency was selected since it corresponds to the excitation energy of the plasmon of a gold nanorod in Figure S1 in SI. All the analysis conducted so far thus represents a preparatory step to the study of the complete system, in the presence of the Au nanorod, which will take place in future work. As a main message, we have verified that regardless of the type of Pd cluster, an injection of electrons to HCOO is verified; this will allow us greater flexibility of reactor choice in modeling the antenna-reactor complex, with the understanding that differences between 2L3, 2L4 and 3L3 in photoinduced processes have been found and discussed here.

Using the P1 pulse thus allows adherence to the experimental work [63]. What if we used instead a pulse frequency that facilitates the FA dehydrogenation by populating the proper antibonding molecular orbitals? From the output of the TD-DFT+TB calculation, we can determine the character of the electronic excitations in terms of transition among orbitals. For the P2 pulse we selected a frequency that populates orbitals that facilitate the FA dehydrogenation. In our case, we selected the frequency of an excitation that populates anti-bonding orbitals localized on the C-H bond of HCOO, which leads to hydrogen formation.

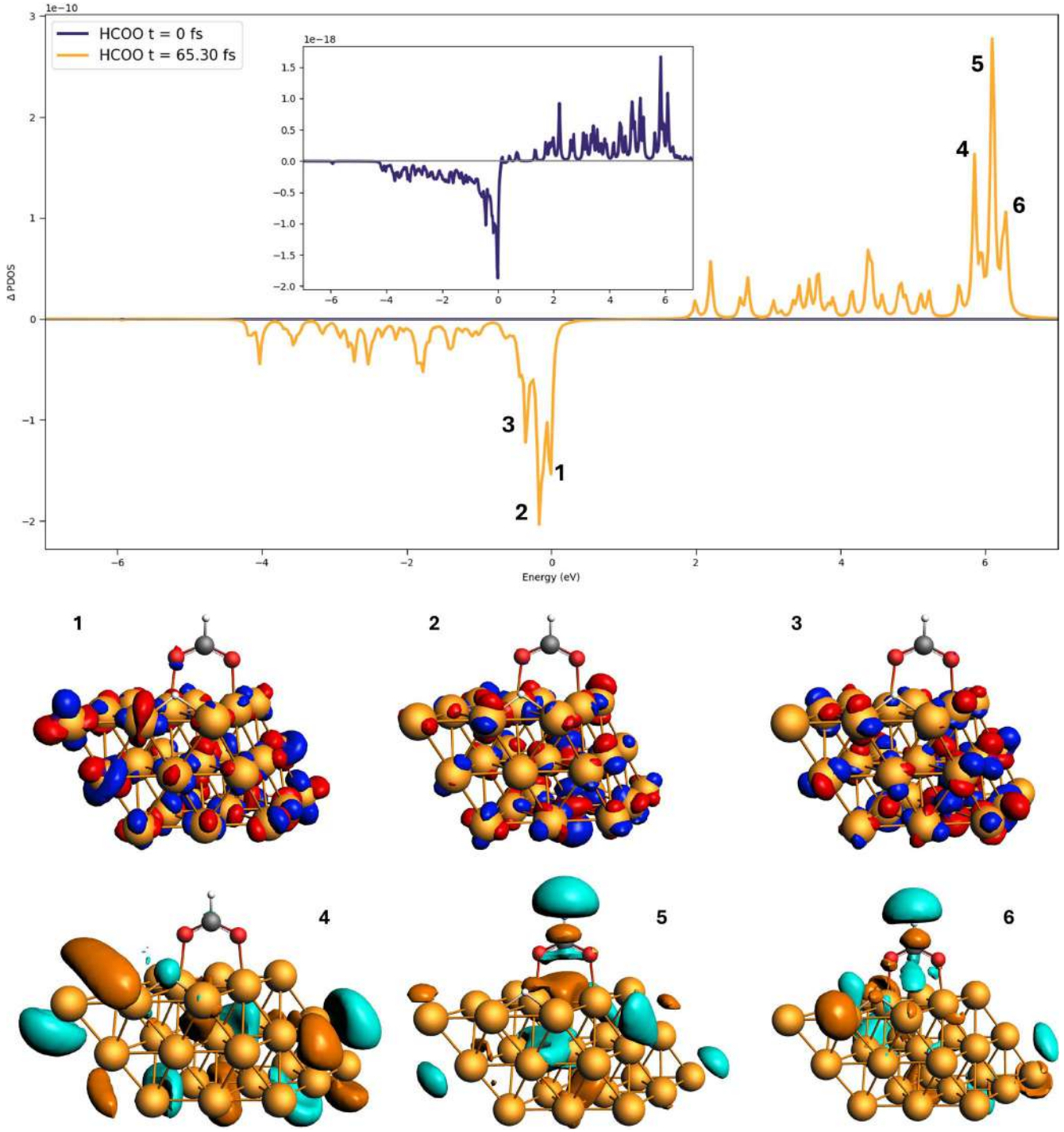

FIGURE 11 | ΔPDOS of the HCOO fragment at $t = 0$ (blue line) and $t = 65.30$ fs (orange line) for the 3L3 system with the P2 pulse. The occupied and virtual orbitals involved in this excitation are also reported.

The selected wavelength for the P2 pulse for the 3L3 system is 198 nm (6.26 eV).

A net positive charge is found in the Pd cluster, as reported in Figure S11 of the SI, even though the upper layer is negatively charged. As expected, tailoring the pulse with the proper frequency maximizes the electron population on HCOO, which is now in percentage much larger than that in P1-based dynamics, as shown in Figure S12 of the SI. In particular, we can notice that the electronic population is accumulated on C and H atoms of HCOO, leaving O atoms with a positive charge, which in turn is consistent with the negative net charge in the upper Pd layer. All these processes can be considered as a photoinduced direct mechanism; the indirect charge transfer is therefore suppressed with a "resonant" light-matter interaction. It is worth noting that only the frequency P1, and frequencies that deviate slightly from P1, will be considered in the work that will contain the coupling with the gold nanorod, to verify the possible enhanced production rate, as reported experimentally. So, the use of P2 frequency, which is not experimentally explored, is limited to this work only.

In Figure 11, we reported the ΔPDOS value before (t=0 fs) and after (t=65.30 fs) the laser peak for the 3L3 system. The orbitals which are getting depopulated are HOMO ("1") or close to it ("2" and "3"), and they are mostly localized on the Pd cluster and the oxygen atoms of the HCOO fragment. The virtual orbitals that are getting populated instead are mostly localized on the HCOO fragment and they are mostly characterized by an antibonding character for the C-H bond (orbitals "5" and "6"). In summary, the chosen pulse allows the transfer of electrons from the Pd cluster to the molecular moiety which, in this case, directly aids the catalytic process which eventually leads to the C-H bond breaking. In Figures S13, S14, and S15 of the SI, we also present the ground-state PDOSs of the Pd layers and HCOO for 2L3, 3L3, and 2L4. They share a similar general profile; some appreciable differences are found in the relative intensity of the peaks around -6 and -6.5 eV. The first peak corresponds to a π-bonding orbital of the O-C-O bond and a σ-bonding orbital of the Pd-H orbital. The second peak presents a similar character, with a smaller degree of hybridization between the molecular moiety and Pd atoms. Moreover, the Pd PDOS of 3L3 shows a maximum at the HOMO energy, at variance with what occurs with 2L3 and 2L4.

To verify the effect of the chosen methodology on the results, we have also carried out full TDDFT calculations with RPBE and B3LYP functionals for 2L3, using the same basis set and Grimme corrections of the TD-DFT+TB calculations. The TD-DFT+TB/RPBE, TDDFT/RPBE, and TDDFT/B3LYP spectra are collected in Figure S16 of the SI: A very good agreement is observed, thus justifying the use of TD-DFT+TB/RPBE. Moreover, electron dynamics based on TDDFT/B3LYP have been generated and analyzed: In Figures S17 and S18 of the SI, we report the time-evolution of the charge population for the Pd layers and HCOO, respectively. Also in this case, a net electron injection into HCOO is predicted, according to the TD-DFT+TB findings: A difference at large times ($>$ 50 fs), where modulation of the HCOO negative charge is observed, perhaps due to an indirect charge transfer, which is not present in TD-DFT+TB/RPE data.

In all the studied systems, finite-size effects are present, especially observed in the virtual molecular orbitals characterized, in some cases, by density at the border of the Pd layers.

Moreover, it is important to note that all results presented in this article were obtained with coherent frozen-nuclei dynamics. More realistic modeling, especially at long times, in which nuclear motion is assumed to have been triggered, would therefore have to take into account environmental effects on electronic degrees of freedom. As we observe in Reference [64]. for the CHO moiety interacting with Rh layers, the effect of the environment in terms of electronic relaxation and dephasing does not affect the sign of the charge injection, thus justifying the use of closed electron dynamics to investigate the photoinduced charge transfer, as we did in this work. One can effectively model the non-radiative decay by using the energy-gap law [64].

5 | Conclusions

In this study, we investigated the electron/hole dynamics of the HCOO moiety and the hydrogen atom, as intermediates in the FAD reaction, in the presence of Pd clusters of different sizes and layer configurations (2L3, 3L3, and 2L4). We used a time-resolved approach based on solving TDSE in the space of DFT-TB pseudo-eigenstates [76, 88–93].

The main goal was to evaluate how the choice of the catalytic cluster affects the dynamics, using mainly the P1 pulse, which is resonant with the plasmonic transition of an Au nanorod (not explicitly included in the TDSE calculations). To achieve this, we analyzed the time-evolution of charge populations by means of ΔPDOS and its energy integral, focusing on the Pd layers, on HCOO as a whole and its atoms, and the adsorbed H. For all the systems, we observed a net transfer of negative charge from the Pd layers to HCOO and H. In the case of 2L3 and 2L4, the transferred charge is mainly localized on the oxygen atoms of HCOO, according to a photoinduced direct mechanism. In contrast, the 3L3 system exhibited much more complex dynamics: The direct process is followed by an indirect one, starting at around 50 fs, which provides a hole injection into HCOO.

Calculations also show an inhomogeneous charge redistribution in the upper Pd layer upon irradiation, which depends on the specific Pd cluster.

We also studied for 3L3 the effect of a pulse tailored to drive the reaction toward dehydrogenation, which consists of populating antibonding orbitals located on the C-H bond of HCOO; C and H atoms of HCOO are indeed characterized by a large photoinduced electron population. In this case, oxygen atoms are positively charged while the upper Pd layer is negatively charged.

As a next step, we plan to include the Au nanorod in the model, to fill the gap with the experimental setup [63]. This will allow us to rationalize the enhancement observed in the plasmon-assisted photocatalytic process.

Acknowledgments

Financial support from ICSC – Centro Nazionale di Ricerca in High-Performance Computing, Big Data, and Quantum Computing, funded by the European Union – NextGenerationEU is gratefully acknowledged. Open access publishing facilitated by Universita degli Studi di Trieste, as part of the Wiley - CRUI-CARE agreement.

Conflicts of Interest

The authors declare no conflicts of interest.

Data Availability Statement

The data that support the findings of this study are available from the corresponding author upon reasonable request.

References

1. P. T. Aakko-Saksa, C. Cook, J. Kiviaho, and T. Repo, "Liquid Organic Hydrogen Carriers for Transportation and Storing of Renewable Energy–Review and Discussion," *Journal of Power Sources* 396 (2018): 803.

2. E. O'Dwyer, I. Pan, S. Acha, and N. Shah, "Smart Energy Systems for Sustainable Smart Cities: Current Developments, Trends and Future Directions," *Applied Energy* 237 (2019): 581.

3. T. Poompavai and M. Kowsalya, "Control and Energy Management Strategies Applied for Solar Photovoltaic and Wind Energy Fed Water Pumping System: A Review," *Renewable and Sustainable Energy Reviews* 107 (2019): 108.

4. P. G. V. Sampaio and M. O. A. González, "Photovoltaic Solar Energy: Conceptual Framework," *Renewable and Sustainable Energy Reviews* 74 (2017): 590.

5. H. Dai, N. Cao, L. Yang, J. Su, W. Luo, and G. Cheng, "Agpd Nanoparticles Supported on Mil-101 as High Performance Catalysts for Catalytic Dehydrogenation of Formic Acid," *Journal of Materials Chemistry A* 2 (2014): 11060.

6. N. Onishi, G. Laurenczy, M. Beller, and Y. Himeda, "Recent Progress for Reversible Homogeneous Catalytic Hydrogen Storage in Formic Acid and in Methanol," *Coordination Chemistry Reviews* 373 (2018): 317.

7. I. Dutta, S. Chatterjee, H. Cheng, et al., "Formic Acid to Power Towards Low-Carbon Economy," *Advanced Energy Materials* 12 (2022): 2103799.

8. R. S. El-Emam and H. Özcan, "Comprehensive Review on the Techno-Economics of Sustainable Large-Scale Clean Hydrogen Production," *Journal of Cleaner Production* 220 (2019): 593.

9. M. Grasemann and G. Laurenczy, "Formic Acid as a Hydrogen Source–Recent Developments and Future Trends," *Energy & Environmental Science* 5 (2012): 8171.

10. A. Kumar, P. Daw, and D. Milstein, "Homogeneous Catalysis for Sustainable Energy: Hydrogen and Methanol Economies, Fuels From Biomass, and Related Topics," *Chemical Reviews* 122 (2021): 385.

11. A. K. Singh, S. Singh, and A. Kumar, "Hydrogen Energy Future With Formic Acid: a Renewable Chemical Hydrogen Storage System," *Catalysis Science & Technology* 6 (2016): 12.

12. S. Verma, R. N. Baig, M. N. Nadagouda, and R. S. Varma, "Visible Light Mediated Upgrading of Biomass to Biofuel," *Green Chemistry* 18 (2016): 1327.

13. A. Boddien, B. Loges, H. Junge, and M. Beller, "Hydrogen Generation at Ambient Conditions: Application in Fuel Cells," *ChemSusChem* 1 (2008): 751.

14. T. C. Johnson, D. J. Morris, and M. Wills, "Hydrogen Generation From Formic Acid and Alcohols Using Homogeneous Catalysts," *Chemical Society Reviews* 39 (2010): 81.

15. H. Junge, A. Boddien, F. Capitta, et al., "Improved Hydrogen Generation From Formic Acid," *Tetrahedron Letters* 50 (2009): 1603.

16. G. Olah, A. Goeppert, and G. Prakash, *Hydrogen as a Future Energy Carrier* (WILEY-VCH Verlag GmbH & Co., 2008).

17. X. Yu and P. G. Pickup, "Recent Advances in Direct Formic Acid Fuel Cells (Dfafc)," *Journal of Power Sources* 182 (2008): 124.

18. C. Guan, Y. Pan, T. Zhang, M. J. Ajitha, and K.-W. Huang, "An Update on Formic Acid Dehydrogenation by Homogeneous Catalysis," *Chemistry, an Asian Journal* 15 (2020): 937.

19. M. Iglesias and L. A. Oro, "Mechanistic Considerations on Homogeneously Catalyzed Formic Acid Dehydrogenation," *European Journal of Inorganic Chemistry* 2018 (2018): 2125.

20. Y. Noto, K. Fukuda, T. Onishi, and K. Tamaru, "Mechanism of Formic Acid Decomposition Over Dehydrogenation Catalysts," *Transactions of the Faraday Society* 63 (1967): 3081.

21. S. Schlussel and S. Kwon, "A Review of Formic Acid Decomposition Routes on Transition Metals for Its Potential Use as a Liquid H_2 Carrier," *Korean Journal of Chemical Engineering* 39 (2022): 2883.

22. Z.-Y. Hu, L.-H. Luo, C. Shang, and Z.-P. Liu, "Free Energy Pathway Exploration of Catalytic Formic Acid Decomposition on Pt-Group Metals in Aqueous Surroundings," *ACS Catalysis* 14 (2024): 7684.

23. J. S. Yoo, F. Abild-Pedersen, J. K. Nørskov, and F. Studt, "Theoretical Analysis of Transition-Metal Catalysts for Formic Acid Decomposition," *ACS Catalysis* 4 (2014): 1226.

24. N. He and Z. H. Li, "Palladium-Atom Catalyzed Formic Acid Decomposition and the Switch of Reaction Mechanism With Temperature," *Physical Chemistry Chemical Physics* 18 (2016): 10005.

25. S. J. Li, X. Zhou, and W. Q. Tian, "Theoretical Investigations on Decomposition of Hcooh Catalyzed by pd7 Cluster," *Journal of Physical Chemistry. A* 116 (2012): 11745.

26. M. Navlani-García, K. Mori, D. Salinas-Torres, Y. Kuwahara, and H. Yamashita, "New Approaches Toward the Hydrogen Production From Formic Acid Dehydrogenation Over Pd-Based Heterogeneous Catalysts," *Frontiers in Materials* 6 (2019): 44.

27. N. Wang, K. Li, Y. Wang, and Z. Wu, "Density Functional Study on Formic Acid Decomposition on Pd (111) Surface: a Revisit and Comparison With Other Density Functional Methods," *Journal of Molecular Modeling* 27 (2021): 1.

28. Y. Wang, Y. Qi, D. Zhang, and C. Liu, "New Insight Into the Decomposition Mechanism of Formic Acid on Pd (111): Competing Formation of CO_2 and CO," *Journal of Physical Chemistry C* 118 (2014): 2067.

29. S. Zhou, C. Qian, and X. Chen, "Comparative Theoretical Study of Adsorption and Dehydrogenation of Formic Acid, Hydrazine and Isopropanol on Pd (111) Surface," *Catalysis Letters* 141 (2011): 726.

30. N. Govind, M. Petersen, G. Fitzgerald, D. King-Smith, and J. Andzelm, "A Generalized Synchronous Transit Method for Transition State Location," *Computational Materials Science* 28 (2003): 250.

31. G. Henkelman, B. P. Uberuaga, and H. Jónsson, "A Climbing Image Nudged Elastic Band Method for Finding Saddle Points and Minimum Energy Paths," *Journal of Chemical Physics* 113 (2000): 9901.

32. H. Jónsson, G. Mills, and K. W. Jacobsen, "Nudged Elastic Band Method for Finding Minimum Energy Paths of Transitions," in *Classical and Quantum Dynamics in Condensed Phase Simulations* (World Scientific, 1998), 385.

33. E. A. Coronado, E. R. Encina, and F. D. Stefani, "Optical Properties of Metallic Nanoparticles: Manipulating Light, Heat and Forces at the Nanoscale," *Nanoscale* 3 (2011): 4042.

34. S. Ezendam, M. Herran, L. Nan, et al., "Hybrid Plasmonic Nanomaterials for Hydrogen Generation and Carbon Dioxide Reduction," *ACS Energy Letters* 7 (2022): 778.

35. V. Giannini, A. I. Fernández-Domínguez, S. C. Heck, and S. A. Maier, "Plasmonic Nanoantennas: Fundamentals and Their Use in Controlling the Radiative Properties of Nanoemitters," *Chemical Reviews* 111 (2011): 3888.

36. Y. Huang, Y. Chen, L. Deng, Y. Zhu, and Y. Huang, "Expanding the Scope of Antenna–Reactor Photocatalysts for Strong Visible Light Absorption in Small Transition Metal Nanoparticles," *Applied Physics Letters* 119 (2021): 043903.

37. L. Mascaretti and A. Naldoni, "Hot Electron and Thermal Effects in Plasmonic Photocatalysis," *Journal of Applied Physics* 128 (2020): 041101–041123.

38. S. Mubeen, J. Lee, N. Singh, S. Krämer, G. D. Stucky, and M. Moskovits, "An Autonomous Photosynthetic Device in Which all Charge Carriers Derive From Surface Plasmons," *Nature Nanotechnology* 8 (2013): 247.

39. H. Sheng, J. Wang, J. Huang, et al., "Strong Synergy Between Gold Nanoparticles and Cobalt Porphyrin Induces Highly Efficient

Photocatalytic Hydrogen Evolution," *Nature Communications* 14 (2023): 1528.

40. D. F. Swearer, H. Zhao, L. Zhou, et al., "Heterometallic Antenna-Reactor Complexes for Photocatalysis," *Proceedings of the National Academy of Sciences* 113 (2016a): 8916.

41. P. Christopher and M. Moskovits, "Hot Charge Carrier Transmission From Plasmonic Nanostructures," *Annual Review of Physical Chemistry* 68 (2017): 379.

42. J. Gargiulo, R. Berté, Y. Li, S. A. Maier, and E. Cortés, "From Optical to Chemical Hot Spots in Plasmonics," *Accounts of Chemical Research* 52 (2019): 2525.

43. N. Halas, "Spiers Memorial Lecture Introductory Lecture: Hot-Electron Science and Microscopic Processes in Plasmonics and Catalysis," *Faraday Discussions* 214 (2019): 13.

44. E. Kazuma and Y. Kim, "Mechanistic Studies of Plasmon Chemistry on Metal Catalysts," *Angewandte Chemie, International Edition* 58 (2019): 4800.

45. A. Lauchner, A. E. Schlather, A. Manjavacas, et al., "Molecular Plasmonics," *Nano Letters* 15 (2015): 6208.

46. A. Manjavacas, J. G. Liu, V. Kulkarni, and P. Nordlander, "Plasmon-Induced Hot Carriers in Metallic Nanoparticles," *ACS Nano* 8 (2014): 7630.

47. R. Sundararaman, P. Narang, A. S. Jermyn, W. A. Goddard, III, and H. A. Atwater, "Theoretical Predictions for Hot-Carrier Generation From Surface Plasmon Decay," *Nature Communications* 5 (2014): 5788.

48. Y. Zhang, S. He, W. Guo, et al., "Surface-Plasmon-Driven Hot Electron Photochemistry," *Chemical Reviews* 118 (2017): 2927.

49. R.-G. Ciocarlan, N. Blommaerts, S. Lenaerts, P. Cool, and S. W. Verbruggen, "Recent Trends in Plasmon-Assisted Photocatalytic CO_2 Reduction," *ChemSusChem* 16 (2023): e202201647.

50. P. V. Kumar, T. P. Rossi, M. Kuisma, P. Erhart, and D. J. Norris, "Direct Hot-Carrier Transfer in Plasmonic Catalysis," *Faraday Discussions* 214 (2019): 189–197, http://dx.OPTOPTdoi.org/10.1039/C8FD00154E.

51. J. M. P. Martirez, J. L. Bao, and E. A. Carter, "First-Principles Insights Into Plasmon-Induced Catalysis," *Annual Review of Physical Chemistry* 72 (2021): 1–21.

52. D. Mittal, M. Ahlawat, and V. Govind Rao, "Recent Progress and Challenges in Plasmon-Mediated Reduction of CO_2 to Chemicals and Fuels," *Advanced Materials Interfaces* 9 (2022): 1–24.

53. S. Mukherjee, F. Libisch, N. Large, et al., "Hot Electrons Do the Impossible: Plasmon-Induced Dissociation of H_2 on au," *Nano Letters* 13 (2012): 240–247.

54. H. Robatjazi, J. L. Bao, M. Zhang, et al., "Plasmon-Driven Carbon-Fluorine ($C(Sp^3)$-F) Bond Activation With Mechanistic Insights Into Hot-Carrier-Mediated Pathways," *Nature Catalysis* 3 (2020): 564–573.

55. V. A. Spata and E. A. Carter, "Mechanistic Insights Into Photocatalyzed Hydrogen Desorption From Palladium Surfaces Assisted by Localized Surface Plasmon Resonances," *ACS Nano* 12 (2018): 3512–3522.

56. D. F. Swearer, H. Robatjazi, J. M. P. Martirez, et al., "Plasmonic Photocatalysis of Nitrous Oxide Into N_2 Using Aluminum–Iridium Antenna–Reactor Nanoparticles," *ACS Nano* 13 (2019): 8076–8086.

57. D. F. Swearer, H. Zhao, L. Zhou, et al., "Heterometallic Antenna-Reactor Complexes for Photocatalysis," *Proceedings. National Academy of Sciences. United States of America* 113 (2016b): 8916–8920.

58. L. Zhou, Q. Huang, and Y. Xia, "Plasmon-Induced Hot Electrons in Nanostructured Materials: Generation, Collection, and Application to Photochemistry," *Chemical Reviews* 124 (2024): 8597.

59. L. Zhou, M. Lou, J. L. Bao, et al., "Hot Carrier Multiplication in Plasmonic Photocatalysis," *Proceedings of the National Academy of Sciences* 118 (2021): e2022109118.

60. L. Zhou, D. F. Swearer, C. Zhang, et al., "Quantifying Hot Carrier and Thermal Contributions in Plasmonic Photocatalysis," *Science* 362 (2018): 69–72.

61. L. Zhou, J. M. P. Martirez, J. Finzel, et al., "Light-Driven Methane Dry Reforming With Single Atomic Site Antenna-Reactor Plasmonic Photocatalysts," *Nature Energy* 5 (2020): 61–70, https://OPTOPTdoi.org/10.1038/s41560-019-0517-9.

62. Z. Li and D. Kurouski, "Plasmon-Driven Chemistry on Mono-and Bimetallic Nanostructures," *Accounts of Chemical Research* 54 (2021): 2477.

63. Z. Zheng, T. Tachikawa, and T. Majima, "Plasmon-Enhanced Formic Acid Dehydrogenation Using Anisotropic Pd–Au Nanorods Studied at the Single-Particle Level," *Journal of the American Chemical Society* 137 (2015): 948.

64. G. Dall'Osto, M. Vanzan, S. Corni, and M. M. E. Coccia, "Stochastic Schrödinger Equation for Hot-Carrier Dynamics in Plasmonic Systems," *Journal of Chemical Physics* 161 (2024): 124103.

65. G. Dall'Osto, M. Marsili, M. Vanzan, et al., "Peeking Into the Femtosecond Hot-Carrier Dynamics Reveals Unexpected Mechanisms in Plasmonic Photocatalysis," *Journal of the American Chemical Society* 146 (2024): 2208.

66. L. Biancorosso, P. D'Antoni, S. Corni, M. Stener, and E. Coccia, "Time-Dependent Quantum/Continuum Modeling of Plasmon-Enhanced Electronic Circular Dichroism," *Journal of Chemical Physics* 161 (2024): 214104.

67. E. Coccia and S. Corni, "Role of Coherence in the Plasmonic Control of Molecular Absorption," *Journal of Chemical Physics* 151 (2019): 044703.

68. M. Monti, M. Stener, and M. Aschi, "A Computational Approach for Modeling Electronic Circular Dichroism of Solvated Chromophores," *Journal of Computational Chemistry* 43 (2022): 2023.

69. S. Pipolo and S. Corni, "Real-Time Description of the Electronic Dynamics for a Molecule Close to a Plasmonic Nanoparticle," *Journal of Physical Chemistry C* 120 (2016): 28774.

70. M. Monti, M. Stener, and E. Coccia, "Electronic Circular Dichroism From Real-Time Propagation in State Space," *Journal of Chemical Physics* 158 (2023): 084102.

71. F. Ding, E. B. Guidez, C. M. Aikens, and X. Li, "Quantum Coherent Plasmon in Silver Nanowires: A Real-Time Tddft Study," *Journal of Chemical Physics* 140 (2014): 244705–244712.

72. G. Donati, D. B. Lingerfelt, C. M. Aikens, and X. Li, "Molecular Vibration Induced Plasmon Decay," *Journal of Physical Chemistry C* 121 (2017): 15368–15374.

73. "Anisotropic Polarizability-Induced Plasmon Transfer," *Journal of Physical Chemistry C* 122 (2018): 10621–10626.

74. G. U. Kuda-Singappulige, D. B. Lingerfelt, X. Li, and C. M. Aikens, "Ultrafast Nonlinear Plasmon Decay Processes in Silver Nanoclusters," *Journal of Physical Chemistry C* 124 (2020): 20477–20487.

75. R. Rüger, E. van Lenthe, T. Heine, and L. Visscher, "Tight-Binding Approximations to Time-Dependent Density Functional Theory - a Fast Approach for the Calculation of Electronically Excited States," *Journal of Chemical Physics* 144 (2016): 184103.

76. P. Hoerner, M. K. Lee, and B. Schlegel, "Angular Dependence of Strong Field Ionization of N_2 by Time-Dependent Configuration Interaction Using Density Functional Theory and the Tamm-Dancoff Approximation," *Journal of Chemical Physics* 151 (2019a): 054201.

77. R. Rüger, M. Franchini, T. Trnka, et al., *Ams 2022.1, Scm, Theoretical Chemistry*, (2022), http://www.scm.com.

78. P. Grobas Illobre, M. Marsili, S. Corni, M. Stener, D. Toffoli, and E. Coccia, "Time-Resolved Excited-State Analysis of Molecular Electron

Dynamics by Tddft and Bethe–Salpeter Equation Formalisms," *Journal of Chemical Theory and Computation* 17 (2021): 6314.

79. P. E. Blöchl, "Projector Augmented-Wave Method," *Physical Review B* 50 (1994): 17953.

80. J. Hafner, "Ab-Initio Simulations of Materials Using Vasp: Density-Functional Theory and Beyond," *Journal of Computational Chemistry* 29 (2008): 2044.

81. J. P. Perdew, K. Burke, and M. Ernzerhof, "Generalized Gradient Approximation Made Simple," *Physical Review Letters* 77 (1996): 3865.

82. S. Grimme, "Accurate Description of Van der Waals Complexes by Density Functional Theory Including Empirical Corrections," *Journal of Computational Chemistry* 25 (2004): 1463.

83. M. Methfessel and A. Paxton, "High-Precision Sampling for Brillouin-Zone Integration in Metals," *Physical Review B* 40 (1989): 3616.

84. H. J. Monkhorst and J. D. Pack, "Special Points for Brillouin-Zone Integrations," *Physical Review B* 13 (1976): 5188.

85. Q. Luo, G. Feng, M. Beller, and H. Jiao, "Formic Acid Dehydrogenation on Ni (111) and Comparison With Pd (111) and Pt (111)," *Journal of Physical Chemistry C* 116 (2012): 4149.

86. E. Coccia, J. Fregoni, C. A. Guido, M. Marsili, and S. Corni, "Hybrid Theoretical Models for Molecular Nanoplasmonics," *Journal of Chemical Physics* 153 (2020): 200901.

87. B. Hammer, L. B. Hansen, and J. K. Nørskov, "Improved Adsorption Energetics Within Density-Functional Theory Using Revised Perdew-Burke-Ernzerhof Functionals," *Physical Review B* 59 (1999): 7413.

88. M. E. Casida, "Time-Dependent Density Functional Response Theory for Molecules," in *Recent Advances in Density Functional Methods*, vol. Part I (World Scientific, 1995), 155–192.

89. G. Dall'Osto and S. Corni, "Time Resolved Raman Scattering of Molecules: A Quantum Mechanics Approach With Stochastic Schroedinger Equation," *Journal of Physical Chemistry. A* 126 (2022): 8088.

90. E. Luppi and M. Head-Gordon, "Computation High-Harmonic Generation Spectra H_2 and N_2 in Intense Laser Pulses Using Quantum Chemistry Methods and Time-Dependent Density Functional Theory," *Molecular Physics* 110 (2012): 909.

91. C. F. Pauletti, E. Coccia, and E. Luppi, "Role of Exchange and Correlation in High-Harmonic Generation Spectra of H_2, N_2, and CO_2: Real-Time Time-Dependent Electronic-Structure Approaches," *Journal of Chemical Physics* 154 (2021): 014101.

92. E. Tapavicza, I. Tavernelli, and U. Rothlisberger, "Trajectory Surface Hopping Within Linear Response Time-Dependent Density-Functional Theory," *Physical Review Letters* 98 (2007): 023001.

93. E. Tapavicza, I. Tavernelli, U. Rothlisberger, C. Filippi, and M. E. Casida, "Mixed Time-Dependent Density-Functional Theory/Classical Trajectory Surface Hopping Study of Oxirane Photochemistry," *Journal of Chemical Physics* 129 (2008): 124108.

Supporting Information

Additional supporting information can be found online in the Supporting Information section.

Supporting Information of "Study of the photoinduced charge injection in the reaction intermediate of the dehydrogenation of formic acid on palladium"

L. Biancorosso[1] and E. Coccia[1, a)]

Dipartimento di Scienze Chimiche e Farmaceutiche, Università di Trieste, via L. Giorgieri 1, 34127, Trieste, Italy

(Dated: 6 March 2025)

[a)]Electronic mail: ecoccia@units.it

2L3 Cartesian Coordinates (Å)

Pd 20.18687 5.43823 2.29461
Pd 21.52310 7.77654 2.33418
Pd 22.87753 10.10346 2.31024
Pd 14.79856 5.44551 2.29707
Pd 16.14919 7.77636 2.32525
Pd 17.48698 10.10152 2.32705
Pd 17.48831 5.43919 2.29520
Pd 18.83717 7.77355 2.31898
Pd 20.18622 10.09607 2.34379
Pd 20.18573 8.53739 4.72623
Pd 21.56223 10.89762 4.64912
Pd 18.84032 6.21292 4.58033
Pd 22.87430 8.55204 4.61971
Pd 24.21889 10.89466 4.62662
Pd 21.53419 6.22063 4.61695
Pd 17.47678 8.55372 4.66778
Pd 18.81765 10.90645 4.63550
Pd 16.14256 6.21964 4.60739
C 18.72573 8.30817 7.35710
O 17.60863 8.50129 6.77983
O 19.88217 8.17731 6.85923
H 18.66924 8.24703 8.46262
H 20.19139 10.38844 5.55268

3L3 Cartesian Coordinates (Å)

Pd 20.18397 6.99194 0.00000
Pd 21.52957 9.32259 0.00000
Pd 18.83837 4.66129 0.00000
Pd 14.80158 6.99194 0.00000
Pd 16.14717 9.32259 0.00000
Pd 13.45598 4.66129 0.00000

Pd 17.49278 6.99194 0.00000
Pd 18.83837 9.32259 0.00000
Pd 16.14718 4.66129 0.00000
Pd 20.18687 5.43823 2.29461
Pd 21.52310 7.77654 2.33418
Pd 22.87753 10.10346 2.31024
Pd 14.79856 5.44551 2.29707
Pd 16.14919 7.77636 2.32525
Pd 17.48698 10.10152 2.32705
Pd 17.48831 5.43919 2.29520
Pd 18.83717 7.77355 2.31898
Pd 20.18622 10.09607 2.34379
Pd 20.18573 8.53739 4.72623
Pd 21.56223 10.89762 4.64912
Pd 18.84032 6.21292 4.58033
Pd 22.87430 8.55204 4.61971
Pd 24.21889 10.89466 4.62662
Pd 21.53419 6.22063 4.61695
Pd 17.47678 8.55372 4.66778
Pd 18.81765 10.90645 4.63550
Pd 16.14256 6.21964 4.60739
C 18.72573 8.30817 7.35710
O 17.60863 8.50129 6.77983
O 19.88217 8.17731 6.85923
H 18.66924 8.24703 8.46262
H 20.19139 10.38844 5.55268

2L4 Cartesian Coordinates

Pd 12.113285 5.438224 2.294608
Pd 16.150080 12.430161 2.294608
Pd 20.186874 5.438225 2.294608
Pd 24.223669 12.430162 2.294608

Pd 13.449510 7.776541 2.334179
Pd 21.523100 7.776542 2.334179
Pd 14.803942 10.103462 2.310241
Pd 22.877531 10.103463 2.310241
Pd 14.798557 5.445513 2.297070
Pd 18.835352 12.437450 2.297070
Pd 16.149195 7.776364 2.325246
Pd 17.486977 10.101517 2.327051
Pd 17.488312 5.439194 2.295195
Pd 21.525107 12.431130 2.295195
Pd 18.837171 7.773547 2.318975
Pd 20.186215 10.096067 2.343794
Pd 20.185733 8.537391 4.726230
Pd 21.562227 10.897619 4.649117
Pd 18.840324 6.212923 4.580329
Pd 22.877120 13.204860 4.580329
Pd 14.800712 8.552035 4.619706
Pd 22.874302 8.552036 4.619706
Pd 16.145299 10.894657 4.626615
Pd 24.218888 10.894659 4.626615
Pd 13.460604 6.220634 4.616947
Pd 17.497399 13.212570 4.616947
Pd 21.534193 6.220635 4.616947
Pd 25.570989 13.212571 4.616947
Pd 17.476777 8.553720 4.667777
Pd 18.817653 10.906448 4.635504
Pd 16.142561 6.219642 4.607392
Pd 20.179356 13.211578 4.607392
C 18.725727 8.308168 7.357103
O 17.608634 8.501294 6.779830
O 19.882169 8.177310 6.859234
H 18.669235 8.247030 8.462624

H 20.191394 10.388443 5.552682

Bond Pair	Distance (Å)	Distance (Å) from Ref. [81]
Pd1-H1	1.719	1.748
Pd2-H1	2.027	1.878
Pd3-H1	1.731	1.765
Pd2-O1	2.184	2.195
Pd4-O2	2.117	2.133
C-O1	1.266	1.266
C-O2	1.272	1.272
C-H2	1.109	1.111

TABLE S1: Bond distances among Pd atoms and those from HCOO, and H.

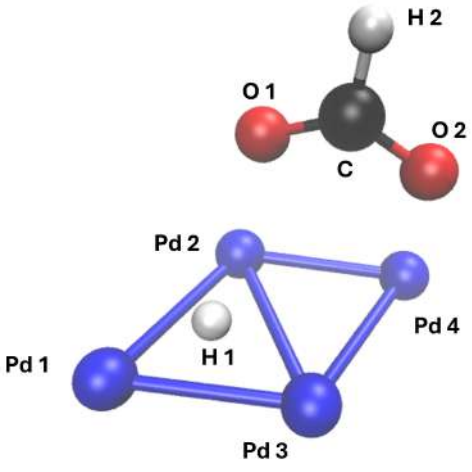

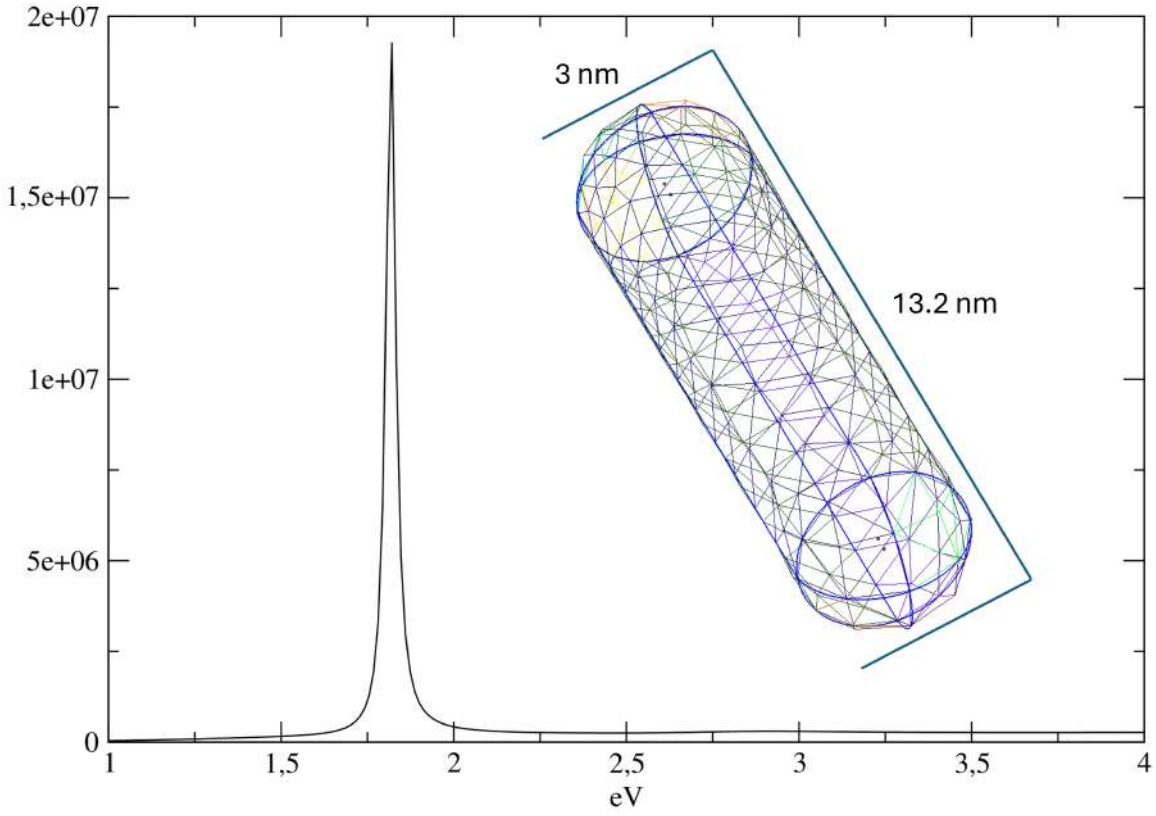

FIG. S1: Absorption spectrum of the Au nanorod of 13 nm full length and 3 nm diameter. An inhomogeneous mesh size was used in the BEM calculation with a total of 504 triangular tesserae. A denser mesh wash used on one of the caps of the nanorod. Gold dielectric function fitted with a sum of Drude-Lorentz terms was used, taken from Ref. 1.

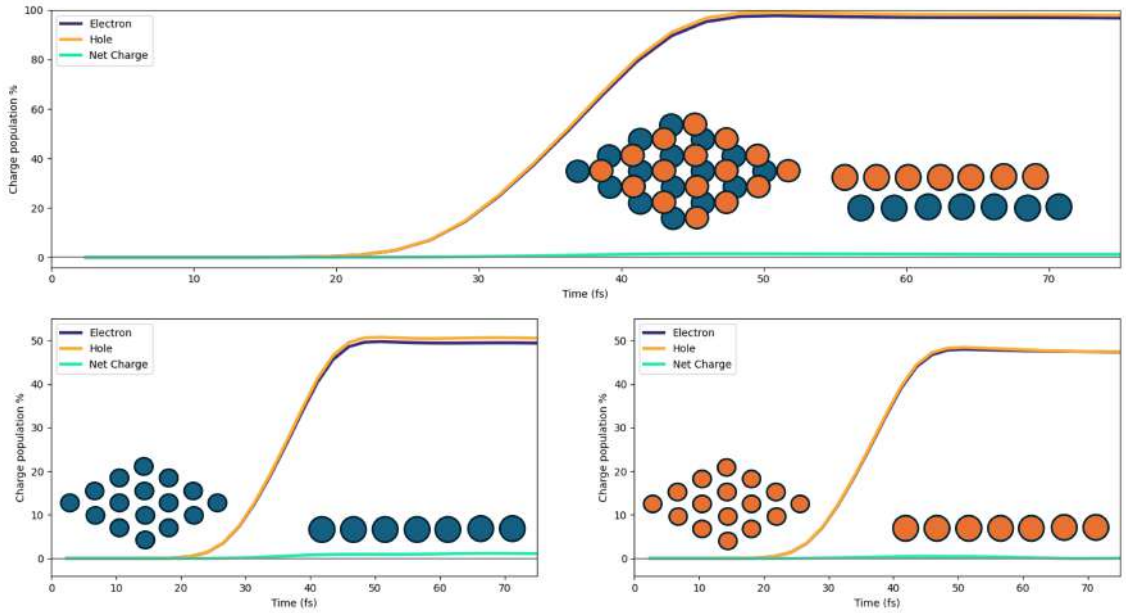

FIG. S2: Upper panel: time evolution of the photoinduced charge populations (electron, hole and net) in the 2L4 system with P1 pulse for the Pd cluster. Bottom panel: time evolution of the photoinduced charge populations (electron, hole and net) of the two lower layers (left) and of the upper layer (right) of Pd atoms.

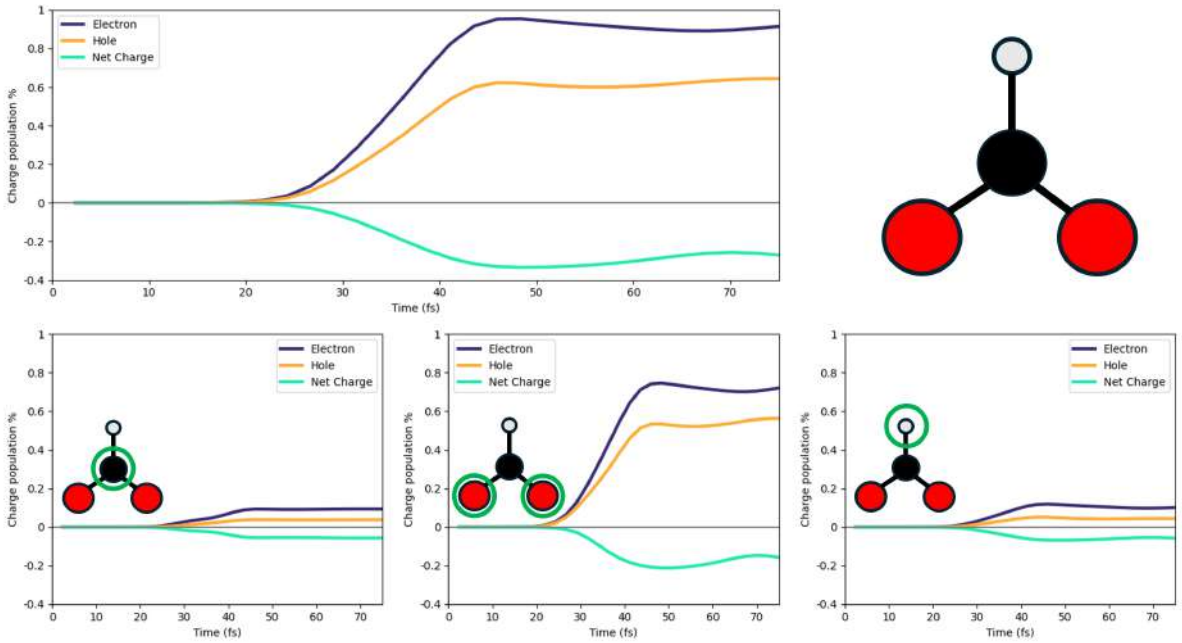

FIG. S3: Upper panel: time-evolution of the photoinduced charge populations (electron, hole and net) of the HCOO moiety in the 2L4 system with P1 pulse. Bottom panel: on the left, time-evolution of the photoinduced charge populations (electron, hole and net) of the carbon atom; in the middle, the same for the oxygen atoms; on the right, the same for the hydrogen atom of HCOO.

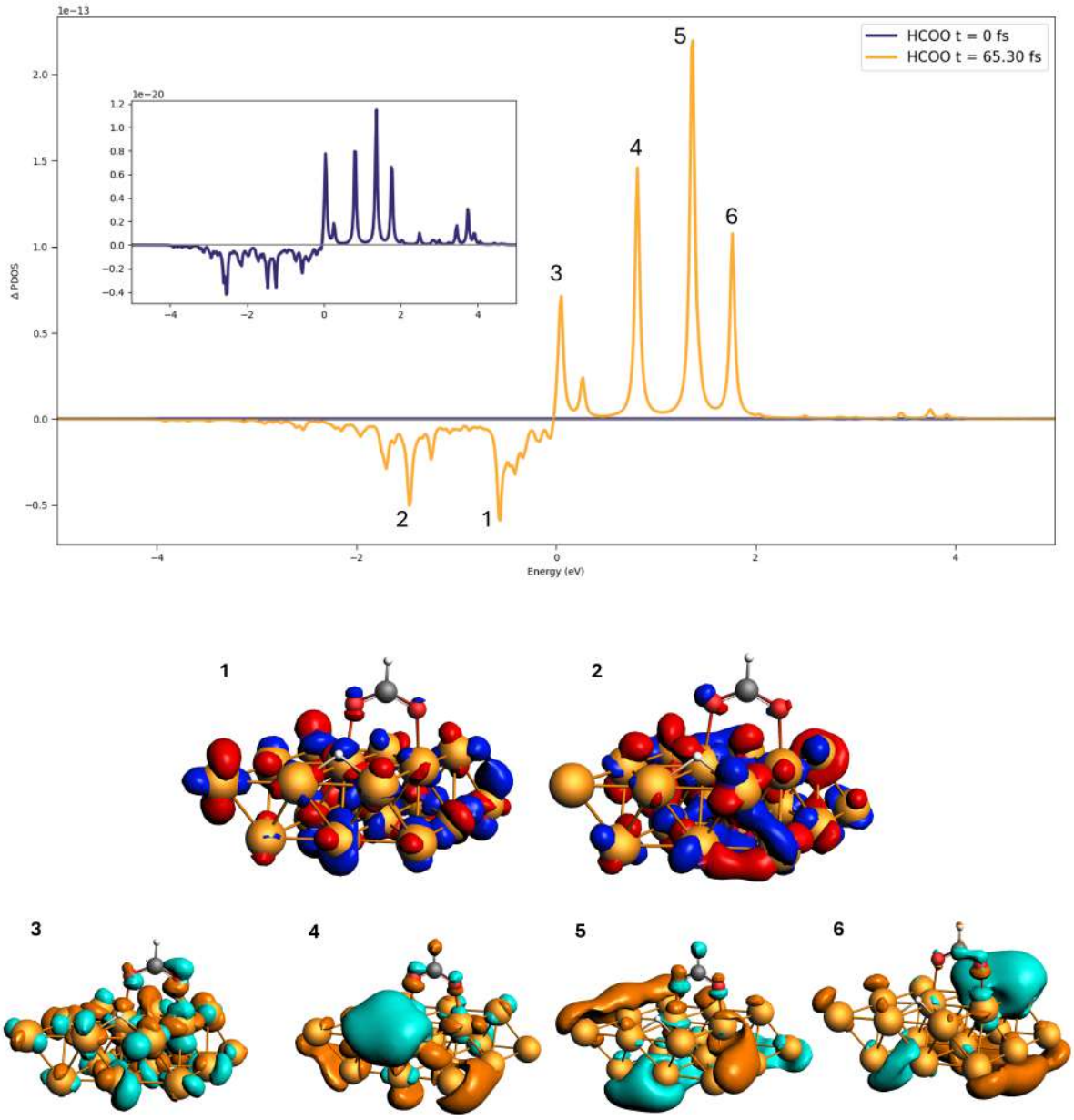

FIG. S4: ΔPDOS of HCOO before (blue line) and after the pulse (yellow line) for the 2L3 system with the P1 pulse. Occupied and virtual orbitals involved in the dynamics are also shown.

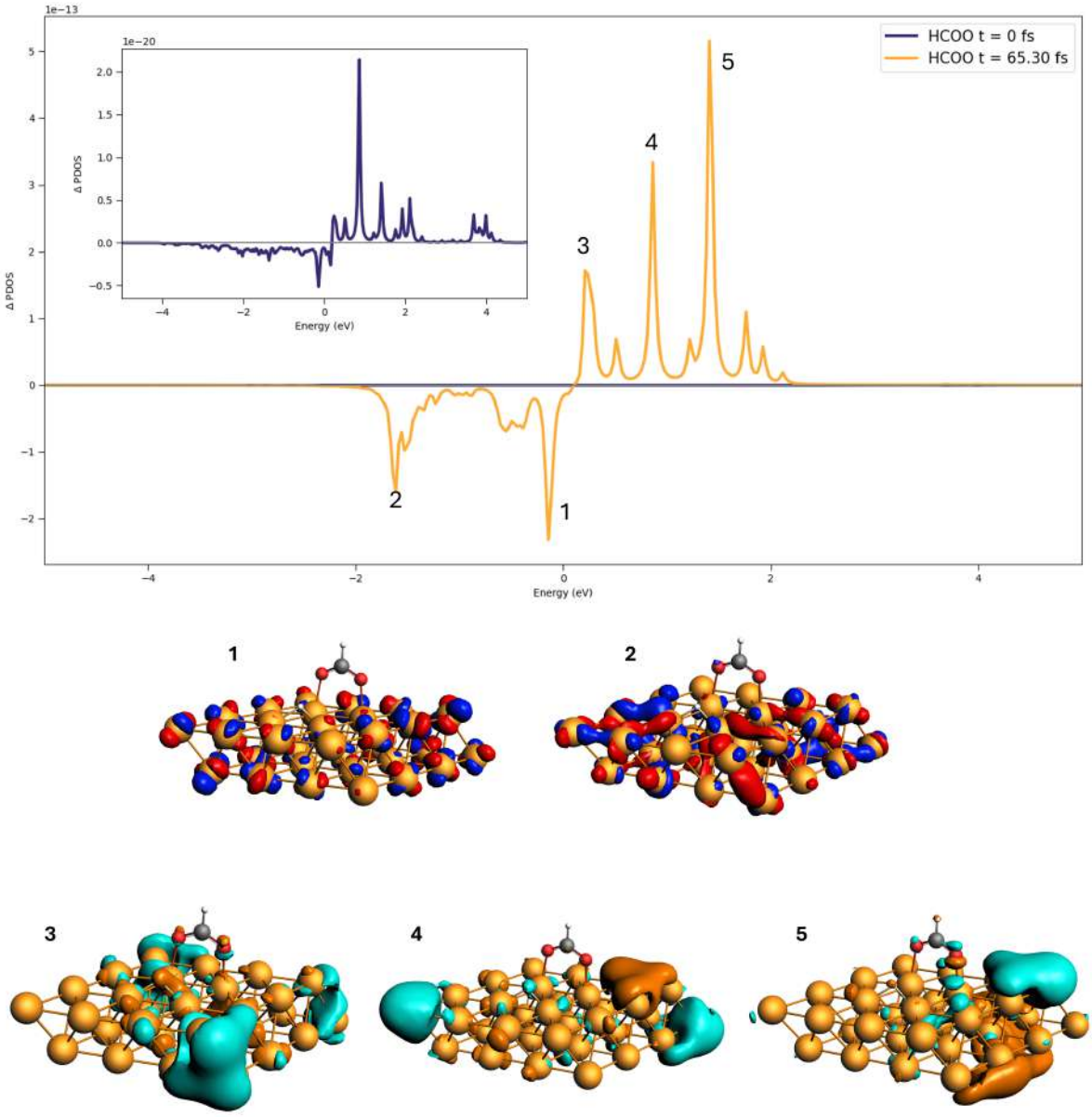

FIG. S5: ΔPDOS of HCOO before (blue line) and after the pulse (yellow line) for the 2L4 system with the P1 pulse. Occupied and virtual orbitals involved in the dynamics are also shown.

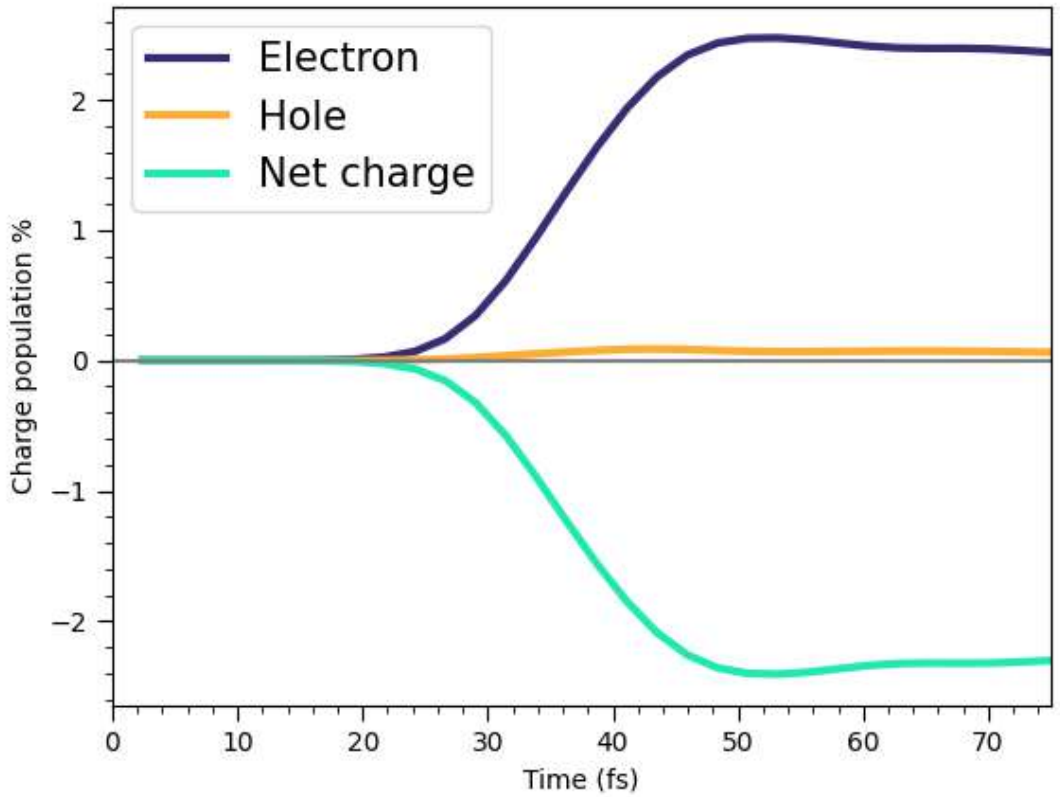

FIG. S6: Time-evolution of the photoinduced charge populations (electron, hole and net) of the H atom adsorbed on the Pd surface in the 2L3 system with P1 pulse.

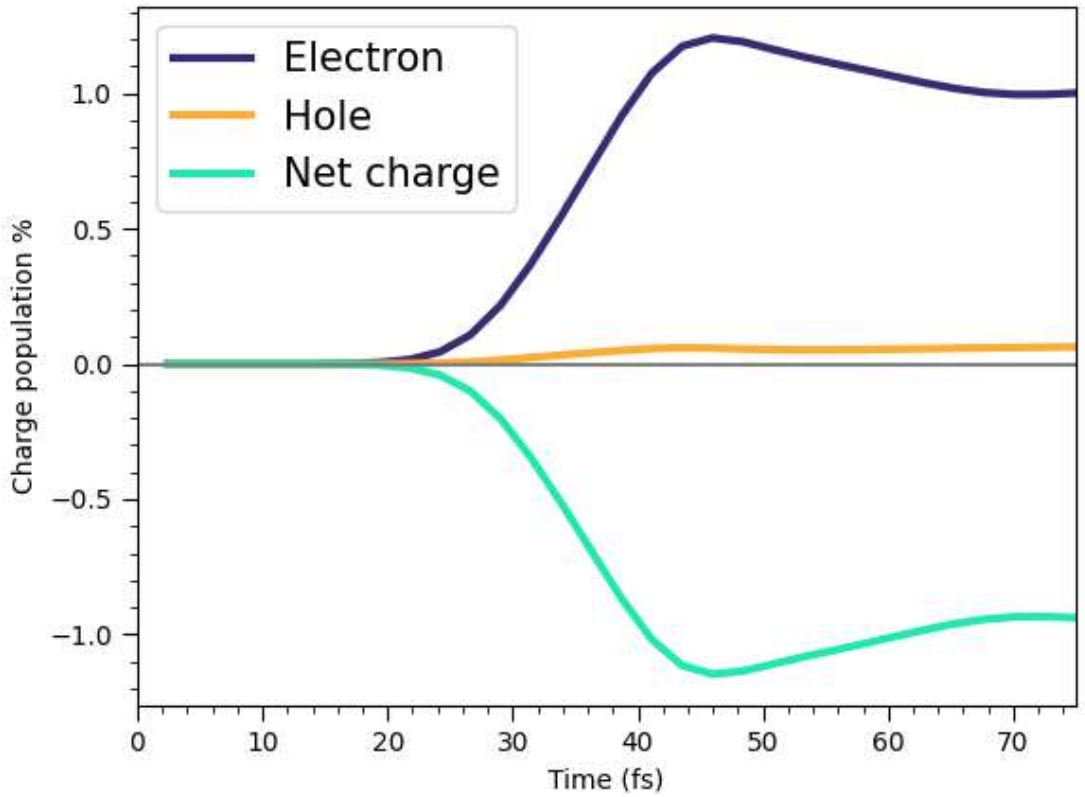

FIG. S7: Time-evolution of the photoinduced charge populations (electron, hole and net) of the H atom adsorbed on the Pd surface in the 2L4 system with P1 pulse.

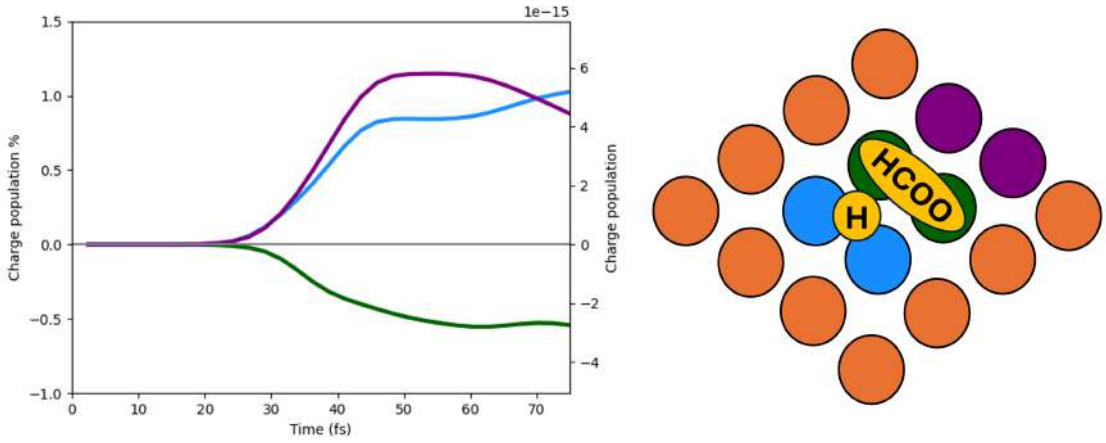

FIG. S8: Time-evolution of the photoinduced net charge population of the Pd atoms of the upper layer in the 2L4 system with P1 pulse. Green: Pd pairs interacting with HCOO. Blue: Pd pairs interacting with H. Purple: Pd pairs not interacting with any molecular species.

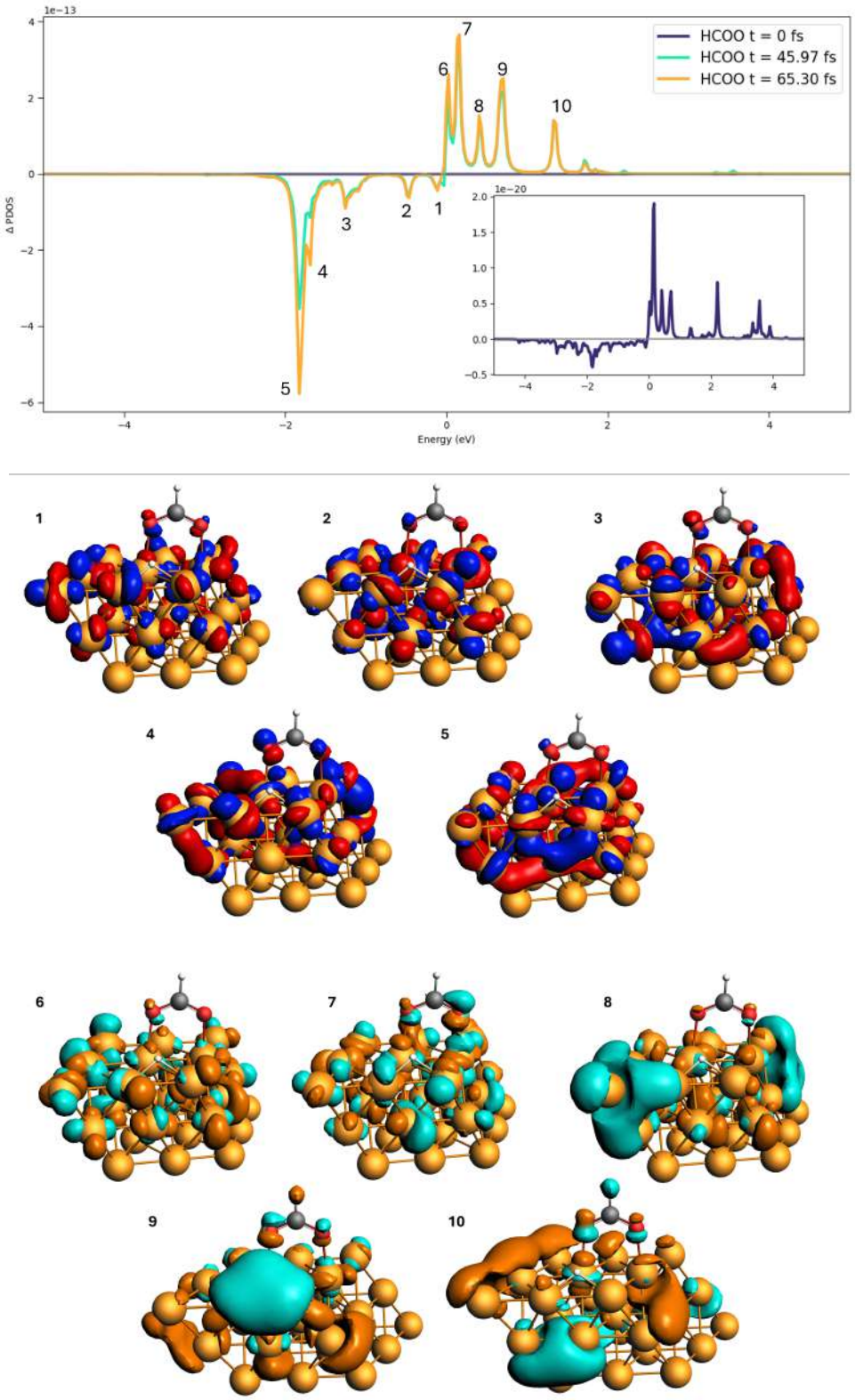

FIG. S9: ΔPDOS of the formate fragment before (blue line) and after the pulse (yellow line) for the 3L3 system with the P1 pulse. The involved occupied and virtual orbitals are also shown.

Orbitals	**ΔPDOS(t=65.50 fs)/ΔPDOS(t=45.97 fs)**
1	1.21
2	1.11
3	1.03
4	2.09
5	1.63
6	1.37
7	1.12
8	1.16
9	1.16
10	1.00

TABLE S2: Ratio between ΔPDOS at 65.50 fs and at 45.97 fs for 2L3 molecular orbitals.

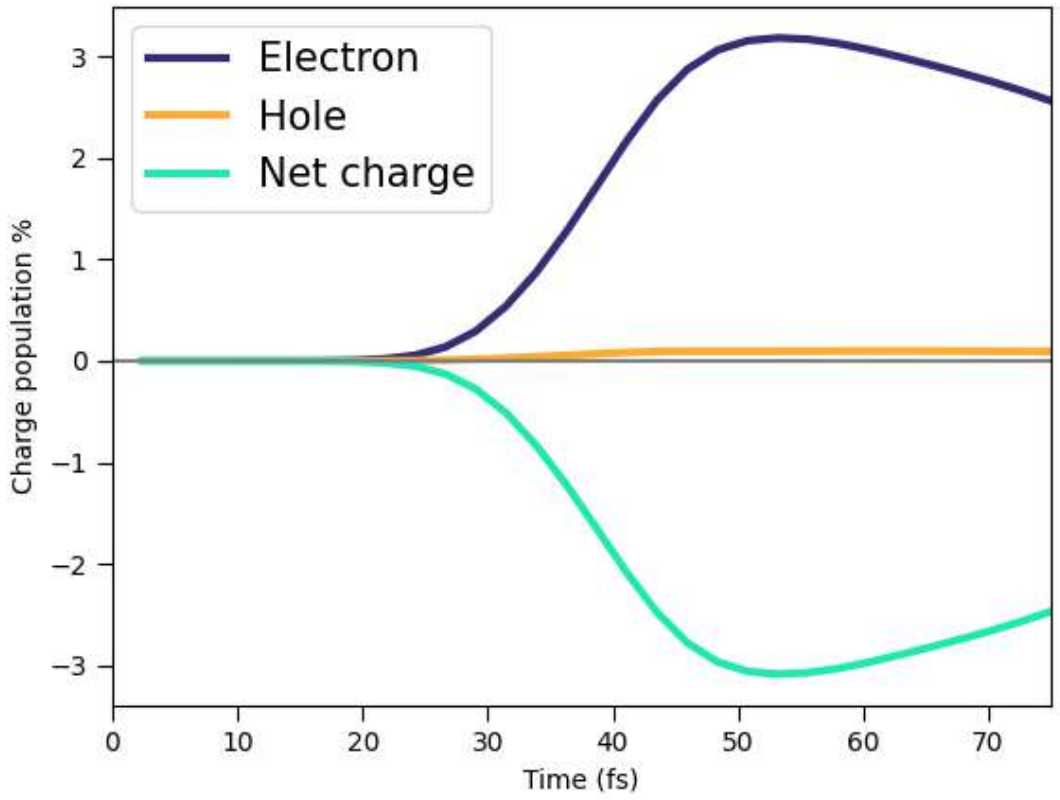

FIG. S10: Time-evolution of the photoinduced charge populations (electron, hole and net) of the H atom adsorbed on the Pd surface in the 3L3 system with P1 pulse.

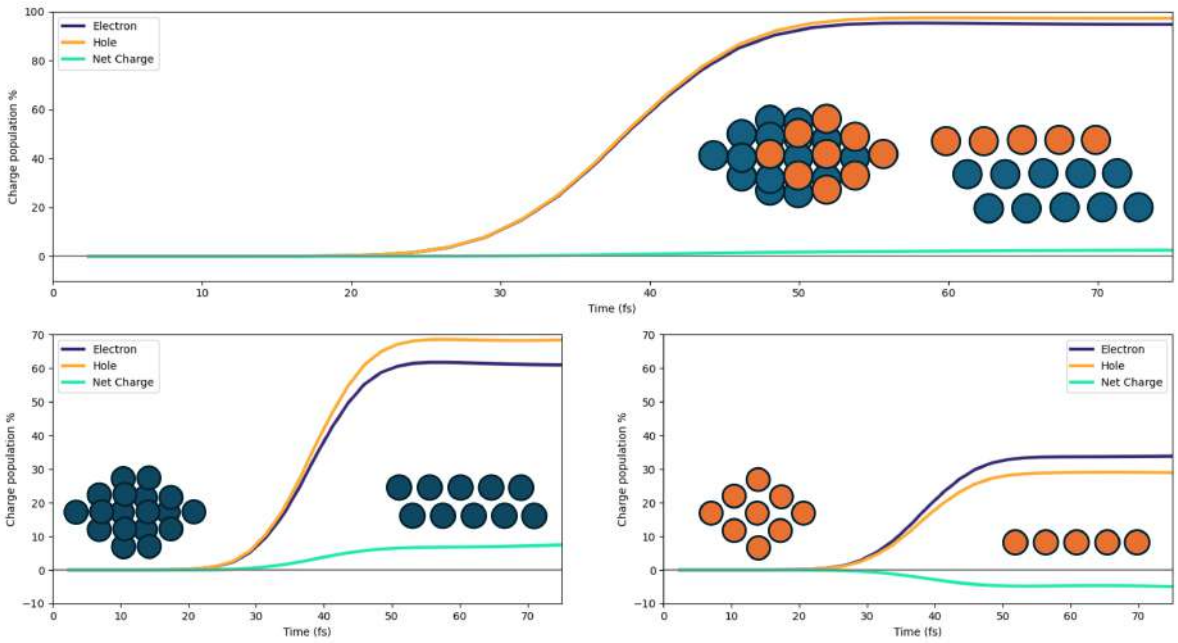

FIG. S11: Upper panel: time-evolution of the photoinduced charge populations (electron, hole and net) of the Pd cluster in the 3L3 system with P2 pulse. Bottom panel: time-evolution of the photoinduced charge populations (electron, hole and net) of the lower layers (left) and of the upper layer (right).

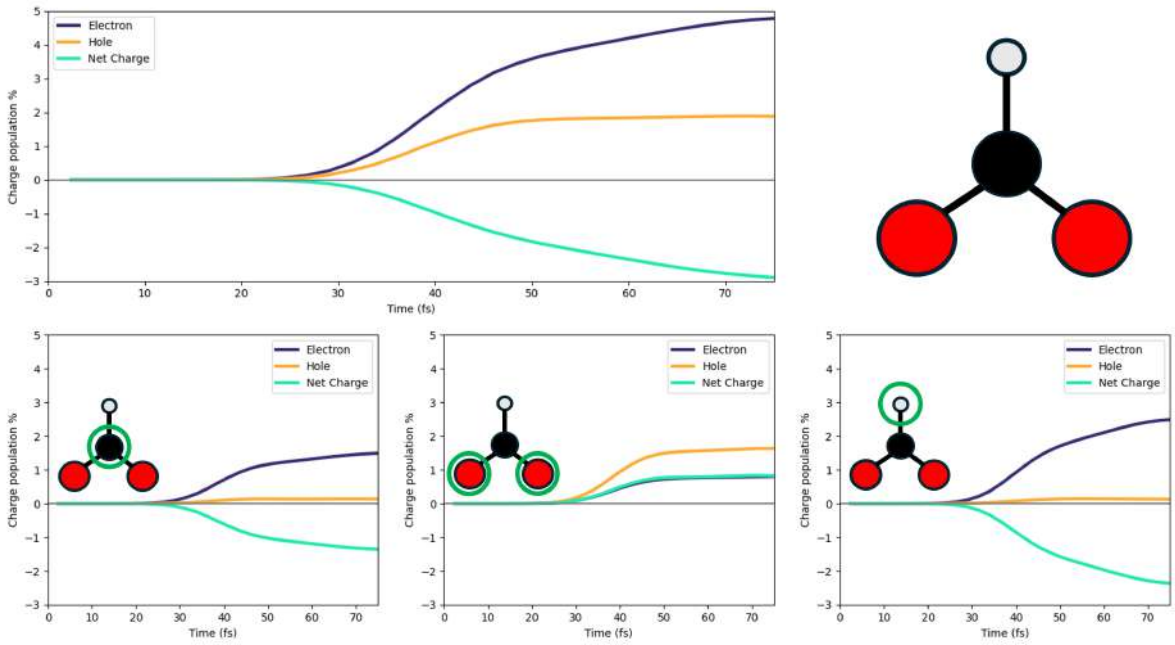

FIG. S12: Upper panel: time-evolution of the photoinduced charge populations (electron, hole and net) of the HCOO fragment in the 3L3 system with P2 pulse. Bottom panel: on the left, time-evolution of the photoinduced charge populations (electron, hole and net) of the carbon atom; in the middle, the same for the oxygen atoms; on the right, the same for the hydrogen atom of HCOO.

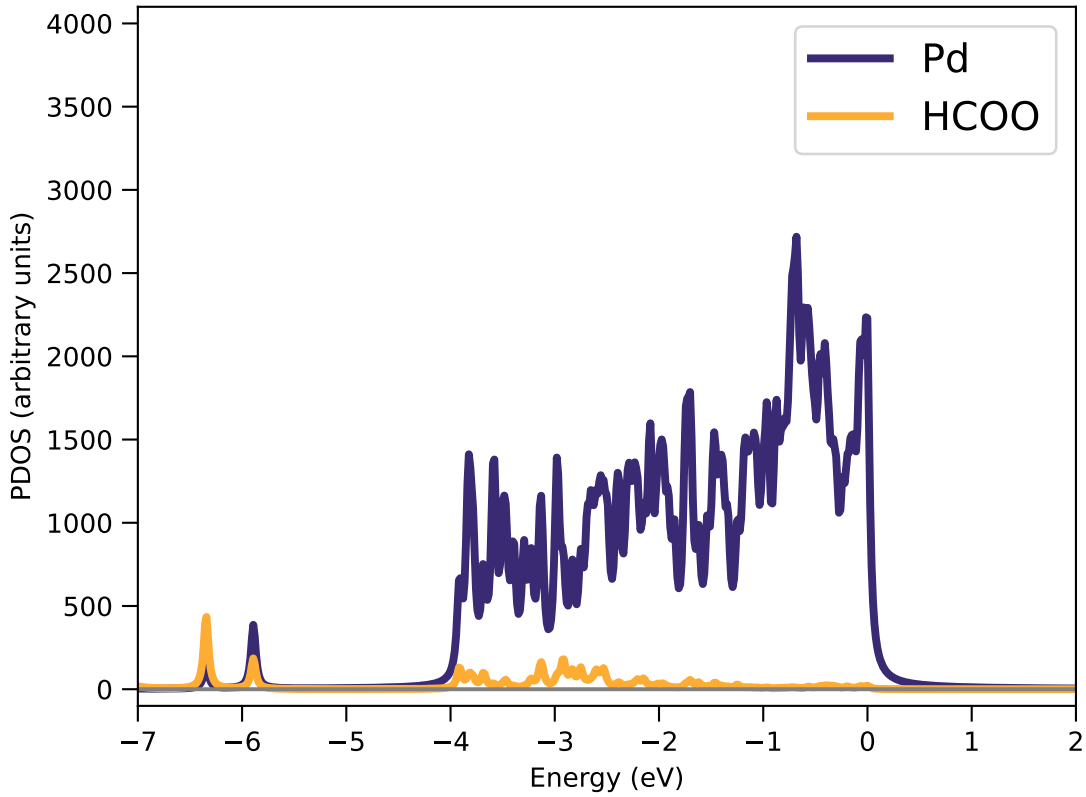

FIG. S13: PDOS of the 2L3 system. PDOS of the Pd atoms is in blue, the PDOS of the HCOO is in yellow.

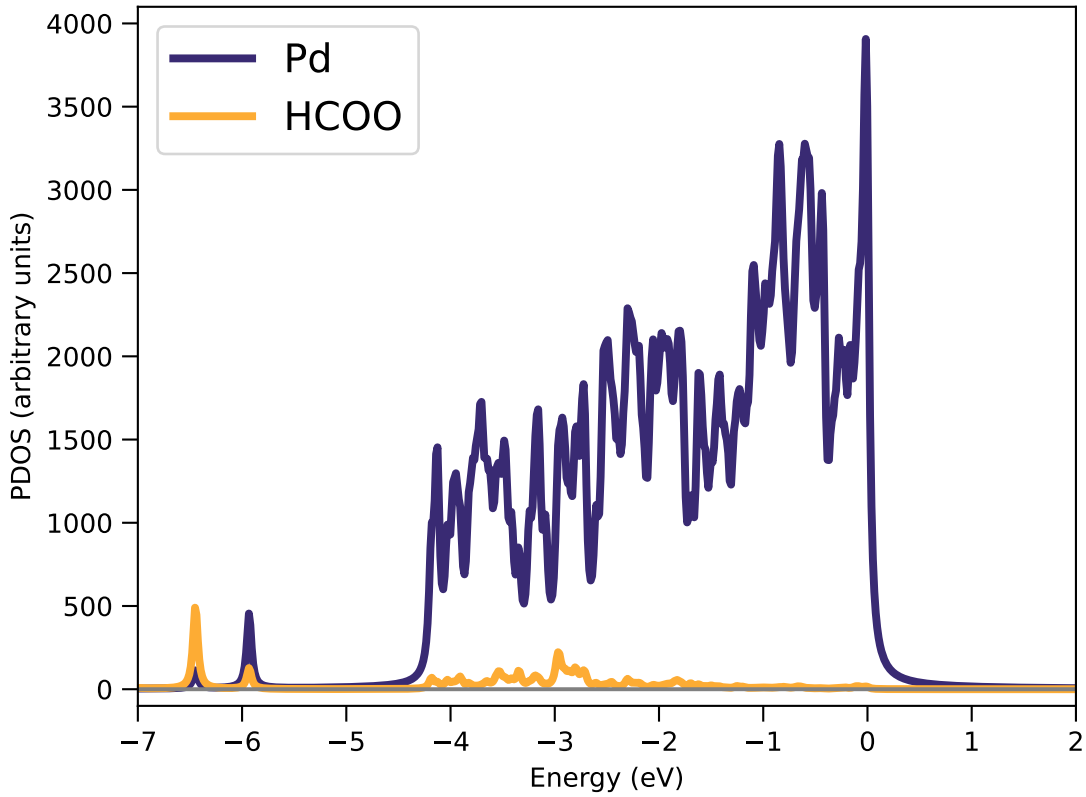

FIG. S14: PDOS of the 3L3 system. PDOS of the Pd atoms is in blue, the PDOS of the HCOO is in yellow.

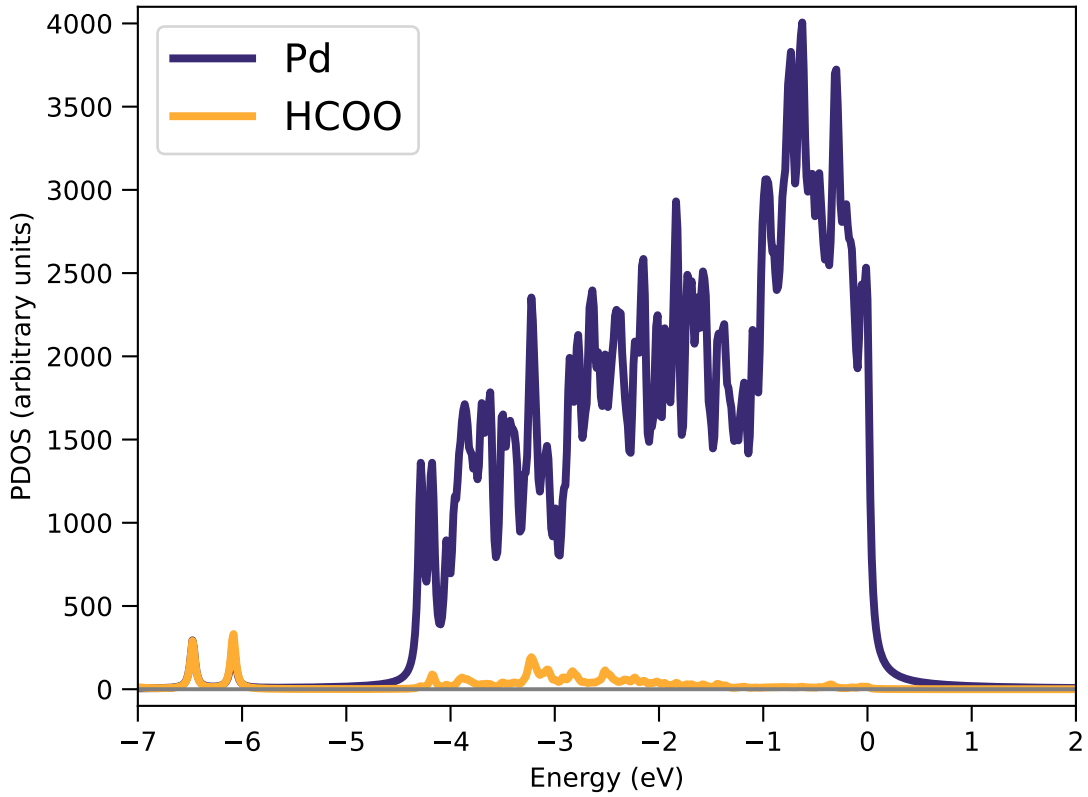

FIG. S15: PDOS of the 2L4 system. PDOS of the Pd atoms is in blue, the PDOS of the HCOO is in yellow.

	2L3	3L3	2L4
C	0.361	0.357	0.357
O	-0.563	-0.556	-0.558
O	-0.545	-0.545	-0.541
H	0.270	0.289	0.272
Tot	-0.477	-0.455	-0.470
H_{ads}	0.031	0.013	-0.033

TABLE S3: Ground-state Mulliken charges for HCOO and H in 2L3, 3L3 and 2L4.

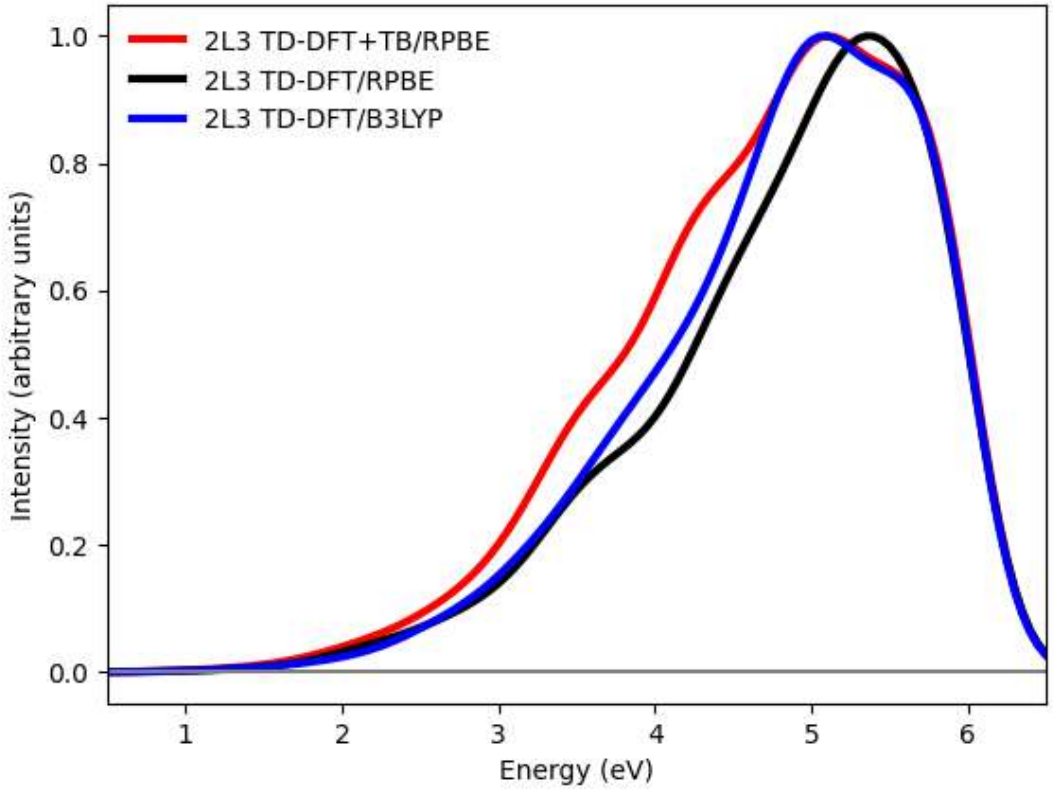

FIG. S16: Absorption spectrum for 2L3 at TD-DFT+TB/RPBE, TDDFT/RPBE and TDDFT/B3LYP level of theory.

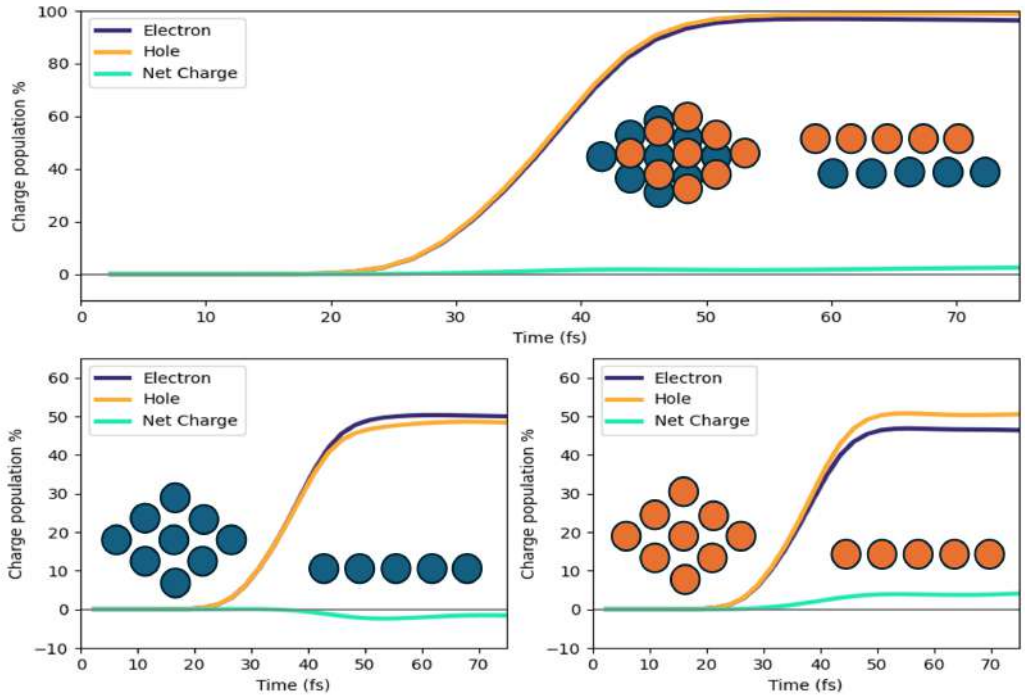

FIG. S17: Time-dependent charge population of the Pd layers for the 2L3 system, using TD-DDFT/B3LYP.

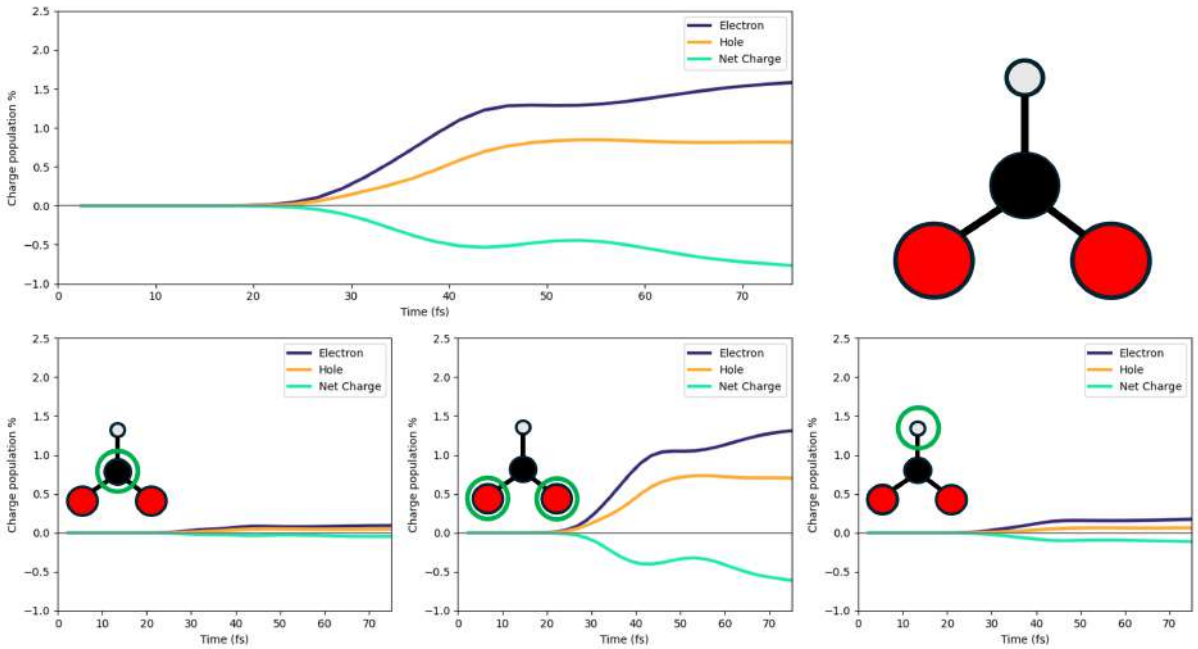

FIG. S18: Time-dependent charge population of HCOO for the 2L3 system, using TD-DDFT/B3LYP.

REFERENCES

[1]G. Dall'Osto, G. Gil, S. Pipolo, and S. Corni, J. Chem. Phys. **153**, 184114 (2020).

4.2 Role of the Au Nanorod

The results of the study, reported in the previous section, showed that when the catalytic system interacts with an external pulse resonant with the plasmonic frequency of a nanorod, an electron transfer process occurs from the Pd reactor to the adsorbed molecular system [66]. We also assessed the influence of slab topology and identified a stable structure suitable for further analysis.

Building on these findings, the present work expands the investigation to include an external gold nanorod, which is known experimentally to enhance both selectivity and hydrogen production. Our aim was to unravel the origin of this enhancement and to determine how the plasmonic nanorod modifies the electronic dynamics of the catalytic system. The simulations revealed that plasmonic excitations do not qualitatively alter the electron transfer process identified earlier but instead amplify it substantially, increasing the amount of injected charge by nearly three orders of magnitude. A similar enhancement was observed in surface charge heterogeneity, which is considered a key factor in promoting catalytic efficiency [132].

The decisive evidence for explaining the experimentally observed enhancement in the H_2 production rate emerged from the analysis of charge asymmetry in the oxygen atoms of $HCOO^*$. In the presence of plasmonic excitations, this intrinsic asymmetry is strongly amplified, driving the intermediate toward the next step of the catalytic cycle-namely, the transition from a bidentate bridge configuration to a monodentate adsorption of $HCOO^*$ on the Pd surface.

In this project, I carried out all simulations and analysis, and contributed to the interpretation of the results, the writing of the manuscript, and the final editing. The work has been recently published as Biancorosso, L., and E. Coccia. (2025) "Plasmon-enhanced asymmetry in the charge distribution explains the increased H_2 production rate from formic acid with a Pd-tipped Au nanorod", *J. Phys. Chem. Lett.* **16** p. 12931.

THE JOURNAL OF PHYSICAL CHEMISTRY LETTERS
A JOURNAL OF THE AMERICAN CHEMICAL SOCIETY

pubs.acs.org/JPCL
Letter

Plasmon-Enhanced Asymmetry in the Charge Distribution Explains the Increased H_2 Production Rate from Formic Acid with a Pd-Tipped Au Nanorod

Leonardo Biancorosso and Emanuele Coccia*

Cite This: *J. Phys. Chem. Lett.* 2025, 16, 12931−12938
Read Online

ABSTRACT: Plasmonic nanostructures offer a promising route to increase efficiency in photocatalysis. This study provides a microscopic explanation for the enhanced H_2 production rate from formic acid under plasmonic-resonance conditions of the photocatalytic reaction on a Pd-tipped Au nanorod (NR), observed experimentally. Using electron-dynamics multiscale simulations for a system composed of a classical Au NR and a DFT-described subsystem of Pd atoms and adsorbed reaction intermediates (bidentate HCOO* and H*) in the presence of a femtosecond pulse, we observe a net electron injection into HCOO*, which takes on the highest value in plasmon-resonance conditions. We find an asymmetry in the injection of electronic charge into the two oxygen atoms even in the absence of NR. The plasmonic field in resonant conditions significantly increases this asymmetry, thus representing the key to understanding the greater efficiency in H_2 generation, since the next reaction step is the formation of the monodentate HCOO*. Also, a greater spatial heterogeneity of the charge on the Pd surface has been found in the case of resonance with the NR plasmon, which can promote the advancement of the reactive process.

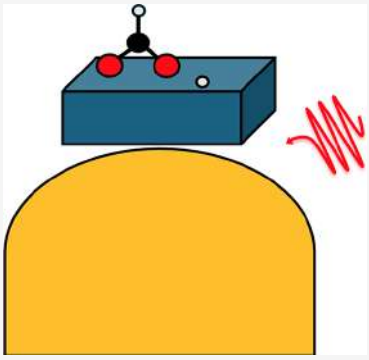

The search for alternatives to fossil fuel-based technologies has been one of the most prominent areas of research in recent decades.[1−3] One of the most compelling directions in this area involves hydrogen production and storage, which holds great promise for clean energy applications.[4−9] Plasmonic materials have successfully been exploited in photocatalysis through the concept of antenna−reactor complex, which has gained significant interest due to encouraging experimental and theoretical results.[10−16] This hybrid system, which combines the light-harvesting properties of plasmonic systems and the catalytic features of metals such as Pd and Pt, offers a powerful platform for light-assisted chemical transformations thereby opening new avenues for plasmon-assisted catalysis.[17−27]

In the context of hydrogen generation, formic acid has been extensively used as hydrogen-rich compound.[28] Herran et al. investigated various nanostructured configurations of palladium and Au, such as core−shell configurations and antenna−reactor assemblies, where small Pd particles are dispersed on the surface of a larger Au nanoparticle.[15] They observed a pronounced boost in H_2 production when the system was exposed to light, observing the best performance from antenna-reactor assemblies. Zheng and et al.[13] have highlighted the role of localized surface plasmon resonances (LSPRs) in the catalytic enhancement of this reaction. In that work, the authors employed a tipped Au nanorod (NR) to investigate the decomposition of formic acid in H_2. They observed a production rate of molecular hydrogen typically achieved at high temperature in thermal catalysis, highlighting a clear role of the plasmonic excitation of the NR.

By applying the same computational strategy recently adapted by some of us to explain the enhanced selectivity toward methane against carbon monoxide in the photocatalytic reduction of carbon dioxide in the presence of rhodium nanocubes,[10,29] in this work we provide a microscopic explanation of the enhanced H_2 production rate from formic acid in plasmonic-resonance conditions of the photocatalytic process on the tipped Au NR of ref 13. The analysis is based on the photo- and plasmon-induced charge injection into the stable reaction intermediate, i.e. the HCOO* moiety adsorbed with both oxygen atoms on the Pd surface.[30−38] According to minimum-energy path calculations,[30,32] the next step in the reaction is the formation of the monodentate HCOO* with only one oxygen adsorbed, which then leads to H_2 and CO_2. The key experimental quantity is the H_2 production rate,[13] which is enhanced in the presence of the gold NR and maximized at the NR plasmon frequency. In ref 13, the authors focus on the plasmonic near field to explain the observation without, however, proposing an atomistic description of the plasmon-

Received: September 15, 2025
Revised: November 20, 2025
Accepted: December 4, 2025

https://doi.org/10.1021/acs.jpclett.5c02858
J. Phys. Chem. Lett. 2025, 16, 12931−12938

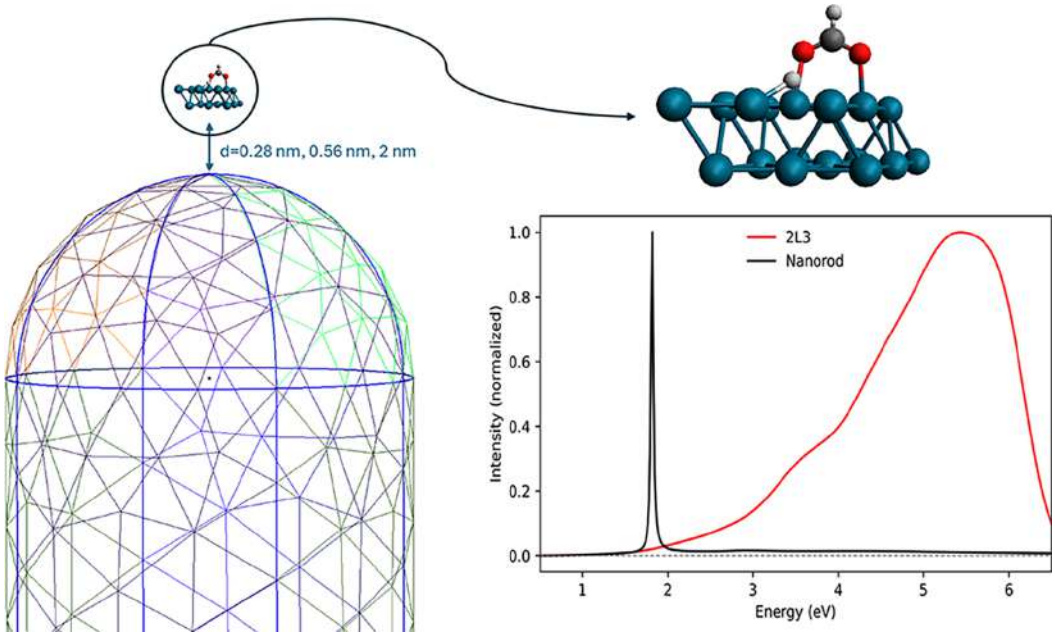

Figure 1. Multiscale model with a classical Au NR, and the QM subsystem. The normalized absorption spectra of the two subsystems are also reported.

mediated process. The idea behind our work is providing a direct link between the observed increase in H_2 production and the plasmonic effects that modify the charge injection in the bidentate HCOO*, thus making the reaction more efficient toward the products.

The antenna-reactor complex plus HCOO* and H* is modeled as the following: the Au NR is treated by means of the polarizable continuum model (PCM), the reactor is given by two 2×3 layers of Pd atoms (2L3, details are provided in ref 38), and HCOO* and H* are adsorbed on the outer Pd layer. An explicit first-principle (QM) representation of the electronic degrees of freedom of Pd atoms, HCOO* and H* is given. The simulated Au NR has a radius of 3 nm and a length of 13.2 nm. It has the same aspect ratio of the reference NR in ref 13. A sketch representation of the simulated system is found in Figure 1. The theoretical framework is formulated in time domain using the time-dependent Schrödinger Equation (TDSE, eqs. 1−3 of the Supporting Information) and the PCM model as well (TD-PCM-NP). The wavefunction of QM subsystem, i.e., Pd atoms + HCOO* + H*, $|\Psi(t)\rangle$ (eq. 4 of Supporting Information) is defined in terms of the eigenstates of an effective Hamiltonian which contains the field-free Hamiltonian and the ground-state polarization of the NR.[39] The NR surface is discretized in a set of N_T triangular tesserae, on which apparent charges are located.[40] The time evolution of these charges allows us to describe the polarization of the NR according to the boundary-element method,[40,41] and it takes into account the presence of the external pulse and of the time-dependent electronic density of the molecular system.[42,43] Even though our quantum model of the reactor is far from the experimental size, the Pd layer being 2-nm thick as shown in ref. [38], our recent study on the shape and size of Pd cluster allows us to consider the present results, specifically the sign of charge injection, as robust. Real-time calculations for electron/hole dynamics were carried out using the WaveT/TDPlas package,[17] interfaced with AMS[44] for extracting energies, electric transition dipole moments and electrostatic potential on the N_T tesserae,[38,45] computed using TD-DFT+TB[46] with the RPBE functional[47] combined with Grimme corrections within a singly excited ansatz (eq 5 of Supporting Information), and a double-ζ basis set. In our recent work,[38] we have shown that B3LYP provides the same physical information, i.e., an electron injection into HCOO*, thus providing additional control over the reliability of the current results. Using more refined approaches such as GW/BSE would be computationally too demanding, since 1808 electronic states have been computed and then propagated in this work.

In all simulations, the electric field was linearly polarized perpendicular to the Pd surface and parallel along the NR longitudinal axis. Two central frequencies for the pulse have been used: the plasmonic resonance of the NR at 1.82 eV (P1, Figure 1) and an off-resonant frequency at 3.0 eV (P2). The pulse peak intensity is equal to 10^2 W/cm^2, and a Gaussian envelope with a full width at half-maximum (FWHM) of 21 fs has been adopted, see eq. 6 of Supporting Information. This FWHM was chosen to approximate the effect of continuous-wave light with a coherence length of a few microns, consistent with experimental conditions.[10] The photoresponse is therefore in the linear regime. Details on our theoretical approach to plasmon-mediated photocatalysis, which has been already described elsewhere,[10,29,38] and on the computational strategy are provided in Supporting Information. All the simulations refer to a closed system, according to which electron dynamics is coherent. When the pulse is switched off, no other perturbation affects the electronic degrees of freedom. Effective approaches to account for charge relaxation and backtransfer could be used without an explicit nuclear dynamics.[29] The photocatalytic pathway has been assumed to be the same occurring in the thermal reaction.[10] Explicit nuclei were held fixed during the dynamics.

The selected distances between the Au NR and the bottom Pd layer of the QM subsystem (Figure 1) correspond to 0.28 nm, which is the sum of Au and Pd atomic radii,[48] 0.56 and 2 nm. This last value allows us to control the decrease in plasmonic effects on the QM subsystem.

The first aspect to be addressed is the nature of the charge injection into HCOO* from the Pd layers. In our recent work on

https://doi.org/10.1021/acs.jpclett.5c02858
J. Phys. Chem. Lett. 2025, 16, 12931−12938

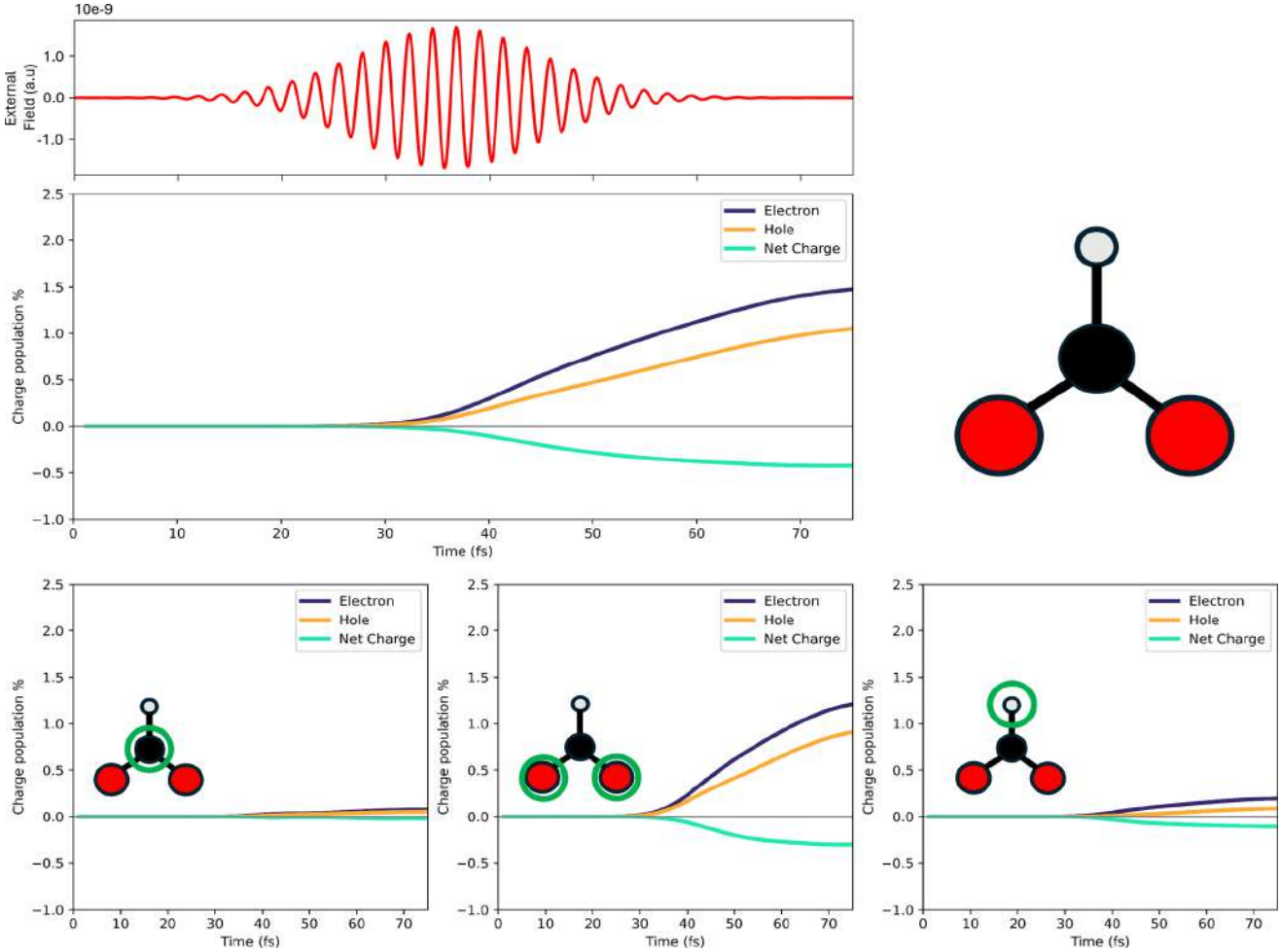

Figure 2. Upper panels: external P1 pulse and time evolution of the photoinduced charge populations (electron, hole and net) of the HCOO* fragment in the presence of the Au NR at 0.28 nm. Bottom panels: on the left, time evolution of the photoinduced charge populations (electron, hole and net) of the carbon atom; in the middle, the same for the oxygen atoms; on the right, the same for the hydrogen atom of HCOO*.

the QM subsystem only and using the P1 frequency,[38] which is not resonant with any HCOO* excitation, we have found a net electron injection. Such charge populations (electron, hole and corresponding net one) are computed according to eqs. 8 and 9 of Supporting Information, which define differential electron and hole populations with respect to the initial, i.e. in light-off conditions, electronic density.[10,29,38] This charge-transfer mechanism is also confirmed in the presence of the Au NR, as shown in Figure 2 for the distance of 0.28 nm. The net charge (presented as a percentage of the total charge population of the QM subsystem) on HCOO* is indeed negative. A closer inspection of the atomic contributions, given in the lower panels of Figure 2, reveals that this trend is consistent across all atoms: carbon (left), oxygen (center), and hydrogen (right). While both carbon and hydrogen atoms exhibit a modest increase in electron population, the oxygen atoms are the primary recipients of the transferred charge, indicating that they are the main targets of the electron donation process. This behavior is consistent with the previous observation in absence of a nearby plasmonic NR.[38] However, introducing the Au NR determines a notable difference in the charge dynamics. In presence of the NR, the system experiences an additional electromagnetic contribution due to the plasmonic near field. This secondary field emerges shortly after the peak of the external pulse,[49] with the electromagnetic response of the NR persisting for approximately 10−20 fs after the external field maximum. As a result, the QM subsystem is exposed to a prolonged and more complex electromagnetic environment. This leads to a more gradual increase in the electron and hole populations over time, producing a gentler slope in their temporal evolution compared to the case without the NR (for comparison, see Figure 4 of ref. 38). Additional evidence supporting this interpretation is given by the results of the control simulation presented in Figure S1, where the P2 pulse (central frequency of 3 eV) has been used. Despite the NR being present, the electron and hole populations exhibit the same sharp rise and rapid plateau observed in the absence of NR. This comparison further confirms that the prolonged and nontrivial charge redistribution observed here is specifically driven by resonant coupling between the external field and the NR plasmonic excitation.

Moreover, Figure S2 presents the evolution of the electron and hole populations within the Pd cluster over the first 75 fs of real-time dynamics with the P1 pulse: an overall positive net charge is observed, as expected, since no source of sink of charges is present in the simulation.

By varying the frequency of the external pulse, we are able to disentangle in the electronic dynamics of the QM subsystem the contributions of direct polarization effects from those arising

https://doi.org/10.1021/acs.jpclett.5c02858
J. Phys. Chem. Lett. 2025, 16, 12931−12938

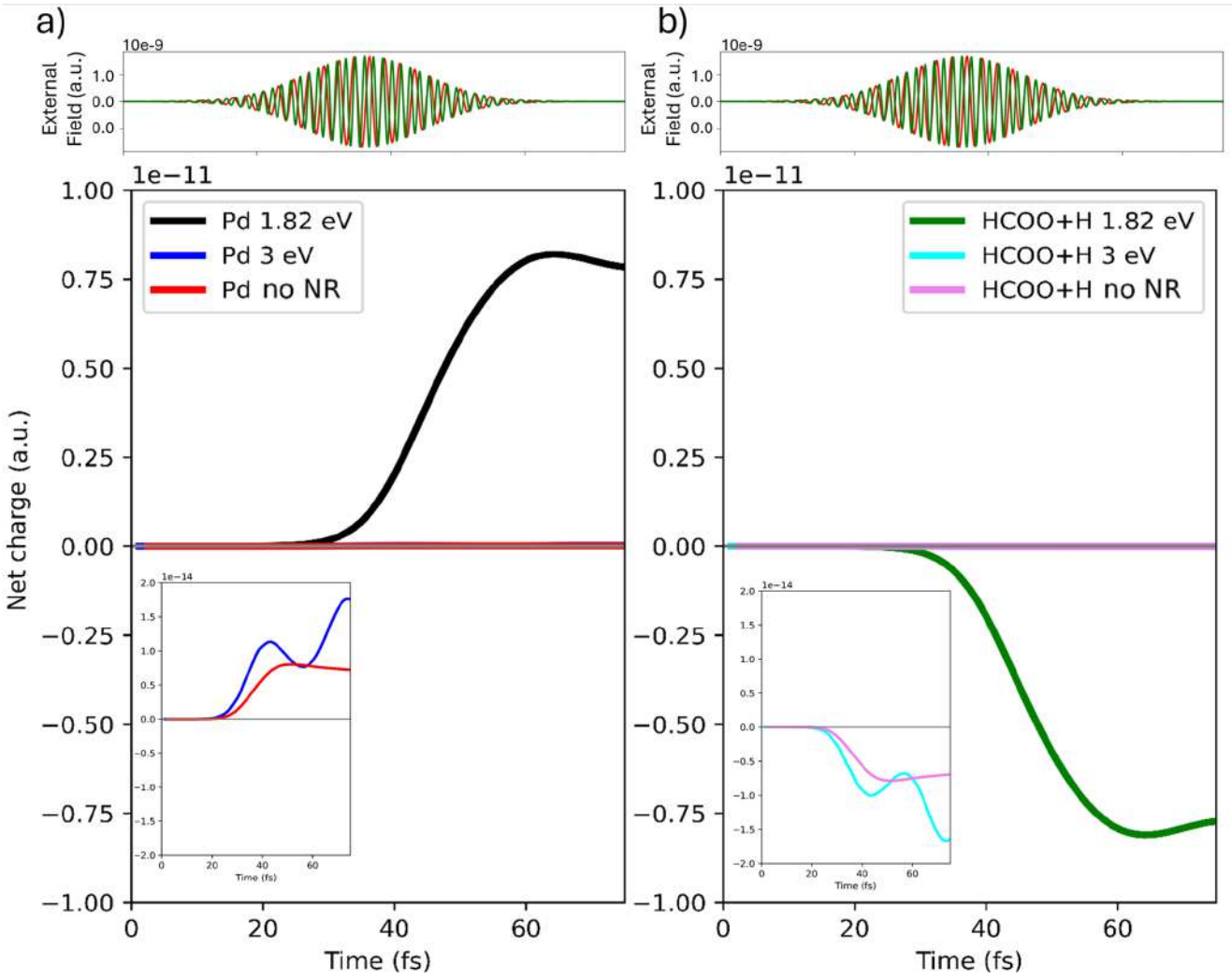

Figure 3. Panel a): time evolution of the net charge of the Pd cluster at 0.28 nm from the NR with the P1 pulse (reported in red), with the P2 pulse (reported in green) and without NR. Panel b): time evolution of the net charge of the HCOO* and H* species at 0.28 nm from the NR with P1 pulse, with P2 pulse and without NR. In both cases, a zoom for the second and third configurations is also shown. P1 (red) and P2 (green) pulses are also shown.

due to the plasmonic excitation. In Figure 3, we report the time evolution of the net charge on both the Pd cluster and on HCOO*+H* for three configurations: (i) with the NR present and excited about the plasmonic resonance (P1 pulse), (ii) with the NR excited off-resonance (P2 pulse), and (iii) in the absence of the NR with the P1 pulse (data taken from ref 38). Results for the two first cases refer to the distance of 0.28 nm.

The interaction at the plasmonic resonance (1.82 eV) produces a net charge transfer that is approximately 3 orders of magnitude larger than that observed in the off-resonant case or when the NR is not present. Also, the temporal profile of the curves is different, indicating an active role played by the plasmonic field during the dynamics. Indeed, the differential projected DOS (ΔPDOS, eq. 7 of Supporting Information) of HCOO* collected in Figures S3 and S4 for P1 and P2 pulses at 0.28 nm and for t = 60 fs (tail of the pulse), respectively, shows a different depopulation/population of molecular orbitals: with the P2 pulse, lower-energy orbitals are depopulated and virtual ones at higher energy are populated, as expected. In both cases, the involved orbitals exhibit a hybrid character, with electron density delocalized between the Pd atoms and the molecular fragment. A snapshot at 60 fs has been taken.

We have also analyzed how varying the distance between the QM subsystem and the NR influences the observed electron (hole) injection into HCOO* (Pd atoms). This analysis is presented in Figure S5, which shows the total charge displacement induced by the P1 pulse for the three configurations with increasing separation: 0.28, 0.56, and 2 nm. The total charge displacement at 0.28 nm is nearly 1 order of magnitude larger than that at 2 nm. Despite these quantitative differences, the overall charge transfer mechanism remains qualitatively consistent across all distances. As shown in Figures S6−S9, the spatial distribution of electron and hole populations for both the Pd layers and the adsorbed HCOO* follows the same pattern at 0.28, 0.56, and 2 nm. This suggests that the primary effect of decreasing the distance is not to alter the nature of the electron transfer process, but rather to amplify it via stronger electromagnetic coupling with the NR. Comparing the ΔPDOS of HCOO* at three distances (0.28, 0.56, and 2 nm, Figure S3) under excitation by the P1 pulse, one observes that

https://doi.org/10.1021/acs.jpclett.5c02858
J. Phys. Chem. Lett. 2025, 16, 12931−12938

the most striking difference lies in the intensity of the peaks, which are all scaled homogeneously.

The analysis conducted so far does not yet provide elements to understand the increase in H_2 production due to plasmonic effects. As mentioned above, the bidentate adsorbed HCOO* species becomes monodentate, with an oxygen atom released from the Pd surface. Figure 4 shows the asymmetry of electron injection into the two oxygen atoms of HCOO*, in terms of the absolute value of the relative difference.

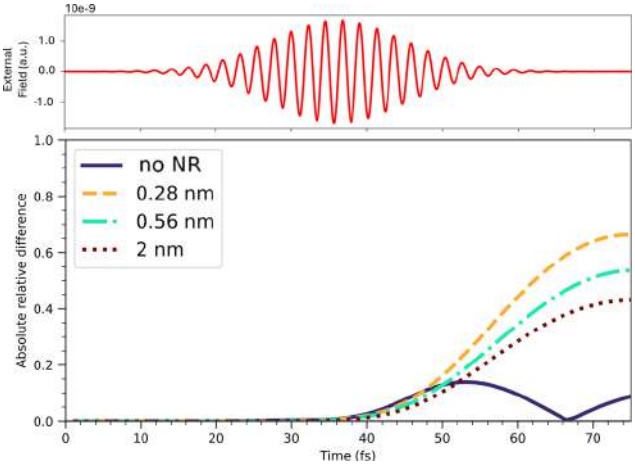

Figure 4. Absolute relative difference of the electron population of the two O atoms of HCOO* with the P1 pulse, at various distances between the QM subsystem and the NR. The case of the isolated QM subsystem is also reported for comparison. The time profile of the pulse is given.

Two different behaviors can be inferred. The asymmetry becomes more pronounced as a function of time by decreasing the distance, being maximum for the configuration at 0.28 nm, at larger times, when the plasmonic field becomes active.

It is the inner oxygen atom to be less negatively charged at any time in the presence of the NR, and therefore the candidate to leave the Pd surface (Figure S10). The two oxygen atoms are labeled as shown in Figure S10. Instead, without the NR, the time profile is rather different and is characterized by a change in the asymmetry (the singularity at around 67 fs). Distances are 2.12 (2.18) Å for the O1 (O2) O atom. Asymmetry is inherent in the system, as can be seen from the result without NR: an asymmetrical charge population is present due to the adsorption of HCOO* on the Pd surface. We emphasize that, as described in detail in the Supporting Information, the geometry optimization was conducted in periodic boundary conditions, starting from literature data. The presence of NR increases the asymmetry, thus leading more quickly to the monodentate species and to the final product, i.e., H_2. In Figure S11, we present the same analysis using the P2 pulse. In the absence of the NR, a slight asymmetry emerges, similar to what is observed with the P1 pulse without NR. This behavior is expected, as the system naturally tends toward the monodentate configuration even under excitation with the P2 pulse. Importantly, the presence of the NR does not alter this asymmetry: the charge distribution remains essentially unchanged when reducing the catalyst-NR distance from 2 to 0.28 nm with the P2 pulse, closely resembling the case without NR. This observation is highly significant, as it highlights the central role of plasmonic excitation in the H_2 enhancement observed in this reaction.

To verify that the asymmetry described is not an artifact due to the choice of the QM subsystem, we calculated the charge population on the two oxygen atoms for the isolated cluster (i.e., no NR) with two layers of Pd, with 16 atoms per layer (2L4), reported in Figure S12. Asymmetry in 2L4 is much larger than in 2L3. The reason for that is the two atoms being characterized by a net charge of opposite sign, with the electron one larger in absolute value (Figure S13). This result depends on the shape of the molecular orbitals involved in the dynamics, which differ from those in the 2L3 case, where both oxygen atoms are negatively charged and border effects play a non-neglible role. In 2L4, finite-size effects should be partially reduced, since the two oxygen atoms are centered with respect to the cut surface.

Assuming that the asymmetry in the photoinduced charge distribution is the driving force for hydrogen formation, our results confirm that this effect becomes even more pronounced under plasmonic conditions—specifically at 0.28 nm and with the excitation resonant with the NR LSPR. This provides a microscopic explanation for the enhanced H_2 production rate.

We have also analyzed the charge evolution of the H* atom. Figure S14 of Supporting Information shows the time-resolved electron and hole populations for the hydrogen fragment under P1 pulse at a separation of 0.28 nm: a net electron injection is observed, as in the case without NR.[38]

Surface-charge heterogeneity of the Pd surface has been identified as a key factor contributing to photocatalytic enhancement, as it can promote substrate adsorption and stabilize reaction intermediates.[50] According to Zheng et al.,[13] this heterogeneity plays a central role in explaining the increased catalytic activity observed in the presence of a plasmonic nanostructure.

Panel a) of Figure 5 shows the net charge distribution over selected pairs of Pd atoms located in the upper layer of the slab when the system is separated by 0.28 nm from the nanorod and excited with the P1 pulse. The pair marked in blue becomes more positively charged, while the purple pair accumulates negative charge. The central pair (green curve), which directly interacts with HCOO*, remains nearly neutral. Panel b) of Figure 5 explores how this surface-charge pattern changes with distance from the NR. Although the qualitative shape of the charge distribution remains similar, the total amount of displaced charge is significantly decreased—by about 1 order of magnitude—when the distance is increased to 2 nm, again under P1 excitation. Panels (c) and (d) of Figure 5 extend this comparison to the nonresonant case (P2 pulse), where the system is no longer excited at the plasmonic frequency. In these conditions, the charge separation on the Pd surface is much smaller (2 orders of magnitude) than what is observed in resonant conditions at the corresponding distances. On the other hand, the spatial pattern remains consistent when changing the distance. The data in Figure 5 are reported as both percentage and absolute values.

In this work, we have provided an original interpretation of the plasmon-mediated enhancement of hydrogen production from formic acid in the presence of a Pd-tipped Au NR. Our analysis shows that (i) a net electron charge is injected from Pd atoms to HCOO*, which is the reaction intermediate; (ii) the asymmetry in the charge distribution on the oxygen atoms is maximum in plasmon-resonance conditions, thus explaining how the plasmonic field affects the hydrogen production rate; (iii) a greater spatial heterogeneity of the charge on the Pd surface was found in the case of resonance with the plasmon of the NR. Since the plasmonic field decays in 10−20 fs, we have

https://doi.org/10.1021/acs.jpclett.5c02858
J. Phys. Chem. Lett. 2025, 16, 12931−12938

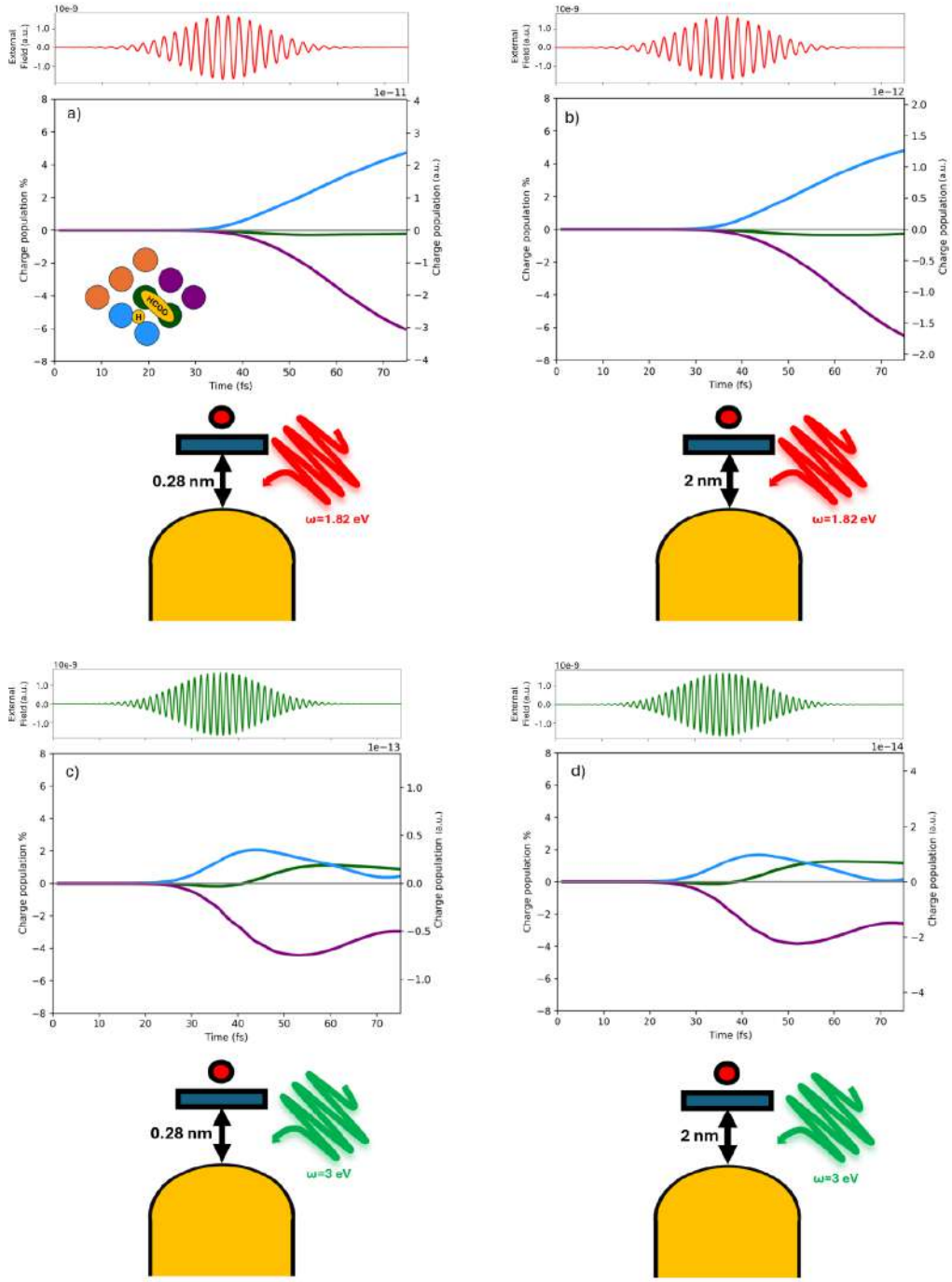

Figure 5. Panel a) Time evolution of the photoinduced charge populations (electron, hole and net) of the Pd atoms of the upper layer interacting with the molecular species at 0.28 nm with P1 pulse reported on top of each graph. In green are the Pd pairs interacting with HCOO*, in blue Pd pairs interacting with H* and in purple Pd pairs not interacting with any molecular species. Panel b) at 2 nm from NR with P1 pulse. Panel c) at 0.28 nm from the NR with P2 pulse. Panel d) at 2.0 nm from the NR with P2 pulse.

assumed that nuclear motion is decoupled from the electron dynamics occurring in this time window, assuming the reaction pathway from literature. Though freezing nuclei can be a crude assumption, however, we believe that reliable information about the plasmonic role in modifying reaction steps can be provided by such a modeling.

■ ASSOCIATED CONTENT

Data Availability Statement

Data are available from the authors (L.B. and E.C.) upon reasonable request.

Supporting Information

The Supporting Information is available free of charge at https://pubs.acs.org/doi/10.1021/acs.jpclett.5c02858.

https://doi.org/10.1021/acs.jpclett.5c02858
J. Phys. Chem. Lett. 2025, 16, 12931−12938

Theoretical approach and computational details. Charge population of HCOO* at 0.28, 0.56, and 2 nm and with P2 pulse (results for 0.56 and 2 nm also with P1). Charge population of Pd atoms at 0.28, 0.56, and 2 nm and with P1 and P2 pulse. ΔPDOS of HCOO* at various configurations. Net total charge at various configurations. Charge population of O atoms at 0.28 nm and with P1 pulse. Absolute relative difference of charge population of O atoms in different conditions, also for the 2L4 subsystem. Charge population of H* at 0.28 nm and with the P1 pulse (PDF)

Transparent Peer Review report available (PDF)

AUTHOR INFORMATION

Corresponding Author

Emanuele Coccia − *Dipartimento di Scienze Chimiche e Farmaceutiche, University of Trieste, 34127 Trieste, Italy;* orcid.org/0000-0003-3389-0989; Email: ecoccia@units.it

Author

Leonardo Biancorosso − *Dipartimento di Scienze Chimiche e Farmaceutiche, University of Trieste, 34127 Trieste, Italy;* orcid.org/0009-0002-2180-5898

Complete contact information is available at: https://pubs.acs.org/10.1021/acs.jpclett.5c02858

Notes

The authors declare no competing financial interest.

ACKNOWLEDGMENTS

Financial support from ICSC − Centro Nazionale di Ricerca in High Performance Computing, Big Data and Quantum Computing, funded by European Union − NextGenerationEU is gratefully acknowledged. This work has been supported by the project CHANGE funded by the PRIN 2022 - Progetti di Rilevante Interesse Nazionale (grant 20224KAC28).

REFERENCES

(1) O'Dwyer, E.; Pan, I.; Acha, S.; Shah, N. Smart energy systems for sustainable smart cities: Current developments, trends and future directions. *Appl. Energy* **2019**, *237*, 581.

(2) Poompavai, T.; Kowsalya, M. Control and energy management strategies applied for solar photovoltaic and wind energy fed water pumping system: A review. *Renew. Sustain. Energy Rev.* **2019**, *107*, 108.

(3) Rennert, K.; Errickson, F.; Prest, B. C.; Rennels, L.; Newell, R. G.; Pizer, W.; Kingdon, C.; Wingenroth, J.; Cooke, R.; Parthum, B.; et al. Comprehensive evidence implies a higher social cost of CO_2. *Nature* **2022**, *610*, 687.

(4) Onishi, N.; Laurenczy, G.; Beller, M.; Himeda, Y. Recent progress for reversible homogeneous catalytic hydrogen storage in formic acid and in methanol. *Coord. Chem. Rev.* **2018**, *373*, 317.

(5) Dai, H.; Cao, N.; Yang, L.; Su, J.; Luo, W.; Cheng, G. AgPd nanoparticles supported on MIL-101 as high performance catalysts for catalytic dehydrogenation of formic acid. *J. Mater. Chem. A* **2014**, *2*, 11060.

(6) El-Emam, R. S.; Özcan, H. Comprehensive review on the techno-economics of sustainable large-scale clean hydrogen production. *J. Clean. Prod.* **2019**, *220*, 593.

(7) Grasemann, M.; Laurenczy, G. Formic acid as a hydrogen source−recent developments and future trends. *Energy Environ. Sci.* **2012**, *5*, 8171.

(8) Singh, A. K.; Singh, S.; Kumar, A. Hydrogen energy future with formic acid: a renewable chemical hydrogen storage system. *Catal. Sci. Technol.* **2016**, *6*, 12.

(9) Lucarini, F.; Bongni, D.; Schiel, P.; Bevini, G.; Benazzi, E.; Solari, E.; Fadaei-Tirani, F.; Scopelliti, R.; Marazzi, M.; Natali, M.; Pastore, M.; Ruggi, A. Rationalizing Photo-Triggered Hydrogen Evolution Using Polypyridine Cobalt Complexes: Substituent Effects on Hexadentate Chelating Ligands. *ChemSusChem* **2021**, *14*, 1874.

(10) Dall'Osto, G.; Marsili, M.; Vanzan, M.; Toffoli, D.; Stener, M.; Corni, S.; Coccia, E. Peeking into the Femtosecond Hot-Carrier Dynamics Reveals Unexpected Mechanisms in Plasmonic Photocatalysis. *J. Am. Chem. Soc.* **2024**, *146*, 2208.

(11) Swearer, D. F.; Zhao, H.; Zhou, L.; Zhang, C.; Robatjazi, H.; Martirez, J. M. P.; Krauter, C. M.; Yazdi, S.; McClain, M. J.; Ringe, E.; et al. Heterometallic antenna-reactor complexes for photocatalysis. *Proc. Natl. Acad. Sci. U. S. A.* **2016**, *113*, 8916.

(12) Swearer, D. F.; Robatjazi, H.; Martirez, J. M. P.; Zhang, M.; Zhou, L.; Carter, E. A.; Nordlander, P.; Halas, N. J. Plasmonic Photocatalysis of Nitrous Oxide into N_2 and O_2 Using Aluminum−Iridium Antenna−Reactor Nanoparticles. *ACS Nano* **2019**, *13*, 8076.

(13) Zheng, Z.; Tachikawa, T.; Majima, T. Plasmon-enhanced formic acid dehydrogenation using anisotropic Pd−Au nanorods studied at the single-particle level. *J. Am. Chem. Soc.* **2015**, *137*, 948.

(14) Jin, H.; Herran, M.; Cortés, E.; Lischner, J. Theory of hot-carrier generation in bimetallic plasmonic catalysts. *ACS photonics* **2023**, *10*, 3629.

(15) Herran, M.; Sousa-Castillo, A.; Fan, C.; Lee, S.; Xie, W.; Döblinger, M.; Auguié, B.; Cortés, E. Tailoring plasmonic bimetallic nanocatalysts toward sunlight-driven H_2 production. *Adv. Funct. Mater.* **2022**, *32*, 2203418.

(16) Wach, A.; et al. The dynamics of plasmon-induced hot carrier creation in colloidal gold. *Nat. Commun.* **2025**, *16*, 2274.

(17) Coccia, E.; Fregoni, J.; Guido, C. A.; Marsili, M.; Pipolo, S.; Corni, S. Hybrid theoretical models for molecular nanoplasmonics. *J. Chem. Phys.* **2020**, *153*, 200901.

(18) Sivan, Y.; Dubi, Y. Recent developments in plasmon-assisted photocatalysis—a personal perspective. *Appl. Phys. Lett.* **2020**, *117*, 130501.

(19) Puértolas, B.; Comesaña-Hermo, M.; Besteiro, L. V.; Vázquez-González, M.; Correa-Duarte, M. A. Challenges and opportunities for renewable ammonia production via plasmon-assisted photocatalysis. *Adv. Energy Mater.* **2022**, *12*, 2103909.

(20) Zhang, Z.; Zhang, C.; Zheng, H.; Xu, H. Plasmon-driven catalysis on molecules and nanomaterials. *Acc. Chem. Res.* **2019**, *52*, 2506.

(21) Biancorosso, L.; Coccia, E. Recent advances in modelling plasmon-assisted electron dynamics. *Chem. Modell.* **2024**, *18*, 102.

(22) Giannini, V.; Fernández-Domínguez, A. I.; Heck, S. C.; Maier, S. A. Plasmonic nanoantennas: fundamentals and their use in controlling the radiative properties of nanoemitters. *Chem. Rev.* **2011**, *111*, 3888.

(23) Coronado, E. A.; Encina, E. R.; Stefani, F. D. Optical properties of metallic nanoparticles: manipulating light, heat and forces at the nanoscale. *Nanoscale* **2011**, *3*, 4042.

(24) Mubeen, S.; Lee, J.; Singh, N.; Krämer, S.; Stucky, G. D.; Moskovits, M. An autonomous photosynthetic device in which all charge carriers derive from surface plasmons. *Nat. nanotechnol.* **2013**, *8*, 247.

(25) Sheng, H.; Wang, J.; Huang, J.; Li, Z.; Ren, G.; Zhang, L.; Yu, L.; Zhao, M.; Li, X.; Li, G.; et al. Strong synergy between gold nanoparticles and cobalt porphyrin induces highly efficient photocatalytic hydrogen evolution. *Nat. Commun.* **2023**, *14*, 1528.

(26) Mascaretti, L.; Naldoni, A. Hot electron and thermal effects in plasmonic photocatalysis. *J. Appl. Phys.* **2020**, *128*, 041101.

(27) Huang, Y.; Chen, Y.; Deng, L.; Zhu, Y.; Huang, Y. Expanding the scope of antenna−reactor photocatalysts for strong visible light absorption in small transition metal nanoparticles. *Appl. Phys. Lett.* **2021**, *119*, 043903.

(28) Ezendam, S.; Herran, M.; Nan, L.; Gruber, C.; Kang, Y.; Gröbmeyer, F.; Lin, R.; Gargiulo, J.; Sousa-Castillo, A.; Cortés, E. Hybrid Plasmonic Nanomaterials for Hydrogen Generation and Carbon Dioxide Reduction. *ACS Energy Lett.* **2022**, *7*, 778.

(29) Dall'Osto, G.; Vanzan, M.; Corni, S.; Marsili, M.; Coccia, E. Stochastic Schrödinger equation for hot-carrier dynamics in plasmonic systems. *J. Chem. Phys.* **2024**, *161*, 124103.
(30) Li, S. J.; Zhou, X.; Tian, W. Q. Theoretical investigations on decomposition of HCOOH catalyzed by Pd7 cluster. *J. Phys. Chem. A* **2012**, *116*, 11745.
(31) Wang, N.; Li, K.; Wang, Y.; Wu, Z. Density functional study on formic acid decomposition on Pd (111) surface: a revisit and comparison with other density functional methods. *J. Mol. Model.* **2021**, *27*, 1.
(32) Wang, Y.; Qi, Y.; Zhang, D.; Liu, C. New insight into the decomposition mechanism of formic acid on Pd (111): competing formation of CO_2 and CO. *J. Phys. Chem. C* **2014**, *118*, 2067.
(33) He, N.; Li, Z. H. Palladium-atom catalyzed formic acid decomposition and the switch of reaction mechanism with temperature. *Phys. Chem. Chem. Phys.* **2016**, *18*, 10005.
(34) Navlani-García, M.; Mori, K.; Salinas-Torres, D.; Kuwahara, Y.; Yamashita, H. New approaches toward the hydrogen production from formic acid dehydrogenation over Pd-based heterogeneous catalysts. *Front. Mater.* **2019**, *6*, 44.
(35) Schlussel, S.; Kwon, S. A review of formic acid decomposition routes on transition metals for its potential use as a liquid H_2 carrier. *Korean J. Chem. Eng.* **2022**, *39*, 2883.
(36) Yoo, J. S.; Abild-Pedersen, F.; Nørskov, J. K.; Studt, F. Theoretical analysis of transition-metal catalysts for formic acid decomposition. *ACS Catal.* **2014**, *4*, 1226.
(37) Hu, Z.-Y.; Luo, L.-H.; Shang, C.; Liu, Z.-P. Free Energy Pathway Exploration of Catalytic Formic Acid Decomposition on Pt-Group Metals in Aqueous Surroundings. *ACS Catal.* **2024**, *14*, 7684.
(38) Biancorosso, L.; Coccia, E. Study of the Photoinduced Charge Injection in the Reaction Intermediate of the Dehydrogenation of Formic Acid on Palladium. *J. Comput. Chem.* **2025**, *46*, No. e70087.
(39) Coccia, E. How electronic dephasing affects high-harmonic generation in atoms. *Mol. Phys.* **2020**, *118*, No. e1769871.
(40) Mennucci, B.; Corni, S. Multiscale modelling of photoinduced processes in composite systems. *Nat. Rev. Chem.* **2019**, *3*, 315.
(41) Hohenester, U.; Trügler, A. MNPBEM: A Matlab toolbox for the simulation of plasmonic nanoparticles. *Comput. Phys. Commun.* **2012**, *183*, 370.
(42) Pipolo, S.; Corni, S. Real-Time Description of the Electronic Dynamics for a Molecule Close to a Plasmonic Nanoparticle. *J. Phys. Chem. C* **2016**, *120*, 28774.
(43) Pipolo, S.; Corni, S.; Cammi, R. Equation of Motion for the Solvent Polarization Apparent Charges in the Polarizable Continuum Model: Application to Real-Time TDDFT. *J. Phys. Chem. A* **2015**, *119*, 5405.
(44) Rüger, R.; Franchini, M.; Trnka, T.; Yakovlev, A.; van Lenthe, E.; Philipsen, P.; van Vuren, T.; Klumpers, B.; Soini, T. *AMS 2025.1, SCM, Theoretical Chemistry*; Vrije Universiteit: Amsterdam, The Netherlands, 2025.
(45) Biancorosso, L.; D'Antoni, P.; Corni, S.; Stener, M.; Coccia, E. Time-dependent quantum/continuum modeling of plasmon-enhanced electronic circular dichroism. *J. Chem. Phys.* **2024**, *161*, 214104.
(46) Rüger, R.; van Lenthe, E.; Heine, T.; Visscher, L. Tight-Binding Approximations to Time-Dependent Density Functional Theory - a fast approach for the calculation of electronically excited states. *J. Chem. Phys.* **2016**, *144*, 184103.
(47) Hammer, B.; Hansen, L. B.; Nørskov, J. K. Improved adsorption energetics within density-functional theory using revised Perdew-Burke-Ernzerhof functionals. *Phys. Rev. B* **1999**, *59*, 7413.
(48) Slater, J. C. Atomic Radii in Crystals. *J. Chem. Phys.* **1964**, *41*, 3199.
(49) Dall'Osto, G.; Gil, G.; Pipolo, S.; Corni, S. Real-time dynamics of plasmonic resonances in nanoparticles described by a boundary element method with generic dielectric function. *J. Chem. Phys.* **2020**, *153*, 184114.
(50) Sarina, S.; Bai, S.; Huang, Y.; Chen, C.; Jia, J.; Jaatinen, E.; Ayoko, G. A.; Bao, Z.; Zhu, H. Visible light enhanced oxidant free dehydrogenation of aromatic alcohols using Au−Pd alloy nanoparticle catalysts. *Green chem.* **2014**, *16*, 331.

https://doi.org/10.1021/acs.jpclett.5c02858
J. Phys. Chem. Lett. 2025, 16, 12931−12938

Supporting Information for "Plasmon-enhanced asymmetry in the charge distribution explains the increased H_2 production rate from formic acid with a Pd-tipped Au nanorod"

Leonardo Biancorosso and Emanuele Coccia*

Dipartimento di Scienze Chimiche e Farmaceutiche, Università di Trieste, via L. Giorgieri 1, 34127, Trieste, Italy

E-mail: ecoccia@units.it

Theory and computational details

TDSE in length gauge for TD-PCM-NP can be rewritten as

$$i\frac{d}{dt}|\Psi(t)\rangle = \hat{H}(t)|\Psi(t)\rangle, \tag{1}$$

with $\hat{H}(t)$ being the time-dependent Hamiltonian

$$\hat{H}(t) = \hat{H}_0 - \vec{\boldsymbol{\mu}} \cdot \vec{E}_{ext}(t) + \mathbf{q}(t) \cdot \hat{\mathbf{V}}_{\mathrm{BEM}}. \tag{2}$$

In Eq. 2, $\vec{\boldsymbol{\mu}}$ denotes the dipole operator of the molecule, $\vec{E}_{ext}(t)$ represents the time-dependent external electric field, $\mathbf{q}(t)$ corresponds to the time-dependent BEM charges,[1,2] and $\hat{\mathbf{V}}_{\mathrm{BEM}}$ is the operator describing the electrostatic potential evaluated at the positions of the sur-

face charges on the nanoparticle (NP). Both $\mathbf{q}(t)$ and $\hat{\mathbf{V}}_{\mathrm{BEM}}$ are vectors of dimension N_T, corresponding to the number of surface elements.

The field-free electronic Hamiltonian, $\hat{H}_0$, is given by:

$$\hat{H}_0 = \hat{H}_{el} + \mathbf{q}_{GS} \cdot \hat{\mathbf{V}}_{\mathrm{BEM}} \tag{3}$$

where $\hat{H}el$ is the electronic Hamiltonian of the isolated QM subsystem, and $\mathbf{q}_{GS}$ denotes the ground-state BEM charges. These charges are determined through a self-consistent procedure that accounts for the polarization response of the nanoparticle to the molecular ground-state electronic density.[3]

The time-dependent wavefunction, $|\Psi(t)\rangle$, is defined as a linear combination of the N_{states} eigenstates of the effective field-free Hamiltonian $\hat{H}_0$, also containing the ground-state polarization of the molecule and the NP

$$|\Psi(t)\rangle = \sum_{M=0}^{N_{\mathrm{states}}-1} C_M(t)|M\rangle \tag{4}$$

where $C_M(t)$ are time-dependent coefficients, and $|M\rangle$ is the M-th eigenstate of the system, with eigenvalue E_M. The initial guess for the self-consistent calculation is provided by the eigenstates of H_{el}.

In this work, we employ an approximate time-dependent density functional theory approach with tight-binding corrections (TD-DFT+TB),[4] formulated within a configuration-interaction singles (CIS) framework,[5] as implemented in the Amsterdam Modeling Suite (AMS).[6] Within this formalism, the excited states $|M\rangle$ are expressed as linear combinations of singly excited Slater determinants:

$$|M\rangle = \sum_{i}^{occ} \sum_{a}^{vir} d_{i,M}^{a} |\Phi_i^a\rangle \tag{5}$$

where $|\Phi_i^a\rangle$ represents a determinant formed by promoting one electron from an occu-

pied molecular orbital i to a virtual orbital a, and $d^a_{i,M}$ are the corresponding excitation amplitudes.

The system is perturbed by a time-dependent external electric field $\vec{E}_{ext}(t)$, defined as:

$$\vec{E}_{ext}(t) = \vec{E}_{max} \exp\left(-\frac{(t-t_0)^2}{2\sigma^2}\right) \sin(\omega t), \tag{6}$$

where $\vec{E}_{max}$ denotes the peak field amplitude, ω is the carrier frequency, t_0 is the temporal center of the pulse, and σ controls the width of the Gaussian envelope.

In order to analyze the electronic dynamics, we use the time-dependent projected density of states (PDOS(t,ϵ)),[7] defined as the expectation values of the number operator $\hat{n}$ with respect to the wavefunction $|\psi(t)\rangle$. In particular, we define the differential PDOS (ΔPDOS) at a certain time t in respect to the initial condition at time $t = 0$.

$$\begin{aligned}\Delta\text{PDOS}_K(t,\epsilon) = &-\sum_i^{occ} w_i^K \text{Re}[\sum_{M,L} C_L^*(t) C_M(t) \sum_a^{vir} d_{i,L}^{a*} d_{i,M}^a] F_\eta(\epsilon - \epsilon_i) \\ &+\sum_a^{vir} w_a^K \text{Re}[\sum_{M,L} C_L^*(t) C_M(t) \sum_i^{occ} d_{i,L}^{a*} d_{i,M}^a] F_\eta(\epsilon - \epsilon_i).\end{aligned} \tag{7}$$

In this equation, $d^a_{i,M}$ ($d^a_{i,L}$) are the linear coefficients of the expansion for state $|M\rangle$ ($\langle L|$) and F_η is a Lorentzian function centered on the MO energies ϵ_i, with width η, used to obtain a smooth profile. Mulliken weights w_i^K are used in the fragmentation of the studied system. Details are found in Ref. 7. The subscript/superscript K refers to the fragment, i.e. the single atom or group of atoms, regarding which one computes the charge population.

Integrating over the energy range allows us to obtain the time-dependent charge (electron and hole) population regarding the initial condition[8,9]

$$\text{electron population} = \frac{1}{2}\int_{-\infty}^{+\infty} [\Delta\text{PDOS}_K(t,\epsilon) + |\Delta\text{PDOS}_K(t,\epsilon)|] d\epsilon \tag{8}$$

and

$$\text{hole population} = \frac{1}{2}\int_{-\infty}^{+\infty} \left[\Delta\text{PDOS}_K(t,\epsilon) + |\Delta\text{PDOS}_K(t,\epsilon)|\right] d\epsilon. \tag{9}$$

The geometries of the Pd(111) slab and the molecular species were taken from the optimized structures reported in Ref.[10] Two layers and 9 atoms per layer with HCOO* and H* form the molecular system (2L3). Real-time electronic dynamics were simulated using the `WaveT/TDPlas` package,[11] interfaced with `AMS` to extract both electric transition dipole moments and the transition potential.[7,12,13] Input parameters—including excitation energies, transition dipole moments, and transition potentials—were obtained from TD-DFT+TB calculations[4] including 1808 excited states covering excitations up to 6 eV, using the RPBE exchange-correlation functional,[14] Grimme dispersion corrections, and a double-zeta (DZ) basis set.

Simulations were carried out for a duration of 100 fs. The external field $\vec{E}_{\text{ext}}(t)$ is described by Eq. 6. The plasmonic frequency was computed using the boundary element method (BEM) coupled with a polarizable continuum model.[11]

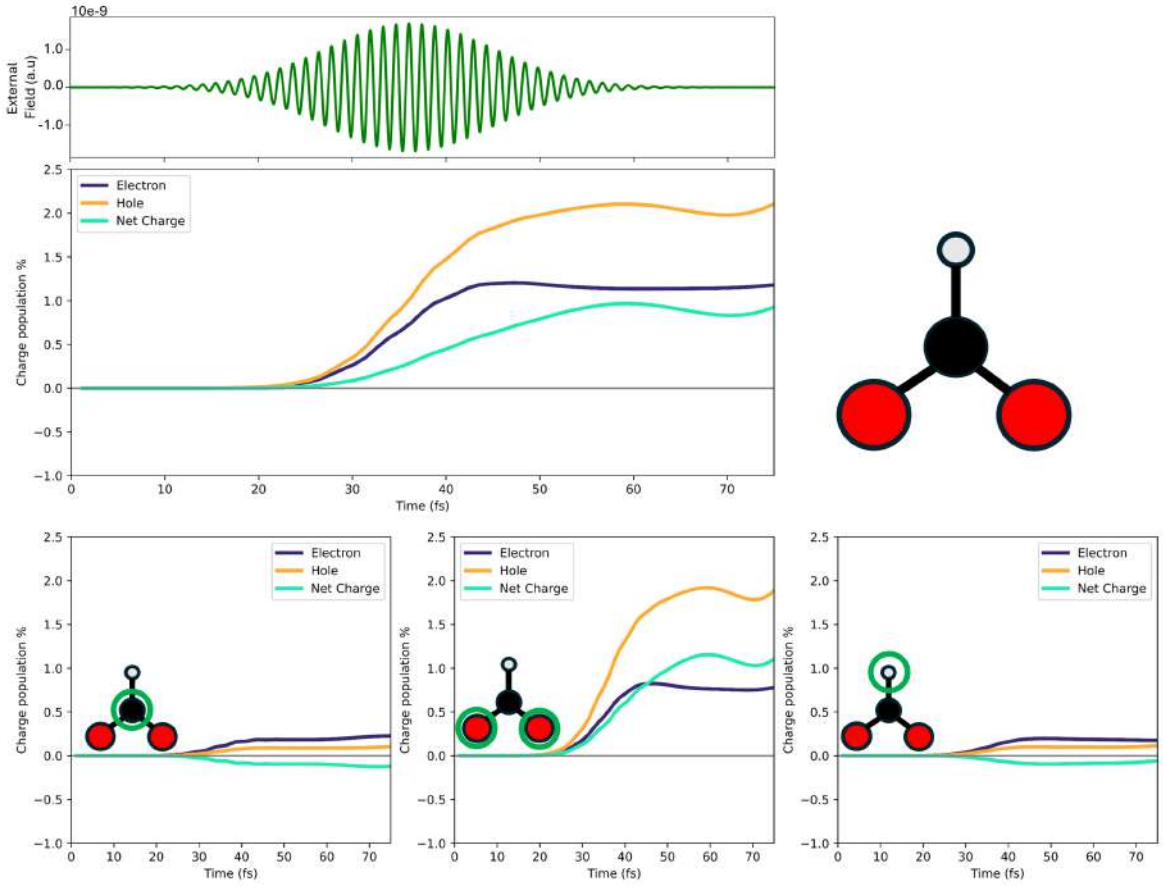

Figure S1: Upper panels: external pulse and time evolution of the photoinduced charge populations (electron, hole and net) of the HCOO* fragment in the presence of the Au NR at 0.28 nm of distance with P2 pulse reported on top. Bottom panels: on the left, time evolution of the photoinduced charge populations (electron, hole and net) of the carbon atom; in the middle, the same for the oxygen atoms; on the right, the same for the hydrogen atom of HCOO*.

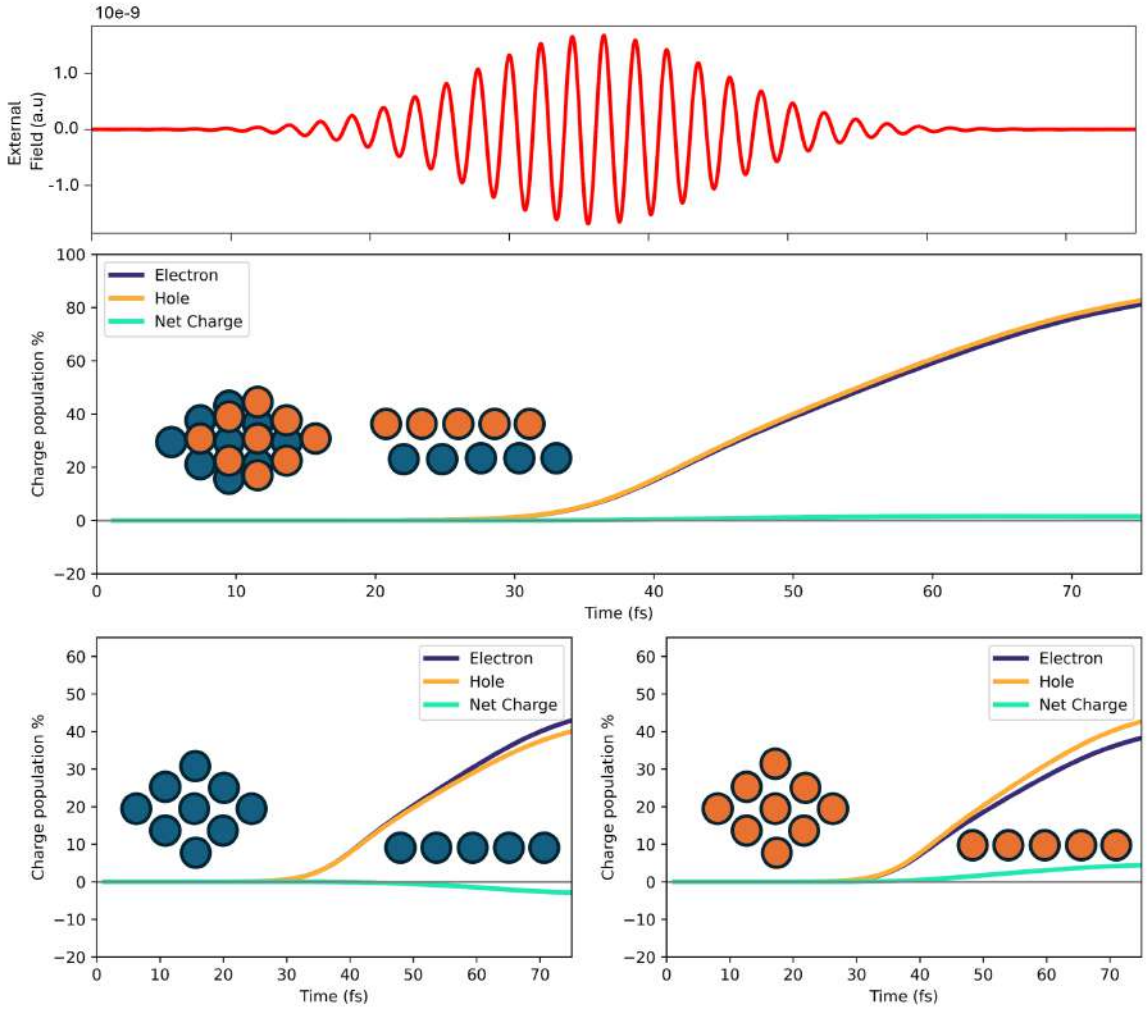

Figure S2: Upper panels: external pulse and time evolution of the photoinduced charge populations (electron, hole and net) of the full Pd cluster in the 2L3 system in the presence of the Au NR at 0.28 nm of distance with P1 pulse. Bottom panels: time evolution of the photoinduced charge populations (electron, hole and net) of the bottom layer (left) and of the upper layer (right)

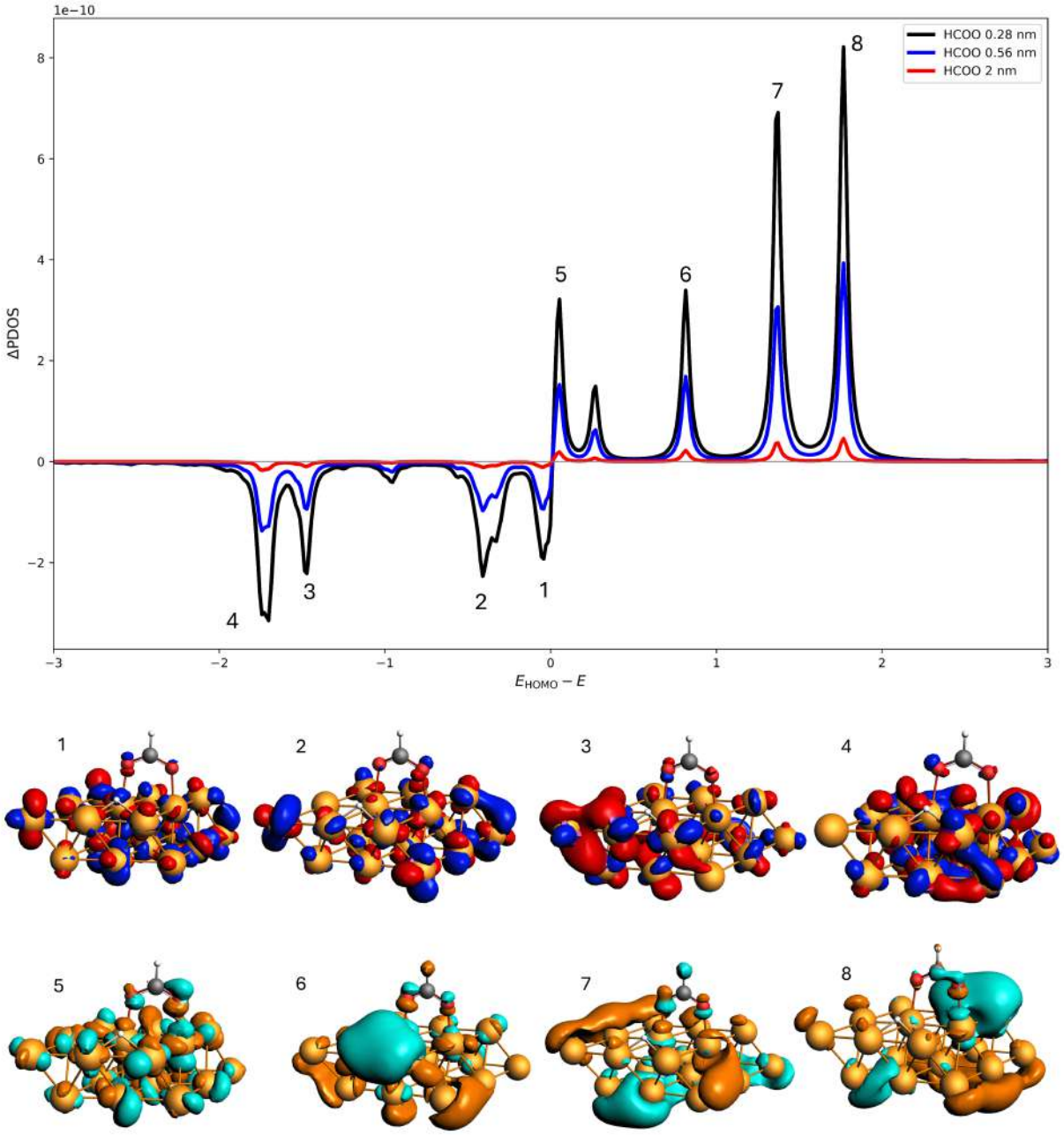

Figure S3: ΔPDOS of the HCOO* fragment at $t = 60$ fs for the system at 0.28 nm, 0.56 nm and 2 nm with the P1 pulse. In the inset, ΔPDOS of the HCOO* fragment at $t = 60$ fs for the system without NR. Reported are the main orbitals involved in the electronic process.

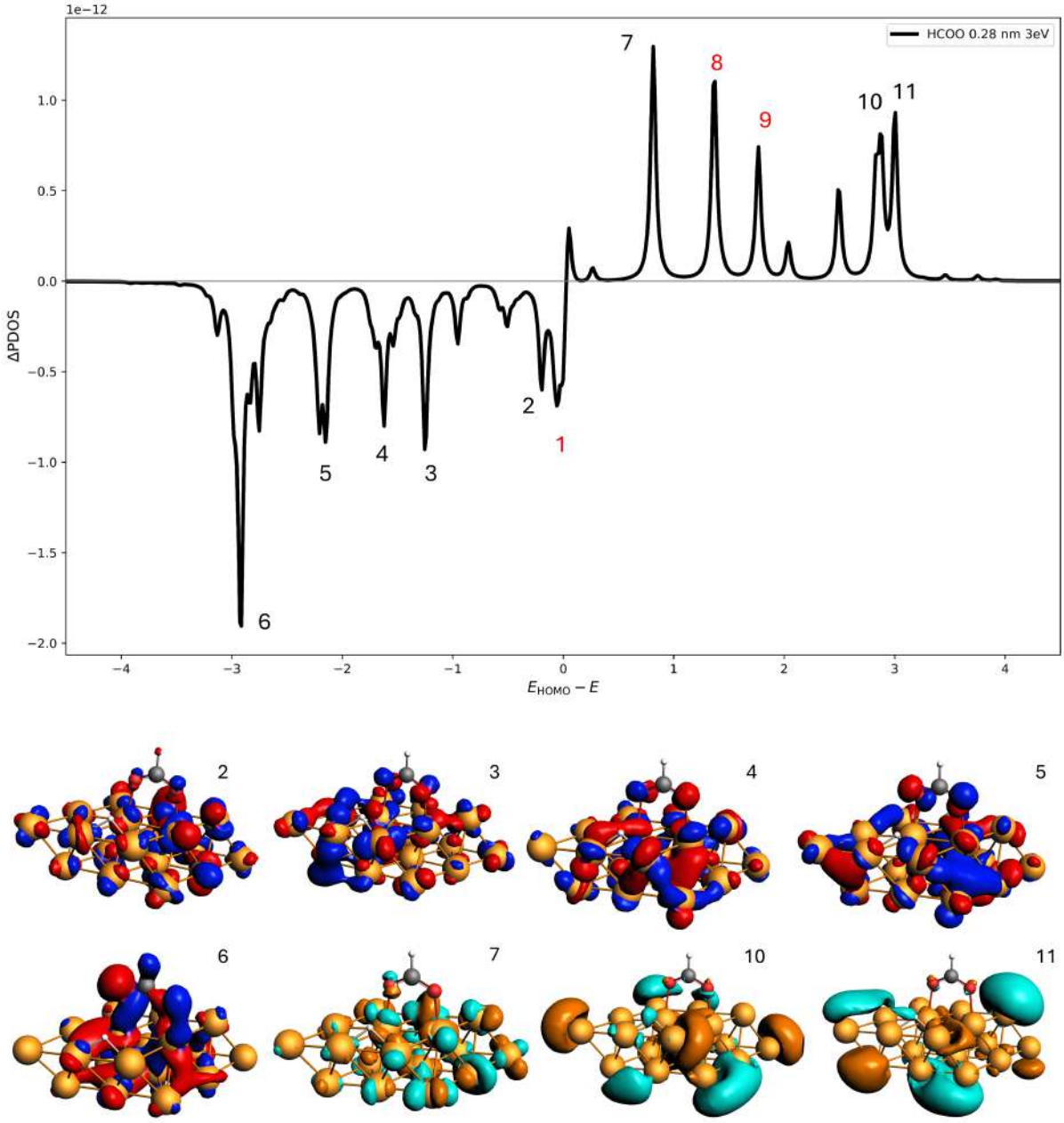

Figure S4: ΔPDOS of the HCOO* fragment at $t = 60$ fs for the system at 0.28 nm with the P2 pulse. Reported are the main orbitals involved in the electronic process. In red orbital 1, 8 and 9 are the same orbitals already reported in Figure 6 and correspond, respectively, to orbitals 1, 6 and 7.

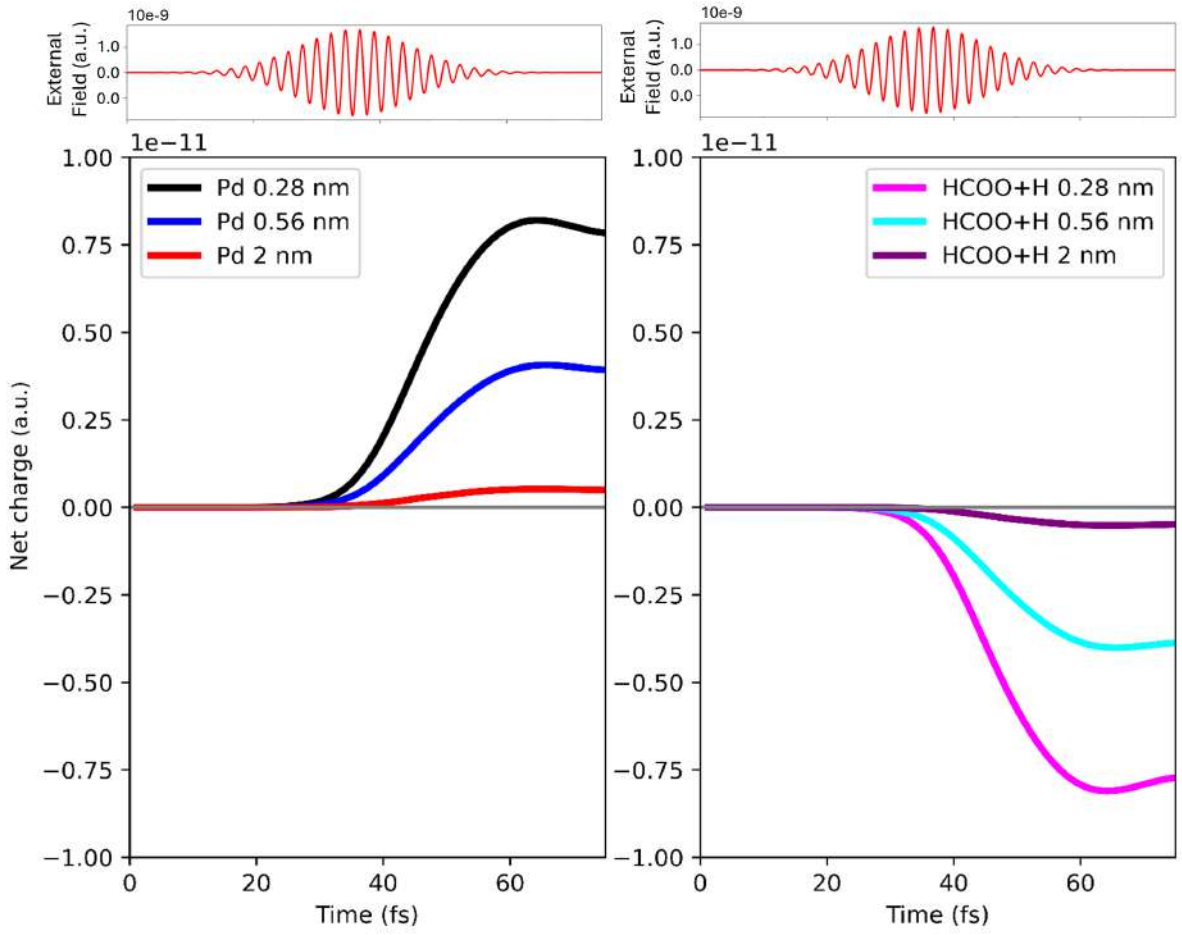

Figure S5: On the left, time evolution of the net charge of the Pd cluster at 0.28 nm, 0.56 nm and 2 nm from the NR with the P1 pulse; on the right, time evolution of the net charge of the HCOO* fragment at 0.28 nm, 0.56 nm and 2 nm from the NR with the P1 pulse. Time profile of the pulse is also reported.

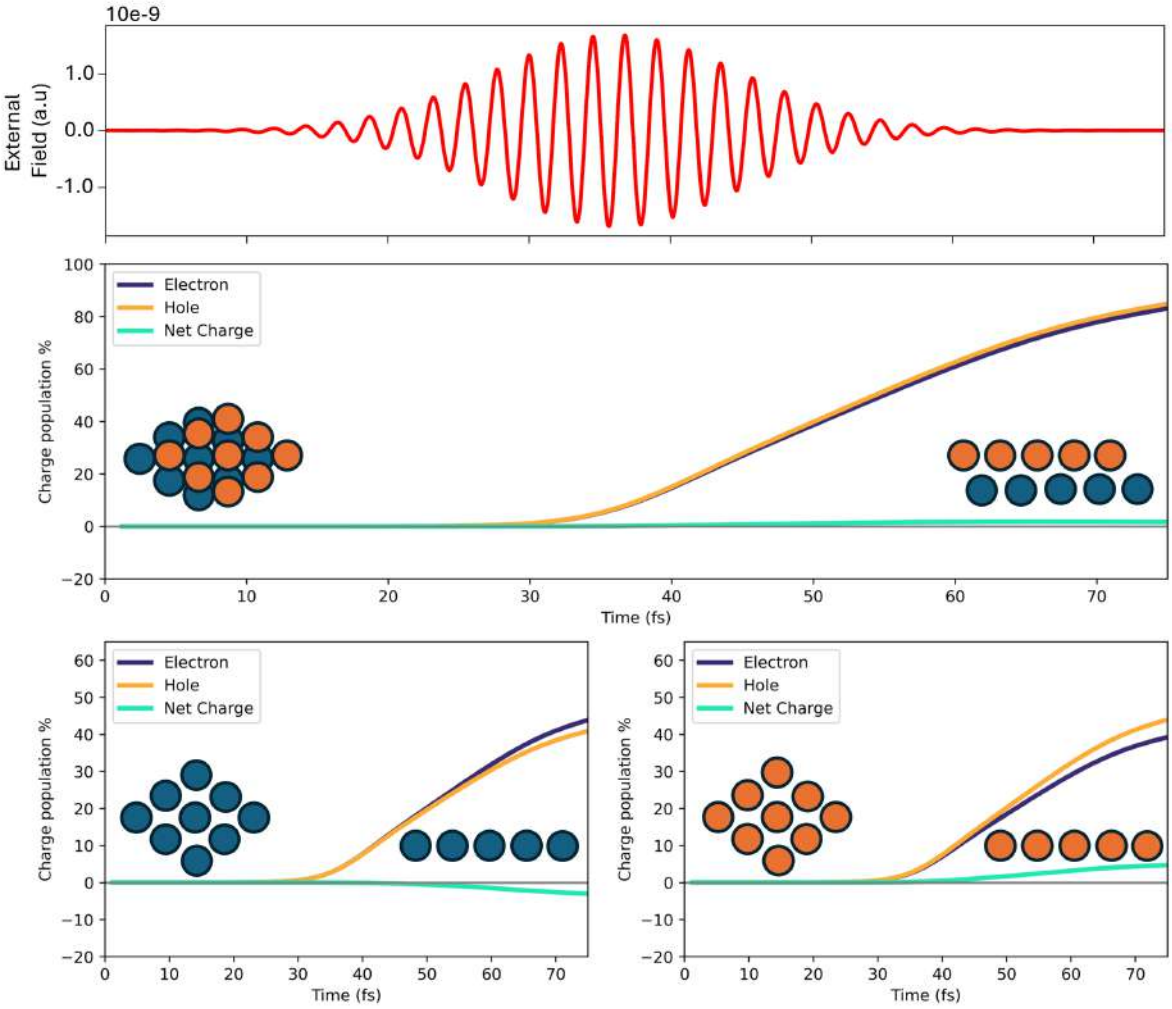

Figure S6: Upper panels: external pulse and time evolution of the photoinduced charge populations (electron, hole and net) of the full Pd cluster in the presence of the NR at 0.56 nm with P1 pulse. Bottom panels: time evolution of the photoinduced charge populations (electron, hole and net) of the bottom layer (left) and of the upper layer (right)

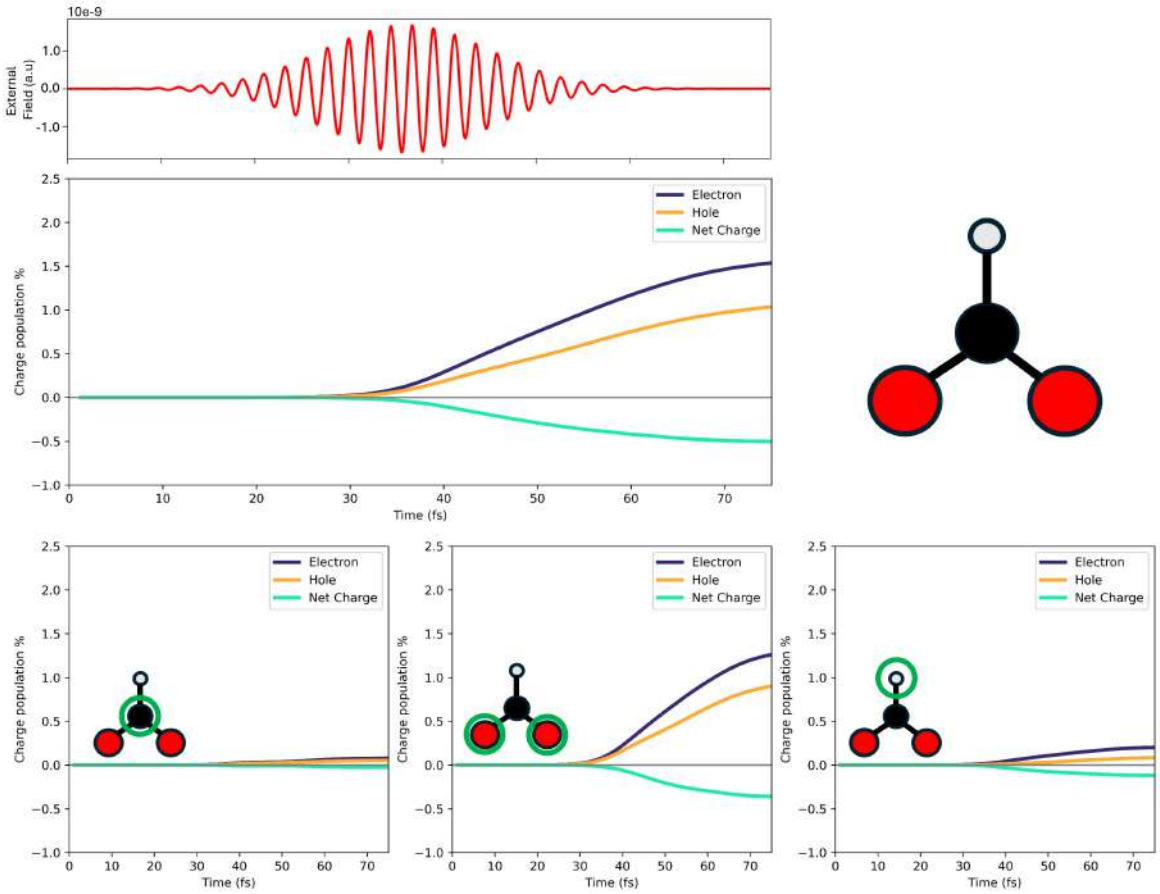

Figure S7: Upper panels: external pulse and time evolution of the photoinduced charge populations (electron, hole and net) of the HCOO* fragment in presence of the NR at 0.56 nm with P1 pulse. Bottom panels: on the left, time evolution of the photoinduced charge populations (electron, hole and net) of the carbon atom; in the middle, the same for the oxygen atoms; on the right, the same for the hydrogen atom of HCOO*.

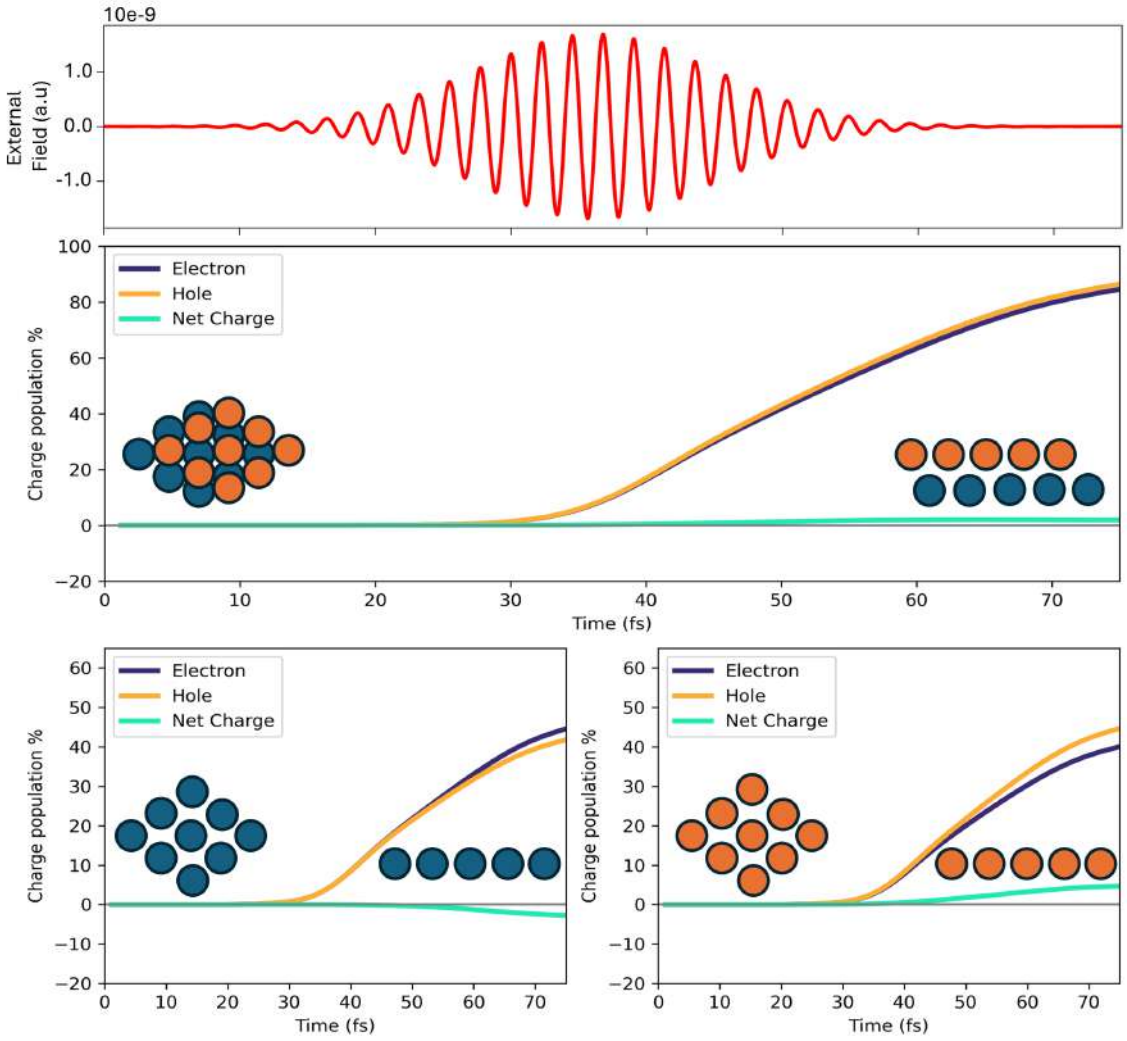

Figure S8: Upper panels: external pulse and time evolution of the photoinduced charge populations (electron, hole and net) of the full Pd cluster in presence of the NR at 2 nm with P1 pulse. Bottom panels: time evolution of the photoinduced charge populations (electron, hole and net) of the bottom layer (left) and of the upper layer (right)

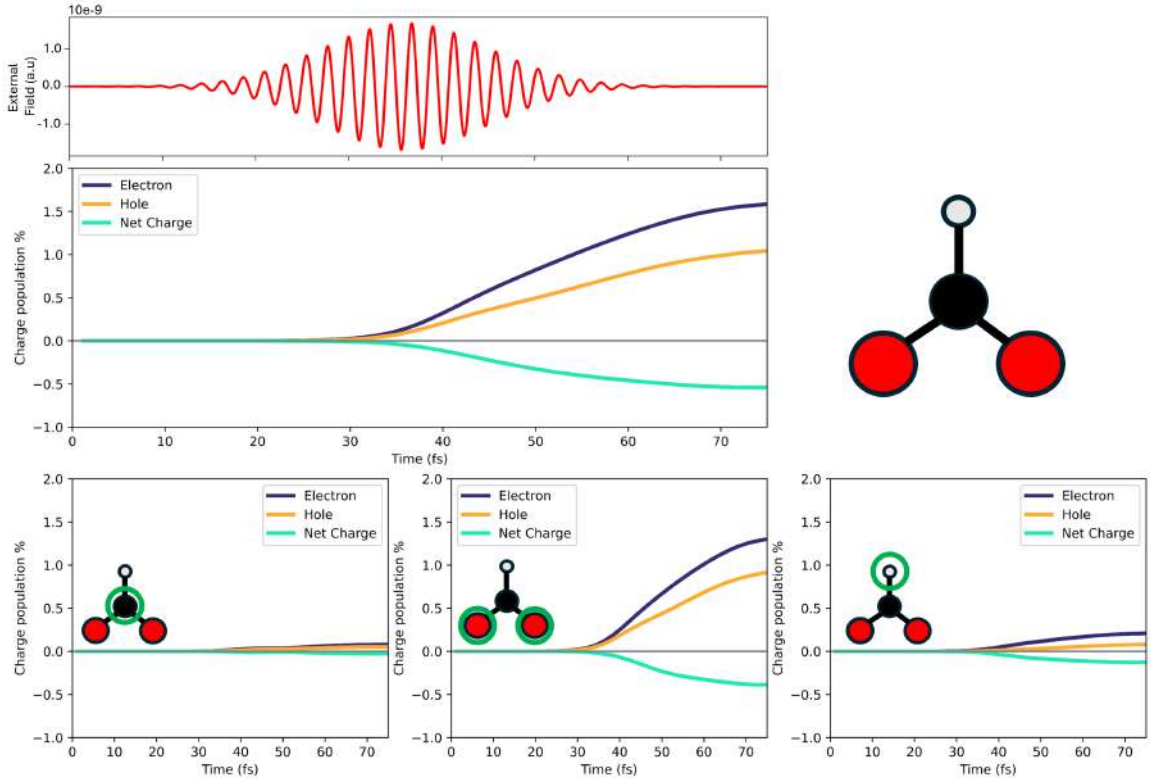

Figure S9: Upper panels: external pulse and time evolution of the photoinduced charge populations (electron, hole and net) of the HCOO* fragment in presence of the NR at 2 nm with P1 pulse. Bottom panels: on the left, time evolution of the photoinduced charge populations (electron, hole and net) of the carbon atom; in the middle, the same for the oxygen atoms; on the right, the same for the hydrogen atom of HCOO*.

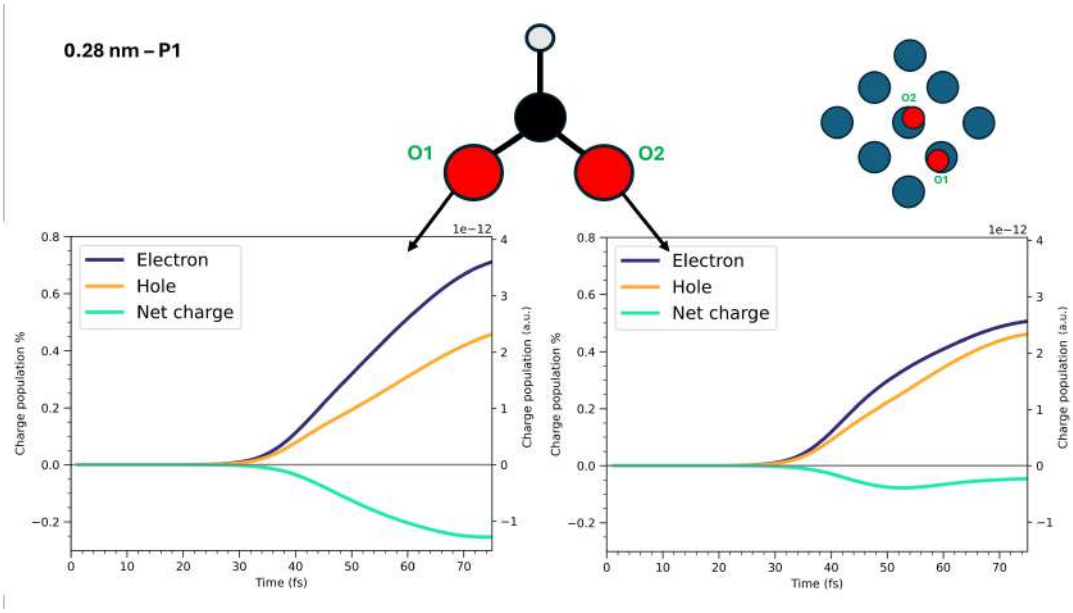

Figure S10: Time evolution of the photoinduced charge populations (electron, hole and net) of O1 and O2 atoms in the presence of the Au NR at 0.28 nm of distance with P1 pulse.

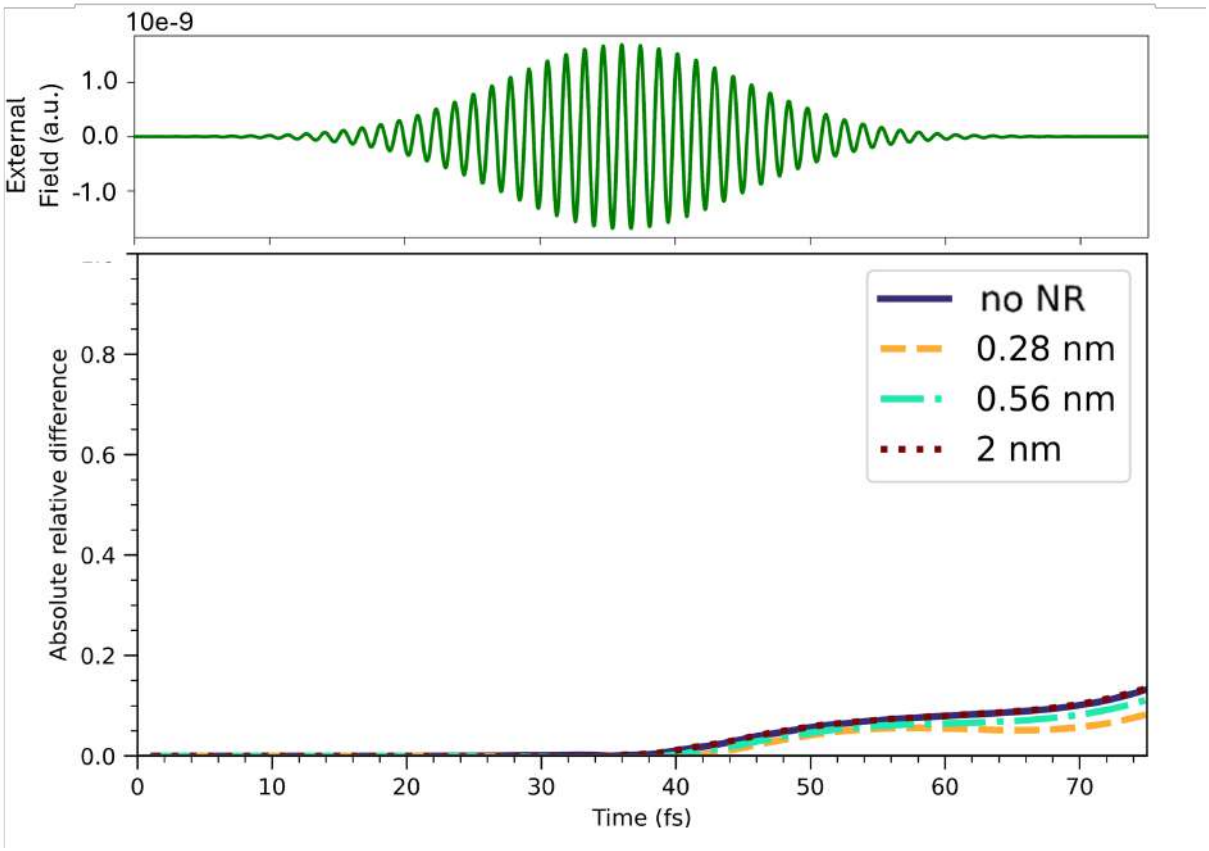

Figure S11: Absolute relative difference of the electron population of the two O atoms of HCOO* with the P2 pulse, at various distances between the QM subsystem and the NR. The case of the isolated QM subsystem is also reported for comparison. External pulse is also given.

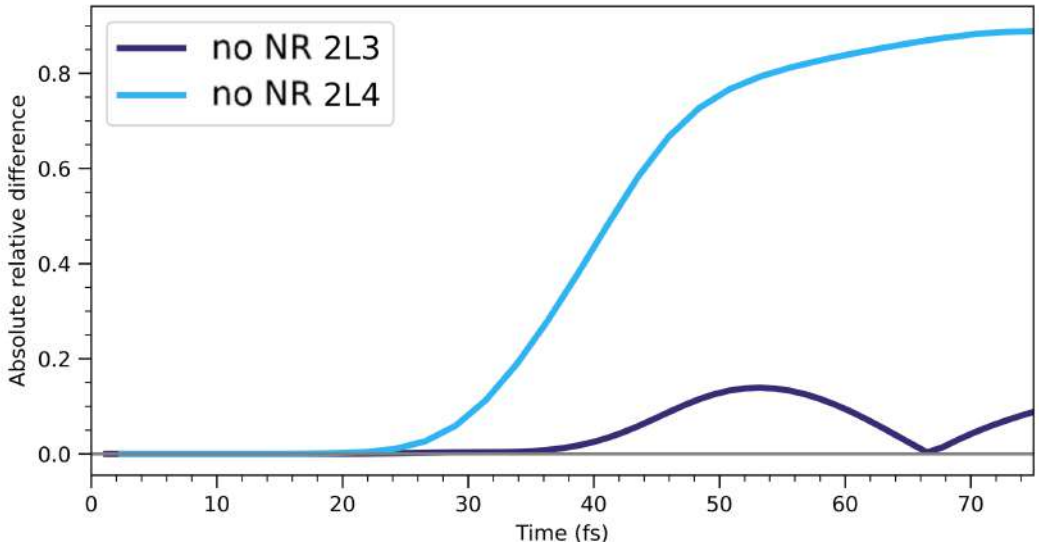

Figure S12: Absolute relative difference of the electron population of the two O atoms of HCOO* with the P1 pulse, for 2L3 and 2L4, without NR.

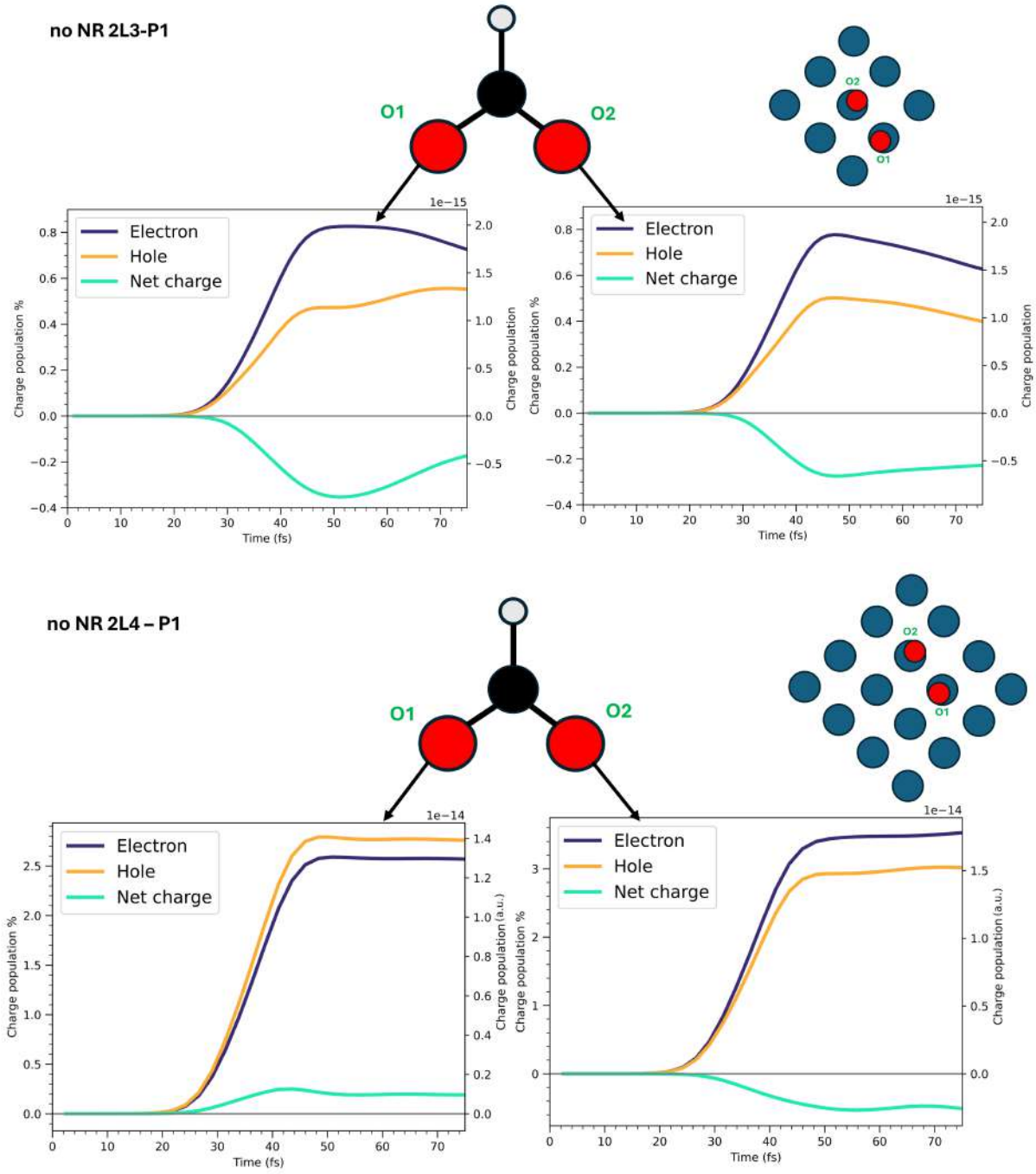

Figure S13: Top: Time evolution of the photoinduced charge populations (electron, hole and net) of O1 and O2 atoms in the bare 2L3 cluster (no NR) with P1 pulse. Bottom: Time evolution of the photoinduced charge populations (electron, hole and net) of O1 and O2 atoms in the bare 2L4 cluster (no NR) with P1 pulse.

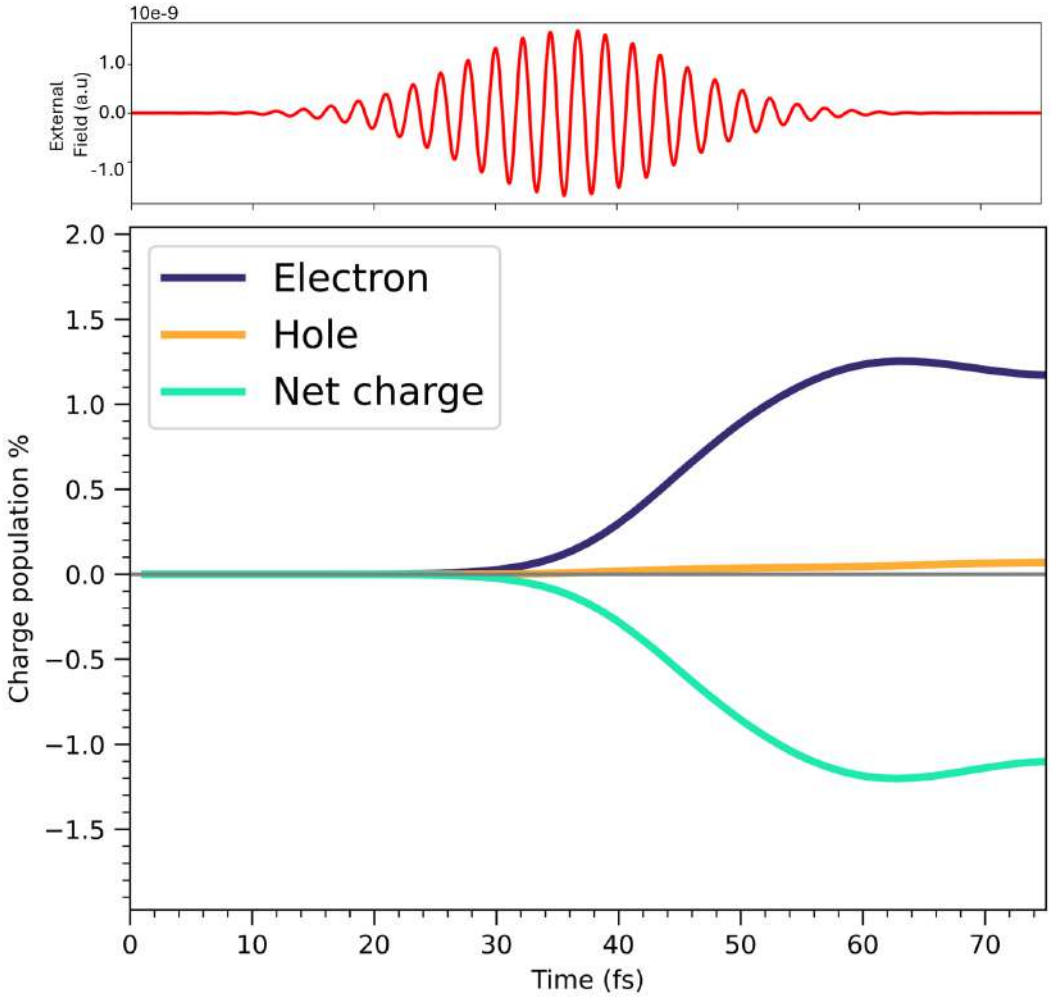

Figure S14: Time evolution of the photoinduced charge populations (electron, hole and net) of the H* fragment in presence of the NR at 0.28 nm with P1 pulse.

References

(1) Pipolo, S.; Corni, S. Real-Time Description of the Electronic Dynamics for a Molecule Close to a Plasmonic Nanoparticle. *J. Phys. Chem. C* **2016**, *120*, 28774.

(2) Dall'Osto, G.; Coccia, E.; Guido, C. A.; Corni, S. Investigating ultrafast two-pulse experiments on single DNQDI fluorophores: a stochastic quantum approach. *Phys. Chem. Chem. Phys.* **2020**, *22*, 16734.

(3) Marsili, M.; Corni, S. Electronic Dynamics of a Molecular System Coupled to a Plasmonic Nanoparticle Combining the Polarizable Continuum Model and Many-Body Perturbation Theory. *J. Phys. Chem. C* **2022**, *126*, 8768.

(4) Rüger, R.; van Lenthe, E.; Heine, T.; Visscher, L. Tight-Binding Approximations to Time-Dependent Density Functional Theory - a fast approach for the calculation of electronically excited states. *J. Chem. Phys.* **2016**, *144*, 184103.

(5) Hoerner, P.; Lee, M. K.; Schlegel, H. B. Angular dependence of strong field ionization of N_2 by time-dependent configuration interaction using density functional theory and the Tamm-Dancoff approximation. *J. Chem. Phys.* **2019**, *151*.

(6) Rüger, R.; Franchini, M.; Trnka, T.; Yakovlev, A.; van Lenthe, E.; Philipsen, P.; van Vuren, T.; Klumpers, B.; Soini, T. AMS 2025.1, SCM, Theoretical Chemistry, Vrije Universiteit, Amsterdam, The Netherlands. 2025; `http://www.scm.com`.

(7) Grobas Illobre, P.; Marsili, M.; Corni, S.; Stener, M.; Toffoli, D.; Coccia, E. Time-Resolved Excited-State Analysis of Molecular Electron Dynamics by TDDFT and Bethe–Salpeter Equation Formalisms. *J. Chem. Theory Comput.* **2021**, *17*, 6314.

(8) Dall'Osto, G.; Marsili, M.; Vanzan, M.; Toffoli, D.; Stener, M.; Corni, S.; Coccia, E. Peeking into the Femtosecond Hot-Carrier Dynamics Reveals Unexpected Mechanisms in Plasmonic Photocatalysis. *J. Am. Chem. Soc.* **2024**, *146*, 2208.

(9) Dall'Osto, G.; Vanzan, M.; Corni, S.; Coccia, M. M. E. Stochastic Schrödinger equation for hot-carrier dynamics in plasmonic systems. *J. Chem. Phys.* **2024**, *161*, 124103.

(10) Biancorosso, L.; Coccia, E. Study of the Photoinduced Charge Injection in the Reaction Intermediate of the Dehydrogenation of Formic Acid on Palladium. *J. Comput. Chem.* **2025**, *46*, e70087.

(11) Coccia, E.; Fregoni, J.; Guido, C. A.; Marsili, M.; Corni, S. Hybrid theoretical models for molecular nanoplasmonics. *J. Chem. Phys.* **2020**, *153*, 200901.

(12) Monti, M.; Stener, M.; Coccia, E. Electronic circular dichroism from real-time propagation in state space. *J. Chem. Phys* **2023**, *158*, 084102.

(13) Biancorosso, L.; D'Antoni, P.; Corni, S.; Stener, M.; Coccia, E. Time-dependent quantum/continuum modeling of plasmon-enhanced electronic circular dichroism. *J. Chem. Phys.* **2024**, *161*, 214104.

(14) Hammer, B.; Hansen, L. B.; Nørskov, J. K. Improved adsorption energetics within density-functional theory using revised Perdew-Burke-Ernzerhof functionals. *Phys. Rev. B* **1999**, *59*, 7413.

Chapter 5

Probing fast internal conversion in gas-phase thymine via TR-NEXAFS

In this project, we investigated the internal conversion dynamics of thymine using TR-NEXAFS [29]. This study highlights the potential of our theoretical framework for computing excited-state spectra of molecular systems. While the ultrafast $\pi\pi^* \rightarrow n\pi^*$ relaxation in thymine has been the subject of extensive experimental and theoretical research [185, 186, 187, 30, 188, 29], with our approach we want to go beyond the core–valence separation by efficiently evaluating excited–state transition dipole moments that couple core– and valence–excited states [189, 190, 191]. This enables the calculation of NEXAFS spectra of molecular valence–excited states at remarkably low computational cost [192].

Within the UV/visible pump–X–ray probe scheme, thymine is first excited by a $\pi \rightarrow \pi^*$ transition [29]. The $\pi\pi^*$ (S_2) state subsequently decays via internal conversion to an $n\pi^*$ (S_1) state [29]. A delayed X-ray probe then promotes an oxygen $1s$ electron into the partially vacant n orbital, yielding a characteristic $1s \rightarrow n$ feature in the NEXAFS spectrum. While ground-state molecules exhibit the lowest $1s \rightarrow \pi^*$ transition, the valence–preexcited system reveals the $1s \rightarrow n$ peak, whose time-dependent growth provides a direct measure of the $\pi\pi^* \rightarrow n\pi^*$ conversion time–on the order of a few tens of femtoseconds [29, 188].

This pump–probe NEXAFS methodology thus not only tracks ultrafast internal conversion, but also allows indirect observation of the optically dark $n\pi^*$ state, with enhanced sensitivity due to the strong, localized $1s \rightarrow n$ transition.

In order to account for the relaxation mechanism from the optically active state to the dark state we employed the SSE which models the relaxation mechanism between these two states, as described in Section 2.1.2 of Chapter 2. Selecting the pulse delay we can track the evolution of the NEXAFS spectra transitioning from those of the bright state (S_2) to the dark state (S_1).

My personal contribution to this work was to perform all the calculations along with Simone Pistillo and contributed to the interpretation of the results and to the writing of the paper. The draft of this work has been recently submitted as Pistillo

S., Biancorosso L., Dall'Osto G., Toffoli D., Fronzoni G., Coccia E. (2025) "Open–Quantum approach to time–resolved NEXAFS".

Open-quantum approach to time-resolved NEXAFS

Simone Pistillo[a], Leonardo Biancorosso[a], Giulia Dall'Osto[b], Daniele Toffoli,*

Giovanna Fronzoni,* and Emanuele Coccia*

Dipartimento di Scienze Chimiche e Farmaceutiche, Università di Trieste, via L. Giorgieri 1, 34127, Trieste, Italy

E-mail: toffoli@units.it; fronzoni@units.it; ecoccia@units.it

[a]S.P. and L.B. contributed equally to this paper.

[b]Present affiliation: Elettra Sincrotrone Trieste, SS 14 Km 163.5 in AREA Science Park, Basovizza, Trieste, Italy

Abstract

We present a real-time method based on the propagation of the time-dependent Schrödinger equation in the space of electronic states to compute NEXAFS spectra of molecules from the ground or a valence excited state. Transition dipole moments between a core and a valence state, which are needed in the case of electron dynamics from an excited state, are computed from linear-response time-dependent density functional theory implemented in the AMS package by using Slater-Condon rules following two distinct core and valence excited-state calculations. The implementation is general and compatible with any singly-excited ansatz, such as linear response GW/BSE. The method has been applied to the ultrafast internal conversion observed in the gas-phase thymine, when excited to the bright $\pi\pi^*$ (S_2) state. We have computed NEXAFS for the K-edge of oxygen from the electronic GS, from S_2 and also from the dark $n\pi^*$ (S_1) state. We have properly reproduced the experimental spectrum [Nat. Commun.,

8, 29 (2017)] after the pump, showing the peak at 526.5 eV associated with S_1. The stochastic Schrödinger equation has been used to get a time-resolved NEXAFS signal, introducing the phenomenological $S_2 \rightarrow S_1$ decay time of 60 fs from the aforementioned experimental work, thus mimicking the internal conversion without an explicit nuclear dynamics. An implicit pump initializes the thymine in the S_2 state, and an X-ray probe interrogates the system at various delay times (and distinct thymine structures), leading to a time-resolved spectral profile that captures the $S_2 \rightarrow S_1$ population transfer.

1 Introduction

In the last years, many efforts have been dedicated to studying the photophysics of nucleobases.[1–8] These molecules are central to understanding the intrinsic photostability of DNA and RNA. Thymine, in particular, exhibits unusually long excited-state lifetimes in the gas phase compared to its ultrafast relaxation in biological environments.[9–16] Time-resolved near-edge X-ray absorption fine structure (TR-NEXAFS) spectroscopy at the oxygen K-edge has provided direct insight into the internal conversion dynamics underlying this behavior.[17] TR-NEXAFS spectroscopy uses a UV or visible pump pulse to induce a valence excitation, followed by an X-ray probe pulse that excites core electrons into the newly, partially empty valence orbitals. This technique offers crucial insights into valence-excited states, and it allows access to electronic excited–states of molecular systems and probe their photophysical evolution over time.

In the case of gas-phase thymine, upon photoexcitation to the bright $\pi\pi^*$ (S_2) state, a characteristic $1s \rightarrow n$ resonance (S_1 dark state) at 526.4 eV emerges with a delay of (60 ± 30) fs, indicating an ultrafast $\pi\pi^* \rightarrow n\pi^*$ population transfer.[17] The subsequent decay of the $n\pi^*$ signal proceeds biexponentially, with lifetimes of (1.9 ± 0.1) ps and (10.5 ± 0.2) ps. Complementary non-adiabatic molecular dynamics simulations have confirmed an S_1-trapping mechanism,[18] involving rapid $S_2 \rightarrow S_1$ internal conversion via a bond-length alternation conical

intersection, followed by slow relaxation from the S_1 minimum through puckering-mediated intersections with the ground state (GS).

To fill the gap with experiments, different theoretical methods have been developed to compute NEXAFS spectra from excited states.[17,19–24] Most of the developed methods are based on a correlated wavefunction approach,[25–33] which has been widely used, offering excellent accuracy in the prediction of core excitations.[34–36] However, their high computational cost restricts their use to small or medium-sized molecules. For this reason, there has been great interest in the development of computationally cheaper DFT–based methods, such as the transition-potential DFT (TP-DFT).[37–41] This approach removes a fraction of an electron from the core orbitals, allowing orbital relaxation. It has been widely used to calculate GS NEXAFS spectra, yielding excitation energies in good agreement with experiments. Ehlert et al.[39] extended TP-DFT to core excitations from valence-excited states. This method is computationally efficient, describing core-excited states with a single electronic configuration, and is applicable to medium-to-large systems. The valence-excited state is represented by promoting an electron from an occupied to an unoccupied orbital, potentially combined with the maximum overlap method (MOM). However, both approaches may not fully ensure an accurate description of the initial valence state, which is important for capturing spectral features correctly.

Alternatively, linear response time-dependent density functional theory (LR-TDDFT), is largely used to calculate core excitations under the core valence separation scheme (CVS).[42] In the CVS, only single-electron excitations involving the core orbitals are maintained in the 1h-1p space, while excitations from valence electrons are suppressed, drastically reducing the dimension of the Casida matrix. This is justified because there is negligible coupling between valence and core excitations, due to the localized nature of the core and the large energetic gap between the core and the valence orbitals. In general, TDDFT with CVS provides good results in terms of spectral profile but can lead to errors in the calculation of absolute excitation energy ($\sim 15\,\mathrm{eV}$).[43] MOM can be combined with TDDFT under CVS to simulate

TR-NEXAFS.[44] MOM is based on the generation of new occupied molecular orbitals (MOs) from a self-consistent field (SCF) procedure, that are those most overlapped with the span of old occupied orbitals. This method provides a simple scheme to access excited-state SCF and generate relaxed molecular orbitals. This method is computationally inexpensive and provides a simple way to calculate NEXAFS spectra starting from valence-excited states.[45]

In this article, we show how NEXAFS spectra can be computed through an approach based on the propagation of the time-dependent Schrödinger equation (TDSE). The Hamiltonian eigenstates include both the core and the valence electronic states, going beyond the core-valence separation.[42] TDSE is propagated in the space of the target electronic states, setting the system in the excited state as the initial condition.

We avoid the complete calculation including both core and valence states simultaneously by reconstructing the aforementioned dipole moments using the Slater-Condon rules.[46,47] The electronic-structure approach employed in this work is standard LR-TDDFT, but the TDSE-based computational strategy is general, not depending on how electronic states are generated.

Moreover, we propose to combine the stochastic Schrödinger equation (SSE)[48–56] with TDDFT for the computation of NEXAFS spectra of thymine at various delay times between the implicit pump, which populates the S_2 state, and the X-ray probe. SSE allows us to effectively include the presence of a generic environment in the calculation, such as the photoinduced change in the molecular geometry. SSE simulations implement the relaxation from the bright S_2 to the dark S_1 state, taking as decay rate the inverse of the relaxation time T_1 (60 fs) from Ref. 17. This approach represents an effective way with an external parameter to account for population transfer in the time-resolved spectroscopic signal.

The work is organized as follows: in Section 2 the theoretical framework is given, emphasizing how our approach breaks the assumption of core-valence separation, and the use of SSE as an effective method to simulate time-resolved spectroscopic signals; computational details are collected in Section 3; results are shown and discussed in Section 4; conclusions

are reported in Section 5.

2 Theory

2.1 Electron dynamics from ground state

TDSE is given by (atomic units are used throughout the paper):

$$i\frac{d}{dt}\left|\Psi(t)\right\rangle = \hat{H}(t)\left|\Psi(t)\right\rangle, \tag{1}$$

where $|\Psi(t)\rangle$ is the electronic wavefunction and $\hat{H}(t)$ represents the time-dependent Hamiltonian operator. The Hamiltonian is partitioned as follows:

$$\hat{H}(t) = \hat{H}_0 + \hat{H}_F(t), \tag{2}$$

with $\hat{H}_0$ representing the field-free electronic Hamiltonian of the molecular system and $\hat{H}_F(t)$ describing the coupling to an external field. $\hat{H}_F(t)$ in length gauge reads as

$$\hat{H}_F(t) = -\vec{\hat{\mu}} \cdot \vec{F}(t), \tag{3}$$

where $\vec{\hat{\mu}}$ is the electric dipole operator and $\vec{F}(t)$ is the classical electric field. The external electric field is modeled as:

$$\vec{F}(t) = \vec{F}_{max} \exp\left(-\frac{(t-t_0)^2}{2\sigma^2}\right) \sin\omega t, \tag{4}$$

where $\vec{F}_{max}$ is the pulse maximum amplitude and also provides the polarization direction, t_0 and σ are the center and width of the Gaussian envelope and ω is the pulse frequency.

The wavefunction in Eq. (1) is expanded in terms of the eigenstates of $\hat{H}_0$. In case of GS NEXAFS, this expansion only includes the GS and a set of selected core excited states according to the CVS,[42] i.e.

$$|\Psi(t)\rangle = C_0(t)\,|0\rangle + \sum_{\lambda_{\text{core}}=1}^{N_{\text{core}}} C_{\lambda_{\text{core}}}(t)\,|\lambda_{\text{core}}\rangle\,, \tag{5}$$

where the GS is indicated with the ket $|0\rangle$ and its time evolution is encoded in $C_0(t)$, while $C_{\lambda_{\text{core}}}(t)$ are the time-dependent expansion coefficients of the N_{core} $|\lambda_{\text{core}}\rangle$, that denote the core eigenstates of the system.

In the 1h-1p configuration space of LR-TDDFT each eigenstate $|\lambda_{\text{core}}\rangle$ is written as a linear combination of singly excited determinants:

$$|\lambda_{\text{core}}\rangle = \sum_{i\in\text{core}}^{\text{occ}} \sum_{a}^{\text{vir}} d^a_{i,\lambda_{\text{core}}} |\psi^a_i\rangle, \tag{6}$$

where $|\psi^a_i\rangle = \hat{a}^\dagger_a \hat{a}_i |\psi_0\rangle$ represents a singly excited configuration obtained by promoting an electron from an occupied orbital i to a virtual orbital a, taking the Kohn-Sham GS determinant $|\psi_0\rangle$ as reference. According to the CVS approximation, index i in Eq.(6) is restricted to the manifold of core orbitals. The coefficients $d^a_{i,\lambda_{\text{core}}}$ are expansion parameters that specify the electronic structure of $|\lambda_{\text{core}}\rangle$.

2.2 Electron dynamics from excited state

To compute NEXAFS spectra from valence excited spectra, the wavefunction is expanded on a superposition of two subsets of eigenstates plus the GS,

$$|\Psi(t)\rangle = C_0(t)\,|0\rangle + \sum_{\lambda=0}^{N_{\text{core}}} C_{\lambda_{\text{core}}}(t)\,|\lambda_{\text{core}}\rangle + \sum_{\lambda'=0}^{N_{\text{val}}} C_{\lambda_{\text{val}}}(t)\,|\lambda_{\text{val}}\rangle\,, \tag{7}$$

where $C_{\lambda_{\text{val}}}(t)$ are the time-dependent expansion coefficients associated with the N_{val} valence-excited eigenstates $|\lambda_{\text{val}}\rangle$, while the core subset has the same meaning as in Eq. (5).

The eigenstates $|\lambda_{\text{core}}\rangle$ and $|\lambda_{\text{val}}\rangle$ are obtained from separate TDDFT calculations restricted to the corresponding excitation subspaces, using the same xc functional and basis set. Each $|\lambda_{\text{val}}\rangle$ is in turn expressed as a linear combination of singly excited determinants

spanning the valence-orbital space only

$$|\lambda_{\text{val}}\rangle = \sum_{j\in\text{val}}^{\text{occ}} \sum_{b}^{\text{vir}} d^{b}_{j,\lambda_{\text{val}}} |\psi^{b}_{j}\rangle \,. \tag{8}$$

The computational procedure for the calculation of the full matrix of transition dipole moments (TDM) is reported in Figure 1.

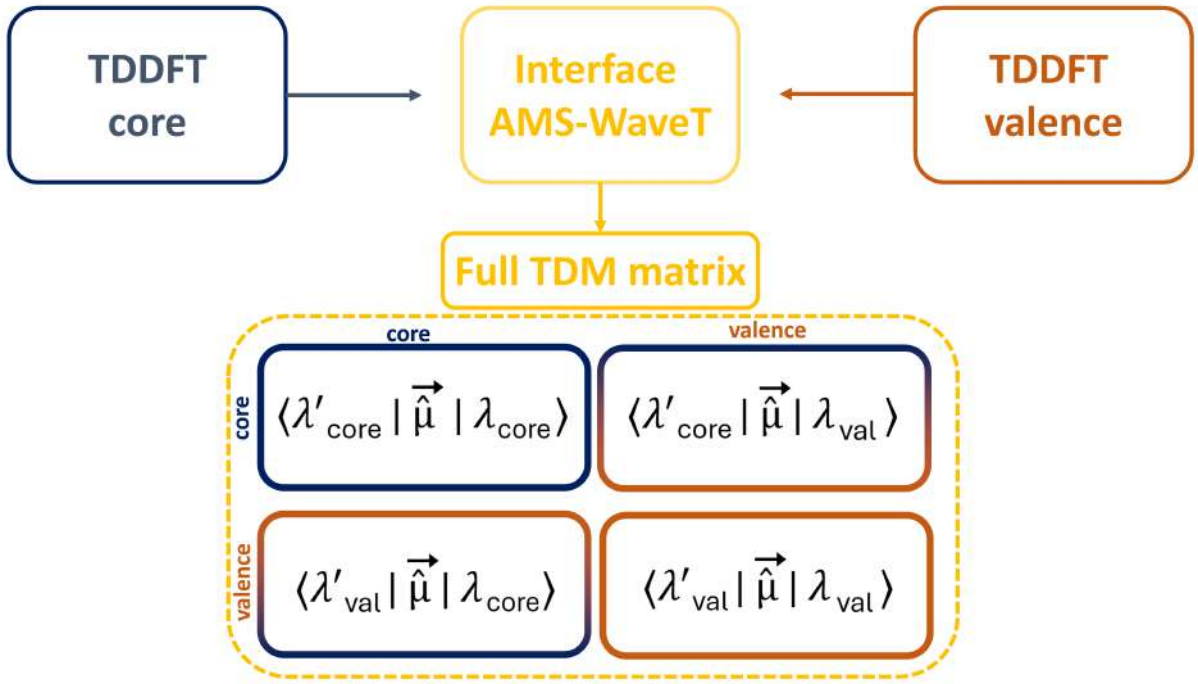

Figure 1: Scheme of the computational procedure employed to obtain the full transition dipole moments matrix among excited states.

Since having all, i.e. core+valence, excitations from TDDFT is impractical with a reasonably large basis set, the transition dipole moments between one $|\lambda_{\text{core}}\rangle$ and one $|\lambda_{\text{val}}\rangle$ is computed a posteriori using the Slater-Condon rules.[47] The strategy we followed is: i) running a TDDFT calculation for core using CVS, which provides $|\lambda_{\text{core}}\rangle$ and core-core transition dipole moments $\langle\lambda'_{\text{core}}|\vec{\hat{\mu}}|\lambda_{\text{core}}\rangle$; ii) running a TDDFT calculation for valence excitations, which gives $|\lambda_{\text{val}}\rangle$ and $\langle\lambda'_{\text{val}}|\vec{\hat{\mu}}|\lambda_{\text{val}}\rangle$; iii) exploiting that TDDFT eigenstates from the two simulations are orthogonal, we build $\langle\lambda'_{\text{core}}|\vec{\hat{\mu}}|\lambda_{\text{val}}\rangle$ ($\langle\lambda'_{\text{val}}|\vec{\hat{\mu}}|\lambda_{\text{core}}\rangle$) using the Slater-

Condon rules for one-electron operators. Constructing the TDM matrix is accomplished by a postprocessing code,[47,57] which interfaces AMS,[58] i.e. the quantum-chemistry code, with WaveT,[59] i.e. the propagation code. This choice allows us to go beyond the CVS.
After energies and transition dipole moments are computed, TDSE propagation is performed setting as an initial condition $|C_0(t=0)|^2 = 1$ or $|C_{\lambda_{\mathrm{val}}}(t=0)|^2 = 1$, to get GS or excited-state NEXAFS spectra respectively, as shown below.

2.3 Computing the absorption spectrum

Substituting Eq. (5) or Eq. (7) into Eq. (1) allows us to write a matrix formulation of the TDSE:

$$i\frac{d\mathbf{C}(t)}{dt} = \mathbf{H}(t)\mathbf{C}(t), \tag{9}$$

with $\mathbf{C}(t)$ the coefficient vector and $\mathbf{H}(t)$ the matrix representation of the Hamiltonian at time t. For generic states $|\lambda\rangle$ and $|\lambda'\rangle$ one obtains

$$\langle\lambda'|\,\hat{H}(t)\,|\lambda\rangle = E_\lambda\delta_{\lambda'\lambda} - \vec{F}(t)\,\langle\lambda'|\,\vec{\hat{\mu}}\,|\lambda\rangle\,. \tag{10}$$

Equation (10) for the ground- or excited-state dynamics is in practice propagated. The time–dependent electric dipole moment from the electronic dynamics simulation is then written as:

$$\vec{\mu}(t) = \sum_{\lambda_{core}} C^*_{\lambda_{core}}(t)C_0(t)\,\langle\lambda_{core}|\,\vec{\hat{\mu}}\,|0\rangle + \sum_{\lambda'_{\mathrm{core}}\neq\lambda_{\mathrm{core}}} C^*_{\lambda'_{\mathrm{core}}}(t)\,C_{\lambda_{\mathrm{core}}}(t)\;\langle\lambda'_{\mathrm{core}}|\,\vec{\hat{\mu}}\,|\lambda_{\mathrm{core}}\rangle \quad + \mathrm{cc}, \tag{11}$$

for GS NEXAFS, or as:

$$\begin{aligned}\vec{\mu}(t) &= \sum_{\lambda_{core}} C^*_{\lambda_{core}}(t)C_0(t)\,\langle\lambda_{core}|\,\vec{\hat{\mu}}\,|0\rangle + \sum_{\lambda_{val}} C^*_{\lambda_{val}}(t)C_0(t)\,\langle\lambda_{val}|\,\vec{\hat{\mu}}\,|0\rangle \\ &+ \sum_{\lambda'_{\rm val}\lambda_{\rm core}} C^*_{\lambda'_{\rm val}}(t)\,C_{\lambda_{\rm core}}(t)\;\langle\lambda'_{\rm val}|\,\vec{\hat{\mu}}\,|\lambda_{\rm core}\rangle \\ &+ \sum_{\lambda'_{\rm core}\neq\lambda_{\rm core}} C^*_{\lambda'_{\rm core}}(t)\,C_{\lambda_{\rm core}}(t)\;\langle\lambda'_{\rm core}|\,\vec{\hat{\mu}}\,|\lambda_{\rm core}\rangle \\ &+ \sum_{\lambda'_{\rm val}\neq\lambda_{\rm val}} C^*_{\lambda'_{\rm val}}(t)\,C_{\lambda_{\rm val}}(t)\;\langle\lambda'_{\rm val}|\,\vec{\hat{\mu}}\,|\lambda_{\rm val}\rangle \quad + \text{cc},\end{aligned} \tag{12}$$

for excited-state NEXAFS.

The absorption spectrum is finally given by:

$$P_{nl}(\omega) = \frac{1}{2\pi F^0_n(\omega)} \int_0^{+\infty} \Delta\mu_l(t)\, e^{i(\omega+i\Gamma)t}\, dt, \tag{13}$$

where $\Delta\mu_l(t) = \mu_l(t) - \mu_l(0)$ represents the lth component of the induced electric dipole moment, the factor Γ is a damping parameter that is used to describe the excited state lifetime, and $F^0_n(\omega)$ is the Fourier transform of the nth component of the external electric field. When rotationally averaged, the spectrum is indicated as P.

It is important to note that the spectrum obtained with the dipole in Eq. (12) contains both the valence and core contributions; the core spectrum of interest relates to the excited state used to define the initial condition of the TDSE and to the terms in Eq. (13) involving core states only.

2.4 Stochastic Schrödinger equation

SSE extends the traditional time-dependent Schrödinger equation to account for interactions with an external environment, allowing the treatment of the quantum system as open. SSE has been implemented in the WaveT suite[60] within the Markovian limit,[56] and used in many spectroscopic applications, such as in the detection of quantum coher-

ence in isolated molecules,[61,62] the study of the role of coherence in plasmonic-mediated enhancement/quenching of a signal, Raman[63] and hot-carrier dynamics in plasmonic photocatalysis.[64,65] In the Markovian limit, SSE is given by:

$$i\frac{d}{dt}|\Psi_S(t)\rangle = \hat{H}(t)|\Psi_S(t)\rangle + \sum_q^M l_q(t)\hat{S}_q|\Psi_S(t)\rangle - \frac{i}{2}\sum_q^M \hat{S}_q^\dagger \hat{S}_q|\Psi_S(t)\rangle, \tag{14}$$

where the operator $\hat{S}_q$ is representative of the environment effect through the M interaction channels indexed by q. The dissipation induced by the environment is included by the non-Hermitian term $-\frac{i}{2}\sum_q^M \hat{S}_q^\dagger \hat{S}_q$. The fluctuation term $\sum_q^M l_q(t)\hat{S}_q$ is modeled by a Wiener process $l_q(t)$, also generated by the environment. The environment generates population and/or coherence relaxation, depending on the form of $\hat{S}_q$. The system S coincides with the electronic degrees of freedom of the molecule. Thus, $|\Psi_S(t)\rangle$ coincides with $|\Psi(t)\rangle$ introduced in Section 2.1. By averaging a large enough number of independent SSE realizations, one converges to the outcome of the Lindblad equation,[66] obtaining population and coherence dynamics.[61]

Excited state relaxation is the only decay channel included in this work, therefore the definition $\hat{S}_\lambda \equiv \hat{S}_q$ is used to define relaxation of the generic state $|\lambda\rangle$.[67] Generally, it can be due to photon emission (radiative decay) or to nonradiative decay (e.g. through internal conversion). The former can be seen as an effect of the electromagnetic field seen as an environment; the latter can be an internal conversion due to a conical intersection, as in the present case of thymine.[68,69] In the SSE framework, such a process is simply modeled by the operator

$$\hat{S}_{\lambda\lambda'} = \sqrt{\Gamma_{\lambda\lambda'}}|\lambda'\rangle\langle\lambda|, \tag{15}$$

which induces an exponential decay of the population $|C_\lambda(t)|^2$, with a rate given by $\Gamma_{\lambda\lambda'}$. The value of $\Gamma_{\lambda\lambda'}$ is provided by experimental work or by simulation of nonadiabatic molecular dynamics. The complexity of the internal conversion is therefore encoded in a quantum operator which promotes population transfer between two electronic states. The operator

in Eq. (15) has been applied to a single pair of valence excited states $|\lambda_{\text{val}}\rangle$ to model the internal conversion in thymine ($M = 1$ in Eq. 14).

3 Computational details

Geometry optimization of the GS was performed at the B3LYP/TZP level, whereas excited–state geometry optimizations were performed at the B3LYP/TZP level within the Tamm–Dancoff approximation (TDA) implementation of the Amsterdam Modeling Suite (AMS).[58] All Cartesian coordinates are collected in the Supporting Information (SI, Figure S1-S3). Excited-state properties were then computed using TDDFT at the CAM-B3LYP/TDA level with a TZP basis set for all atoms, except for oxygen, for which an ET-QZ3P-1DIFFUSE basis set was employed. The TDA approximation was adopted to correctly reproduce the expected ordering of excited states across all geometries. A comparison between TDA and full TDDFT calculations is provided in Figure S4 of the SI.

For core excitations, we apply the CVS approximation whereby only electron excitations from the two lowest occupied orbitals (the oxygen 1s orbitals) were considered. A total of 100 excited states were included for the core calculations, whereas 10 states were considered for valence excitations. For the subsequent electronic dynamics, 24 excited states were included in total: 10 valence and 14 core excitations. The number of core states was restricted to those lying below the ionization threshold of the highest energy O 1s orbital, corresponding to the negative of the KS eigenvalue (-522.6 eV).

Electronic dynamics were propagated for 100 fs using a time step of $\delta t = 1.2$ as. The external field was modeled as a Gaussian-enveloped sinusoidal pulse with intensity $I = 10^8$ W/cm^2, photon energy $\omega = 522.38$ eV, and a FWHM of 94 as. SSE simulations were carried out under the same conditions, averaging over 180 trajectories. The NEXAFS spectrum is fully converged with 180 SSE trajectories, as shown in Figure S5 of SI. Laser pulse time delays were set at 10, 20, 60, and 70 fs.

4 Results and discussion

In the approach used in the present work, the wavefunction is expanded as a superposition of eigenstates obtained from two separate TDDFT/TDA calculations: one including only core excitations, and obtained within the CVS approximation, and the other including both core and valence excitations, both referenced to the GS (see Eq. (11) and Eq. (12) respectively). A subsequent real-time propagation of the wavefunction allows us to calculate the spectrum starting from a specific state within the expansion.

Figure 2 shows a comparison of GS oxygen K-edge NEXAFS spectrum of thymine calculated within LR-TDDFT/TDA with AMS using the Casida approach (bottom spectrum) and real-time propagation of the expanded wavefunction (top spectrum) with WaveT. The real time propagation was performed, including only core excitations to bound excited states, i.e. below the O1s threshold. In this way, only states whose excitation energy is below 522.6 eV were propagated. The two computed spectra are in perfect agreement. The GS NEXAFS spectrum of thymine is characterized by two main peaks with similar intensity, originating from the oxygen $1s$ (O1s) transitions to π^* virtual orbitals of the two nonequivalent O sites shown in the right panel of Figure 2. Atom labels are also provided in the same Figure. The first peak at 517.9 eV is assigned to a transition dominated by $1s_{\mathrm{O2}} \rightarrow \pi^*$ configuration, with a smaller contribution of the $1s_{\mathrm{O2}} \rightarrow 2\pi^*$ configuration. In Figure 2 the occupied/virtual MO pairs involved in the main transitions are reported. The $1\pi^*$ MO has a strong C-O antibonding character localized on O2, resulting in a strong spatial overlap between the initial and final states, leading to a high transition dipole moment. The second peak at 518.8 eV is originated by a transition dominated by the $1\mathrm{s}_{\mathrm{O1}} \rightarrow 2\pi^*$ configuration. The $2\pi^*$ MO has a strong C-O antibonding character of both non-equivalent thymine oxygen atoms, with prevalence of O1. In the energy region above 521 eV the transitions are characterized mainly by excitations described by $1s_{\mathrm{O1/O2}} \rightarrow ns, np$ Rydberg states, with minor contribution from $1s_{\mathrm{O1/O2}} \rightarrow \pi^*$ configurations. Figure S6 of SI shows the comparison between the computed GS spectrum (in frequency domain by using the AMS code) with the experimental one from

Ref. 17, resulting in a good agreement.

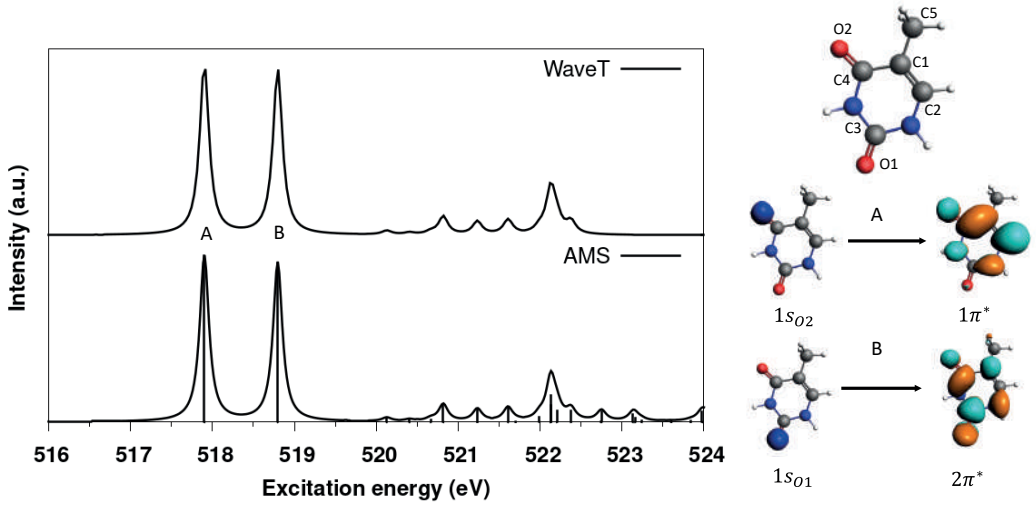

Figure 2: Comparison of the TDDFT/TDA GS O1s NEXAFS spectrum of thymine computed in time- (top) and frequency domain (bottom). Also reported are the occupied/virtual MO pairs mostly involved in the excitations labelled with A and B in the Figure and the chemical structure of thymine with the indication of the non equivalent O/C atoms.

As mentioned in the Introduction, thymine is characterized by a $\pi\pi^*$ excited state (S_2) that is optically bright, and a dark lower-energy $n\pi^*$ state (S_1). From the work of Wolf et al. in Ref. 17 it was observed that internal conversion process ($S_2 \rightarrow S_1$) leads the system to relax into the $n\pi^*$ state, with a measured lifetime for this process of 60 $\pm$ 30 fs. To correctly simulate time-resolved spectra, it is necessary to calculate core-level spectra starting from excited states. Simulation of the valence spectra provides insights into the nature of the lowest excited states of the system; the valence absorption spectrum is reported in Figure S7 in SI together with an assignment of the main features. In agreement with experimental observations, the first excitation (S_1) at 5.14 eV, exhibits low intensity, and it is mainly characterized by a $n\rightarrow$ $1\pi^*$ transition. The second, much more intense excitation (S_2), appears at 5.50 eV and corresponds predominantly to a $\pi \rightarrow \pi^*$ transition. Table S1 of the SI collects the excitation, oscillator strength, and composition of the low-lying valence states of thymine.

To capture the effect of structural relaxation on computed spectral features, the NEXAFS

spectrum of the S_1 excited state was calculated at its optimized geometry, and it is reported in Figure 3. With respect to the GS Franck-Condon (FC) geometry, the O2–C4 bond elongates from 1.22 Å to 1.34 Å, while the O1–C3 bond remains essentially unchanged. A contraction of the C1–C4 bond from 1.47 Å to 1.37 Å is also observed, accompanied by a reduction of the O2–C4–N bond angle from 120° to 112°. These structural modifications do not affect the planarity of the molecule. According to Ref. 14, the relaxation pathway occurs rapidly through the $\pi\pi^*/n\pi^*$ conical intersection, which is directly accessible without an intervening barrier. Once the system has transferred to the $n\pi^*$ state, it can remain trapped and decay slowly to the GS over a timescale of approximately 6 ps. This relatively long lifetime allows the system to relax to a local minimum on the potential energy surface. The NEXAFS spectrum reported in Figure 3 is calculated for the first excited state geometry, under the assumption that the population resides entirely in S_1. The S_1 spectrum is characterized by a single strong peak at 513.0 eV (peak A), which is red-shifted by 4.9 eV regarding the first peak of the GS spectrum. The high intensity of this transition is consistent with the non-bonding character of the MO involved. Analysis shows that this excitation is dominated by $1s_{O2} \rightarrow n$ transition. The n orbital is strongly localized on O2 of thymine, which enables a large spatial overlap between the initial and final states, resulting in a strong transition dipole moment. By contrast, the analogous $1s_{O1} \rightarrow n$ transition involves a much weaker overlap, since the n orbital has a small contribution from O1, leading to a low intensity peak appearing at 515.6 eV (peak B). A comparison between the spectra computed for the S_1 state at the FC geometry and at the nπ^* local minimum is presented in the left panel of Figure S8 of SI.

Note that in this approach, all excitations are defined regarding the GS reference. Calculation of NEXAFS spectra from excited states means that in the initial state the system has a hole localized in the n or π MOs and an electron in the $1\pi^*$ MO. Consequently, our method provides a reliable description of all excitations involving $1s \rightarrow$ SOMO transitions, since these can be represented as singly excited Slater determinants with respect to the GS.

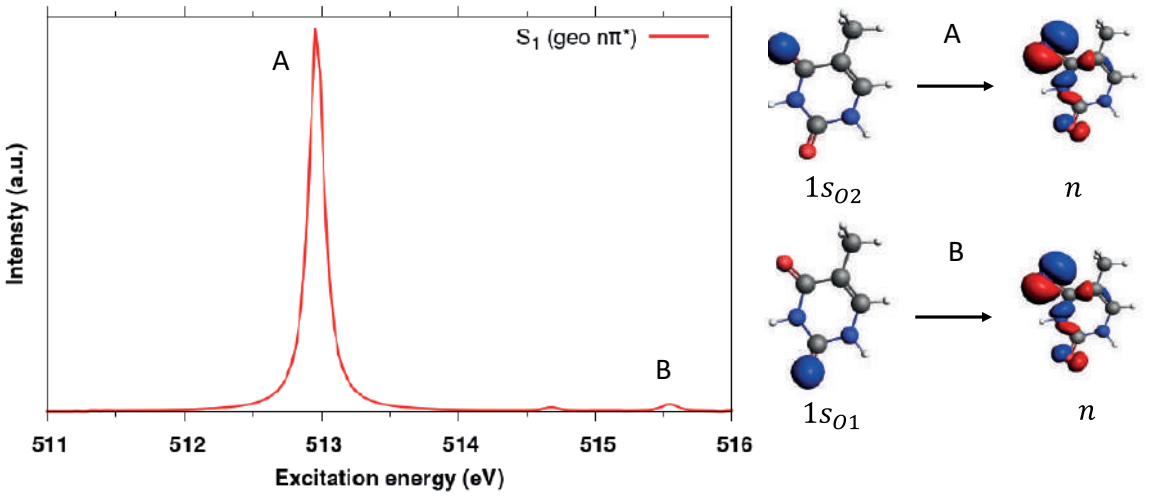

Figure 3: O1s NEXAFS spectrum of the S_1 excited state of thymine at the optimized nπ^* equilibrium geometry. Also reported are the occupied/virtual MO pairs involved in the transitions corresponding to the peaks labelled with A and B.

Excitations at higher energies are treated as processes in which the $1s \rightarrow$ SOMO excitation is accompanied by promotion of the electron from the $1\pi^*$ orbital into a higher-lying MO. In Figure 4 a comparison between the experimental measurement from Ref. 17 and the computed spectrum is shown. In the experiment an initial pump at 267 nm was used to promote the optically bright transition, and after 2 ps a probe in region of the NEXAFS oxygen K-edge was used to map the electronic states. Within 2 ps, the system has the time to relax into local minima, justifying the use of $n\pi^*$ optimized geometry for the calculated spectrum. The effect of the pump is observed by the presence of new spectral feature appearing at lower energy compared to the first spectral feature visible in the GS spectrum. To compare the experiment with theory, a rigid shift of the computed spectra of +13.5 eV was applied. From the experiment, it was estimated that 13% of the population was transferred from GS to the excited state. The rotationally-averaged GS and S_1 spectra (Section 2.3) were weighted with respect to the population transfer by using the formula:

$$\mathrm{P}_{tot} = \mathrm{p} \cdot \mathrm{P}_{S_1} + (1 - \mathrm{p}) \cdot \mathrm{P}_{GS} \tag{16}$$

where p is the fraction of population transferred into excited state while P_{S_1} and P_{GS} denote the NEXAFS spectra of the first excited state and the GS respectively. According to the findings of Ref. 70, the S_1 spectrum is weighted by a factor of 0.13 and the GS spectrum by a factor of 0.87. The calculation shows excellent agreement with the experimental results, accurately reproducing both the separation in energy of the peaks (4.9 eV from the calculation compared with 5 eV from the experiment) and the relative intensity between S_1 and GS main peaks.

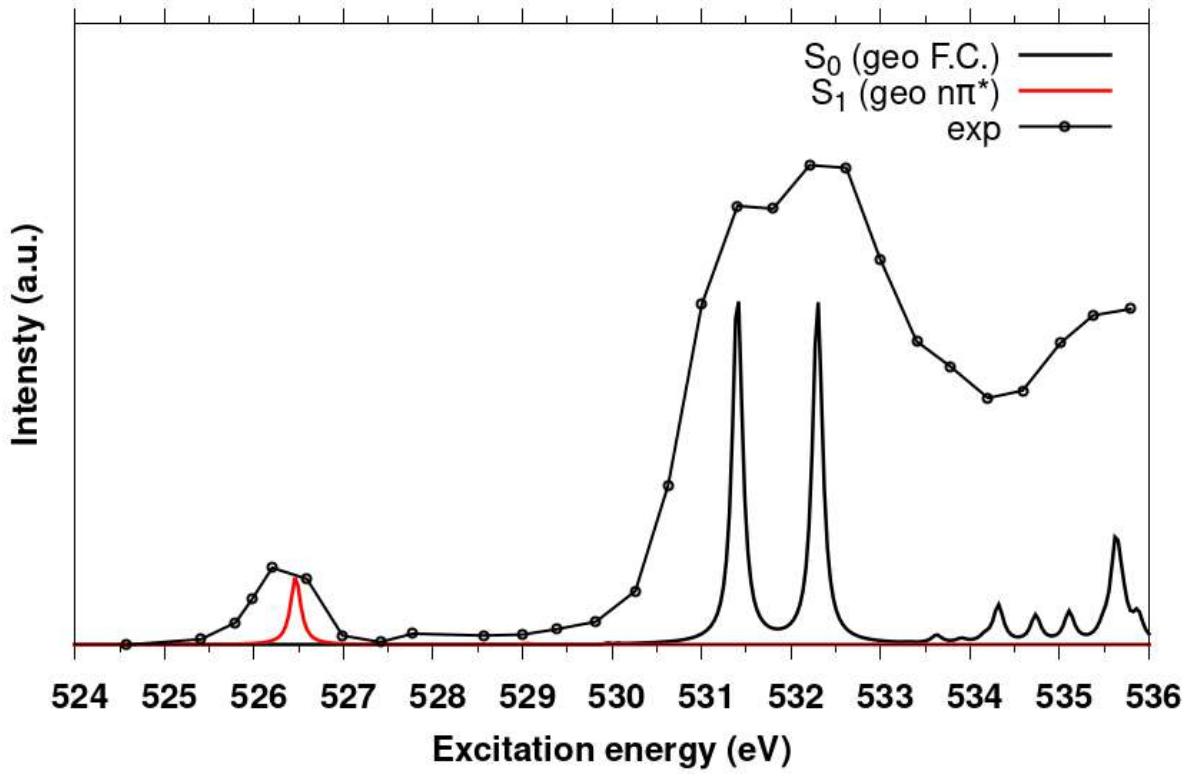

Figure 4: Comparison between theoretical and experimental O1s NEXAFS spectra of thymine. The intensity of the GS and S_1 theoretical NEXAFS spectra are scaled according to the populations reported in Ref. 70. A rigid energy shift of +13.5 eV was applied to the computed spectrum for a better comparison with the experiment.

In Figure 5 the NEXAFS spectra calculated starting from the S_2 electronic state is reported. Since the internal conversion process occurs rapidly, it is assumed that evolution of the spectra from $S_2 \rightarrow S_1$ start from the FC geometry, i.e. the optimized GS one. The main peak B appears at 514.6 eV, shifted by -3.3 eV with respect to the first peak (A) of the

GS spectrum of Figure 2. This feature is characterized mainly by the $1s_{O1} \rightarrow \pi$ transition. The weaker peak A centered at 512.4 eV is dominated by a $1s_{O2} \rightarrow \pi$ transition and appears at energies closer to the main peak of the S_1 spectrum. In principle, the NEXAFS spectrum from S_2 shows a signature fingerprint at 514.6 eV that could be detected by a time-resolved experiment, since it appears in a region that does not overlap other signals. The absence of any spectral feature associated with the spectrum from S_2 in the 2-ps experimental spectrum provides further confirmation that thymine has fully relaxed into a low-lying electronic state. The comparison between the spectra calculated from S_2 in the FC geometry and in the optimized S_2 geometry is reported in the right panel of Figure S8 of SI. Contrary to what was obtained for the spectrum from S_1, in this case the different geometries have a more pronounced impact on the spectral shape.

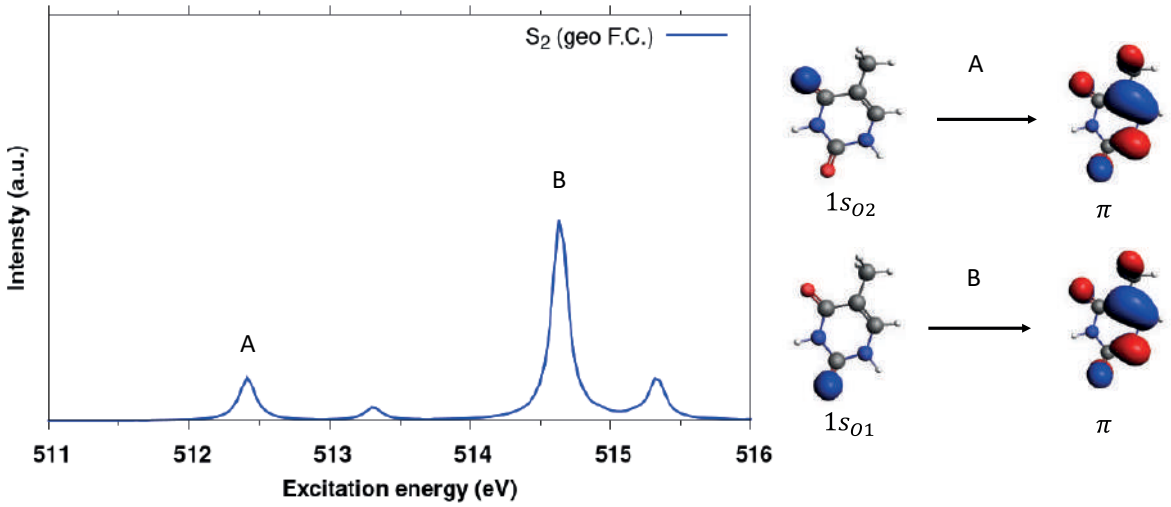

Figure 5: NEXAFS spectrum calculated from S_2 state using FC geometry and the main MOs involved in the transitions.

So far, NEXAFS spectra at fixed excited-state geometry (S_1 or S_2) have been reported. In order to get a time-resolved NEXAFS signal in an effective way, we have used SSE to take into account the effect of $S_2 \rightarrow S_1$ relaxation process due to internal conversion. This formalism allows to incorporate relaxation channels into the electronic dynamics and thus to simulate the evolution of the spectra during the $S_2 \rightarrow S_1$ transition. As described previously,

a relaxation time of 60 ± 30 fs was estimated experimentally for the gas-phase thymine,[17] with the subsequently $S_1 \rightarrow S_0$ relaxation that takes place in the picosecond scale. This process is schematically described in Figure 6.

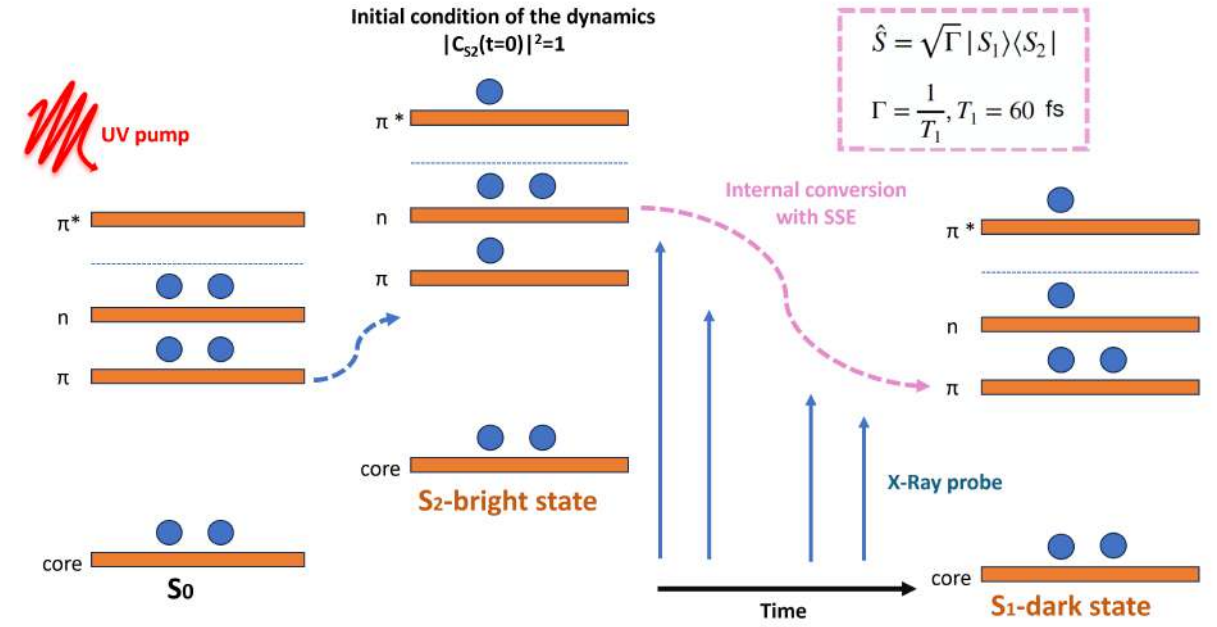

Figure 6: Representation of the UV pump/X-ray probe setup used to study the internal conversion from the S_2-bright state to the S_1-dark state. The scheme shows the initial photo–excitation, the electronic relaxation described by SSE dynamics, and the computational framework used to simulate the process. Since only a single channel is used, no subscript is applied to $\hat{S}$ and Γ.

Relaxation was included through a decay channel modeled as in Eq. 15, $\hat{S} = \sqrt{\Gamma}|S_1\rangle\langle S_2|$, with $\Gamma = 1/60$ fs^{-1} that regulates the exponential decay of the population from S_2 to S_1. Since only a single channel is defined, subscript in $\hat{S}$ and Γ have been removed. The response of the system was computed at four representative time delays: 10, 20, 60, and 70 fs. For time delays of 10 and 20 fs, the calculation was performed at the FC geometry, reflecting that the S_2 energy surface is flat and the geometry could remain close to the GS immediately after excitation. For time delays of 60 and 70 fs, the calculation has been performed at the optimized S_1 geometry, as structural relaxation toward S_1 is expected to occur already within 30 fs. Figure 7 reports both the population dynamics of S_2 and S_1 and the associated spectra.

As anticipated, the S_2 population decays exponentially while S_1 increases correspondingly. The spectral evolution closely reflects these dynamics. At 10 and 20 fs, clear contributions from S_1 are already visible despite its low population, a result of the strong intensity of its FC spectral features. This implies that even small population of S_1 can produce a pronounced spectral fingerprint. At 60 and 70 fs, the spectra are dominated by S_1, with its main peak at 513 eV increasing in intensity, while features at 514.6 and 511.9 eV associated with S_2 decrease.

The similarity of the spectra at 60 and 70 fs reflects the near-saturation of the S_1 population by that stage. An additional interesting observation concerns the intensity evolution of the S_1 peak around 512–513 eV. Between 10 and 20 fs, this peak gains intensity even though the total S_1 population is still very low. This behavior highlights the sensitivity of NEXAFS on the nature of the electronic state and shows that S_1 can be spectroscopically detected well before it dominates the population dynamics.

In Figure S9 we reported the time-resolved spectra of thymine calculated using S_2 geometry for 10 and 20 fs and S_1 geometry for the calculation at 60 and 70 fs. In this case, we assume that relaxation towards the S_2 geometry occurs within 10 fs. It is also worth pointing out that at the TDDFT level of theory, the S_2 geometry is more a saddle point than a minimum, in agreement with coupled cluster findings.[17] Without an explicit nuclear dynamics, this choice and that done in Figure 6 are equally acceptable, and therefore should be considered on the same level. On the other hand, Figure S10 reports the spectra calculated at the same delay times but only at FC geometry. In both cases we can see a dominating contribution from the S_1 signal even when its population is low and the main differences between the two sets of spectra are mainly related to the signal from S_2 at 10 and 20 fs, due to the different geometries used for those calculations.

By combining accurate excited-state calculations with SSE dynamics, we can reproduce experimental time-resolved spectra and interpret them in terms of underlying electronic and structural processes. In particular, our analysis confirms that the experimentally observed

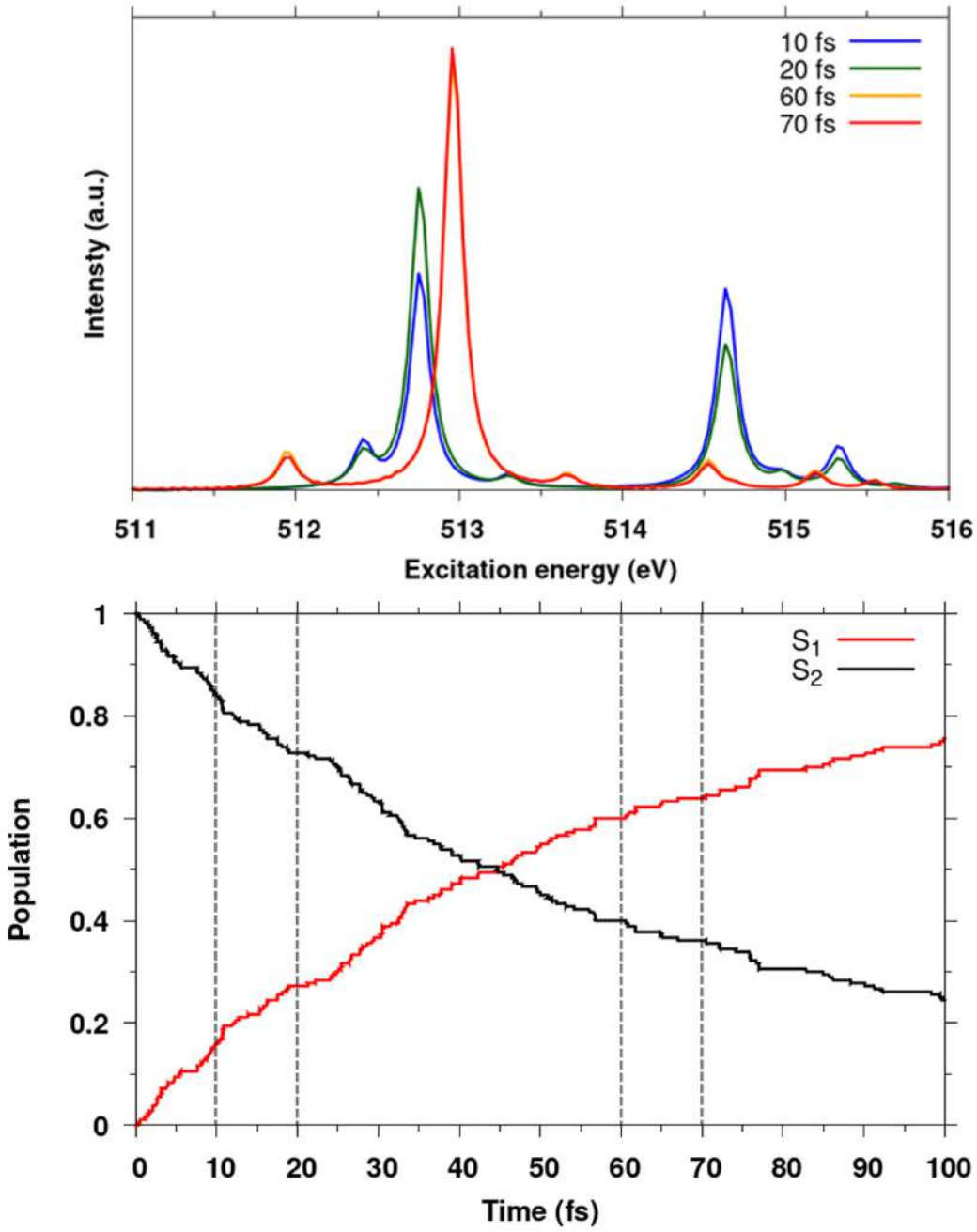

Figure 7: Top panel: Time–resolved NEXAFS spectra of thymine at 10, 20, 60 and 70 fs. Bottom panel: Time evolution of the electronic state populations, showing the ultrafast population transfer from S_2 (black) to S_1 (red) within the first tens of femtoseconds. The vertical dashed lines indicate the time delays at which the NEXAFS spectra are evaluated.

low-energy peaks originates from S_1. This work shows how theoretical spectroscopy can serve as a bridge between ultrafast experiments and microscopic dynamics, providing a detailed

understanding of photophysical relaxation in nucleobases.

5 Conclusions

This work shows an effective strategy and a successful application, within a theoretical and computational framework, for calculating time-resolved NEXAFS spectra from excited states. A novel real-time method based on the propagation of the TDSE in the space of electronic states is presented. Within this approach, NEXAFS spectra are computed from the GS or a valence excited state, thus going beyond the CVS scheme. To simulate the time-resolved NEXAFS signal, real-time propagation was combined with the SSE. This allowed for the inclusion of relaxation dynamics, modeling the ultrafast population transfer from the bright S_2 state to the dark S_1 state by introducing a phenomenological $S_2 \rightarrow S_1$ T_1 of 60 fs. The method was applied to the ultrafast internal conversion observed in gas-phase thymine when excited to the bright $\pi\pi^*$ (S_2) state, successfully calculating NEXAFS for the K-edge of oxygen from the GS, S_2, and the $n\pi^*$ (S_1) state. The calculations properly reproduced the experimental spectrum observed after the UV pump. The analysis confirms that the experimentally observed low-energy peak is associated with the S_1 state. This peak is calculated at 526.5 eV (or 513.0 eV before applying a 13.5 eV shift for comparison with experiment), and its high intensity is consistent with the non-bonding character of the molecular orbital involved (the $1s_{O2} \rightarrow n$ transition).

The simulations highlighted that clear contributions from S_1 are visible in the spectra at early times (10 and 20 fs), even when the population of S_1 is low. This is attributed to the strong intensity of the S_1 spectral features, demonstrating that this state can be detected spectroscopically well before it dominates the population dynamics.

Acknowledgement

Financial support from ICSC – Centro Nazionale di Ricerca in High Performance Computing, Big Data and Quantum Computing, funded by European Union – NextGenerationEU is gratefully acknowledged. This work has been supported by the project CHANGE funded by the PRIN 2022 - Progetti di Rilevante Interesse Nazionale (grant 20224KAC28). We also acknowledge the financial contribution provided by Italian MIUR through PRIN project "ODYSSEY" (grant 2022AXN9EK).

Supporting Information Available

Cartesian coordinates for GS, S_1 and S_2 optimized geometry of thymine. Comparison between full TDDFT and TDDFT/TDA. Convergence of SSE calculations. Comparison between the computed and the experimental GS NEXAFS spectrum. Valence spectrum and excited states. Excited-state NEXAFS spectra at different geometries. Time-resolved NEXAFS spectra at different geometries.

Data Availability

The data that support the findings of this study are available from the corresponding authors upon reasonable request.

References

(1) Ullrich, S.; Schultz, T.; Zgierski, M. Z.; Stolow, A. Electronic relaxation dynamics in DNA and RNA bases studied by time-resolved photoelectron spectroscopy. *Phys. Chem. Chem. Phys.* **2004**, *6*, 2796.

(2) Yu, H.; Sanchez-Rodriguez, J. A.; Pollum, M.; Crespo-Hernández, C. E.; Mai, S.; Marquetand, P.; González, L.; Ullrich, S. Internal conversion and intersystem crossing pathways in UV excited, isolated uracils and their implications in prebiotic chemistry. *Phys. Chem. Chem. Phys.* **2016**, *18*, 20168.

(3) McFarland, B.; Farrell, J.; Miyabe, S.; Tarantelli, F.; Aguilar, A.; Berrah, N.; Bostedt, C.; Bozek, J.; Bucksbaum, P.; Castagna, J.; others Ultrafast X-ray Auger probing of photoexcited molecular dynamics. *Nat. Commun.* **2014**, *5*, 4235.

(4) Gador, N.; Samoylova, E.; Smith, V. R.; Stolow, A.; Rayner, D. M.; Radloff, W.; Hertel, I. V.; Schultz, T. Electronic structure of adenine and thymine base pairs studied by femtosecond electron- ion coincidence spectroscopy. *J. Phys. Chem. A* **2007**, *111*, 11743.

(5) Canuel, C.; Mons, M.; Piuzzi, F.; Tardivel, B.; Dimicoli, I.; Elhanine, M. Excited states dynamics of DNA and RNA bases: Characterization of a stepwise deactivation pathway in the gas phase. *J. Chem. Phys* **2005**, *122*, 074316.

(6) Kang, H.; Lee, K. T.; Jung, B.; Ko, Y. J.; Kim, S. K. Intrinsic lifetimes of the excited state of DNA and RNA bases. *J. Am. Chem. Soc.* **2002**, *124*, 12958.

(7) Barbatti, M.; Aquino, A. J.; Szymczak, J. J.; Nachtigallová, D.; Hobza, P.; Lischka, H. Relaxation mechanisms of UV-photoexcited DNA and RNA nucleobases. *Proc. Natl. Acad. Sci.* **2010**, *107*, 21453.

(8) Improta, R.; Santoro, F.; Blancafort, L. Quantum Mechanical Studies on the Photophysics and the Photochemistry of Nucleic Acids and Nucleobases. *Chem. Rev.* **2016**, *116*, 3540.

(9) González-Vázquez, J.; González, L.; Samoylova, E.; Schultz, T. Thymine relaxation after UV irradiation: the role of tautomerization and $\pi\sigma^*$ states. *Phys. Chem. Chem. Phys.* **2009**, *11*, 3927.

(10) Samoylova, E.; Schultz, T.; Hertel, I.; Radloff, W. Analysis of ultrafast relaxation in photoexcited DNA base pairs of adenine and thymine. *Chem. Phys.* **2008**, *347*, 376.

(11) Ligare, M.; Siouri, F.; Bludsky, O.; Nachtigallova, D.; De Vries, M. Characterizing the dark state in thymine and uracil by double resonant spectroscopy and quantum computation. *Phys. Chem. Chem. Phys.* **2015**, *17*, 24336.

(12) Stojanović, L.; Bai, S.; Nagesh, J.; Izmaylov, A. F.; Crespo-Otero, R.; Lischka, H.; Barbatti, M. New insights into the state trapping of UV-excited thymine. *Molecules* **2016**, *21*, 1603.

(13) Szymczak, J. J.; Barbatti, M.; Soo Hoo, J. T.; Adkins, J. A.; Windus, T. L.; Nachtigallová, D.; Lischka, H. Photodynamics simulations of thymine: Relaxation into the first excited singlet state. *J. Phys. Chem. A* **2009**, *113*, 12686.

(14) Parker, S. M.; Roy, S.; Furche, F. Multistate hybrid time-dependent density functional theory with surface hopping accurately captures ultrafast thymine photodeactivation. *Phys. Chem. Chem. Phys.* **2019**, *21*, 18999.

(15) Lan, Z.; Fabiano, E.; Thiel, W. Photoinduced nonadiabatic dynamics of pyrimidine nucleobases: On-the-fly surface-hopping study with semiempirical methods. *J. Phys. Chem. B* **2009**, *113*, 3548.

(16) Picconi, D.; Barone, V.; Lami, A.; Santoro, F.; Improta, R. The Interplay between $\pi\pi^*/n\pi^*$ Excited States in Gas- Phase Thymine: A Quantum Dynamical Study. *ChemPhysChem* **2011**, *12*, 1957.

(17) Wolf, T.; Myhre, R. H.; Cryan, J.; Coriani, S.; Squibb, R.; Battistoni, A.; Berrah, N.; Bostedt, C.; Bucksbaum, P.; Coslovich, G.; others Probing ultrafast $\pi\pi^*/\mathrm{n}\pi^*$ internal conversion in organic chromophores via K-edge resonant absorption. *Nat. Commun.* **2017**, *8*, 29.

(18) Park, W.; Lee, S.; Huix-Rotllant, M.; Filatov, M.; Choi, C. H. Impact of the dynamic electron correlation on the unusually long excited-state lifetime of thymine. *J. Phys. Chem. Lett.* **2021**, *12*, 4339.

(19) Montorsi, F.; Segatta, F.; Mukamel, A. N. S.; Garavelli, M. Soft X-ray Spectroscopy Simulations with Multiconfigurational Wave Function Theory: Spectrum Completeness, Sub-eV Accuracy, and Quantitative Reproduction of Line Shape. *J. Chem. Theory Comput.* **2022**, *18*, 1003.

(20) Segatta, F.; Aranda, D.; Aleotti, F.; Montorsi, F.; Mukamel, S.; Garavelli, M.; Santoro, F.; Nenov, A. Time-Resolved X-ray Absorption Spectroscopy: An MCTDH Quantum Dynamics Protocol. *J. Chem. Theory Comput.* **2024**, *20*, 307.

(21) Coriani, S.; Christiansen, O.; Fransson, T.; Norman, P. Coupled-cluster response theory for near-edge X-ray-absorption fine structure of atoms and molecules. *Phys. Rev. A* **2012**, *85*, 022507.

(22) Norman, P.; Dreuw, A. Simulating X-ray spectroscopies and calculating core-excited states of molecules. *Chem. Rev.* **2018**, *118*, 7208.

(23) Li, J.; Jin, Y.; Rinke, P.; Yang, W.; Golze, D. Benchmark of GW methods for core-level binding energies. *J. Chem. Theory Comput.* **2022**, *18*, 7570.

(24) Segatta, F.; Nenov, A.; Orlandi, S.; Arcioni, A.; Mukamel, S.; Garavelli, M. Exploring the capabilities of optical pump X-ray probe NEXAFS spectroscopy to track photo-induced dynamics mediated by conical intersections. *Faraday Discuss.* **2020**, *221*, 245.

(25) Fransén, L.; Roux, B.; Coriani, S.; Nandi, S.; Vacher, M. Tracking photophysical relaxation in spiropyran with simulated time-resolved X-ray absorption spectroscopy. *Commun. Phys.* **2025**, *8*, 263.

(26) Rogvall, J.; Singh, R.; Vacher, M.; Lundberg, M. Sensitivity of Kβ mainline X-ray emission to Struct. Dyn. in iron photosensitizer. *Phys. Chem. Chem. Phys.* **2023**, *25*, 10447.

(27) Vacher, M.; Kunnus, K.; Delcey, M. G.; Gaffney, K. J.; Lundberg, M. Origin of core-to-core x-ray emission spectroscopy sensitivity to structural dynamics. *Struct. Dyn.* **2020**, *7*, 044102.

(28) Nooijen, M.; Bartlett, R. J. Description of core-excitation spectra by the open-shell electron-attachment equation-of-motion coupled cluster method. *J. Chem. Phys.* **1995**, *102*, 6735.

(29) Myhre, R. H.; Coriani, S.; Koch, H. Near-edge X-ray absorption fine structure within multilevel coupled cluster theory. *J. Chem. Theory Comput.* **2016**, *12*, 2633.

(30) Ehlert, C.; Klamroth, T. The quest for best suited references for configuration interaction singles calculations of core excited states. *J. Comput. Chem.* **2017**, *38*, 116.

(31) Fronzoni, G.; Decleva, P. Ab-initio CI calculations of the C1s and Cl1s and 2p core excitation spectra of the freon molecules: CCl_4, $CFCl_3$, CF_2Cl_2 and CF_3Cl. *Chem. Phys.* **1998**, *237*, 21.

(32) Fronzoni, G.; Stener, M.; Decleva, P. Theoretical study of the excited and continuum states in the NEXAFS regions of Cl2. *Phys. Chem. Chem. Phys.* **1999**, *1*, 1405.

(33) Plekan, O.; Feyer, V.; Richter, R.; Coreno, M.; De Simone, M.; Prince, K.; Trofimov, A.; Gromov, E.; Zaytseva, I.; Schirmer, J. A theoretical and experimental study of the near edge X-ray absorption fine structure (NEXAFS) and X-ray photoelectron spectra (XPS) of nucleobases: Thymine and adenine. *Chem. Phys.* **2008**, *347*, 360.

(34) Wenzel, J.; Wormit, M.; Dreuw, A. Calculating X-ray absorption spectra of open-shell molecules with the unrestricted algebraic-diagrammatic construction scheme for the polarization propagator. *J. Chem. Theory Comput.* **2014**, *10*, 4583.

(35) Neville, S. P.; Averbukh, V.; Ruberti, M.; Yun, R.; Patchkovskii, S.; Chergui, M.; Stolow, A.; Schuurman, M. S. Excited state X-ray absorption spectroscopy: Probing both electronic and structural dynamics. *J. Chem. Phys.* **2016**, *145*, 144307.

(36) Neville, S. P.; Chergui, M.; Stolow, A.; Schuurman, M. S. Ultrafast X-ray spectroscopy of conical intersections. *Phys. Rev. Lett.* **2018**, *120*, 243001.

(37) Slater, J. C. Statistical Exchange-Correlation in the Self-Consistent Field. *Adv. Quantum Chem.* **1972**, *6*, 1.

(38) Triguero, L.; Pettersson, L.; Ågren, H. Calculations of near-edge x-ray-absorption spectra of gas-phase and chemisorbed molecules by means of density-functional and transition-potential theory. *Phys. Rev. B* **1998**, *58*, 8097.

(39) Ehlert, C.; Gühr, M.; Saalfrank, P. An efficient first principles method for molecular pump-probe NEXAFS spectra: Application to thymine and azobenzene. *J. Chem. Phys.* **2018**, *149*.

(40) Besley, N. A. Modeling of the spectroscopy of core electrons with density functional theory. *Wiley Interdiscip. Rev. Comput. Mol. Sci.* **2021**, *11*, e1527.

(41) Ponzi, A. et al. Carbon and Nitrogen K-Edge NEXAFS Spectra of Indole, 2,3-Dihydro-7-azaindole, and 3-Formylindole. *J. Phys. Chem. A* **2021**, *125*, 4160.

(42) Stener, M.; Fronzoni, G.; de Simone, M. Time dependent density functional theory of core electrons excitations. *Chem. Phys. Lett.* **2003**, *373*, 15.

(43) Tsuru, S.; Vidal, M. L.; Pápai, M.; Krylov, A. I.; Møller, K. B.; Coriani, S. An assessment of different electronic structure approaches for modeling time-resolved x-ray absorption spectroscopy. *Struct. Dyn.* **2021**, *8*, 024101.

(44) Gilbert, A. T.; Besley, N. A.; Gill, P. M. Self-consistent field calculations of excited states using the maximum overlap method (MOM). *J. Phys. Chem. A* **2008**, *112*, 13164.

(45) Northey, T.; Norell, J.; Fouda, A. E.; Besley, N. A.; Odelius, M.; Penfold, T. J. Ultrafast nonadiabatic dynamics probed by nitrogen K-edge absorption spectroscopy. *Phys. Chem. Chem. Phys.* **2020**, *22*, 2667.

(46) Szabo, A.; Ostlund, N. S. *Modern Quantum Chemistry*; MacMillan, 1982.

(47) Grobas Illobre, P.; Marsili, M.; Corni, S.; Stener, M.; Toffoli, D.; Coccia, E. Time-Resolved Excited-State Analysis of Molecular Electron Dynamics by TDDFT and Bethe–Salpeter Equation Formalisms. *J. Chem. Theory Comput.* **2021**, *17*, 6314.

(48) Dalibard, J.; Castin, Y.; Mølmer, K. Wave-function Approach to Dissipative Processes in Quantum Optics. *Phys. Rev. Lett.* **1992**, *68*, 580.

(49) Mølmer, K.; Castin, Y.; Dalibard, J. Wave-function Approach to Dissipative Processes in Quantum Optics. *J. Opt. Soc. Am. B* **1993**, *10*, 524.

(50) Dum, R.; Zoller, P.; Ritsch, H. Monte Carlo simulation of the atomic master equation for spontaneous emission. *Phys. Rev. A* **1992**, *45*, 4879.

(51) Schlosshauer, M. Decoherence, the measurement problem, and interpretations of quantum mechanics. *Rev. Mod. Phys.* **2005**, *76*, 1267.

(52) Breuer, H.-P.; Petruccione, F. *The Theory of Open Quantum Systems*; Oxford University Press, Oxford, 2006.

(53) Saalfrank, P. Stochastic wave packet vs. direct density matrix solution of Liouville-von Neumann equations for photodesorption problems. *Chem. Phys.* **1996**, *211*, 265.

(54) Appel, H.; Di Ventra, M. Stochastic quantum molecular dynamics for finite and extended systems. *Chem. Phys.* **2011**, *391*, 27.

(55) Füchsel, G.; Klamroth, T.; Tremblay, J. C.; Saalfrank, P. Stochastic approach to laser-induced ultrafast dynamics: the desorption of H_2/D_2 from Ru(0001). *Phys. Chem. Chem. Phys.* **2010**, *12*, 14082.

(56) Biele, R.; D'Agosta, R. A stochastic approach to open quantum systems. *J. Phys.: Condens. Matter* **2012**, *24*, 273201.

(57) Biancorosso, L.; D'Antoni, P.; Corni, S.; Stener, M.; Coccia, E. Time-dependent quantum/continuum modeling of plasmon-enhanced electronic circular dichroism. *J. Chem. Phys.* **2024**, *161*.

(58) Rüger, R.; Franchini, M.; Trnka, T.; Yakovlev, A.; van Lenthe, E.; Philipsen, P.; van Vuren, T.; Klumpers, B.; Soini, T. AMS 2025.1, SCM, Theoretical Chemistry, Vrije Universiteit, Amsterdam, The Netherlands. 2025; `http://www.scm.com`.

(59) Coccia, E.; Fregoni, J.; Guido, C. A.; Marsili, M.; Corni, S. Hybrid theoretical models for molecular nanoplasmonics. *J. Chem. Phys.* **2020**, *153*, 200901.

(60) Coccia, E.; Dall'Osto, G.; Fregoni, J.; Gil, G.; Marsili, M.; Pipolo, S.; Romanelli, M.; Rosa, M.; Corni, S. WaveT-TDPlas. `https://github.com/stefano-corni/WaveT_TDPlas`, 2024; [Online; accessed 12-January-2024].

(61) Coccia, E.; Troiani, F.; Corni, S. Probing quantum coherence in ultrafast molecular

processes: An *ab initio* approach to open quantum systems. *J. Chem. Phys.* **2018**, *148*, 204112.

(62) Dall'Osto, G.; Coccia, E.; Guido, C. A.; Corni, S. Investigating ultrafast two-pulse experiments on single DNQDI fluorophores: a stochastic quantum approach. *Phys. Chem. Chem. Phys.* **2020**, *22*, 16734.

(63) Dall'Osto, G.; Corni, S. Time Resolved Raman Scattering of Molecules: A Quantum Mechanics Approach with Stochastic Schroedinger Equation. *J. Phys. Chem. A* **2022**, *126*, 8088.

(64) Dall'Osto, G.; Marsili, M.; Vanzan, M.; Toffoli, D.; Stener, M.; Corni, S.; Coccia, E. Peeking into the Femtosecond Hot-Carrier Dynamics Reveals Unexpected Mechanisms in Plasmonic Photocatalysis. *J. Am. Chem. Soc.* **2024**, *146*, 2208.

(65) Dall'Osto, G.; Vanzan, M.; Corni, S.; Coccia, M. M. E. Stochastic Schrödinger equation for hot-carrier dynamics in plasmonic systems. *J. Chem. Phys.* **2024**, *161*, 124103.

(66) Lindblad, G. On the generators of quantum dynamical semigroups. *Commun. Math. Phys.* **1976**, *48*, 119.

(67) Tremblay, J. C.; Klamroth, T.; Saalfrank, P. Time-dependent configuration-interaction calculations of laser-driven dynamics in presence of dissipation. *J. Chem. Phys.* **2008**, *129*, 084302.

(68) Toniolo, A.; Persico, M. Efficient calculation of Franck-Condon factors and vibronic couplings in polyatomics. *J. Comput. Chem.* **2001**, *22*, 968.

(69) Santoro, F.; Lami, A.; Improta, R.; Barone, V. Effective method to compute vibrationally resolved optical spectra of large molecules at finite temperature in the gas phase and in solution. *J. Chem. Phys.* **2007**, *126*, 184102.

(70) Wolf, T. J.; Paul, A. C.; Folkestad, S. D.; Myhre, R. H.; Cryan, J. P.; Berrah, N.; Bucksbaum, P. H.; Coriani, S.; Coslovich, G.; Feifel, R.; others Transient resonant Auger–Meitner spectra of photoexcited thymine. *Faraday Discuss.* **2021**, *228*, 555.

Supporting Information for "Open-quantum approach to time-resolved NEXAFS"

Simone Pistillo, Leonardo Biancorosso, Giulia Dall'Osto,[a] Daniele Toffoli,*

Giovanna Fronzoni,* and Emanuele Coccia*

Dipartimento di Scienze Chimiche e Farmaceutiche, Università di Trieste, via L. Giorgieri 1, 34127, Trieste, Italy

E-mail: toffoli@units.it; fronzoni@units.it; ecoccia@units.it

[a]Present affiliation: Elettra Sincrotrone Trieste, SS 14 Km 163.5 in AREA Science Park, Basovizza, Trieste, Italy

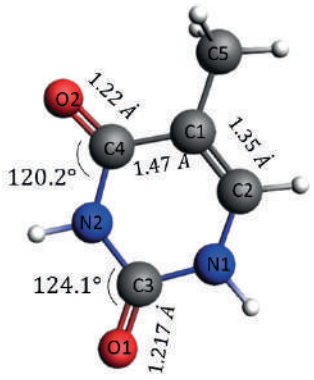


```
15

N  1.093075 -1.249983  0.000000
C -0.246795 -1.605964  0.000000
N -1.089463 -0.509110  0.000000
C -0.738592  0.852530  0.000000
C  0.705781  1.112920  0.000000
C  1.539304  0.054502  0.000000
H  1.742844 -2.021056  0.000000
O -0.629367 -2.760992  0.000000
H -2.080430 -0.716558  0.000000
O -1.606692  1.709786  0.000000
C  1.168135  2.538618  0.000000
H  2.615802  0.168947  0.000000
H  2.256892  2.596696  0.000000
H  0.788767  3.068789 -0.875707
H  0.788767  3.068789  0.875707
```

Figure S1: Ground state equilibrium geometry of thymine optimized at the B3LYP/TZP level. Also reported are the atomic coordinates in .xyz format and selected bond distances and angles.

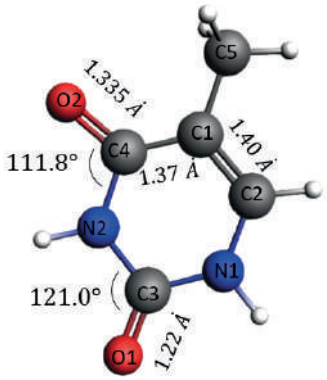

15

N	1.086757	-1.263852	0.000000
C	-0.232295	-1.602958	0.000000
N	-1.097044	-0.502033	0.000000
C	-0.653799	0.817506	0.000000
C	0.681674	1.124560	0.000000
C	1.584905	0.049775	0.000000
H	1.720762	-2.047489	0.000000
O	-0.665767	-2.743292	0.000000
H	-2.082709	-0.715059	0.000000
O	-1.670941	1.681738	0.000000
C	1.1498956	2.557044	0.000000
H	2.6544312	0.161746	0.000000
H	2.2385440	2.596478	0.000000
H	0.7968071	3.096876	-0.881363
H	0.7968071	3.096876	0.881363

Figure S2: S_1 equilibrium geometry optimized at the B3LYP/TDA/TZP level. Also reported are the atomic coordinates in .xyz format and selected bond distances and angles.

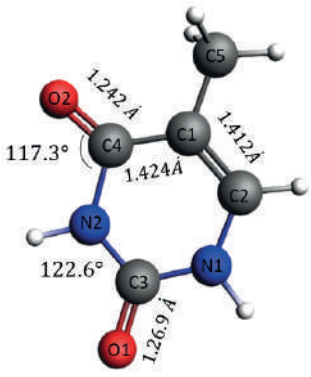

15

N	1.090137	-1.256706	0.000000
C	-0.233365	-1.542456	0.000000
N	-1.099775	-0.523650	0.000000
C	-0.729252	0.902521	0.000000
C	0.678325	1.118726	0.000000
C	1.607363	0.055127	0.000000
H	1.698819	-2.063056	0.000000
O	-0.605371	-2.755925	0.000000
H	-2.086803	-0.744025	0.000000
O	-1.653318	1.732028	0.000000
C	1.163678	2.523794	0.000000
H	2.677251	0.160166	0.000000
H	2.251782	2.576972	0.000000
H	0.774278	3.062199	-0.870764
H	0.774278	3.062199	0.870764

Figure S3: S_2 equilibrium geometry optimized at the B3LYP/TDA/TZP level. Also reported are the atomic coordinates in .xyz format and selected bond distances and angles.

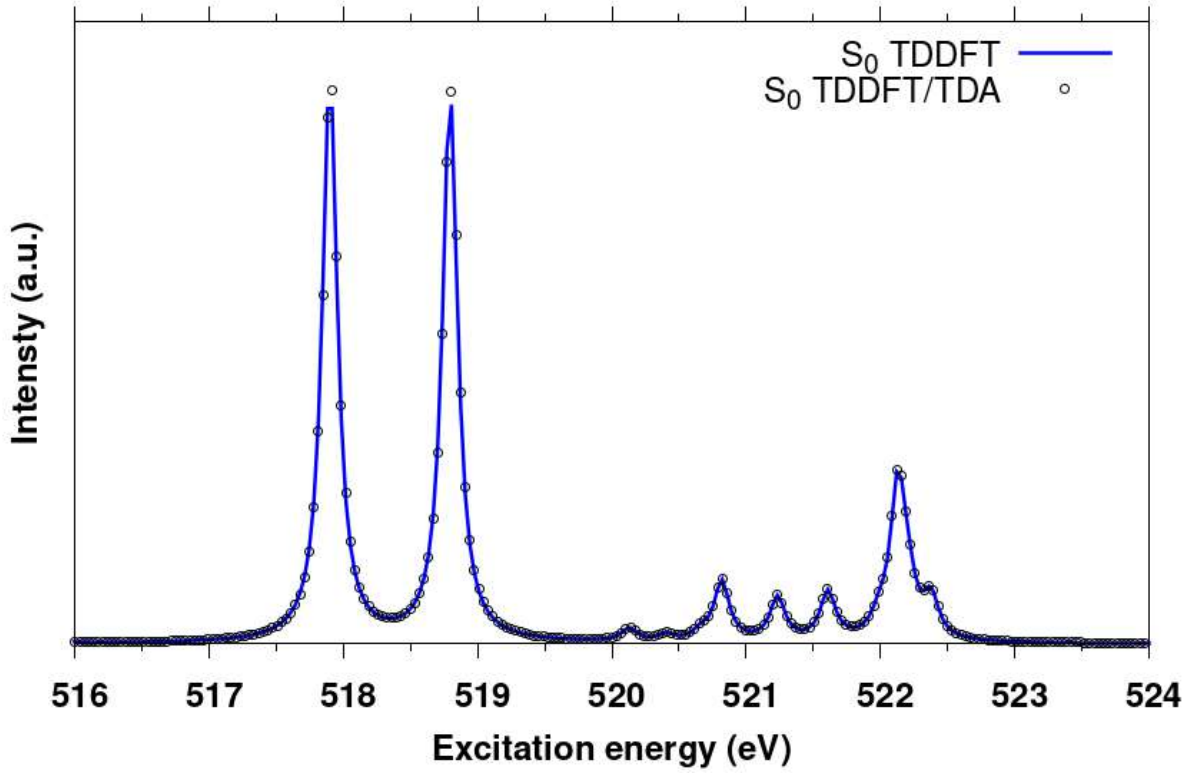

Figure S4: O1s NEXAFS spectra of ground-state thymine: comparison between the spectra computed at full TDDFT and at the TDDFT/TDA level of theory.

Table S1: Excitation energies, oscillator strengths, and main 1h-1p configurations of the first valence excited states of thymine. The 33a MO corresponds to the HOMO and the 34a MO to the LUMO. The percentage contribution of the oxygen atoms to the relevant MOs is also reported.

Excitation	Excitation energy (eV)	Oscillator strength	Main configurations	Initial orbital component	Final orbital component
S_1	5.14	$6.5 \cdot 10^{-8}$	$32a \rightarrow 34a$	$p_y\left(O_{(2)}(\mathbf{34.5\%})\right); p_x\left(O_{(2)}(\mathbf{31.8\%})\right);$ $\pi^*(CC); \pi^*(CN)$	$\pi^*(CC); \pi^*\left(C0_{(2)}(\mathbf{14.2\%})\right);$ $\pi^*(CN)$
S_2	5.49	$2.2 \cdot 10^{-1}$	$33a \rightarrow 34a$	$\pi^*\left(C0_{(1)}(\mathbf{11.5\%})\right); \pi^*\left(C0_{(2)}(\mathbf{9\%})\right);$ $\pi^*(CC); \pi^*(CN)$	$\pi^*(CC); \pi^*\left(C0_{(2)}(\mathbf{14.2\%})\right);$ $\pi^*(CN)$
S_5	6.73	$1.2 \cdot 10^{-1}$	$31a \rightarrow 34a$	$p_z(N_{(2)}(\mathbf{44.5\%})); \pi^*\left(C0_{(1)}(\mathbf{28.9\%})\right);$ $\pi^*\left(C0_{(1)}(\mathbf{24\%})\right)$	$\pi^*(CC); \pi^*\left(C0_{(2)}(\mathbf{14.2\%})\right);$ $\pi^*(CN)$
S_6	6.81	$2.0 \cdot 10^{-1}$	$33a \rightarrow 37a$	$\pi^*\left(C0_{(1)}(\mathbf{11.5\%})\right); \pi^*\left(C0_{(2)}(\mathbf{9\%})\right);$ $\pi^*(CC); \pi^*(CN)$	$\pi^*\left(C0_{(1)}(\mathbf{22.7\%})\right); \pi^*(CC);$ $\pi^*(CN)$

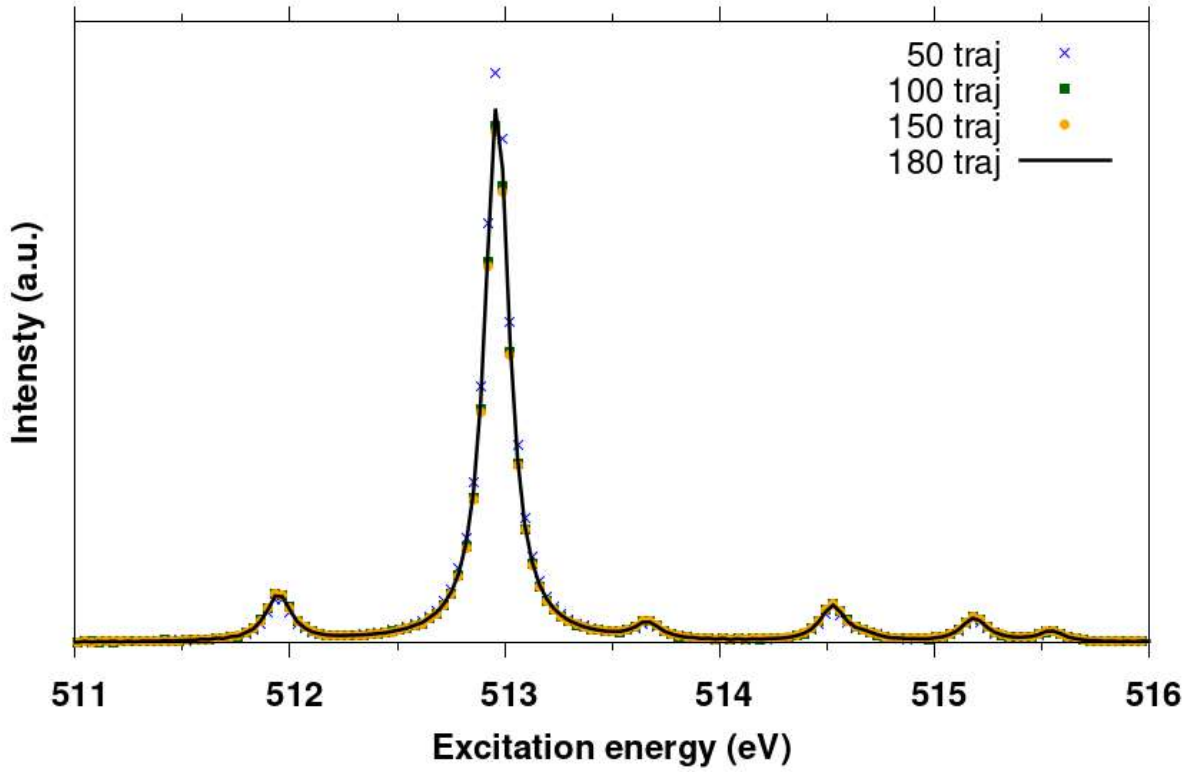

Figure S5: Spectra at delay time of 60 fs with the S_1 geometry obtained averaging over 50, 100, 150 and 180 SSE trajectories.

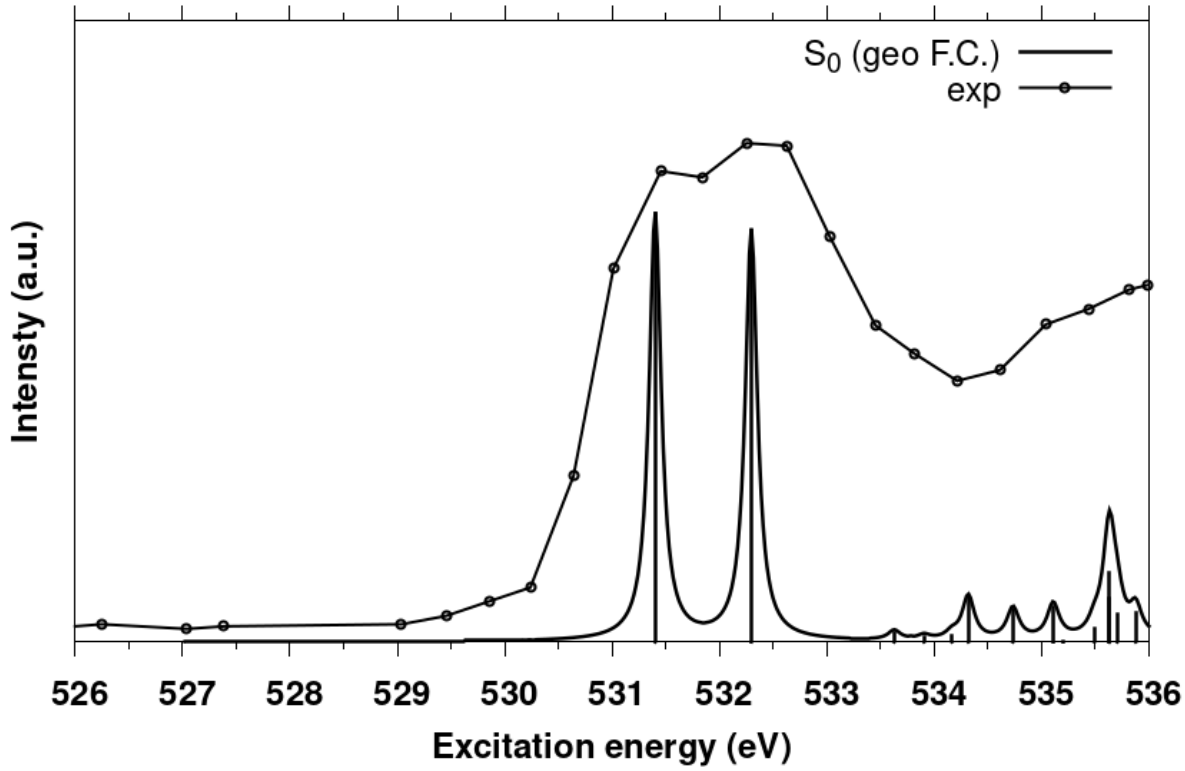

Figure S6: O1s NEXAFS spectra of thymine: comparison between theoretical and experimental ground state spectra. A rigid shift of 13.5 eV was applied to the theoretical spectrum. Lorentzian profile was convolved with γ=0.068 eV.

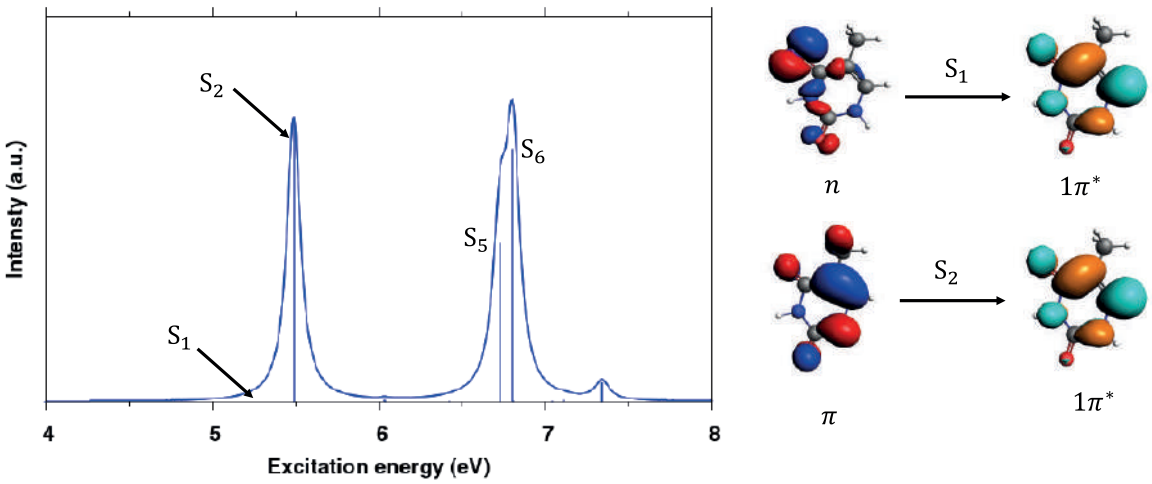

Figure S7: Valence absorption spectrum of thymine calculated at the TDDFT/TDA level. The occupied/virtual MO pairs corresponding to the dominant 1h-1p excited configurations of the $S_0 \longrightarrow S_1$ and $S_0 \longrightarrow S_2$ transitions are shown. Lorentzian profile was convolved with amplitude γ=0.068 eV.

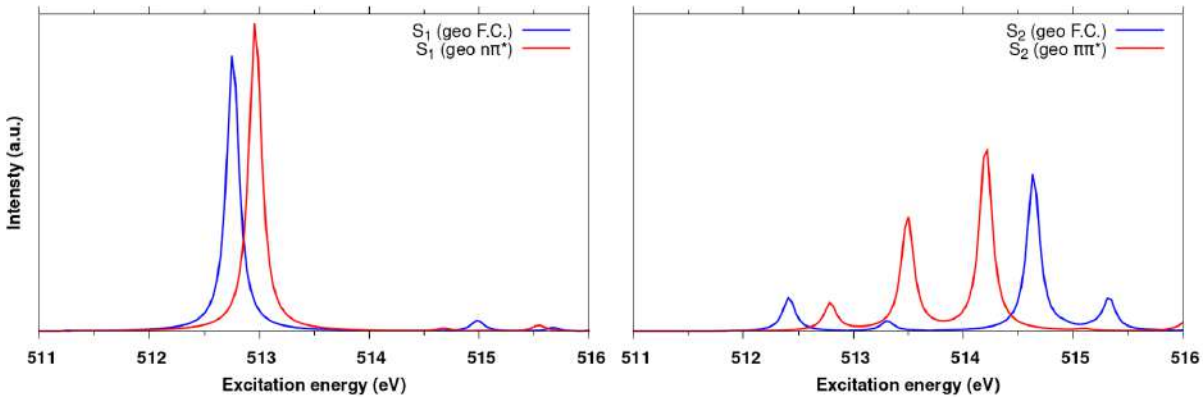

Figure S8: Left panel: Oxygen K-edge first-excited state NEXAFS spectra of thymine in the S_1-optimized geometry (red) and in the FC geometry (blue). Right panel: Oxygen K-edge second-excited state NEXAFS spectra of thymine in the S_2-optimized geometry (red) and in the FC geometry (blue).

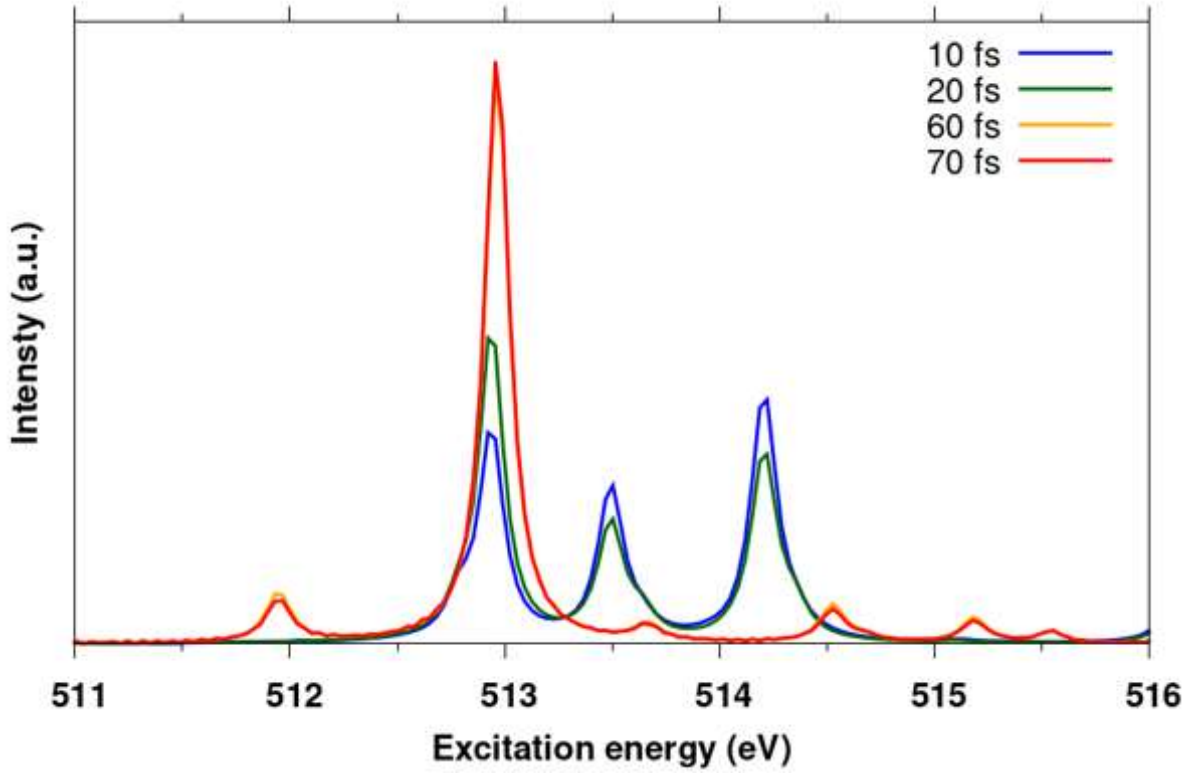

Figure S9: Time–resolved NEXAFS spectra of thymine at 10, 20, 60 and 70 fs. Spectra captured at 10 and 20 fs are extracted from dynamics performed on the S_2 optimized geometry, while the S_1 optimized geometry has been used for delay times of 60 and 70 fs.

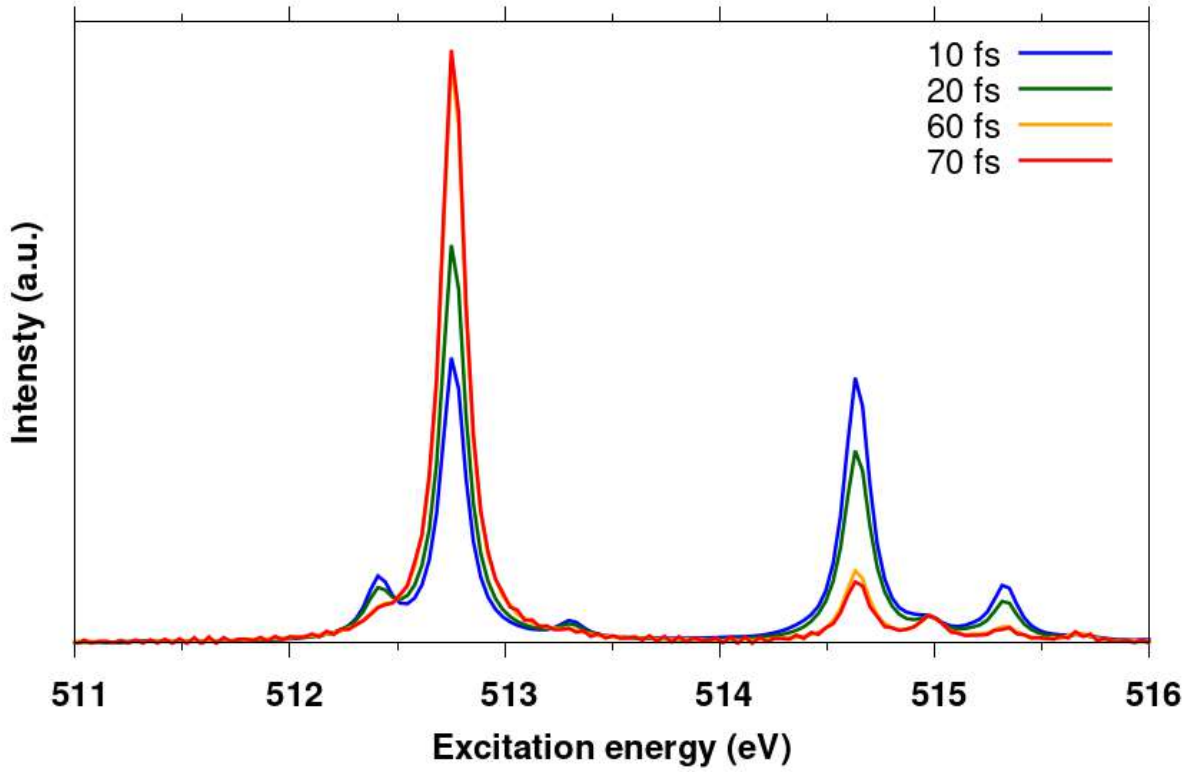

Figure S10: Time–resolved NEXAFS spectra of thymine at 10, 20, 60 and 70 fs. All spectra were calculated at the FC geometry.

Chapter 6

Conclusions

The main goal of my research over the past three years has been to investigate phenomena related to the electronic dynamics of molecular and composite systems. To this end, I explored different aspects of the field, ranging from theoretical spectroscopy to photocatalysis. This diversity reflects not only the breadth of the questions addressed, but also the versatility and effectiveness of the methodologies developed within my research group in Trieste.

Despite this apparent heterogeneity, the projects presented in this thesis can be organized into three main themes that serve as the common thread of my doctoral work:

1. **Investigation of Chirality**
   My first line of research focused on how chiral molecules interact with light, and conversely, how chiral light couples to molecular systems (Chapter 3). In Section 3.1, I describe the project carried out in Metz with Professor Jean Christophe Tremblay, where we studied the interaction between endohedral fullerenes and a chiral external pulse. We demonstrated that the angular momentum transfer to molecular electrons depends strongly on the nature of the atoms encapsulated inside the fullerene cage. The long-term goal of this line is to embed such endofullerenes in carbon nanotubes and investigate how their response to chiral pulses is further modified.

   Thanks to methodological developments achieved in Trieste, we were also able to compute spectra of molecules in their excited states. An application of this approach is presented in Section 3.2, where we studied the photoisomerization of a molecular motor using TR-ECD. This allowed us to track the geometrical evolution of the system, from its spectroscopic response in S_1 during the early stages of the dynamics, to its return to the ground state in the final steps of the reaction. This project bridges the investigation of chirality with that of excited–state dynamics, thus connecting the first two overarching themes of this thesis.

   Another key methodological advance of my doctoral work has been the inclusion of a plasmonic NP in electronic dynamics simulations (Chapter 2, Section 2.5). In Section 3.3, I applied this framework to analyze the influence of

a NP on the ECD spectra of chiral molecules. We demonstrated an enhancement of the spectra for molecular systems with absorption energies close to the plasmon resonance, while far–detuned excitations showed negligible effects. Together with a detailed analysis of the role of the NP, laser polarization, and molecular excitations, these results provided valuable insight into the underlying physical mechanism of the enhancement.

2. **Investigation of Photocatalysis**
   The second major theme of my PhD is the investigation of photocatalytic processes. This topic is closely linked to the first, as it relies on the methodology developed for describing NP–molecule interactions. The original motivation of this line of work was to establish computational strategies for studying antenna–reactor complexes, coupling plasmonic nanoantennas with catalytic nanostructures. Inspired by experimental studies [132], we focused on the effect of a gold plasmonic nanorod on the electronic dynamics of a catalytic system consisting of Pd as the catalytic center and the intermediates of formic acid dehydrogenation (HCOO* and H*).

   In the study presented in Section 4.1, we analyzed the electron dynamics of the Pd cluster and the molecular intermediates in the absence of the gold nanorod. We observed a net electron injection from the Pd slab into formate and hydrogen. Building on these results, we then included the plasmonic nanorod to compare the electron transfer processes with and without plasmonic excitation (Section 4.2). Our simulations revealed that while the qualitative features of the dynamics remained similar, the magnitude of electron transfer increased by up to three orders of magnitude. Moreover, we discovered an asymmetry in the charge injection into the two oxygen atoms of formate, a feature that became even more pronounced when the NP was placed in close proximity to the catalytic system. These findings, combined with the observed surface charge heterogeneity on the Pd reactor, provide a microscopic explanation for the experimentally observed enhancement of catalytic activity under plasmonic excitation.

3. **TR-NEXAFS**

   In Chapter 5, I extended the investigation of excited states to TR-NEXAFS and the internal conversion process of thymine. This study led to the development of a novel computational framework that goes beyond the conventional core–valence separation, enabling the calculation of excited–state NEXAFS spectra with unprecedented accuracy. Moreover, using the theory of open quantum systems via SSE allows us to effectively compute NEXAFS spectra along the internal conversion of the thymine.

Overall, the results presented in this thesis extend the theoretical and computational toolbox available for the study of electronic dynamics in molecular systems and offer new insights into fundamental processes ranging from chirality to photocatalysis.

I believe that the methodologies and findings developed here will serve as a foundation for future research, helping to bridge the gap between theory and experiment and contributing to a deeper understanding of light–matter interactions at the molecular and nanoscale.

List of Publications

1. Monti, M., Biancorosso L. & Coccia E. (2024) Time-Resolved Circular Dichroism in Molecules: Experimental and Theoretical Advances. *Molecules*, 29, 4049.

2. Biancorosso, L., DAntoni, P., Corni, S., Stener, M. & Coccia, E. (2024). Time-dependent quantum/continuum modeling of plasmon-enhanced electronic circular dichroism. *J. Chem. Phys.*, 161, 214104.

3. Biancorosso, L., Coccia, E. & Tremblay, J. C. (2024). Laser-Induced Circular Charge Migration in Endohedral Fullerenes in the Presence of Ionization. *J. Phys. Chem. C*, 129, 464.

4. Biancorosso, L. & Coccia, E. (2024). Recent advances in modelling plasmon-assisted electron dynamics. *Chem. Modell.*, 18, 102.

5. Biancorosso, L. & Coccia, E. (2025). Study of the Photoinduced Charge Injection in the Reaction Intermediate of the Dehydrogenation of Formic Acid on Palladium. *J. Comput. Chem.*, 46, e70087.

6. Biancorosso, L., & Coccia, E. (2025). Plasmon-induced asymmetry in the charge distribution explains the enhanced H_2 production rate from formic acid with a Pd-tipped Au nanorod. *J. Phys. Chem. Lett.* , 16, 12931.

7. Plakaj, R., Biancorosso L., Luppi E. & Coccia E. (2025) Simulating the electronic circular dichroism of Chlorophyll b in presence of a gold nanosphere. *J. Phys Chem B*, https://doi.org/10.1021/acs.jpcb.5c06445

8. Pistillo, S., Biancorosso, L., Dall'Osto, G., Toffoli, D., Fronzoni, G. & Coccia, E. (2025) Open–Quantum approach to time–resolved NEXAFS. Submitted.

Bibliography

[1] Braden M Weight, Xinyang Li, and Yu Zhang. "Theory and modeling of light-matter interactions in chemistry: current and future". In: *Phys. Chem. Chem. Phys.* 25 (2023), p. 31554.

[2] R Guy Woolley. *Foundations of Molecular Quantum Electrodynamics*. Cambridge University Press, 2022.

[3] Henrik Bruus and Karsten Flensberg. *Many-body quantum theory in condensed matter physics: an introduction*. Oxford university press, 2004.

[4] Attila Szabo and Neil S Ostlund. *Modern quantum chemistry: introduction to advanced electronic structure theory*. Courier Corporation, 1996.

[5] Walter Greiner and Joachim Reinhardt. *Quantum electrodynamics*. Springer Science & Business Media, 2008.

[6] James D Bjorken, Sidney D Drell, and JE Mansfield. *Relativistic quantum mechanics*. New York: McGrawHill, 1965.

[7] Max Diem. *Quantum Mechanical Foundations of Molecular Spectroscopy*. John Wiley & Sons, 2021.

[8] Haim Suchowski, Gil Porat, and Ady Arie. "Adiabatic processes in frequency conversion". In: *Laser & Photonics Rev.* 8 (2014), p. 333.

[9] Guang S He et al. "Multiphoton absorbing materials: molecular designs, characterizations, and applications". In: *Chem. rev.* 108 (2008), p. 1245.

[10] Vaidya Nathan, Arthur H Guenther, and Shashanka S Mitra. "Review of multiphoton absorption in crystalline solids". In: *J. Opt. Soc. Am. B* 2 (1985), p. 294.

[11] W. H. Brooks, W. C. Guida, and K. G. Daniel. "The significance of chirality in drug design and development". In: *Curr. Top. Med. Chem.* 11 (2011), p. 760.

[12] Christiane Müller, Andreas Bauer, and Thorsten Bach. "Licht-getriebene enantioselektive Organokatalyse". In: *Angew. Chem.* 121 (2009), p. 6767.

[13] Naohiro Kameta, Mitsutoshi Masuda, and Toshimi Shimizu. "Qualitative/chiral sensing of amino acids by naked-eye fluorescence change based on morphological transformation and hierarchizing in supramolecular assemblies of pyrene-conjugated glycolipids". In: *Chem. Commun.* 51 (2015), p. 11104.

[14] Mikhail Maslov et al. "Theory of angular momentum transfer from light to molecules". In: *Phys. Rev. Res.* 6 (2024), p. 033277.

[15] Yae-Chan Lim et al. “Strong Chiral Response of Chiral Plasmonic Nanoparticles to Photonic Orbital Angular Momentum”. In: *Adv. Opt. Mat.* 13 (2025), p. 2402268.

[16] Saeideh Ostovar pour et al. “Through-space transfer of chiral information mediated by a plasmonic nanomaterial”. In: *Nat. Chem.* 7 (2015), p. 591.

[17] Zongxia Guo et al. “Nucleoside-assisted self-assembly of oligo (p-phenylenevinylene) s at liquid/solid interface: Chirality and nanostructures”. In: *J. Am. Chem. Soc.* 133 (2011), p. 17764.

[18] Nina Berova, Koji Nakanishi, and Robert W Woody. *Circular dichroism: principles and applications*. John Wiley & Sons, 2000.

[19] Philip J Stephens. “Theory of vibrational circular dichroism”. In: *J. Phys. Chem.* 89 (1985), p. 748.

[20] James P Riehl and Frederick S Richardson. “Circularly polarized luminescence spectroscopy”. In: *Chem. Rev.* 86 (1986), p. 1.

[21] C M Jones et al. “Fast events in protein folding initiated by nanosecond laser photolysis.” In: *Proc. Natl. Acad. Sci.* 90 (1993), p. 11860.

[22] Gulnur A Elove et al. “Early steps in cytochrome c folding probed by time-resolved circular dichroism and fluorescence spectroscopy”. In: *Biochemistry* 31 (1992), p. 6876.

[23] Johannes Lehmann et al. “Near-edge X-ray absorption fine structure (NEXAFS) spectroscopy for mapping nano-scale distribution of organic carbon forms in soil: Application to black carbon particles”. In: *Glob. Biogeochem. Cycles* 19 (2005), p. GB1013.

[24] Tirandai Hemraj-Benny et al. “Near-edge X-ray absorption fine structure spectroscopy as a tool for investigating nanomaterials”. In: *small* 2 (2006), p. 26.

[25] Dean M DeLongchamp, Eric K Lin, and Daniel A Fischer. “Organic semiconductor structure and chemistry from near-edge X-ray absorption fine structure (NEXAFS) spectroscopy”. In: *Organic Field-Effect Transistors IV*. Vol. 5940. SPIE. 2005, p. 54.

[26] Joachim Stöhr. *NEXAFS spectroscopy*. Vol. 25. Springer Science & Business Media, 2013.

[27] Holger Stiel et al. “Towards understanding excited-state properties of organic molecules using time-resolved soft X-ray absorption spectroscopy”. In: *Int. J. Mol. Sci.* 22 (2021), p. 13463.

[28] P. Grossmann et al. “Time-resolved near-edge x-ray absorption fine structure spectroscopy on photo-induced phase transitions using a tabletop soft-x-ray spectrometer”. In: *Rev. Sci. Instrum.* 83 (2012), p. 053110.

[29] TJA Wolf et al. “Probing ultrafast $\pi\pi^*/n\pi^*$ internal conversion in organic chromophores via K-edge resonant absorption”. In: *Nat. Comm.* 8 (2017), p. 29.

[30] Thomas JA Wolf et al. “Transient resonant Auger–Meitner spectra of photoexcited thymine”. In: *Faraday Discuss.* 228 (2021), p. 555.

[31] Sergey V Gaponenko. *Introduction to nanophotonics*. Cambridge University Press, 2010.

[32] Zhenglong Zhang et al. “Plasmon-driven catalysis on molecules and nanomaterials”. In: *Acc. Chem. Res.* 52 (2019), p. 2506.

[33] E. Kazuma and Y. Kim. “Mechanistic Studies of Plasmon Chemistry on Metal Catalysts”. In: *Angew. Chem. Int. Ed.* 58 (2019), p. 4800.

[34] Y. Zhang et al. “Surface-Plasmon-Driven Hot Electron Photochemistry”. In: *Chem. Rev.* 118 (2018), p. 2927.

[35] Mark L Brongersma, Naomi J Halas, and Peter Nordlander. “Plasmon-induced hot carrier science and technology”. In: *Nat. nanotech.* 10 (2015), p. 25.

[36] E. Coccia et al. “Hybrid theoretical models for molecular nanoplasmonics”. In: *J. Chem. Phys.* 153 (2020), p. 200901.

[37] J. Gersten and A. Nitzan. “Spectroscopic properties of molecules interacting with small dielectric particles”. In: *J. Chem. Phys.* 75 (1981), p. 1139.

[38] O. Andreussi et al. “Radiative and Nonradiative Decay Rates of a Molecule Close to a Metal Particle of Complex Shape.” In: *J. Chem. Phys.* 121 (2004), p. 10190.

[39] E. Dulkeith et al. “Gold Nanoparticles Quench Fluorescence by Phase Induced Radiative Rate Suppression”. In: *Nano Lett.* 5 (2005), p. 585.

[40] V. Jain, R. K. Kashyap, and P. P. Pillai. “Plasmonic Photocatalysis: Activating Chemical Bonds through Light and Plasmon”. In: *Adv. Opt. Mater.* 10 (2022), p. 2200463.

[41] S. Ezendam et al. “Hybrid Plasmonic Nanomaterials for Hydrogen Generation and Carbon Dioxide Reduction”. In: *ACS Energy Lett.* 7 (2022), p. 778.

[42] J. Gersten and A. Nitzan. “Spectroscopic properties of molecules interacting with small dielectric particles”. In: *J. Chem. Phys.* 75 (1981), p. 1139.

[43] A. Lauchner et al. “Molecular Plasmonics”. In: *Nano Lett.* 15 (2015), p. 6208.

[44] Andrew J. Wilson and Katherine A. Willets. “Molecular Plasmonics”. In: *Annu. Rev. Anal. Chem.* 9 (2016), p. 27.

[45] B. Mennucci and S. Corni. “Multiscale modelling of photoinduced processes in composite systems”. In: *Nat. Rev. Chem.* 3 (2019), p. 315.

[46] R. Pilot et al. “A review on surface-enhanced Raman scattering”. In: *Biosensors* 9 (2019), p. 57.

[47] H. Yu et al. “Plasmon-enhanced lightmatter interactions and applications”. In: *Npj Comput. Mater.* 5 (2019), p. 45.

[48] J. F. Li, Chao Y. Li, and R. F. Aroca. “Plasmon-enhanced fluorescence spectroscopy”. In: *Chem. Soc. Rev.* 46 (2017), p. 3962.

[49] N. J. Halas. “Spiers Memorial Lecture: Introductory lecture: Hot-electron science and microscopic processes in plasmonics and catalysis”. In: *Faraday Discuss.* 214 (2019), p. 13.

[50] J. Gargiulo et al. “From Optical to Chemical Hot Spots in Plasmonics”. In: *Acc. Chem. Res.* 52 (2019), p. 2525.

[51] L. V. Besteiro et al. “Hot electron physics and applications”. In: *J. Appl. Phys.* 129 (2021), p. 150401.

[52] C. Zhan et al. “From plasmon-enhanced molecular spectroscopy to plasmon-mediated chemical reactions”. In: *Nat. Rev. Chem.* 2 (2018), p. 216.

[53] S. Schlücker. “Surface-enhanced raman spectroscopy: concepts and chemical applications”. In: *Angew. Chem. Int. Ed.* 53 (2014), p. 4756.

[54] A. B. Zrimsek et al. “Single-Molecule Chemistry with Surface- and Tip-Enhanced Raman Spectroscopy”. In: *Chem. Rev.* 117 (2017), p. 7583.

[55] J. Dong et al. “Recent progress on plasmon-enhanced fluorescence”. In: *Nanophotonics* 4 (2015), p. 472.

[56] S. Kim et al. “High-harmonic generation by resonant plasmon field enhancement”. In: *Nature* 453 (2008), p. 757.

[57] M. Sivis et al. “Nanostructure-enhanced atomic line emission”. In: *Nature* 485 (2012), p. E1.

[58] M. B. Raschke. “High-harmonic generation with plasmonics: feasible or unphysical?” In: *Ann. Phys. (Berlin)* 525 (2013), p. A40.

[59] M. Blanco et al. “Phase matching effects in high harmonic generation at the nanometer scale”. In: *Opt. Express* 25 (2017), p. 14974.

[60] M. L Nesterov et al. “The role of plasmon-generated near fields for enhanced circular dichroism spectroscopy”. In: *Acs Photonics* 3 (2016), p. 578.

[61] A. O. Govorov. “Plasmon-Induced Circular Dichroism of a Chiral Molecule in the Vicinity of Metal Nanocrystals. Application to Various Geometries”. In: *J. Phys. Chem. C* 115 (2011), p. 7914.

[62] S. Linic et al. “Photochemical transformations on plasmonic metal nanoparticles”. In: *Nat. Mater.* 14 (2015), p. 567.

[63] C. Zhan et al. “From plasmon-enhanced molecular spectroscopy to plasmon-mediated chemical reactions”. In: *Nat. Rev. Chem.* 2 (2018), p. 216.

[64] F. Lu et al. “Discrete Nanocubes as Plasmonic Reporters of Molecular Chirality”. In: *Nano Lett.* 13 (2013), p. 3145.

[65] D. F. Swearer et al. “Plasmonic Photocatalysis of Nitrous Oxide into N_2 and O_2 Using AluminumIridium AntennaReactor Nanoparticles”. In: *ACS Nano* 13 (2019), p. 8076.

[66] L Biancorosso and E Coccia. “Study of the Photoinduced Charge Injection in the Reaction Intermediate of the Dehydrogenation of Formic Acid on Palladium”. In: *J. Comput. Chem.* 46 (2025), e70087.

[67] L Biancorosso et al. “Time-dependent quantum/continuum modeling of plasmon-enhanced electronic circular dichroism”. In: *J. Chem. Phys.* 161 (2024), p. 214104.

[68] G. Dall’Osto et al. “ Peeking into the Femtosecond Hot-Carrier Dynamics Reveals Unexpected Mechanisms in Plasmonic Photocatalysis”. In: *J. Am. Chem. Soc.* 146 (2024), p. 2208.

[69] G. DallOsto et al. “Real-time dynamics of plasmonic resonances in nanoparticles described by a boundary element method with generic dielectric function”. In: *J. Chem. Phys.* 153 (2020), p. 184114.

[70] M. Vanzan et al. “Energy Transfer to Molecular Adsorbates by Transient Hot Electron Spillover”. In: *Nano Lett.* 23 (2023), p. 2719.

[71] D. F. Swearer et al. “Heterometallic antenna-reactor complexes for photocatalysis”. In: *Proc. Natl. Acad. Sci. U.S.A.* 113 (2016), p. 8916.

[72] A. García-Etxarri and J. A. Dionne. “Surface-enhanced circular dichroism spectroscopy mediated by nonchiral nanoantennas”. In: *Phys. Rev. B* 87 (2013), p. 235409.

[73] T. J. Davis and D. E. Gomez. “Interaction of localized surface plasmons with chiral molecules”. In: *Phys Rev. B* 90 (2014), p. 235424.

[74] E. Hendry et al. “Ultrasensitive detection and characterization of biomolecules using superchiral fields”. In: *Nat. nanotechnol.* 5 (2010), p. 783.

[75] R. Tullius et al. “Superchiral spectroscopy: detection of protein higher order hierarchical structure with chiral plasmonic nanostructures”. In: *J. Am. Chem. Soc.* 137 (2015), p. 8380.

[76] M. Hentschel et al. “Chiral plasmonics”. In: *Sci. Adv.* 3 (2017), e1602735.

[77] G. Zheng et al. “Discrete metal nanoparticles with plasmonic chirality”. In: *Chem. Soc. Rev.* 50 (2021), p. 3738.

[78] E. S. A. Goerlitzer et al. “The Beginner’s Guide to Chiral Plasmonics: Mostly Harmless Theory and the Design of Large-Area Substrates”. In: *Adv. Opt. Mater.* 9 (2021), p. 2100378.

[79] S. Wang et al. “Chiral Au Nanorods: Synthesis, Chirality Origin, and Applications”. In: *ACS Nano* 16 (2022), p. 19789.

[80] S. Both et al. “Nanophotonic Chiral Sensing: How Does It Actually Work?” In: *ACS Nano* 16 (2022), p. 2822.

[81] W. Wu and M. Pauly. “Chiral plasmonic nanostructures: recent advances in their synthesis and applications”. In: *Mater. Adv.* 3 (2022), p. 186.

[82] H. Zhang and A. O. Govorov. “Giant circular dichroism of a molecule in a region of strong plasmon resonances between two neighboring gold nanocrystals”. In: *Phys Rev. B* 87 (2013), p. 075410.

[83] T. Wu et al. “Competition of Chiroptical Effect Caused by Nanostructure and Chiral Molecules”. In: *J. Phys. Chem. C* 118 (2014), p. 20529.

[84] R. Y. Wang et al. “Experimental Observation of Giant Chiroptical Amplification of Small Chiral Molecules by Gold Nanosphere Clusters”. In: *J. Phys. Chem. C* 118 (2014), p. 9690.

[85] D. Zhai et al. “Plasmonic polymers with strong chiroptical response for sensing molecular chirality”. In: *Nanoscale* 7 (2015), p. 10690.

[86] M. C. di Gregorio et al. “Chiroptical Study of PlasmonMolecule Interaction: The Case of Interaction of Glutathione with Silver Nanocubes”. In: *J. Phys. Chem. C* 119 (2015), p. 17111.

[87] T. L. Belenkova, A. O. Govorov, and G. Markovich. “Orientation-Sensitive Peptide-Induced Plasmonic Circular Dichroism in Silver Nanocubes”. In: *J. Phys. Chem. C* 120 (2016), p. 12751.

[88] Weixuan Zhang et al. “Surface-Enhanced Circular Dichroism of Oriented Chiral Molecules by Plasmonic Nanostructures”. In: *J. Phys. Chem. C* 121 (2017), p. 666.

[89] S. Lee et al. “Robust numerical evaluation of circular dichroism from chiral medium/nanostructure coupled systems using the finite-element method”. In: *Sci. Rep.* 8 (2018), p. 8406.

[90] W. Wang et al. “Boosting chiral amplification in plasmon-coupled circular dichroism using discrete silver nanorods as amplifiers”. In: *Chem. Commun.* 57 (2021), p. 7390.

[91] Matteo Venturi et al. “Plasmon-enhanced circular dichroism spectroscopy of chiral drug solutions”. In: *J. Chem. Phys.* 159 (2023), p. 154703.

[92] J. George and K. G. Thomas. "Surface Plasmon Coupled Circular Dichroism of Au Nanoparticles on Peptide Nanotubes". In: *J. Am. Chem. Soc.* 132 (2010), p. 2502.

[93] X. Shen et al. "Rolling Up Gold Nanoparticle-Dressed DNA Origami into Three-Dimensional Plasmonic Chiral Nanostructures". In: *J. Am. Chem. Soc.* 134 (2012), p. 146.

[94] M. J. Urban et al. "Plasmonic Toroidal Metamolecules Assembled by DNA Origami". In: *J. Am. Chem. Soc.* 138 (2016), p. 5495.

[95] X. Lan et al. "Au Nanorod Helical Superstructures with Designed Chirality". In: *J. Am. Chem. Soc.* 137 (2017), p. 457.

[96] Jino George et al. "Chiral Plasmons: Au Nanoparticle Assemblies on Thermoresponsive Organic Templates". In: *ACS Nano* 13 (2019), p. 4392.

[97] J. Lu et al. "Enhanced optical asymmetry in supramolecular chiroplasmonic assemblies with long-range order". In: *Science* 371 (2021), p. 1368.

[98] Yang Zhao et al. "Chirality detection of enantiomers using twisted optical metamaterials". In: *Nat. comm.* 8 (2017), p. 14180.

[99] Itai Lieberman et al. "Plasmon-Resonance-Enhanced Absorption and Circular Dichroism". In: *Angew. Chem. Int. Ed.* 47 (2008), p. 4855.

[100] Maxim L. Nesterov et al. "The Role of Plasmon-Generated Near Fields for Enhanced Circular Dichroism Spectroscopy". In: *ACS Photonics* 3 (2016), p. 578.

[101] Lauren A Warning et al. "Nanophotonic approaches for chirality sensing". In: *ACS nano* 15 (2021), p. 15538.

[102] Itai Carmeli et al. "Broad band enhancement of light absorption in photosystem I by metal nanoparticle antennas". In: *Nano Lett.* 10 (2010), p. 2069.

[103] Tiago Ramos Leite et al. "Resonant Plasmonic–Biomolecular Chiral Interactions in the Far-Ultraviolet: Enantiomeric Discrimination of sub-10 nm Amino Acid Films". In: *Nano Lett.* 22 (2022), p. 7343.

[104] Wei Ma et al. "Attomolar DNA detection with chiral nanorod assemblies". In: *Nat. comm.* 4 (2013), p. 2689.

[105] B. M. Maoz. et al. "Amplification of Chiroptical Activity of Chiral Biomolecules by Surface Plasmons". In: *Nano Lett.* 13 (2013), p. 1203.

[106] N. A. Abdulrahman et al. "Induced Chirality through Electromagnetic Coupling between Chiral Molecular Layers and Plasmonic Nanostructures". In: *Nano Lett.* 12 (2012), p. 977.

[107] B. M. Maoz et al. "Plasmonic Chiroptical Response of Silver Nanoparticles Interacting with Chiral Supramolecular Assemblies". In: *J. Am. Chem. Soc.* 134 (2012), p. 17807.

[108] T. Wu et al. “A giant chiroptical effect caused by the electric quadrupole”. In: *Nanoscale* 9 (2017), p. 5110.

[109] W. Zhan et al. “Surface-Enhanced Circular Dichroism of Oriented Chiral Molecules by Plasmonic Nanostructures”. In: *J. Phys. Chem. C* 121 (2017), p. 666.

[110] L. M. Kneer et al. “Circular Dichroism of Chiral Molecules in DNA-Assembled Plasmonic Hotspots”. In: *ACS Nano* 12 (2018), p. 9110.

[111] S. Adhikari and M. Orrit. “Optically Probing the Chirality of Single Plasmonic Nanostructures and of Single Molecules: Potential and Obstacles”. In: *ACS Photonics* 9 (2022), p. 3486.

[112] K. Takanabe. “Photocatalytic water splitting: quantitative approaches toward photocatalyst by design”. In: *Acs Catal.* 7 (2017), p. 8006.

[113] A. Madani and B. Pieber. “In situ reaction monitoring in photocatalytic organic synthesis”. In: *ChemCatChem* 15 (2023), e202201583.

[114] J. Xie et al. “Highly selective oxidation of methane to methanol at ambient conditions by titanium dioxide-supported iron species”. In: *Nature Cat.* 1 (2018), p. 889.

[115] A. Chatterjee, L. Wang, and P. Voort. “Metalorganic frameworks in photocatalytic z-scheme heterojunctions: an emerging technology”. In: *Chem. Comm.* 59 (2023), p. 3627.

[116] L. Zhou et al. “Hot carrier multiplication in plasmonic photocatalysis”. In: *Proc. Natl. Acad. Sci. U.S.A.* 118 (2021), e2022109118.

[117] B. Puértolas et al. “Challenges and Opportunities for Renewable Ammonia Production via Plasmon-Assisted Photocatalysis”. In: *Adv. Energy Mater.* 12 (2022), p. 2103909.

[118] J. Huang et al. “Understanding the mechanism of plasmon-driven water splitting: Hot electron injection and a near field enhancement effect”. In: *Phys. Chem. Chem. Phys.* 23 (2021), p. 25629.

[119] R. Verma, R. Belgamwar, and V. Polshettiwar. “Plasmonic Photocatalysis for CO_2 Conversion to Chemicals and Fuels”. In: *ACS Mater. Lett.* 3 (2021), p. 574.

[120] Zhijie Zhu et al. “Promises of Plasmonic Antenna-Reactor Systems in Gas-Phase CO_2 Photocatalysis”. In: *Adv. Sci.* 10 (2023), p. 2302568.

[121] P. Christopher and M. Moskovits. “Hot Charge Carrier Transmission from Plasmonic Nanostructures”. In: *Annu. Rev. Phys. Chem.* 68 (2017), p. 379.

[122] P. Narang, R. Sundararaman, and H. A. Atwater. “Plasmonic hot carrier dynamics in solid-state and chemical systems for energy conversion”. In: *Nanophotonics* 5 (2016), p. 96.

[123] A. Manjavacas et al. “Plasmon-induced hot carriers in metallic nanoparticles”. In: *ACS Nano* 8 (2014), p. 7630.

[124] Z. Li and D. Kurouski. “Plasmon-Driven Chemistry on Mono- And Bimetallic Nanostructures”. In: *Acc. Chem. Res.* 54 (2021), p. 2477.

[125] H. Lee et al. “Surface Plasmon-Induced Hot Carriers: Generation, Detection, and Applications”. In: *Acc. Chem. Res.* 55 (2022), p. 3727.

[126] E. R. Newmeyer, J. D. North, and D. F. Swearer. “Hot carrier photochemistry on metal nanoparticles”. In: *J. Appl. Phys.* 132 (2022), p. 230901.

[127] Yonatan Sivan and Yonatan Dubi. “Recent developments in plasmon-assisted photocatalysisa personal perspective”. In: *Appl. Phys. Lett.* 117 (2020), p. 130501.

[128] Begoña Puértolas et al. “Challenges and opportunities for renewable ammonia production via plasmon-assisted photocatalysis”. In: *Adv. Energy Mater.* 12 (2022), p. 2103909.

[129] Luca Mascaretti and Alberto Naldoni. “Hot electron and thermal effects in plasmonic photocatalysis”. In: *J. Appl. Phys.* 128 (2020), p. 041101.

[130] Ye Huang et al. “Expanding the scope of antenna–reactor photocatalysts for strong visible light absorption in small transition metal nanoparticles”. In: *Appl. Phys. Lett.* 119 (2021), p. 043903.

[131] L. Zhou et al. “Light-driven methane dry reforming with single atomic site antenna-reactor plasmonic photocatalysts”. In: *Nat. Energy* 5 (2020), p. 61.

[132] Zhaoke Zheng, Takashi Tachikawa, and Tetsuro Majima. “Plasmon-enhanced formic acid dehydrogenation using anisotropic Pd–Au nanorods studied at the single-particle level”. In: *J. Am. Chem. Soc.* 137 (2015), p. 948.

[133] S. Pipolo and S. Corni. “Real-Time Description of the Electronic Dynamics for a Molecule Close to a Plasmonic Nanoparticle”. In: *J. Phys. Chem. C* 120 (2016), p. 28774.

[134] E. Coccia, F. Troiani, and E. Coccia. “Probing quantum coherence in ultrafast molecular processes: An ab initio approach to open quantum systems”. In: *J. Chem. Phys.* 148 (2018), p. 204112.

[135] E. Coccia et al. “Hybrid theoretical models for molecular nanoplasmonics”. In: *J. Chem. Phys.* 153 (2020).

[136] R. Rüger et al. *AMS 2022.1, SCM, Theoretical Chemistry, Vrije Universiteit, Amsterdam, The Netherlands*. 2022.

[137] H.-P. Breuer and F. Petruccione. *The Theory of Open Quantum Systems*. Oxford University Press, Oxford, 2006.

[138] R. Biele and R. D’Agosta. “A stochastic approach to open quantum systems”. In: *J. Phys.: Condens. Matter* 24 (2012), p. 273201.

[139] Robert Biele and Roberto DAgosta. "A stochastic approach to open quantum systems". In: *J. Phys. Condens. Matter* 24 (2012), p. 273201.

[140] E. Coccia and S. Corni. "Role of coherence in the plasmonic control of molecular absorption". In: *J. Chem. Phys.* 151 (2019), p. 044703.

[141] G. Dall'Osto et al. "Investigating ultrafast two-pulse experiments on single DNQDI fluorophores: a stochastic quantum approach". In: *Phys. Chem. Chem. Phys.* 22 (2020), p. 16734.

[142] G. Dall'Osto et al. "Stochastic Schrödinger equation for hot-carrier dynamics in plasmonic systems". In: *J. Chem. Phys.* 161 (2024), p. 124103.

[143] J. Dalibard, Y. Castin, and K. Mølmer. "Wave-function Approach to Dissipative Processes in Quantum Optics". In: *Phys. Rev. Lett.* 68 (1992), p. 580.

[144] K. Mølmer, Y. Castin, and J. Dalibard. "Wave-function Approach to Dissipative Processes in Quantum Optics". In: *J. Opt. Soc. Am. B* 10 (1993), p. 524.

[145] R. Dum, P. Zoller, and H. Ritsch. "Monte Carlo simulation of the atomic master equation for spontaneous emission". In: *Phys. Rev. A* 45 (1992), p. 4879.

[146] S. Klinkusch and J. C. Tremblay. "Resolution-of-identity stochastic time-dependent configuration interaction for dissipative electron dynamics in strong fields". In: *J. Chem. Phys.* 144 (2016), p. 184108.

[147] Gunter Hermann, Vincent Pohl, and Jean Christophe Tremblay. "An open-source framework for analyzing N-electron dynamics. II. Hybrid density functional theory/configuration interaction methodology". In: *J. Comput. Chem.* 38 (2017), p. 2378.

[148] Shaul Mukamel. *Principles of nonlinear optical spectroscopy*. Vol. 6. Oxford university press New York, 1995.

[149] ORBKIT *download link*. https://github.com/orbkit/orbkit. Accessed: 2020-10-05.

[150] Stefan Klinkusch, Peter Saalfrank, and Tillmann Klamroth. "Laser-induced electron dynamics including photoionization: A heuristic model within time-dependent configuration interaction theory". In: *J. Chem. Phys.* 131 (2009), p. 114304.

[151] J. C. Tremblay et al. "Dissipative many-electron dynamics of ionizing systems". In: *J. Chem. Phys.* 134 (2011), p. 044311.

[152] Vincent Pohl, Gunter Hermann, and Jean Christophe Tremblay. "An open-source framework for analyzing N-electron dynamics. I. Multideterminantal wave functions". In: *J. Comput. Chem.* 38 (2017), p. 1515.

[153] J. C. Tremblay and T. Carrington Jr. "Using preconditioned adaptive step size Runge-Kutta methods for solving the time-dependent Schrödinger equation". In: *J. Chem. Phys.* 121 (2004), p. 11535.

[154] Jacopo Tomasi et al. "Molecular properties in solution described with a continuum solvation model". In: *Phys. Chem. Chem. Phys.* 4 (2002), p. 5697.

[155] Luca Frediani et al. "A polarizable continuum model for molecules at diffuse interfaces". In: *J. Chem. Phys.* 120 (2004), p. 3893.

[156] S Miertu, E Scrocco, and JJCP Tomasi. "Electrostatic interaction of a solute with a continuum. A direct utilizaion of AB initio molecular potentials for the prevision of solvent effects". In: *Chem. Phys.* 55 (1981), p. 117.

[157] Benedetta Mennucci. "Polarizable continuum model". In: *Wiley Interdiscip. Rev. Comput. Mol. Sci.* 2 (2012), p. 386.

[158] Eric Cancès, Benedetta Mennucci, and Jacopo Tomasi. "A new integral equation formalism for the polarizable continuum model: Theoretical background and applications to isotropic and anisotropic dielectrics". In: *J. Chem. Phys.* 107 (1997), p. 3032.

[159] Filippo Lipparini et al. "A variational formulation of the polarizable continuum model". In: *J. Chem. Phys.* 133 (2010), p. 014106.

[160] S Corni and J Tomasi. "Enhanced response properties of a chromophore physisorbed on a metal particle". In: *J. Chem. Phys.* 114 (2001), p. 3739.

[161] Jacopo Tomasi, Benedetta Mennucci, and Roberto Cammi. "Quantum mechanical continuum solvation models". In: *Chem. Rev.* 105 (2005), p. 2999.

[162] Stefano Corni and Jacopo Tomasi. "Studying SERS from metal nanoparticles and nanoparticles aggregates with continuum models". In: *Surface-Enhanced Raman Scattering: Physics and Applications*. Springer, 2006, p. 105.

[163] S. Corni, S. Pipolo, and R. Cammi. "Equation of Motion for the Solvent Polarization Apparent Charges in the Polarizable Continuum Model: Application to Real-Time TDDFT". In: *J. Phys. Chem. A* 119 (2015), p. 5405.

[164] John David Jackson. *Classical electrodynamics*. John Wiley & Sons, 2021.

[165] M. Marsili and S. Corni. "Electronic Dynamics of a Molecular System Coupled to a Plasmonic Nanoparticle Combining the Polarizable Continuum Model and Many-Body Perturbation Theory". In: *J. Phys. Chem. C* 126 (2022), p. 8768.

[166] P. Grobas Illobre et al. "Time-Resolved Excited-State Analysis of Molecular Electron Dynamics by TDDFT and BetheSalpeter Equation Formalisms". In: *J. Chem. Theory Comput.* 17 (2021), p. 6314.

[167] M. Monti, M. Stener, and E. Coccia. "Electronic circular dichroism from real-time propagation in state space". In: *J. Chem. Phys* 158 (2023), p. 084102.

[168] Gonzalo Díaz Mirón et al. “Non-adiabatic couplings in surface hopping with tight binding density functional theory: The case of molecular motors”. In: *J. Chem. Theory Comput.* 20 (2024), p. 10602.

[169] Javier Vicario, Auke Meetsma, and Ben L Feringa. “Controlling the speed of rotation in molecular motors. Dramatic acceleration of the rotary motion by structural modification”. In: *Chem. Comm.* 47 (2005), p. 5910.

[170] Víctor García-López, Dongdong Liu, and James M Tour. “Light-activated organic molecular motors and their applications”. In: *Chem. Rev.* 120 (2019), p. 79.

[171] Nagatoshi Koumura et al. “Second generation light-driven molecular motors. Unidirectional rotation controlled by a single stereogenic center with near-perfect photoequilibria and acceleration of the speed of rotation by structural modification”. In: *J. Am. Chem. Soc.* 124 (2002), p. 5037.

[172] Nagatoshi Koumura et al. “Light-driven monodirectional molecular rotor”. In: *Nature* 401 (1999), p. 152.

[173] Richard A van Delden et al. “Exploring the boundaries of a light-driven molecular motor design: new sterically overcrowded alkenes with preferred direction of rotation”. In: *Org. Biomol. Chem.* 2 (2004), p. 1531.

[174] Edzard M Geertsema et al. “In control of the speed of rotation in molecular motors. Unexpected retardation of rotary motion”. In: *Chem. Comm.* 24 (2002), p. 2962.

[175] Matthijs KJ ter Wiel et al. “Increased speed of rotation for the smallest light-driven molecular motor”. In: *J. Am. Chem. Soc.* 125 (2003), p. 15076.

[176] Palas Roy et al. “Excited state dynamics in unidirectional photochemical molecular motors”. In: *J. Am. Chem. Soc.* 146 (2024), pp. 12255–12270.

[177] Marcus Elstner et al. “Self-consistent-charge density-functional tight-binding method for simulations of complex materials properties”. In: *Phys. Rev. B* 58 (1998), p. 7260.

[178] Ben Hourahine et al. “DFTB+, a software package for efficient approximate density functional theory based atomistic simulations”. In: *J. Chem. Phys.* 152 (2020), p. 124101.

[179] Sebastian Mai, Philipp Marquetand, and Leticia González. “Nonadiabatic dynamics: The SHARC approach”. In: *Wiley Interdiscip. Rev. Comput. Mol. Sci.* 8 (2018), e1370.

[180] Chunping Hu, Osamu Sugino, and Kazuyuki Watanabe. “Performance of Tamm-Dancoff approximation on nonadiabatic couplings by time-dependent density functional theory”. In: *J. Chem. Phys.* 140 (2014), p. 054106.

[181] Basile FE Curchod and Todd J Martínez. "Ab initio nonadiabatic quantum molecular dynamics". In: *Chem. Rev.* 118 (2018), p. 3305.

[182] Giovanni Granucci and Maurizio Persico. "Critical appraisal of the fewest switches algorithm for surface hopping". In: *J. Chem. Phys.* 126 (2007), p. 134114.

[183] Christopher R Hall et al. "Ultrafast dynamics in light-driven molecular rotary motors probed by femtosecond stimulated Raman spectroscopy". In: *J. Am. Chem. Soc.* 139 (2017), p. 7408.

[184] Matias Herran et al. "Tailoring plasmonic bimetallic nanocatalysts toward sunlight-driven H_2 production". In: *Adv. Funct. Mater.* 32 (2022), p. 2203418.

[185] Dennis Mayer, Fabiano Lever, and Markus Gühr. "Time-resolved x-ray spectroscopy of nucleobases and their thionated analogs". In: *Photochem. Photobiol.* 100 (2024), p. 275.

[186] Christopher Ehlert, Markus Gühr, and Peter Saalfrank. "An efficient first principles method for molecular pump-probe NEXAFS spectra: Application to thymine and azobenzene". In: *J. Chem. Phys.* 149 (2018), p. 144112.

[187] Shota Tsuru et al. "An assessment of different electronic structure approaches for modeling time-resolved x-ray absorption spectroscopy". In: *Struct. Dyn.* 8 (2021), p. 024101.

[188] Woojin Park et al. "Impact of the dynamic electron correlation on the unusually long excited-state lifetime of thymine". In: *J. Phys. Chem. Lett.* 12 (2021), p. 4339.

[189] M. Stener, G. Fronzoni, and M. de Simone. "Time dependent density functional theory of core electrons excitations". In: *Chem. Phys. Lett.* 373 (2003), p. 15.

[190] Francesco Montorsi et al. "Soft X-ray Spectroscopy Simulations with Multiconfigurational Wave Function Theory: Spectrum Completeness, Sub-eV Accuracy, and Quantitative Reproduction of Line Shape". In: *J. Chem. Theory Comput.* 18 (2022), p. 1003.

[191] Sonia Coriani et al. "Coupled-cluster response theory for near-edge x-ray-absorption fine structure of atoms and molecules". In: *Phys. Rev. A* 85 (2012), p. 022507.

[192] Christopher Ehlert and Tillmann Klamroth. "The quest for best suited references for configuration interaction singles calculations of core excited states". In: *J. Comput. Chem.* 38 (2017), p. 116.